

https://dspace.org/

The design and implementation of an acoustic phased array transmitter for the demonstration of MIMO techniques

Middleton, Sarah

2011-11-07
http://hdl.handle.net/10539/10713

Downloaded from a DSpace repository. https://dspace.org/

THE DESIGN AND IMPLEMENTATION OF AN ACOUSTIC PHASED ARRAY TRANSMITTER FOR THE DEMONSTRATION OF MIMO TECHNIQUES

Sarah Middleton

A dissertation submitted to the Faculty of Engineering and the Built Environment, University of the Witwatersrand, Johannesburg, in fulfilment of the requirements for the degree of Master of Science in Engineering.

Johannesburg, 2011

Declaration

I declare that this dissertation is my own, unaided work, other than where specifically acknowledged. It is being submitted for the degree of Master of Science in Engineering in the University of the Witwatersrand, Johannesburg. It has not been submitted before for any degree or examination in any other university.

Signed this _____ day of _____ 2011

_____

Sarah Middleton

Abstract

MIMO radar algorithms are the latest generation of techniques that can be applied to array radars. They offer the potential to improve the radar resolution, increase the number of targets that can be identified and give added flexibility in beampattern design. However, little experimental data demonstrating MIMO radar is available because radar arrays are already expensive systems and MIMO extends the complexity and cost further. An acoustic array, which works on the same principles as a radio frequency radar array, can be built at a fraction of the cost of a real radar system. The novel contribution of this project was the demonstration of MIMO radar techniques on an acoustic array, which was designed and built for this purpose.

To achieve the project objectives, the theory of traditional phased array radar techniques and MIMO techniques was researched. The phased array and MIMO techniques were also simulated under narrowband and wideband conditions, and the strengths and weaknesses of each were highlighted. This was followed by the design and implementation of a low cost audible acoustic transmitter array to be used with an existing receiver array to demonstrate the investigated array radar techniques. Finally, the techniques were tested on the hardware platform.

The simulation and hardware test results were used to evaluate and compare the performance of phased array and MIMO radar techniques. The beampattern design flexibility that is offered by MIMO radar was demonstrated with the transmission and measurement of omnidirectional, single-lobed and multi-lobed MIMO beampatterns. Also, parameter estimation experiments were performed where phased array and MIMO radar signals were transmitted. Phased array techniques were shown to be simple, effective and robust. The MIMO Capon, APES and GLRT parameter estimation techniques were shown to be sensitive to the type of signals transmitted, and in most cases, the added complexity of these techniques did not lead to improved target parameter estimation results. However, the MIMO technique of transmitter beamforming on reception gave high resolution target range and angle estimates, living up to the expectations placed on MIMO radar.

I dedicate this dissertation to my parents

∽ Jill and Ian Middleton ∼

and to my grandparents

∽ Pat and Frank Lucas, and Kathleen Middleton ∼

who are my inspiration in all I do.

Acknowledgements

I would like to extend my thanks to my four supervisors, Anton van Wyk, Jacques Cilliers, Pascale Jardin and Florence Nadal, who guided and assisted me throughout my Masters. I thank Professor van Wyk of the University of the Witwatersrand who helped me to choose the topic, and was always available to share his expertise. I also thank him for the opportunities of spending 10 months in France and attending a conference in China. I thank Jacques Cilliers of the Defence, Peace, Safety and Security (DPSS) at the CSIR for his quick response to all of my emails, for helping me to get a better understanding of radar in the "real world", and for the valuable advice which helped to bring this dissertation to completion. I thank Pascale Jardin and Florence Nadal of ESIEE, Paris for the many hours that they spent familiarising themselves with my project when I arrived in Paris, and the patience with which they guided me through some of the more challenging mathematics that appears in this dissertation. It was under their guidance that my project began to take form.

I extend my thanks to the many sources of funding that enabled me to do this project. Firstly, I thank the CSIR who awarded me a Ledger Scholarship. I thank the University of the Witwatersrand for the Postgraduate Merit Award which covered my university fees and the National Research Foundation (NRF) who funded my first year of study. I also extend my thanks to the Region Île de France who funded my studies in Paris.

Finally, I would like to thank my family and friends who supported me on my endeavour to complete this Masters. I thank Thomas Sprich for his patience and for the hours he spent reading this work and the honesty with which he evaluated it. I extend my gratitude to my parents who made it possible for me to complete this research. I thank my dad, Ian Middleton, for his many innovative contributions to this project, and his guidance when the going got tough. And lastly, I thank my mom, Jill Middleton, for her endless patience, encouragement and love.

Contents

Declaration i

Abstract ii

Acknowledgements iv

Contents v

List of Figures xi

List of Tables xvi

Nomenclature xxi

1 Introduction 1

1.1 Problem Statement 2

1.1.1 Theoretical Investigation 3

1.1.2 Hardware Design, Implementation and Testing 3

1.2 Approach 3

2 Literature Review and Background Theory 5

2.1 Radar Signal Properties 5

2.1.1 Propagating Plane Waves 5

2.1.2 Signal Modulation 6

2.1.3 Near and Far-Field 8

2.1.4 Narrowband Signals 9

2.1.5 Sampling a Narrowband Signal 10

2.2 Phased Array Model Representation 11

2.2.1 The Steering Vector 11

2.2.2 The Sampled Received Signal 14

2.2.3 Statistical Assumptions and the Covariance Matrix 15

2.2.4 Spectral Representation 16

2.2.5 The Array Beampattern 17

2.3 Phased Array Beamforming Techniques 19

2.3.1 Data Independent Beamforming 20
2.3.2 Statistically Optimum Beamforming 21
2.4 Parameter Estimation Techniques for Phased Array 25
2.4.1 Spectral Techniques 26
2.4.2 Parametric Methods 27
2.5 A Wideband Beamformer 29
2.5.1 Wideband Phased Array Model 29
2.6 Introduction to MIMO Radar 31
2.6.1 Overview of MIMO Radar Operation 32
2.7 The MIMO Signal Model 34
2.8 MIMO Techniques for Parameter Estimation 37
2.8.1 Capon 37
2.8.2 Amplitude and Phase Estimation (APES) 38
2.8.3 Generalised Likelihood Ratio Test (GLRT) 39
2.8.4 Capon Approximate Maximum Likelihood (CAML) 39
2.9 Probing Signal Design 41
2.9.1 Waveform Design for Unknown Target Locations 42
2.9.2 Maximum Power Waveform Design for Localised Targets . . 43
2.9.3 Beampattern Matching Design 44
2.10 Transmitter Beamforming on Reception (TBR) 47
2.11 Analyses of MIMO Radar 48
2.11.1 Practical Applications of MIMO Radar 48
2.11.2 Beamforming 50

3 Project Motivation and Objectives 52
3.1 Project Motivation 52
3.2 Project Objectives 53
3.3 Project Deliverables 53
3.3.1 Algorithms 53
3.3.2 Simulation 54
3.3.3 Hardware System 54
3.3.4 Software Applications 55

4 Narrowband Simulations 57
4.1 Phased Array Simulations 57
4.1.1 Simulation Parameters 57
4.1.2 Phased Array Techniques for Parameter Estimation 58
4.1.3 Beampattern Design 61
4.2 MIMO Simulations 64
4.2.1 Simulation Parameters 65
4.2.2 MIMO Techniques for Parameter Estimation 65

4.2.3 Probing Signal Design 71
4.2.4 Transmitter Beamforming on Reception (TBR) 80
4.3 Summary 82

5 Wideband Beamforming Techniques and Simulations 83
5.1 Breakdown of the Narrowband Assumption 83
5.2 Time Delay Wideband (TDWB) Beamformer 84
5.3 Filter and Weight Wideband (FWWB) Beamformer 85
5.4 Phased Array Simulations 87
5.4.1 Wideband Beampatterns 87
5.4.2 Wideband Simulation Method 89
5.4.3 TDWB Beamformer 90
5.4.4 FWWB Beamformer 91
5.5 MIMO Simulations 93
5.5.1 Wideband Beampatterns 94
5.5.2 Wideband Simulation Method 95
5.5.3 TDWB Beamformer 97
5.5.4 FWWB Beamformer 101
5.6 Summary 105

6 Hardware System Design 107
6.1 System Design Parameters 108
6.2 Receiver Array 108
6.2.1 Microphones 109
6.2.2 Microphone Biasing Circuit 110
6.2.3 Anti-Aliasing Filter 110
6.2.4 High-pass Filter, Gain and DC Bias 111
6.2.5 Analogue to Digital Converter (ADC) 112
6.2.6 Receiver Board Power Supply 113
6.2.7 Additional Amplifier Stage 113
6.3 Transmitter Array 114
6.3.1 Digital to Analogue Converter (DAC) 115
6.3.2 Reconstruction Filter 116
6.3.3 High-pass Filter and Amplifier 118
6.3.4 Speakers 120
6.3.5 Transmitter Board Power Supply 123
6.4 Master Control Unit (MCU) 123
6.4.1 MCU Platform 124
6.4.2 MCU Architecture and Modules 124
6.5 The PC 128
6.5.1 C Application to Receive Ethernet Packets 128

6.5.2 MATLAB Application for Signal Processing 129
6.6 Summary 131

7 System Calibration and Testing 132
7.1 Calibration 132
7.1.1 The Effect of Calibration Errors 133
7.1.2 FIR Filter Calibration Method 135
7.1.3 Transmitter Beampattern Calibration Method 136
7.1.4 Calibration Test Protocol 137
7.2 System Testing 139
7.2.1 Beampattern Design 140
7.2.2 Target Parameter Estimation 143
7.3 Summary 145

8 Results and Analysis 147
8.1 Calibration 147
8.1.1 Receiver Calibration 147
8.1.2 Transmitter Calibration 150
8.2 Beampatterns 155
8.2.1 Omnidirectional MIMO Pattern 155
8.2.2 Patterns with a Single Mainlobe 157
8.2.3 Patterns with Three Mainlobes 161
8.2.4 Analysis of Beampattern Results 164
8.3 Parameter Estimation 168
8.3.1 Range Estimation 169
8.3.2 Angle Estimation 171
8.3.3 Single Target 172
8.3.4 Three Targets 182
8.3.5 Two Closely Spaced Targets 193
8.3.6 Analysis of Parameter Estimation Results 198
8.3.7 Comparison of MIMO and Phased Array 202

9 Conclusions and Recommendations 206
9.1 Conclusions 206
9.1.1 Hardware System 206
9.1.2 Phased Array 207
9.1.3 MIMO Radar 209
9.1.4 Comparison of Phased Array and MIMO Radar 211
9.2 Recommendations 211
9.2.1 Hardware 212
9.2.2 Research Avenues 212

A Mathematical Concepts **214**
A.1 Scalar, Vector and Matrix Operations 214
A.2 Linear Vector Spaces 215
A.2.1 Gram-Schmidt Orthogonalisation Procedure 218
A.3 Matrix Spectral Theory 218
A.4 Lagrange Multipliers 221

B The Covariance Matrix **223**
B.1 The Discrete Time Covariance Matrix 223
B.2 Properties of the Covariance Matrix 225
B.3 Properties of the Covariance Matrix Eigenvalues and Eigenvectors . 225
B.4 The Spatial Covariance Matrix 226
B.5 Methods for Spatial Covariance Matrix Estimation 227

C MIMO Communications **229**
C.1 A Wireless Communication System compared to Radar 229
C.2 Degrees of Freedom 230
C.3 SIMO System 230
C.4 MISO System 231
C.5 MIMO System 232
C.6 MIMO System Architectures 234
C.6.1 Decorrelator Bank Architecture 235
C.6.2 Linear MMSE Receiver Architecture 236
C.6.3 Successive Interference Cancellation (SIC) Architecture . . . 238

D Mathematical Derivations **240**
D.1 Derivation of the Capon Method 241
D.2 Derivation of the APES Method 242
D.3 Derivation of the GLRT 244

E Implementation of the Beampattern Matching Design **250**

F Transmitter Design **256**
F.1 Amplifier Prototypes 256
F.2 Transmitter Prototype Measurements 259

G Photographs of the Hardware System **262**

H PCB Designs **267**
H.1 Microphone Board 267
H.2 Add-on Receiver Amplifier Board 268
H.3 Transmitter Analogue Board 269
H.4 Speaker Board 272

H.5 Chemical Etching Process 273

I MCU Architecture and Operation 276

I.1 MCU Architecture 276
I.2 Ethernet 281
I.3 Receiver SPI 283
I.3.1 SPI Interface 283
I.3.2 VHDL Module for SPI 285
I.4 Transmitter SPI 287
I.4.1 SPI Interface 287
I.4.2 VHDL Module for SPI 288

J Speaker and Array Characterisation 290

K Tables of Results 297

List of Figures

2.1 Definition of θ. 6
2.2 Amplitude modulation. 7
2.3 The baseband frequency spectrum of a band-limited signal $s(t)$. . . . 7
2.4 The frequency spectrum of a signal $s(t)$ modulated by carrier $e(t)$. . 8
2.5 An array receiving the signal transmitted by a point source. 8
2.6 An array receiving the signal from a point source. 12
2.7 Definition of array and source distances. 12
2.8 Derivation of the electric steering angle. 13
2.9 A narrowband beamformer. 20
2.10 The multiple side lobe canceller architecture. 22
2.11 A wideband beamformer 30
2.12 Illustration of MIMO radar. 32
2.13 MIMO Virtual Arrays. 34
2.14 Transmitter and receiver location parameters. 35
2.15 Transmitter beamforming on reception (TBR). 47
4.1 Phased array angle estimation spectrums. 58
4.2 Narrowband phased array estimation MSEs as noise varies. 59
4.3 Phased array angle estimation spectrums for coherent sources. . . . 60
4.4 Narrowband phased array MSEs with coherent signals. 60
4.5 Phased array pattern designed by LCMV. 62
4.6 Phased array pattern designed by beampattern matching. 64
4.7 MIMO parameter estimation spectrums. 65
4.8 Ten independent waveforms. 68
4.9 Six independent waveforms. 68
4.10 Two independent waveforms. 69
4.11 Spectrums when all transmitted waveforms are dependent. 69
4.12 MIMO spectrums illustrating range dependence. 70
4.13 Results for the omnidirectional beampattern design. 72
4.14 Results for the maximum power beampattern design. 73
4.15 Results for Pascale's beampattern design. 75
4.16 Results for the beampattern matching design. 77
4.17 MSE in estimation of θ for narrowband MIMO. 79

4.18 MSE in estimation of β for narrowband MIMO. 80
4.19 MIMO narrowband TBR spectrums. 81
5.1 Illustration of phase variations for a given time delay. 84
5.2 A filter and weight wideband (FWWB) beamformer. 87
5.3 Effect of signal bandwidth on phased array patterns. 88
5.4 Illustration of wideband phased array simulation technique. 90
5.5 Range-angle charts. 91
5.6 Phased array NB and TDWB beamforming spectrums. 91
5.7 FIR filter responses for FWWB processing 92
5.8 MSE in target location estimations for FWWB phased array. 93
5.9 Effect of wideband signals on MIMO beampatterns. 94
5.10 Flow diagram of the wideband simulations. 95
5.11 Simulated MIMO signals. 96
5.12 Simulation technique for TBR. 97
5.13 TBR range-angle charts with Capon weights. 99
5.14 TBR range-angle charts with TDWB beamformer. 99
5.15 TBR spectrums 100
5.16 MIMO spectrums with and without wideband processing. 103
5.17 MSEs in estimation of θ for FWWB MIMO for target at $-40°$. . . . 104
5.18 MSEs in estimation of β for FWWB MIMO for target at $-40°$. . . . 104
5.19 MSEs in estimation of θ for FWWB MIMO for target at $0°$. 105
6.1 The hardware system. 107
6.2 Block diagram of the phased array receiver. 109
6.3 The frequency response of the microphones. 109
6.4 Microphone biasing circuit. 110
6.5 Sixth order Type I Chebyshev anti-aliasing filter on the receiver. . . 111
6.6 Receiver high-pass filter and amplifier with DC bias. 111
6.7 Receiver power supply. 113
6.8 Regulator to convert 5 V to 2.5 V. 113
6.9 Additional receiver amplifier stage. 114
6.10 Block diagram of the phased array transmitter. 114
6.11 DAC on the transmitter. 115
6.12 Reconstruction filter on the transmitter. 117
6.13 Transmitter high-pass filter and amplifier. 118
6.14 Simulation of the transmitter amplifier. 120
6.15 Frequency response of the simulated transmitter amplifier. 121
6.16 Circuit to measure the speaker impedance. 121
6.17 The impedance of the speaker as a function of frequency. 122
6.18 The frequency response of a typical microphone-speaker pair. 123
6.19 Transmitter power supply. 123

6.20 MCU interfaces to a PC, transmitter and receiver. 124
6.21 Top level MCU modules. 125
6.22 Ethernet interface. 125
6.23 SPI interface between FPGA and receiver. 126
6.24 Connections between MCU and transmitter. 127
6.25 Flowchart of the C application. 130
7.1 Effect of variations in array element amplitude on beampattern. . . . 133
7.2 Effect of variations in array element phase on beampattern. 134
7.3 Pattern deviation as a function of phase variation. 135
7.4 Experimental setup for receiver calibration. 138
7.5 Experimental setup for transmitter calibration. 139
7.6 MIMO omnidirectional pattern. 140
7.7 Beampatterns with mainlobes at 20°. 141
7.8 Beampatterns with mainlobes at −20°, 0° and 20°. 141
7.9 Definition of the array DOA angles. 142
7.10 Experimental setup with a single target. 143
7.11 Experimental setup with three targets. 144
7.12 Experimental setup with two closely spaced targets. 145
8.1 The calibration signal received on Channel 1. 148
8.2 A segment of the 16 received signals before and after calibration. . . 148
8.3 Frequency responses of the receiver calibration FIR filters. 149
8.4 FIR filter calibration of received signals. 150
8.5 FIR filter calibration of transmitted signals. 151
8.6 Transmitter calibration on a chirp signal. 152
8.7 Uncalibrated and calibrated beampatterns. 153
8.8 Omnidirectional MIMO beampatterns. 156
8.9 Correlations of the omnidirectional transmitted signals. 156
8.10 Measured patterns with one main lobe in decibels. 158
8.11 Signal PDFs for different beampatterns. 158
8.12 Phased array patterns with one main lobe. 159
8.13 Pascale's MIMO pattern with one main lobe. 160
8.14 Beampattern matching MIMO patterns with one main lobe. 161
8.15 Patterns with three main lobes in decibels. 161
8.16 Beampattern matching phased array patterns with three main lobes. 162
8.17 LCMV phased array patterns with three main lobes. 163
8.18 Pascale's MIMO patterns with three main lobes. 164
8.19 Beampattern matching MIMO patterns with three main lobes. . . . 165
8.20 One target and a phased array pattern. 173
8.21 One target and omnidirectional MIMO pattern. 176
8.22 One target and omnidirectional MIMO pattern with TBR. 177

8.23 One target and Pascale's MIMO pattern. 178
8.24 The signals transmitted by Pascale's design. 179
8.25 One target and Pascale's MIMO pattern with TBR. 180
8.26 One target and beampattern matching MIMO pattern. 181
8.27 One target and beampattern matching MIMO pattern with TBR. . 182
8.28 Three targets and beampattern matching phased array pattern. . . . 183
8.29 Three targets with LCMV phased array pattern. 185
8.30 Three targets and omnidirectional MIMO pattern. 187
8.31 Three targets and omnidirectional MIMO pattern with TBR. 188
8.32 Three targets and Pascale's MIMO pattern. 189
8.33 Three targets and Pascale's MIMO pattern. 190
8.34 Three targets and beampattern matching MIMO pattern. 191
8.35 Three targets and beampattern matching MIMO pattern with TBR. 192
8.36 Two closely spaced targets and phased array results. 194
8.37 Two closely spaced targets and omnidirectional MIMO pattern. . . . 195
8.38 Two closely spaced targets and Pascale's MIMO pattern. 196
8.39 Two closely spaced targets and a beampattern matching pattern. . . 198
A.1 Two dimensional Gram-Schmidt orthogonalisation. 219
A.2 Commutating diagram for solving a matrix equation. 221
C.1 A SIMO system. 231
C.2 Definition of the angle for a SIMO system. 231
C.3 A MISO system. 232
C.4 Definition of the angle for a MISO system. 232
C.5 Line of sight MIMO system. 233
C.6 MIMO system multiple paths. 233
C.7 Successive Interference Cancellation 238
F.1 Prototype 2: Class AB amplifier. 257
F.2 Prototype 3: Audio amplifier chip circuit. 257
F.3 The transmitter prototype board. 259
F.4 Transmitter prototype signals. 260
F.5 Frequency response of the transmitter prototype. 261
G.1 The Virtex 5 FPGA on an ML505 development board. 262
G.2 The transmitter components. 263
G.3 The receiver components 264
G.4 The integrated hardware system. 265
G.5 Angle measurement system. 266
G.6 Target detection. 266
H.1 The microphone PCB. 267
H.2 Add-on Receiver amplifier board. 268
H.3 The transmitter PCB layout with component names and placing. . . 270

H.4 Speaker board PCB design. 273
I.1 MCU system block diagram. 277
I.2 The Ethernet packet with the number of bytes of each component. . 282
I.3 Timing diagram for the receiver SPI. 284
I.4 The receiver ADC SPI control register. 284
I.5 Timing diagram for the receiver SPI VHDL peripheral. 287
I.6 Timing diagram for the transmitter SPI interface 288
I.7 Timing diagram for the transmitter SPI VHDL peripheral. 289
J.1 First investigation of speaker patterns. 291
J.2 Speaker patterns of an element of the original array. 292
J.3 Patterns of a loose speaker under different conditions. 294
J.4 Hardware modifications made to investigate the speaker patterns. . . 295
J.5 8 kHz and 10 kHz beampatterns of individual speakers. 295
J.6 The wooden array prototype. 296
J.7 asdfas 296

List of Tables

4.1 Weights for the LCMV 63
4.2 Mean and standard deviation of estimates of θ (°) 66
4.3 Mean and standard deviation of estimates of $\beta(\theta)$. 67
5.1 The empirically selected phased array tap variables. 93
5.2 Optimum values of the tap variable J. 102
5.3 Empirically selected values of tap variable J. 102
7.1 Beampattern deviation for errors in amplitude calibration. 133
8.1 Comparison of the transmitted beampatterns. 165
F.1 Performance measures of the three prototypes 258
H.1 Bill of materials for the receiver add-on amplifier board. 269
H.2 Bill of materials for the transmitter analogue board. 271
H.3 Achieved spacing of speaker pairs. 274
I.1 FPGA IP modules. 278
I.2 FPGA inputs and outputs. 279
I.3 Receiver ADC control register bit settings. 285
K.1 Received signal SNRs when target detection was performed. 298
K.2 Single target location estimates when PA1 was transmitted. 299
K.3 Single target location estimates when OMNI was transmitted. 300
K.4 Single target location estimates when MIMOPD1 was transmitted. . 301
K.5 Single target location estimates when MIMOBM1 was transmitted. . 302
K.6 Three target location estimates when PABM3 was transmitted. . . . 303
K.7 Three target location estimates when PALCMV3 was transmitted. . 304
K.8 Three target location estimates when OMNI was transmitted. 305
K.9 Three target location estimates when MIMOPD3 was transmitted. . 306
K.10 Three target location estimates when MIMOBM3 was transmitted. . 307
K.11 Small separation location estimates when PA was transmitted. . . . 308
K.12 Small separation location estimates when OMNI was transmitted. . 309
K.13 Small separation location estimates when MIMOPD was transmitted. 310
K.14 Small separation location estimates when MIMOBM was transmitted. 311

Nomenclature

Acronyms

ADC	Analogue to Digital Converter
APES	Amplitude and Phase Estimation
BJT	Bipolar Junction Transistor
CAML	Capon Approximate Maximum Likelihood
CRC	Cyclic Redundancy Check
CSIR	Council for Scientific and Industrial Research
DAC	Digital to Analogue Converter
DARPA	Defense Advanced Research Projects Agency
DML	Deterministic Maximum Likelihood
ECM	Electronic Counter Measures
EM	ElectroMagnetic
FCC	Federal Communications Commission
FD	Fractional Delay
FFT	Fast Fourier Transform
FIR	Finite Impulse Response
FPGA	Field-Programmable Gate Array
FWWB	Filter and Weight WideBand
GLRT	Generalised Likelihood Ratio Test
GMTI	Ground Moving Target Indicator

HF	High Frequency
i.i.d.	Independently and identically distributed
IP	Intellectual Property
LCMV	Linearly Constrained Minimum Variance
LS	Least Squares
MCU	Master Control Unit
MIMO	Multiple Input Multiple Output
MISO	Multiple Input Single Output
ML	Maximum Likelihood
MMSE	Minimum Mean Square Error
MSC	Multiple Side lobe Canceller
MSE	Mean Square Error
MUSIC	MUltiple SIgnal Classification
OTH	Over-The-Horizon
PAPR	Peak to Average Power Ratio
PC	Personal Computer
PCB	Printed Circuit Board
PDF	Probability Density Function
QPSK	Quadrature Phase Shift Keying
RF	Radio Frequency
RFI	Radio Frequency Interference
RMS	Root Mean Square
SFD	Start of Frame Delimiter
SIC	Successive Interference Cancellation
SIMO	Single Input Multiple Output
SNR	Signal to Noise Ratio

SPI	Serial Peripheral Interface
SQP	Semi-definite Quadratic Program
STAP	Space Time Adaptive Processing
TBR	Transmitter Beamforming on Reception
TDWB	Time Delay WideBand
THD	Total Harmonic Distortion
ULA	Uniform Linear Array
UWB	Ultra-Wideband

Circuit Elements

C	Capacitance
G	Gain
i	AC current
Q	Transistor
R	Resistance
U	Application specific chip
V	DC Voltage
v	AC voltage
Z	Impedance

Matrices

$\hat{\mathbf{B}}$	Sum of the squared steering vector for the target locations.
Λ	Diagonal matrix whose entries are the eigenvalues of a covariance matrix.
$\mathbf{A}$	The steering vectors for an array which receive signals from multiple sources.
$\mathbf{B}$	Diagonal matrix whose entries are the target complex amplitudes.
$\mathbf{R}$	Signal covariance matrix.
$\mathbf{S}$	Transmitted signal matrix.

U	Eigenvectors of a covariance matrix.
X	Received signal matrix.
Z	Noise and interference matrix.

Scalars

β	Target complex amplitude which is proportional to radar cross section.
λ	Eigenvalue of the received signal covariance matrix.
λ	Wavelength [m].
μ	Eigenvalue of the transmitted signal covariance matrix.
ω	Temporal frequency [rad/s].
σ	The standard deviation of the noise.
τ	A time delay.
θ	DOA of a wave defined counter-clockwise around the x-axis [°].
B	Signal bandwidth [Hz or rad/s].
b	Array response.
c	Velocity of propagation of a wave [ms^{-1}].
D	Array length [m].
d	The distance between array elements [m].
E	Energy field.
e	A complex plane wave propagating through space.
g	The gain on an array element.
I	Transmitted signal current function.
J	The tap variable for a wideband array.
k	Wave-number ($2\pi/\lambda$) [rad/m].
L	Number of antennas in an array.
M	The number of received signals with discrete DOAs.
N	The number of time samples

P Array power.

p Total power transmitted by an array.

R The distance from a source or target to an array [m].

s Transmitted signal.

t Time [s].

y Beamformer output.

Vectors

$\mathbf{a}$ Array steering vector for a source with DOA θ.

$\mathbf{k}$ Two-dimensional spatial frequency [rad/m].

$\mathbf{p}$ Eigenvector of the transmitted signal covariance matrix.

$\mathbf{q}$ Eigenvector of the received signal covariance matrix.

$\mathbf{s}$ Set of signals transmitted by the elements of an array.

$\mathbf{u}$ Eigenvector associated with the largest eigenvalue of $\hat{\mathbf{B}}$.

$\mathbf{w}$ Narrowband beamformer weights.

$\mathbf{x}$ The set of signals received by the elements of an array.

$\mathbf{z}$ The additive noise and interference received by the elements of an array.

$\mathbf{x}$ A location in two-dimensional space with components x and y [m].

Chapter 1

Introduction

Phased arrays have a wide range of applications in fields such as radar [1], sonar, radio astronomy [2], tomography [3], seismology [4, 5] and cellular telecommunications [6]. However systems in each of these domains require technologically advanced and expensive equipment. A small, low cost system that can illustrate the concepts of phased arrays in a simple manner is a valuable educational tool. Such a system has been realised at the Council for Scientific and Industrial Research (CSIR) where acoustic phased array receivers have been designed and implemented [7, 8]. These systems use low cost and easily available components, such as microphones in the place of antennas, to illustrate phased array concepts. The CSIR's phased array receivers and a single transmitter have been used to successfully demonstrate the operation of angle and range detection techniques for phased array radar.

The development of a phased array transmitter is the natural extension to the system described above, to more closely model a real radar system. A transmitter array is used so that energy can be transmitted in narrow beams [9] by a process known as beamforming. This allows a beam to be focused in the direction of a target which reflects the signals back to the receiver. Also, significantly lower levels of energy are reflected by clutter which can obscure the signal of interest. This ensures a superior signal to noise ratio (SNR).

An emerging field of radar, which has been dubbed a "generalisation of phased array" [10], is Multiple Input Multiple Output (MIMO) radar. Whereas each element in a phased array transmitter transmits the same signal, which may have been multiplied by a complex weight, MIMO radar transmitting elements can transmit signals from a diverse set. In the extreme case, the set of transmitted signals can be orthogonal to one another. Independence between the signals is exploited and

improved performance can be achieved [11].

The complexity of MIMO radar architecture is greater than that of phased array systems leading to increased manufacturing costs when compared to phased array radar. For this reason, most MIMO radar investigation has been performed in the realm of simulations. There is very little MIMO experimental data available in the literature.

Since its introduction in 2003 [12], MIMO radar has roused concerns amongst some radar researchers who consider that its benefits do not outweigh its increased complexity [10]. They believe that in most cases, similar results can be achieved with phased array systems. The current literature lacks a definitive study comparing the performance of phased array and MIMO radar systems [10].

The analogue components of a phased array receiver and a MIMO receiver are identical if the weighting and signal processing are realised in software. Therefore, the previously implemented phased array receivers can also be used as MIMO receivers. In addition, if each channel of an array transmitter can be fed with a separate waveform, it can operate as a phased array and MIMO transmitter.

So, a low cost system capable of testing phased array and MIMO radar algorithms can add great value to the field of radar array processing and aid the understanding of MIMO radar. With slight alterations to the design of a phased array, such a system can be implemented. It is the ultimate aim of this research to be able to shed some light on the practical problems surrounding MIMO radar with a hardware system.

1.1 Problem Statement

The project undertaken was to design and build an acoustic phased array transmitter capable of also operating as a MIMO radar transmitter. The array was used with an existing receiver to test a selection of phased array and MIMO radar algorithms. The steps followed to achieve this outcome were two-fold. Firstly, a theoretical study of phased array and MIMO algorithms was performed. This study included simulation analyses of the different methods. Where necessary, modifications to the algorithms were made. Secondly, the hardware system and the software interfacing to it, were designed, built and tested. The theoretical and hardware requirements are described in more detail below.

1.1.1 Theoretical Investigation

In the theoretical investigation section of this work, classical phased array techniques and modern MIMO techniques were studied. Simulations were performed to demonstrate the capabilities, strengths and weaknesses of the different techniques, and to provide a backdrop against which to compare the results obtained with the hardware system.

Also, since MIMO techniques are a relatively new and unexplored subset of the well-established field of array signal processing, the necessary extensions were made to the MIMO algorithms so that they could be applied on the acoustic system used for testing.

1.1.2 Hardware Design, Implementation and Testing

The crux of the hardware problem was the design and implementation of an acoustic phased array transmitter with MIMO capabilities. The array was designed to be compatible with the 16 element acoustic phased array receiver which was available for testing from the CSIR. A field-programmable gate array (FPGA) development kit was available for the implementation of the hardware control unit. Therefore, the transmitting array, receiving array and a computer were interfaced by a control unit implemented on a FPGA. Software to enable transmission and reception of phased array and MIMO signals on the hardware system were also be developed.

1.2 Approach

This section describes the approach followed to assimilate the required knowledge and achieve the outcomes summarised in the problem statement. It also acts as a guide to the rest of this dissertation.

A background to radar signal processing, phased array techniques and MIMO radar techniques is presented, in the form of an in depth literature review, in Chapter 2. Once the relevant theory has been introduced, the project is further contextualised and the objectives of the project are defined in Chapter 3.

Narrowband simulations of the phased array and MIMO techniques are presented in Chapter 4. This step is included to build familiarity and to highlight the strengths

and weaknesses associated with each of the techniques. This is in preparation for the development of a meaningful set of experiments for the hardware system.

The phased array and MIMO algorithms presented in the background assume narrowband signals. In the hardware system, wideband signals were unavoidable. It was therefore necessary for suitable wideband techniques to be applied to the phased array and MIMO radar systems. The derivation of two wideband beamformers and wideband phased array and MIMO simulations are presented in Chapter 5.

Then, after a thorough understanding of the algorithms that will be applied to the system has been obtained, the design of the hardware system is discussed in Chapter 6. Each design decision is validated and a full description of all components of the hardware system is given.

A hardware system has many challenges associated with it, that are absent from simulations. In particular, the transmitter and receiver channels can vary from one another and therefore equalisation of the channels is required. The channel equalisation is referred to as calibration throughout the rest of the dissertation. Only after the system has been calibrated can the algorithms that were developed and tested by simulation in the early phases of the project be applied. The methods for calibrating and testing the hardware system are introduced in Chapter 7.

Finally, the results obtained from the simulations, and from tests on the hardware system are presented and discussed in Chapter 8 before conclusions and recommendations are given in Chapter 9.

Additional information relevant to the project is provided in Appendices A to K.

Chapter 2

Literature Review and Background Theory

In this chapter a review of phased array radar theory, which is fundamental to this project, is presented. Firstly, radar signal properties are presented, wherein the theory and physics of wave propagation, signal modulation, near and far-field signals, and narrowband signals is discussed. In the three following sections, a model for phased arrays is introduced and techniques of beamforming and target parameter estimation are catalogued for phased array systems. A wideband beamformer is then presented. Extending on phased array radar techniques, MIMO radar is then introduced. The MIMO radar model is presented, and a variety of parameter identification and beamforming techniques that can be applied to it are given. In the final section, an analysis of the practical applications of MIMO is given.

2.1 Radar Signal Properties

A selection of radar signal concepts and properties that form an integral part of phased array and MIMO models are presented in the following subsections.

2.1.1 Propagating Plane Waves

A complex-valued plane wave propagating through space can be represented as

$$e(\mathbf{x}, t) = \mathrm{e}^{j(\omega_0 t - \mathbf{k}^T \mathbf{x})} \tag{2.1}$$

where ω_0 is the temporal frequency, t is the time, $\mathbf{k}$ is the wave-number which can be thought of as the spatial frequency vector and $\mathbf{x}$ is the position vector [13]. Although $\mathbf{x}$ can be used to represent three-dimensional space, it is defined here to be two-dimensional, as the linear arrays of interest in this project can only locate targets in the $x-y$ plane. Then $\mathbf{k}$ can be expressed as

$$\mathbf{k} = k(\ \sin\theta \quad \cos\theta\ )^T \tag{2.2}$$

where θ is the direction of propagation of the wave. θ is defined to increase with clockwise rotation from the y-axis, as illustrated in Figure 2.1. $k = |\mathbf{k}| = \omega/c = 2\pi/\lambda$ where c is the speed of propagation of the wave, and λ is its wavelength [14].

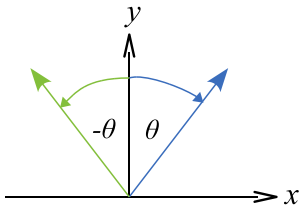

Figure 2.1: Definition of θ.

2.1.2 Signal Modulation

Signal modulation is a method used to transmit a low-pass signal over a band-pass channel. Consider a baseband signal $s(\mathbf{x}, t)$, which varies with position and time and could be complex-valued. This signal can be modulated by multiplication with a carrier signal of the form given in Equation (2.1). Then, the complex modulated signal which is known as the passband signal can be expressed as

$$s'(\mathbf{x}, t) = s(\mathbf{x}, t)e(\mathbf{x}, t) \tag{2.3}$$

as given in [15].

This form of modulation is known as amplitude modulation. The multiplication of the baseband and carrier signal, which is ideally a pure sinusoid, results in the amplitude of the carrier signal changing to take the form of the modulation function, $s(\mathbf{x}, t)$. An example of a baseband signal, a carrier signal and the resulting modulated signal are shown in Figure 2.2.

In the frequency domain, modulation has the effect of shifting the baseband signal to a higher frequency [16]. Consider a baseband signal, $s(t)$, which varies in time only and has the frequency domain characteristics shown in Figure 2.3.

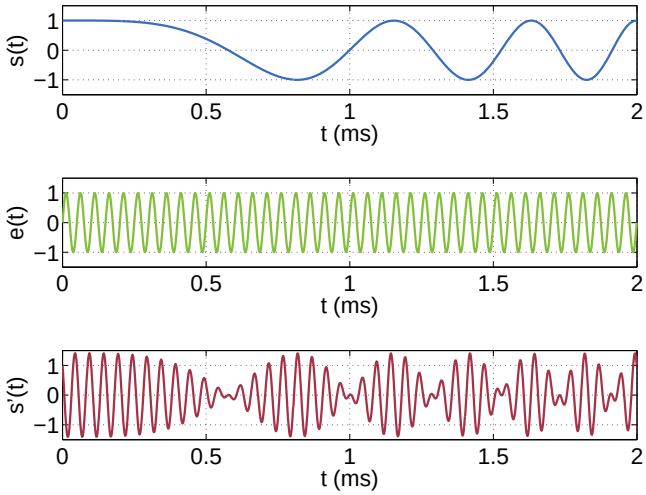

Figure 2.2: Amplitude modulation: an example of a real baseband signal $s(t)$, the real part of the carrier signal $e(t)$ and the modulated signal $s'(t)$.

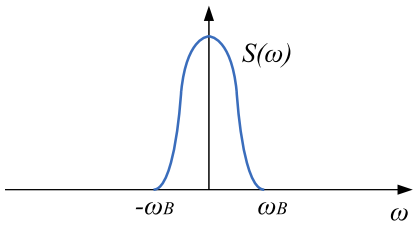

Figure 2.3: The baseband frequency spectrum of a band-limited signal $s(t)$.

When the modulation multiplication is performed, the modulation property of the Fourier transform gives the result

$$\mathfrak{F}\{s(t)e(t)\} = S'(\omega) = S(\omega - \omega_0) \tag{2.4}$$

where $\mathfrak{F}\{\dot{}\}$ represents the Fourier transform. So an image of the baseband function appears around ω_0 as shown in Figure 2.4. This illustrates that the signal spectral characteristics are retained, but the frequency of the signal is shifted upwards.

The signal is demodulated on the receiving end by multiplying it with the conjugated carrier signal $e^*(t)$. This restores the signal to its original baseband form.

Many signal processing algorithms use complex signals. However, a complex signal is a concept which can only exist in the analogue realm when one channel is used for the real part of the signal and a second for the complex part. The signal that is transmitted across the channel has to be real. So if the baseband signal is complex,

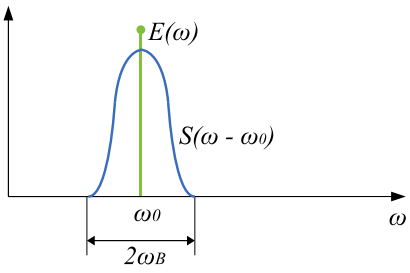

Figure 2.4: The frequency spectrum of a signal $s(t)$ modulated by carrier $e(t)$.

it is modulated by

$$s'(\mathbf{x}, t) = \mathbb{R}\{s(\mathbf{x}, t)e(\mathbf{x}, t)\} \tag{2.5}$$

which results in a real signal. The demodulation is given by

$$s(\mathbf{x}, t) = s'(\mathbf{x}, t)e^*(\mathbf{x}, t) \tag{2.6}$$

which recovers a scaled version of the original complex modulating signal. When real modulation is used, the restoration is not exact and images of the signal are present at other frequencies. With the use of a low-pass filter, these can be removed.

2.1.3 Near and Far-Field

Assume that an omnidirectional point source transmitter transmits spherical waves as shown in Figure 2.5. If the distance from the source to the receiver is large, and the aperture of the receiver is relatively small, the spherical wave-front can be approximated as a plane wave.

In electromagnetic (EM) theory the reactive near-field, the radiating near-field or Fresnel region and the Fraunhofer region which are defined depending on the distance

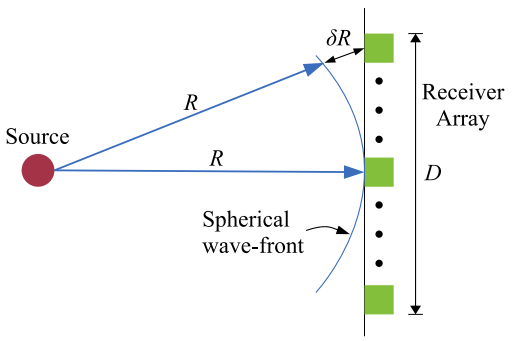

Figure 2.5: An array receiving the signal transmitted by a point source.

from the source, the wavelength of the transmitted waves, and the aperture of the receiving array [17]. In the near-field and Fresnel region, the wave-fronts have to be modelled as spherical. However, in the Fraunhofer region, which is commonly referred to as the far-field region, the wave-fronts can be assumed to be plane waves.

The criterion under which the far-field assumption applies can be formulated by analysing Figure 2.5. A receiver array is located a distance R from the transmitting source. An array of receiving elements has an aperture size given by $D = (L-1)d$ where L is the number of antennas in the array, and d is the separation between adjacent antennas.

The distance δR, which is the phase difference between the spherical wave incident on the array centre, and the array edge is given by

$$\delta R = \sqrt{R^2 + \left(\frac{D}{2}\right)^2} - R. \tag{2.7}$$

In the far-field, $D \ll R$ so using the binomial expansion ($(1+x)^{\frac{1}{2}} = 1 + \frac{x}{2} - \frac{x^2}{8} \ldots$), δR can be approximated as

$$\delta R = \left(\sqrt{1 + \left(\frac{D}{2R}\right)^2} - 1\right) R = \frac{D^2}{8R}. \tag{2.8}$$

In radar literature, it is assumed that an array is in the far-field if the distance δR is less than one sixteenth of a wavelength [18]. Therefore, the receiver array is said to be in the far-field of a source if

$$R \geq \frac{2D^2}{\lambda}. \tag{2.9}$$

If the receiver array is a uniform linear array (ULA) with inter-element spacing $d = \frac{\lambda}{2}$, then this restriction reduces to

$$R \geq \frac{\lambda(L-1)^2}{2}. \tag{2.10}$$

2.1.4 Narrowband Signals

In signal processing theory, the condition for a passband signal to be narrowband in the temporal sense is

$$B < 2\omega \tag{2.11}$$

where B is the bandwidth of the signal and ω is the carrier frequency [19]. In practice a passband signal can be termed narrowband if its bandwidth $\omega_2 - \omega_1$ is

much smaller (say by a factor of ten, or more) than the mean frequency $\frac{1}{2}(\omega_2 + \omega_1)$ which is usually the carrier frequency. Otherwise, the signal is called wideband [20]. The Defense Advanced Research Project Agency (DARPA) which is part of the United States Department of Defence, and later the Federal Communications Commission (FCC) further differentiates and defines ultra-wideband (UWB) signals if the fractional bandwidth is greater than 0.25 [21]. The fractional bandwidth is defined as

$$2\frac{\omega_2 - \omega_1}{\omega_2 + \omega_1} \tag{2.12}$$

and ω_2 and ω_1 are defined as the upper and lower -10 dB emission points. However Taylor [22] defines a signal with a fractional bandwidth above 0.2 as UWB, as this is the point at which angle and time or frequency resolution become coupled [23].

Consider a signal sampled at two points in space. For example, it could be sampled by two elements in an array. At a single moment in time, the signal at each point will differ. To determine by how much the signals vary, the concept of the modulation coherence distance of the signal is defined as $\frac{c}{B}$. The modulation coherence distance is, in effect, the wavelength of the largest frequency component of the baseband signal.

Therefore, in the spatial domain, a signal can be defined as narrowband if the modulation coherence distance, in the signal's direction of propagation, is far greater than the distance between the points at which the signal is sampled. This is expressed as

$$\Delta \ll \frac{c}{B} \tag{2.13}$$

where Δ is the distance by which the sampling points are separated [15].

The narrowband criteria in the spatial domain therefore requires that the amplitude of the baseband signal must not vary significantly between the points where it is sampled.

2.1.5 Sampling a Narrowband Signal

Consider a source transmitting a signal with a current function varying with time given by

$$I(t) = s(t)e^{j\omega t}. \tag{2.14}$$

where $s(t)$ is the complex baseband signal or complex envelope and ω is the carrier frequency. Using the same notation for a propagating plane wave as Section 2.1.1,

the field due to this signal at position $\mathbf{x}_i$ will be of the form [15]

$$E(\mathbf{x}_i, t) = g\frac{1}{|\mathbf{x}_i|}s\left(t - \frac{\mathbf{k}^T\mathbf{x}_i}{\omega}\right)e^{j(\omega t - \mathbf{k}^T\mathbf{x}_i)} \tag{2.15}$$

where g is a gain constant which depends on the directivity of the transmitter and other similar factors that remain constant at the receiving array. The term $1/|\mathbf{x}_i|$ incorporates the relationship of the signal's decreasing amplitude with increasing distance travelled from the source.

The above field is sampled at a number of points, the ith with location $\mathbf{x}_i$. If the points are close enough that the narrowband assumption applies, then we assume that the amplitude of the baseband signal is approximately the same across all points. Therefore, the baseband signal at each sampling location is assumed to be equal and can be simplified to

$$s\left(t - \frac{\mathbf{k}^T\mathbf{x}_i}{\omega}\right) = s\left(t\right). \tag{2.16}$$

Therefore, under the narrowband assumption, Equation (2.15) reduces to

$$E(\mathbf{x}_i, t) = g\frac{1}{|\mathbf{x}_i|}s\left(t\right)e^{j(\omega t - \mathbf{k}^T\mathbf{x}_i)} \tag{2.17}$$

2.2 Phased Array Model Representation

Consider sampling a propagating wave with an array of antennas. The effect of sampling the signal at different points in space is analogous to sampling a signal in time [13]. As frequency information can be determined when a signal is sampled in time, spatial information can be obtained from sampling a signal in space.

Consider the L-element ULA illustrated in Figure 2.6. We consider the case that the array receives a signal from a point source transmitter. The phased array model is built up in the sections that follow.

2.2.1 The Steering Vector

The steering vector of a signal received by an array is denoted $\mathbf{a}$ and is defined as the vector containing all of the space dependent quantities in Equation (2.17) [15].

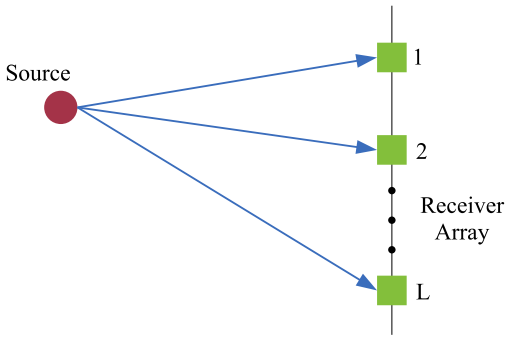

Figure 2.6: An array receiving the signal from a point source.

The unsimplified steering vector is

$$\mathbf{a}(\mathbf{x}) = \begin{bmatrix} \frac{1}{|\mathbf{x}_0|} e^{-j\mathbf{k}^T\mathbf{x}_0} \\ \frac{1}{|\mathbf{x}_1|} e^{-j\mathbf{k}^T\mathbf{x}_1} \\ \vdots \\ \frac{1}{|\mathbf{x}_L|} e^{-j\mathbf{k}^T\mathbf{x}_L} \end{bmatrix}. \tag{2.18}$$

Assume, as illustrated in Figure 2.7, that the source is a distance R from the first element of the array with x and y-components R_x and R_y. The distance between adjacent array elements is d. Assigning the position of the point source as $(0,0)^T$ gives

$$\mathbf{x}_i = (R_x + (i-1)d,\ R_y)^T \tag{2.19}$$

where $i = 1, \ldots, L$.

Therefore,

$$|\mathbf{x}_i| = \sqrt{(R_x + (i-1)d)^2 + R_y^2}. \tag{2.20}$$

But, assume that the source is in the far-field of the array, and therefore $d \ll R$ so

$$|\mathbf{x}_i| \approx R. \tag{2.21}$$

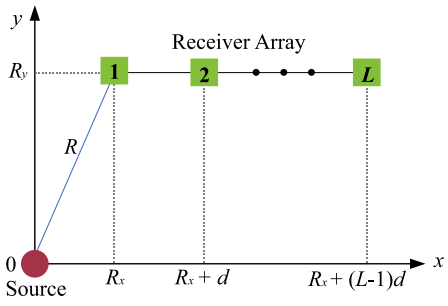

Figure 2.7: Definition of array and source distances.

Another result of assuming that the point source is in the far-field of the array is that the angle θ drawn between the antenna elements and the point source is approximately equal for all elements. This angle θ is shown in Figure 2.8 and is known as the direction of arrival (DOA) of the signal at the array. The vector dot product of the wave-number and the position becomes

$$\mathbf{k}'\mathbf{x}_i = k(R_x + (i-1)d)\sin\theta + kR_y\cos\theta. \tag{2.22}$$

So, the steering vector only depends on the signal DOA θ and can be expressed as

$$\mathbf{a}(\theta) = \frac{1}{R}e^{-jk(R_x\sin\theta + R_y\cos\theta)}\begin{bmatrix} 1 \\ e^{-jkd\sin\theta} \\ \vdots \\ e^{-jk(L-1)d\sin\theta} \end{bmatrix} \tag{2.23}$$

where the terms common to all entries have been placed outside the vector [14].

$kd\sin\theta$ is known as the electrical angle and it can be obtained from the geometric relationship shown in Figure 2.8. $d\sin\theta$ represents the difference in signal path length between two adjacent receiving elements.

The final simplification to the steering vector arises due to analysis of the electrical angle. In the spatial domain, aliasing can occur in the same way that it does in the time domain. Half-wavelength spacing of the array elements is analogous in the spatial domain, to the Nyquist frequency in a system where the signal is sampled in time. Therefore, if the distance between array elements is more than half a wavelength of the highest frequency component in the signal being received, aliasing will occur. Therefore, let $d = \frac{\lambda}{2}$. Also, recall that $k = \frac{\omega}{c} = \frac{2\pi}{\lambda}$. Therefore, for a ULA with half-wavelength spacing, the electrical angle becomes $\pi\sin\theta$.

The final representation for a narrowband steering vector obtained by simplifying Equation (2.23) by neglecting the terms that are constant across all elements of the

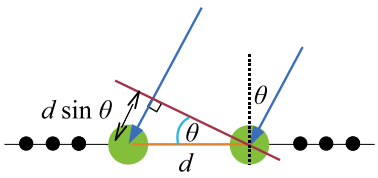

Figure 2.8: Derivation of the electric steering angle.

array is given by

$$\mathbf{a}(\theta) = \begin{bmatrix} 1 \\ e^{-j\pi \sin\theta} \\ \vdots \\ e^{-j\pi(L-1)\sin\theta} \end{bmatrix}. \tag{2.24}$$

The steering vector derived above is used in narrowband phased array processing to account for the time delay between different elements of the array receiving a point of the signal which lies on the same wave-front. The steering vector models the time shift as a phase shift. The assumption of equality between the time shift and phase shift does not hold under wideband conditions and therefore, as the signal bandwidth increases, the steering vector representation does not sufficiently model reality.

2.2.2 The Sampled Received Signal

The development of a model of the signal sampled by the array is based on the work by Krim and Viberg [14]. Let each receiver have gain $g_i(\theta)$. Then, taking all of the above assumptions into account, the signal at the ith receiver is described by

$$x_i(t) = g_i(\theta)a_i(\theta)s(t) = g_i(\theta)e^{-j\pi(i-1)\sin\theta}s(t). \tag{2.25}$$

This is a baseband representation of the received signal. In a real system, all signal processing is performed on the baseband signal, which is obtained by demodulating and filtering the received signal. In the derivations that follow, it is assumed that the antenna gain is unity and equal for all antennas and in all directions, so $g_i(\theta) = 1$ for $i = 1, \ldots, L$.

The signal at each of the L elements of the array can be written in vector notation as

$$\mathbf{x}(t) = \mathbf{a}(\theta)s(t). \tag{2.26}$$

We can observe that for a signal from a point source with DOA θ, the received signals are scalar multiples of the elements of the steering vector.

In the case that there are multiple sources transmitting signals, the principle of superposition applies. If M signals are received by the L element array, from M distinct DOAs $\theta_1, ..., \theta_M$, the received signal is

$$\mathbf{x}(t) = \sum_{m=1}^{M} \mathbf{a}(\theta_m)s_m(t) \tag{2.27}$$

where $s_m(t)$ represents the sampled baseband waveform of the mth source.

This can be represented in matrix notation by defining the L by M matrix

$$\mathbf{A}(\theta) = [\mathbf{a}(\theta_1), ..., \mathbf{a}(\theta_M)]\,. \tag{2.28}$$

A vector of the signal waveforms is also defined as

$$\mathbf{s}(t) = [s_1(t), ..., s_M(t)]^T\,. \tag{2.29}$$

Assuming that additive noise and interference $\mathbf{z}(t)$ is also present in the sample, the signal received by the array can be represented as

$$\mathbf{x}(t) = \mathbf{A}(\theta)\mathbf{s}(t) + \mathbf{z}(t). \tag{2.30}$$

2.2.3 Statistical Assumptions and the Covariance Matrix

To be able to apply techniques of beamforming to a phased array, knowledge of the received signal is required. Many beamformers use the power of the received signals, which can be represented by the spatial covariance matrix, to optimise and adapt their performance [24]. This section discusses the statistical assumptions that can be made to model radar signals, and the development of the representation of the covariance matrices for the signals received by the array. It is again based on the assumptions and derivations by Krim and Viberg [14].

We assume that the data received by the array has zero mean. The covariance matrix (see Appendix B), which represents the power or variance of the received data, is then given by

$$\mathbf{R}_X = \mathrm{E}\left[\mathbf{x}(t)\mathbf{x}^H(t)\right] \tag{2.31}$$

where E[·] is the statistical expectation.

Considering the result given in Equation (2.30), the covariance matrix becomes

$$\mathbf{R}_X = \mathbf{A}\,\mathrm{E}\left[\mathbf{s}(t)\mathbf{s}^H(t)\right]\mathbf{A}^H + \mathrm{E}\left[\mathbf{z}(t)\mathbf{z}^H(t)\right]. \tag{2.32}$$

and has dimensions L-by-L. The source covariance matrix is then defined as

$$\mathrm{E}\left[\mathbf{s}(t)\mathbf{s}^H(t)\right] = \mathbf{R}_S \tag{2.33}$$

and the noise covariance matrix as

$$\mathrm{E}\left[\mathbf{z}(t)\mathbf{z}^H(t)\right] = \sigma^2\mathbf{I} \tag{2.34}$$

where $\mathbf{I}$ is the L-by-L identity matrix. The noise covariance can be expressed in this way, since the noise is assumed to be spatially white. This means that the noise is uncorrelated between all array elements, and has a common variance of σ^2.

Thus, the covariance matrix becomes

$$\mathbf{R}_X = \mathbf{A}\mathbf{R}_S\mathbf{A}^H + \sigma^2\mathbf{I}. \tag{2.35}$$

The covariance matrix and its properties are described in more detail in Appendix B. Also, methods for estimating the covariance matrix are described in this appendix.

2.2.4 Spectral Representation

The signal spectral representation is used extensively in some phased array methods, and its derivation below is based on that by Krim and Viberg [14] and van Wyk [25]. Spectral theory is described generally in Section A.3 in Appendix A.

The spectral representation of the received signal covariance matrix is

$$\mathbf{R}_X = \mathbf{U}\Lambda\mathbf{U}^H \tag{2.36}$$

where $\Lambda = \text{diag}\{\lambda_1, \lambda_2, \ldots, \lambda_L\}$ is a diagonal matrix of the eigenvalues of $\mathbf{R}_X$, and $\mathbf{U}$ is a matrix composed of the eigenvectors of $\mathbf{R}_X$, $\{\mathbf{q}_i\}_{i=1}^{L}$.

The representation of $\mathbf{R}_X$ given in Equation (2.35) can be broken down further and represented as

$$\mathbf{R}_X = \mathbf{U}_s\Lambda_s\mathbf{U}_s^H + \mathbf{U}_n\Lambda_n\mathbf{U}_n^H \tag{2.37}$$

where $\Lambda_s = \text{diag}\{\mu_1, \mu_2, \ldots, \mu_L\}$ is a diagonal matrix of the eigenvalues of $\mathbf{A}\mathbf{R}_S\mathbf{A}^H$ and $\mathbf{U}_s$ is a matrix composed of the corresponding eigenvectors $\{\mathbf{p}_i\}_{i=1}^{M}$. Since $\mathbf{R}_S$ only has M rows corresponding to the M transmitted signals, $\mathbf{U}_S$ only has M eigenvectors and the eigenvalues $\mu_{M+1} \ldots \mu_L$ are equal to zero.

Also, $\Lambda_n = \sigma^2\mathbf{I}$ and $\mathbf{U}_n$ is composed of the eigenvectors of the noise space.

Having considered this decomposition, the eigenvalues of $\mathbf{R}_X$ can be represented as

$$\lambda_i = \begin{cases} \mu_i + \sigma^2, & i = 1, \ldots, M \\ \sigma^2, & i = M+1, \ldots, L. \end{cases} \tag{2.38}$$

It is stated in Appendix B in Section B.3 that the eigenvalues of a covariance matrix are orthogonal to one another. Therefore, the eigenvectors corresponding to the

last $L-(M+1)$ eigenvalues must be orthogonal to $\mathbf{A}$. This can be illustrated by considering that, by the properties of eigenvalues and eigenvectors given in Section A.3 in Appendix A,

$$\mathbf{R}_X\mathbf{q}_i = \sigma^2\mathbf{q}_i, \quad i = M+1, ..., L. \tag{2.39}$$

Using the representation in Equation (2.35),

$$\mathbf{R}_X\mathbf{q}_i = \mathbf{A}\mathbf{R}_S\mathbf{A}^H\mathbf{q}_i + \sigma^2\mathbf{q}_i. \tag{2.40}$$

Substituting Equation (2.39) into Equation (2.40), it can be seen that

$$\mathbf{A}\mathbf{R}_S\mathbf{A}^H\mathbf{q}_i = \mathbf{0}. \tag{2.41}$$

Since the matrix $\mathbf{A}$ has full column rank, and $\mathbf{R}_S$ has full rank, $\mathbf{A}^H\mathbf{q}_i$ must be equal to zero. Thus,

$$\mathbf{a}^H(\theta_m)\mathbf{q}_i = 0. \tag{2.42}$$

This proves that all of the noise eigenvectors $\mathbf{q}_i$ are orthogonal to $\mathbf{A}$. Therefore, the columns of $\mathbf{U}_n$ span the orthogonal complement of $\mathbf{A}$, i.e. the null-space of $\mathbf{A}^H$. In addition, the columns of $\mathbf{U}_s$ must span the range of $\mathbf{A}$.

Projection operators onto the signal and noise subspaces can then be defined as

$$\begin{aligned} \Pi &= \mathbf{U}_s\mathbf{U}_s^H &&= \mathbf{A}\mathbf{A}^\dagger \\ \Pi^\perp &= \mathbf{U}_n\mathbf{U}_n^H &&= \mathbf{I} - \mathbf{A}\mathbf{A}^\dagger \end{aligned} \tag{2.43}$$

where

$$\mathbf{A}^\dagger = (\mathbf{A}^H\mathbf{A})^{-1}\mathbf{A}^H \tag{2.44}$$

is the Moore-Penrose pseudo-inverse.

Then, provided that the inverses exist, it holds that

$$\mathbf{I} = \Pi + \Pi^\perp. \tag{2.45}$$

2.2.5 The Array Beampattern

To derive the beampattern of a phased array antenna, beamforming needs to be defined. Simple beamforming can be accomplished by calculating a weighted and delayed average of the received signals. The output of such a beamformer, known as a delay-and-sum beamformer [13], is defined as

$$y(t) = \frac{1}{L}\sum_{i=1}^{L} w_i x_i(t-\tau_i) \tag{2.46}$$

where w_i and τ_i are the weight and delay implemented on the ith receiver channel.

To receive a plane wave with direction of propagation corresponding to $\boldsymbol{k}_0$, the beamforming delays should be set equal to

$$\tau_i = -\frac{\boldsymbol{k}_0^T \mathbf{x}_i}{\omega} \tag{2.47}$$

as given in [13].

Assume that the received signal $x_i(t)$ is a propagating plane wave $e(t - \frac{\boldsymbol{k}^T \mathbf{x}_i}{\omega})$, as given in Equation (2.1). Therefore, the output of the beamformer, which is weighted to optimally receive signals propagating from direction $\mathbf{k}_0$ is

$$\begin{aligned} y(t) &= \frac{1}{L}\sum_{i=1}^{L} w_i e\left(t - \frac{\boldsymbol{k}^T \mathbf{x}_i}{\omega} + \frac{\boldsymbol{k}_0^T \mathbf{x}_i}{\omega}\right) \\ &= \frac{1}{L}\sum_{i=1}^{L} w_i \, \mathrm{e}^{j\omega\left(t - \frac{\mathbf{k}^T \mathbf{x}_i}{\omega} + \frac{\mathbf{k}_0^T \mathbf{x}_i}{\omega}\right)} \\ &= \frac{1}{L}\sum_{i=1}^{L} w_i \, \mathrm{e}^{-j(\mathbf{k}-\mathbf{k}_0)^T \mathbf{x}_i} \, \mathrm{e}^{j\omega t} \\ &= b(\mathbf{k}-\mathbf{k}_0)\, \mathrm{e}^{j\omega t}\,. \end{aligned} \tag{2.48}$$

Thus, we define the beamformer output, which is not dependent on time, as the array response. It is given by

$$b(\mathbf{k}) = \frac{1}{L}\sum_{i=1}^{L} w_i \, \mathrm{e}^{-j\mathbf{k}^T \mathbf{x}_i}\,. \tag{2.49}$$

On analysis of the array response it can be seen that it represents a Fourier transform of the set of weights w_i applied by the beamformer. In Equation (2.48), the array response $b(\mathbf{k}-\mathbf{k}_0)$ gives the attenuation that will be experienced by a plane wave travelling with propagation direction $\mathbf{k}$, on reception by a beamformer pointing in direction $\mathbf{k}_0$ [13].

The array response can be reformulated to

$$\begin{aligned} b(\mathbf{k}-\mathbf{k}_0) &= \frac{1}{L}\sum_{i=1}^{L} w_i \, \mathrm{e}^{-j(\mathbf{k}-\mathbf{k}_0)^T \mathbf{x}_i} \\ &= \frac{1}{L}\sum_{i=1}^{L} w_i \, \mathrm{e}^{j\omega\tau_i} \, \mathrm{e}^{-j\mathbf{k}^T \mathbf{x}_i} \end{aligned} \tag{2.50}$$

where τ_i is the delay implemented for beamforming.

Now consider a ULA. By the simplifications in Section 2.2.1, the array response becomes

$$b(\theta) = \frac{1}{L}\sum_{i=1}^{L} w_i \, \mathrm{e}^{j\omega\tau_i} \, \mathrm{e}^{-j\pi(i-1)\sin\theta} \, . \tag{2.51}$$

By combining the weight and delay into a complex vector $\mathbf{w}$ with i^{th} element $w_i \, \mathrm{e}^{j\omega\tau_i}$, this can be written in vector form as

$$b(\theta) = \mathbf{w}^T \mathbf{a}(\theta) \tag{2.52}$$

where $\mathbf{a}(\theta)$ is the steering vector as defined in Section 2.2.1.

The beampattern is defined as the square of the array response [24], and is given by

$$\begin{aligned} P(\theta) &= b(\theta) b^H(\theta) \\ &= \mathbf{a}^T(\theta) \mathbf{w} \mathbf{w}^H \mathbf{a}^*(\theta). \end{aligned} \tag{2.53}$$

This expression gives the ideal beampattern for a ULA with beamforming applied.

2.3 Phased Array Beamforming Techniques

A phased array is used to concentrate transmitted energy or maximise received energy in a particular direction by a process called beamforming. This maximises the SNR in the direction of interest and target parameter estimation can be performed. The DOA and other parameters of any targets in the radar's field of view can be determined from the received signals.

Section 2.2.5 introduced the concept of the delay-and-sum beamformer. To receive a signal from a known direction, the signal on the ith channel is delayed by τ_i and summed to all of the other signals. For a transmitting array, beamforming can be applied by delaying the ith transmitted signal by τ_i before transmission. Considering a ULA, with half wavelength spacing, τ_i, first defined in Equation (2.47), reduces to

$$\tau_i = \frac{(i-1)}{2f} \sin\theta. \tag{2.54}$$

A generalised narrowband delay-and-sum beamformer is shown in Figure 2.9. The output, first introduced in Equation (2.46), is repeated below in vector form

$$y(t) = \mathbf{w}^T \mathbf{x}(t) \tag{2.55}$$

where the vector of weights $\mathbf{w}$ is complex and in the narrowband case represents weights and delays.

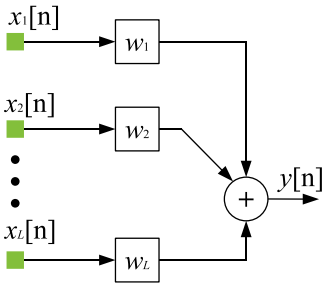

Figure 2.9: A narrowband beamformer.

The output power can then be calculated by

$$P(\mathbf{w}) = \frac{1}{N}\sum_{i=1}^{N}|y(t_i)|^2 = \frac{1}{N}\sum_{i=1}^{N}\mathbf{w}^T\mathbf{x}(t_i)\mathbf{x}^H(t_i)\mathbf{w}^* = \mathbf{w}^T\hat{\mathbf{R}}\mathbf{w}^* \tag{2.56}$$

where $\hat{\mathbf{R}}$ is the covariance matrix of the received signal as estimated using any of the methods in Section B.5 in Appendix B.

Methods for determining appropriate weights for beamforming, and beamforming architectures which are suitable under different circumstances, are discussed below. The techniques are presented in the context of receiving arrays, but the conventional, Capon and Linearly Constrained Minimum Variance beamformers can also be applied to transmitting arrays.

2.3.1 Data Independent Beamforming

Data independent beamformers are designed to approximate a desired response. The beamformer output does not depend on the received array data or data statistics. Usually, the DOA of the signal is assumed to be known, and weights are chosen for a response close to the ideal response of unity gain in the direction of interest, and zero gain elsewhere [24]. The conventional beamformer is described below.

2.3.1.1 Conventional Beamformer

The conventional or Bartlett beamformer maximises the power of the beamformer output for a given input signal [14]. Suppose it is desired that a signal from direction θ be received. Then, the output of the array due to this signal, including the effect of noise is, as given in Equation (2.30)

$$\mathbf{x}(t) = \mathbf{a}(\theta)s(t) + \mathbf{z}(t) \tag{2.57}$$

The power of the weighted signal is then maximised by

$$\begin{aligned} \max_{\mathbf{w}} \ \mathrm{E}[\mathbf{w}^T\mathbf{x}(t)\mathbf{x}^H(t)\mathbf{w}^*] &= \max_{\mathbf{w}} \ \mathbf{w}^T\,\mathrm{E}[\mathbf{x}(t)\mathbf{x}^H(t)]\mathbf{w}^* \\ &= \max_{\mathbf{w}} \ \mathrm{E}\,|s(t)|^2|\mathbf{w}^T\mathbf{a}(\theta)|^2 + \sigma^2|\mathbf{w}^*|^2. \end{aligned} \tag{2.58}$$

The resulting solution to the maximisation, with the constraint $\|\mathbf{w}\| = 1$ is

$$\mathbf{w}_{BF}(\theta) = \frac{\mathbf{a}^*(\theta)}{\sqrt{\mathbf{a}^T(\theta)\mathbf{a}^*(\theta)}}. \tag{2.59}$$

Therefore, the optimum reception of a signal from DOA θ is achieved by assigning $\mathbf{w}$ equal to the normalised steering vector of a signal propagating from direction θ.

The conventional beamformer spatial spectrum is obtained by substituting Equation (2.59) into the power spectrum in Equation (2.56). This spectrum can be plotted as θ is varied and shows peaks at DOAs where targets are located. Spectral techniques will be described in more detail in Section 2.4.1. The conventional spectrum is

$$P_{BF}(\theta) = \frac{\mathbf{a}^H(\theta)\hat{\mathbf{R}}\mathbf{a}(\theta)}{\mathbf{a}^H(\theta)\mathbf{a}(\theta)} \tag{2.60}$$

For a ULA, which has the steering vector $\mathbf{a}(\theta)$ given in Equation (2.24), the standard beam width is given by $\phi_B = 2\pi/L$. Therefore, if two sources have a DOA separated by less than ϕ_B, the conventional beamformer will not be able to resolve the sources [14].

2.3.2 Statistically Optimum Beamforming

Statistically optimum beamformers select weights based on the statistics of the received data. Their aim is to optimise the beamformer output so that it has maximal contributions from the desired signal, and minimal interference from signals and noise arriving from other directions [24]. Examples of statistically optimum beamformers are presented below.

2.3.2.1 Multiple Side lobe Canceller (MSC)

The Multiple Side lobe Canceller (MSC) consists of a main channel and one or more auxiliary channels. The main channel has a highly directional response and is pointed in the direction of the desired signal. This directional response is usually

obtained with a high gain antenna or with a data independent beamformer. Interference is assumed to enter through the side lobes of the main channel, and through the auxiliary channels. The aim of the MSC is for the interference received by the main channel side lobes to be cancelled by that received by the auxiliary channels [24]. The MSC architecture is illustrated in Figure 2.10.

The least squares (LS) criterion used to optimise the weights is described by

$$\min_{\mathbf{w}_a} \mathrm{E}\left[\left|y_m(t) - \mathbf{w}_a^T \mathbf{x}_a(t)\right|^2\right] \tag{2.61}$$

where $\mathbf{x}_a(t)$ is the data received by the auxiliary channels and $y_m(t)$ is the data received by the primary channel [24].

The optimum weights are then

$$\mathbf{w}_a = \mathbf{R}_a^{-1}\mathbf{R}_{am} \tag{2.62}$$

where $\mathbf{R}_a = \mathrm{E}[\mathbf{x}_a(t)\mathbf{x}_a^H(t)]$ and $\mathbf{R}_{am} = \mathrm{E}[\mathbf{x}_a(t)y_m]$.

The output of the MSC is

$$y(t) = y_m(t) - \mathbf{w}_a^T \mathbf{x}_a(t). \tag{2.63}$$

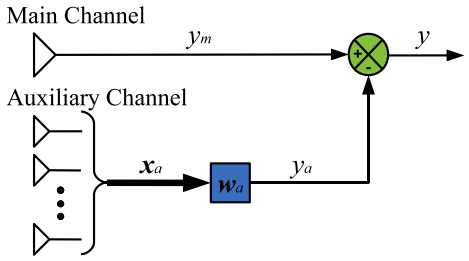

Figure 2.10: The multiple side lobe canceller architecture.

2.3.2.2 Use of Reference Signal

In some applications, the form of the desired signal might be known. In these scenarios, a signal that represents the known and desired signal can be generated at the receiver. It is called the reference signal. Beamformer weights can then be chosen to minimise the error between the beamformer output and the reference signal [24]. The LS optimisation to obtain weights $\mathbf{w}$ is represented by

$$\min_{\mathbf{w}} \mathrm{E}\left[\left|y(t) - y_d(t)\right|^2\right] \tag{2.64}$$

where $y(t)$ is the output of the array given by

$$y(t) = \mathbf{w}^T \mathbf{x}(t) \tag{2.65}$$

and $y_d(t)$ is the reference signal.

Then, the optimum weights are given by

$$\mathbf{w} = \mathbf{R}_x^{-1} \mathbf{R}_{xd} \tag{2.66}$$

where $\mathbf{R}_x = \mathrm{E}[\mathbf{x}(t)\mathbf{x}^H(t)]$ and $\mathbf{R}_{xd} = \mathrm{E}[\mathbf{x}(t)y_d(t)]$.

An advantage of this method of beamforming is that the direction of the desired signal does not need to be known. It must be noted that it is assumed that the reference signal is uncorrelated with any interference which may be received by the antennas.

One case where this method will work well, is if the transmitted signal is an amplitude modulated signal. An acceptable beamformer performance can be obtained by choosing the reference signal to be a sinusoidal signal equal in frequency to the carrier signal of the amplitude modulated signal [24].

2.3.2.3 Maximisation of Signal to Noise Ratio

Weights can be chosen to maximise the SNR. This method requires knowledge of the covariance matrices of the signal ($\mathbf{R}_s$) and the noise ($\mathbf{R}_z$). In an active radar system, $\mathbf{R}_s$ can be obtained from knowledge of the transmitted pulse, and $\mathbf{R}_z$ can be obtained from the signal received by the array, when no signal has been transmitted [24].

Let the signal received by the array be

$$\mathbf{x}(t) = \mathbf{s}_c(t) + \mathbf{z}_c(t) \tag{2.67}$$

where $\mathbf{s}_c(t)$ is the signal component and $\mathbf{z}_c(t)$ is the noise component.

The output of the beamformer is given by

$$y(t) = \mathbf{w}^T \mathbf{x}(t). \tag{2.68}$$

The optimisation to select the weights $\mathbf{w}$ which maximise the SNR is

$$\max_{\mathbf{w}} \frac{\mathbf{w}^H \mathbf{R}_s \mathbf{w}}{\mathbf{w}^H \mathbf{R}_z \mathbf{w}} \tag{2.69}$$

where $\mathbf{R}_s = \mathrm{E}[\mathbf{s}_c\mathbf{s}_c^H]$ and $\mathbf{R}_z = \mathrm{E}[\mathbf{z}_c\mathbf{z}_c^H]$.

An eigenproblem

$$\mathbf{R}_z^{-1}\mathbf{R}_s\mathbf{w} = \lambda_{max}\mathbf{w} \tag{2.70}$$

where λ_{max} is the maximum eigenvalue of $\mathbf{R}_z^{-1}\mathbf{R}_s$ is solved to find the optimum weights.

2.3.2.4 Capon's Beamformer and Linearly Constrained Minimum Variance (LCMV)

All of the above mentioned beamformers make many assumptions about the information that is available. If the signal amplitude varies, signal cancellation can occur with the MSC. If the signal is transmitted continuously, information about the noise will not be obtainable for the maximum SNR beamformer. Also, the exact transmitted signal may not always be known as required for the reference signal beamformer described in Section 2.3.2.2. The Capon [14, 26] and Linearly Constrained Minimum Variance (LCMV) [24] beamformers are more adaptive.

Capon's beamformer was developed by Capon [26] to allow sources closer than a beam width apart to be resolved. The beamformer maintains a fixed gain in the direction of the desired signal. It then attempts to minimise the power contributed by signals and noise arriving from all other directions. The optimisation problem is

$$\begin{aligned} &\min_{\mathbf{w}} \; P(\mathbf{w}) \\ &\text{subject to} \;\; \mathbf{w}^T\mathbf{a}(\theta) = 1 \end{aligned} \tag{2.71}$$

where $P(\mathbf{w})$ is as defined in Equation (2.56). The optimal $\mathbf{w}$ can be found using the method of Lagrange multipliers (given in Section A.4 in Appendix A) and is

$$\mathbf{w}_{CAP} = \frac{\hat{\mathbf{R}}^{-1}\mathbf{a}^*(\theta)}{\mathbf{a}^T(\theta)\hat{\mathbf{R}}^{-1}\mathbf{a}^*(\theta)}. \tag{2.72}$$

When the result is inserted into the spatial spectrum in Equation (2.56), Capon's spectrum is found to be

$$P_{CAP}(\theta) = \frac{1}{\mathbf{a}^T(\theta)\hat{\mathbf{R}}^{-1}\mathbf{a}^*(\theta)}. \tag{2.73}$$

The Capon method can be further generalised for multiple constraints and is known as the LCMV. For example, it might be required that a signal from direction θ_1 be

received with a gain g, and a signal from direction θ_2 be rejected. Therefore, the constraints will be (recalling that the gain of the received signal is given by $\mathbf{w}^T\mathbf{a}(\theta)$)

$$\mathbf{w}^T \begin{bmatrix} \mathbf{a}(\theta_1) & \mathbf{a}(\theta_2) \end{bmatrix} = \begin{bmatrix} g^* & 0 \end{bmatrix}. \tag{2.74}$$

This can be generalised, and the set of constraints is represented by the relationship

$$\mathbf{w}^T\mathbf{C} = \mathbf{f}. \tag{2.75}$$

The optimisation problem then becomes

$$\begin{aligned} &\min_{\mathbf{w}} \ \mathbf{w}^H\mathbf{R}\mathbf{w} \\ &\text{subject to } \mathbf{w}^T\mathbf{C} = \mathbf{f}. \end{aligned} \tag{2.76}$$

This can be solved, to give optimum weights

$$\mathbf{w} = \frac{\mathbf{R}^{-1}\mathbf{C}^*}{\mathbf{C}^T\mathbf{R}^{-1}\mathbf{C}^*}\mathbf{f}. \tag{2.77}$$

As the number of constraints increases, the degrees of freedom for minimising the optimisation problem decrease. If there are K constraints, then there are only $L-K$ degrees of freedom available for optimisation. There are many different methods for selecting constraints. Some of these are point, derivative and eigenvector constraints.

A disadvantage of the Capon and LCMV techniques is that they do not perform well on signals which are coherent [14]. If there are a number of targets which need to be detected simultaneously, the signal received from each target is a time shifted version of the radar transmitted signal. If the time delay between transmission and reception of two target echoes is equal, the target echoes will be coherent. If two targets are at the same range, to within the range resolution of the radar system, the time delays will be almost equal, and the signals will be close to coherent. If only one target is of interest low performance for coherent signals is not a problem.

2.4 Parameter Estimation Techniques for Phased Array

The target direction or DOA can be determined from received signals. Two approaches exist for determining the target location with a phased array. The first allows the DOA to be found by plotting a spectrum across all angles, and finding

the parameters from peaks in the spectrum. The second approach is a parametric approach, where the DOA is returned directly by an algorithm [14]. Examples of each of these techniques are presented below.

2.4.1 Spectral Techniques

The conventional beamformer and Capon beamformer presented in Section 2.3 above both allow spectral techniques to be applied. The spectrums, from which the DOA can be determined, were given in Equation (2.56) and Equation (2.73). Another spectral technique is the MUSIC (MUltiple SIgnal Classification) algorithm. It is a high resolution technique, and is presented below.

2.4.1.1 MUSIC Algorithm

The MUSIC algorithm is a subspace-based spectral technique. It uses the spectral decomposition of the covariance matrix. As previously derived, the covariance matrix is given by

$$\mathbf{R} = \mathbf{A}\mathbf{S}\mathbf{A}^H + \sigma^2\mathbf{I} = \mathbf{U}_s\Lambda_s\mathbf{U}_s^H + \mathbf{U}_n\Lambda_n\mathbf{U}_n^H. \tag{2.78}$$

It was shown in Equation (2.42) that the eigenvectors in $\mathbf{U}_n$ are orthogonal to $\mathbf{A}$. Therefore,

$$\mathbf{U}_n^H\mathbf{a}(\theta) = 0, \quad \theta \in \{\theta_1, ..., \theta_M\} \tag{2.79}$$

where there are M DOA's of interest. However, in reality, since we only have an estimate of $\mathbf{U}_n$, the above product will only approach zero. Therefore, by plotting the inverse of this product against θ, peaks will appear where the product approaches zero, indicating the presence of a source from the DOA specified by θ. It is assumed that any collection of L steering vectors corresponding to distinct DOAs forms a linearly independent set (defined in Appendix A). This allows unique DOA estimates.

The spatial spectrum used by the MUSIC algorithm is then defined as

$$P_M(\theta) = \frac{1}{\mathbf{a}^H(\theta)\hat{\Pi}^{\perp}\mathbf{a}(\theta)} \tag{2.80}$$

where $\hat{\Pi}^{\perp}$ is the estimate of the orthogonal projector $\Pi^{\perp}$ given in Equation (2.43). To obtain $\hat{\Pi}^{\perp}$, the estimated covariance matrix $\hat{\mathbf{R}}$ is determined. The eigenvalues of the covariance matrix are found and the eigenvectors split into the signal eigenvectors

$\hat{\mathbf{U}}_s$ which correspond to the M largest eigenvalues, and the noise eigenvectors $\hat{\mathbf{U}}_n$ which correspond to the $L - M$ smallest eigenvalues. The orthogonal projector estimate can then be determined using the estimate of $\hat{\mathbf{U}}_n$ and Equation (2.43).

$P_M(\theta)$ is not a true power spectrum but can be thought to represent the distance between the signal and noise subspace [14]. However, since it exhibits peaks at the DOAs of signals impinging on an array, it is a sufficient measure. The MUSIC algorithm gives extremely good estimates if data is collected for large periods of time or if the SNR is high. It is however unable to resolve closely spaced signals if only a small number of time samples are available, or the SNR is low. If the signals are coherent, then the property given in Equation (2.79) is no longer true, and the MUSIC algorithm cannot be used.

2.4.2 Parametric Methods

The short-coming of the spectral techniques presented above, is that they do not perform well when the signals are coherent [14]. Parametric methods exploit the data model of the signals to estimate the target parameters. There are a number of parametric methods which continue to provide good DOA estimates for multiple targets even when the target signals are coherent. These include the well known Maximum Likelihood (ML) techniques, and also some subspace techniques such as the Signal, Weighted or Subspace Fitting methods. The disadvantage of parametric methods is that they are generally more computationally complex and it is sometimes necessary to choose the order of the model a-priori. However, a ULA allows simplifications to be made so that the parametric methods become comparable to the spectral techniques. Here, only the Deterministic Maximum Likelihood is presented based on the derivation in Krim and Viberg [14].

2.4.2.1 Deterministic Maximum Likelihood (DML)

The DML model assumes that the received signal is arbitrarily deterministic and unknown, but has a known carrier frequency. (Another ML based technique, the Stochastic ML assumes that the signals can be modelled as Gaussian random processes).

The receiver noise is modelled as a stationary Gaussian white random process which is circularly symmetric. A complex process is circularly symmetric if its

real and imaginary parts are identically distributed, and their cross-covariance is skew symmetric. This means that $\mathrm{E}\left[\Re(\mathbf{z}(t))\Im(\mathbf{z}^T(t))\right] = -\mathrm{E}\left[\Im(\mathbf{z}(t))\Re(\mathbf{z}^T(t))\right]$.

Therefore, the received signal vector $\mathbf{x}(t)$ is also a circularly symmetric Gaussian random process which is temporally white. It has mean $\mathbf{A}(\theta)\mathbf{s}(t)$ and covariance matrix $\sigma^2\mathbf{I}$.

The likelihood function is given by the Probability Density Function (PDF). In the case of a complex Gaussian random process which, when applied to this scenario, is a vector containing a single time sample measured by all L antennas, the PDF is given by

$$PDF = \frac{1}{(\pi\sigma^2)^L}\,\mathrm{e}^{\|\mathbf{x}(t)-\mathbf{A}\mathbf{s}(t)\|^2/\sigma^2} \tag{2.81}$$

where $\|\cdot\|$ is the Euclidean norm defined in A.1 in Appendix A.

Because all N time measurements are independent, the likelihood function for the array is given by

$$L_{DML}(\theta, \mathbf{s}(t), \sigma^2) = \prod_{i=1}^{N}(\pi\sigma^2)^{-L}\,\mathrm{e}^{\|\mathbf{x}(t_i)-\mathbf{A}\mathbf{s}(t_i)\|^2/\sigma^2}\,. \tag{2.82}$$

The arguments by which the ML is maximised are θ, $\mathbf{s}(t)$ and σ^2. However, for computational simplicity, this maximisation problem is turned into the minimisation of the log-likelihood function. Therefore, the DML problem is

$$\min_{\theta,s(t),\sigma^2} L\log\sigma^2 + \frac{1}{\sigma^2 N}\sum_{n=1}^{N}\|\mathbf{x}(t) - \mathbf{A}\mathbf{s}(t)\|^2\,. \tag{2.83}$$

It can be shown that minima are given by

$$\hat{\sigma}^2 = \frac{1}{L}\mathrm{Tr}\left\{\Pi_A^{\perp}\hat{\mathbf{R}}_X\right\} \tag{2.84}$$

and

$$\hat{\mathbf{s}}(t) = \mathbf{A}^{\dagger}\mathbf{x}(t) \tag{2.85}$$

where $\hat{\mathbf{R}}_X$ is the estimated covariance matrix of the received signals, $A^{\dagger}$ is the Moore-Penrose pseudo-inverse of $\mathbf{A}$ defined in Equation (2.44) and $\Pi^{\perp}$ is the orthogonal projector onto the null-space of $\mathbf{A}^H$, as defined in Equation (2.43).

Therefore, using the results in Equation (2.84) and Equation (2.85), the DML estimates of θ can be found by solving the optimisation problem given by

$$\min_{\theta}\mathrm{Tr}\left\{\Pi^{\perp}\hat{\mathbf{R}}_X\right\}. \tag{2.86}$$

This estimation technique can be interpreted as the evaluation of the power when the measured received signals $\mathbf{x}(t)$ are projected onto a subspace which is orthogonal to all of the signal components ($\Pi^{\perp}$). The power should be the smallest when the projector removes all of the components from the true signal DOA.

This problem must be solved numerically. The solution converges quite rapidly to a minimum provided that a good initial estimate is available. One of the spectral techniques can be used to provide the initial estimate [14].

2.5 A Wideband Beamformer

In the narrowband model presented this far, it has been assumed that the time delay between the signal on different transmitter or receiver elements is equivalent to a phase shift in the signal. This is true at the centre frequency of the band-pass signal. However, as the frequency deviates from the centre frequency, the equivalence of the time shift and the phase shift which represents it lessens.

It is possible to reduce errors caused by wideband signals by filtering the received signal. We return to the interpretation of a phased array as a spatial filter [13]. It receives signals from some directions, whilst rejecting signals from other directions. However, if the signal is not narrowband, it becomes necessary to also select which frequency components to receive and which to reject. A wideband beamformer is shown in Figure 2.11. Each channel includes a Finite Impulse Response (FIR) filter. Therefore, the signal is filtered spatially, and then temporally. By restructuring the phased array model for the topology shown in Figure 2.11, the same beamforming, spectral and parametric techniques presented for narrowband signals can also be applied when the signal is wideband. The wideband beamformer is described in Van Veen and Buckley [24] and Frost [27] and summarised in Section 2.5.1.

2.5.1 Wideband Phased Array Model

Consider a wideband array with $J-1$ tap delays. Then, the discrete output of the beamformer is given by

$$y[n] = \sum_{i=1}^{L} \sum_{j=0}^{J-1} w_{ji}^{*} x_i[n-j]. \tag{2.87}$$

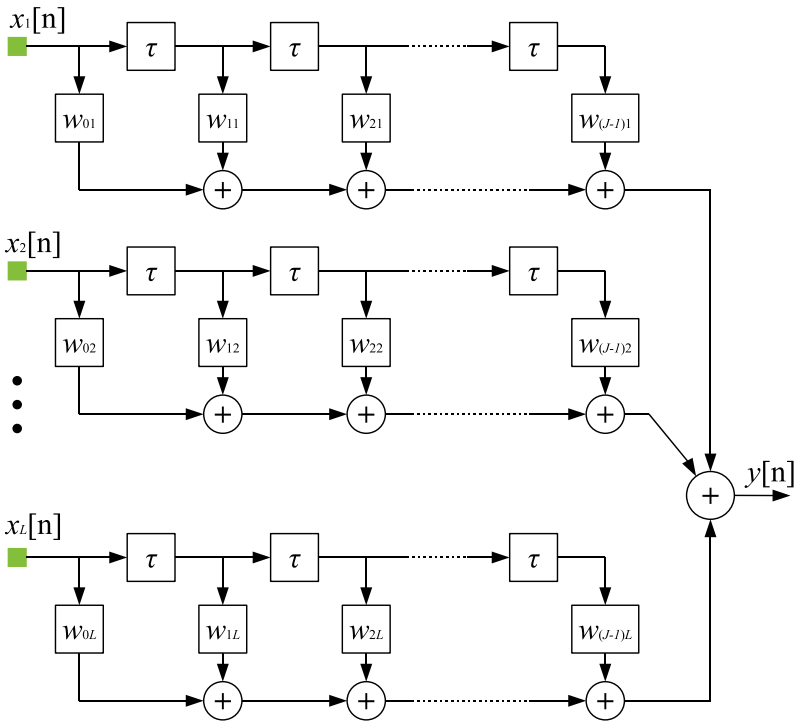

Figure 2.11: A wideband beamformer

This can be written in vector notation as

$$y[n] = \bar{\mathbf{w}}^H \bar{\mathbf{x}}[n] \tag{2.88}$$

where $\bar{\mathbf{w}}$ is the vector of $L \times J$ weights, and

$$\bar{\mathbf{x}}[n] = \begin{bmatrix} x_1[n] \\ \vdots \\ x_L[n] \\ x_1[n-\tau] \\ \vdots \\ x_L[n-\tau] \\ \vdots \\ x_1[n-(J-1)\tau] \\ \vdots \\ x_L[n-(J-1)\tau] \end{bmatrix} \tag{2.89}$$

where τ is the delay introduced by each tap, which is usually equal to the sample period. $\bar{\mathbf{x}}[n]$ is an $L \times J$ dimensional vector.

In the narrowband model, the steering vector $\mathbf{a}(\theta)$ is defined assuming that a pure sinusoidal wave of frequency equal to the carrier, the ultimate narrowband signal, excites the array [24]. It is used to model the time delays between different antennas as phase shifts, and is used in many of the beamforming algorithms as seen in Section 2.3. However, a wideband signal contains many frequency components and therefore a different definition of a steering vector is required. The steering vector is therefore extended to depend on frequency f, as well as DOA θ. To be used with the wideband model defined in Equation (2.88), the wideband steering vector which accounts for the delays added by the FIR filters is defined as

$$\mathbf{a}(\theta, f) = \begin{bmatrix} \mathbf{a}(\theta) \\ \mathbf{a}(\theta)e^{j2\pi f\tau} \\ \mathbf{a}(\theta)e^{j2\pi f2\tau} \\ \vdots \\ \mathbf{a}(\theta)e^{j2\pi f(J-1)\tau} \end{bmatrix} \tag{2.90}$$

where $\mathbf{a}(\theta)$ is the steering vector used in the narrowband model. The wideband steering vector has $L \times J$ entries. Note that usually, the signal is demodulated before it is weighted and filtered, and therefore, f is the baseband frequency component of the desired signal component. By choosing a steering vector $\mathbf{a}(\theta, f)$, weights for both spatial and temporal filtering can be selected so that a signal or signal component from direction θ and frequency f is received, and all other signals are rejected.

Then, all of the beamforming techniques presented in Section 2.3 can be applied with the new data vector $\mathbf{x}[k]$ and the steering vector $\mathbf{a}(\theta, f)$.

2.6 Introduction to MIMO Radar

MIMO radar is an emerging technology which has arisen due to advances in computational power [28]. It was inspired by the use of MIMO system architectures in wireless communication systems [29]. MIMO radar has been developed for a number of purposes, such as to increase robustness in the presence of target scintillations [29], to have more flexibility in the design of transmit beampatterns [30], to generate a transmit beampattern at the receiver [31] and finally, to obtain higher resolution spatial spectrum estimations [28, 32].

In contrast to an ordinary phased array, a MIMO radar system transmits multiple signal waveforms [11]. While the highly correlated phased array signals form a high

resolution directional beam on transmission, MIMO antennas transmit signals from a diverse set, and independence between the signals is exploited.

There are two MIMO radar architecture variations. References [29, 31, 33–35] describe systems in which the transmit antennas are scattered in space. This architecture primarily reduces the effect of target scintillation. The second variation, which is of interest in this project, uses an array of transmitting antennas co-located with an array of receiving antennas with typical inter-element spacing of half a wavelength [11, 28, 30, 32, 36].

2.6.1 Overview of MIMO Radar Operation

The idea of applying multiple input multiple output techniques to radar systems emerged from MIMO telecommunications systems. In the realm of communications, multiple transmitter and receiver antennas are used to provide diversity gain, and increase the reliability of a link. Appendix C introduces MIMO communications systems based on the book by Tse and Viswanath [37]. By understanding the application for which MIMO was pioneered, a better grasp of how it can be applied to radar systems can be obtained.

The MIMO radar architecture is illustrated in Figure 2.12. Each transmitter element simultaneously transmits a waveform which is linearly independent and in some cases orthogonal to every other waveform. The space around the radar system is linear, so the principal of superposition applies. Phased array transmitter beamforming is achieved by applying a complex weight to a base signal to obtain signals for each channel which combine to form a narrow beam on transmission. For MIMO, transmitter beampatterns can be designed by selecting waveforms, such that they

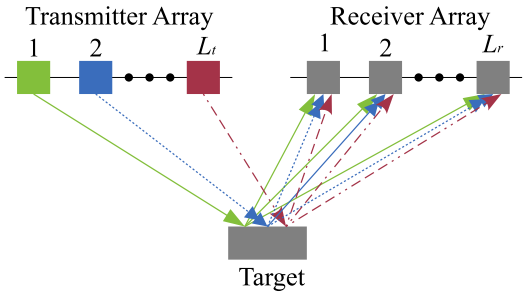

Figure 2.12: Illustration of MIMO radar when an orthogonal set of signals is transmitted.

combine to give the desired beampattern when transmitted. When orthogonal signals are transmitted, power is transmitted in all directions and the resultant beampattern is omnidirectional.

The MIMO receiver architecture is identical to a phased array receiver. However, the processing applied to the signals differs. In some cases an array of filters matched to each of the transmitted signals can be applied to each of the received signals. Therefore, $L_t \times L_r$ outputs are obtained, where L_t is the number of transmitters and L_r is the number of receivers. These signals can be combined to obtain estimates of the target range. Also, techniques of beamforming similar to phased array techniques can be applied to the receiver array. Due to the extra degrees of freedom offered by an independent set of transmitted signals, a set of new spectral and parametric techniques can be devised for estimation of target parameters.

Another result of the MIMO radar architecture, is that the effective array aperture can be increased. Figure 2.13(a) shows three element transmitter and receiver arrays, and the "virtual array" that results. The virtual array has 5 elements and is obtained from the spatial convolution of the antenna array positions [28, 38]. As a result of the convolution, some of the virtual antenna locations are overrepresented. Therefore, if the array elements on one of the arrays are distributed sparsely, as in Figure 2.13(b), the virtual array will have a larger aperture. If the transmitter and receiver arrays are both one-dimensional arrays, orientated at 90° to one another, then the virtual array will be a two-dimensional array as shown in Figure 2.13(c) [39]. The increased virtual array aperture can be used to obtain higher resolution target parameter estimates compared to a phased array system with an equivalent number of transmitter and receiver elements.

In the sections that follow, the MIMO signal model is developed before parameter estimation techniques are presented in Section 2.8 and beampattern design is introduced in Section 2.9.

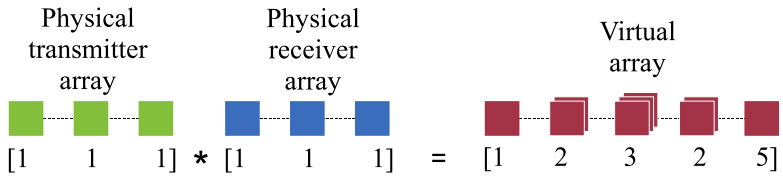

(a) Full transmitter and receiver arrays giving overrepresented virtual elements.

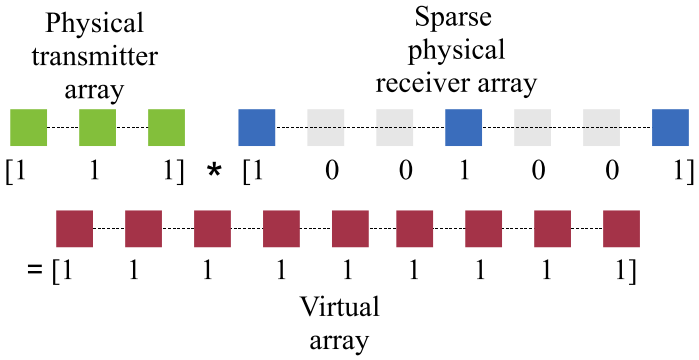

(b) Sparsely populated receiver array giving a full virtual array.

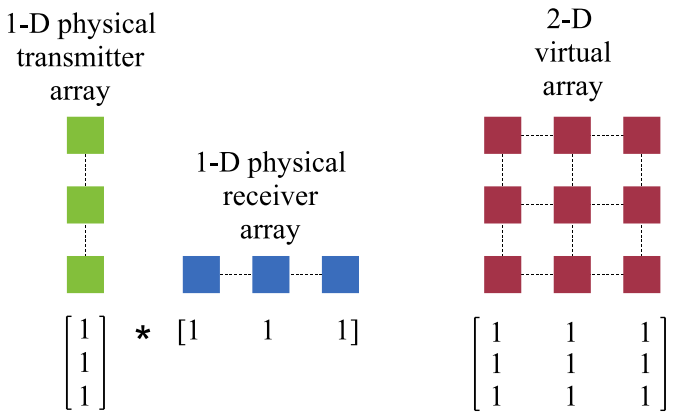

(c) Transmitter and receiver arrays giving a two-dimensional virtual array.

Figure 2.13: Virtual arrays obtained with different transmitter and receiver array architectures.

2.7 The MIMO Signal Model

The signal model for a narrowband MIMO radar system is the generalisation of a narrowband phased array system with the addition that multiple waveforms can be transmitted. A model based on those developed in [11, 32] and [40] is presented. Consider a transmitter with L_t transmitting elements whose locations are arbitrary, and a receiver with L_r receiving elements. Simultaneously, the system transmits L_t

linearly independent waveforms. The set of transmitted waveforms is given by

$$\mathbf{S} = \begin{bmatrix} \mathbf{s}_1 \\ \mathbf{s}_2 \\ \vdots \\ \mathbf{s}_{L_t} \end{bmatrix} \tag{2.91}$$

where $\mathbf{s}_i$ is a snapshot of N time samples of the ith transmitted signal ($\mathbf{s}_i \in \mathbb{C}^{1\times N}$).

The sample covariance matrix of the transmitted signals is estimated by

$$\hat{\mathbf{R}}_S = \frac{1}{N}\mathbf{S}\mathbf{S}^H. \tag{2.92}$$

If the transmitted waveforms are orthogonal to one another, then $\hat{\mathbf{R}}_S$ is a diagonal matrix.

Let a target be located at a position in the far-field of the transmitter and receiver arrays. Let this position relative to the transmitter be denoted by the angle θ_t and the position relative to the receiver be denoted θ_r. Since the target is in the far-field of the arrays the distance in between antennas is negligible in comparison to the distance from the array to the target, making the difference in angles at each transmitter or receiver antenna negligible. This is shown in Figure 2.14. In many cases the transmitter and receiver antennas will be co-located, or the distance between the transmitter and receiver arrays will be small enough that it is negligible when compared to the distance to the target and under these conditions it is reasonable to assume that $\theta_t = \theta_r$. For the following sections, it will be assumed that $\theta_t = \theta_r = \theta$.

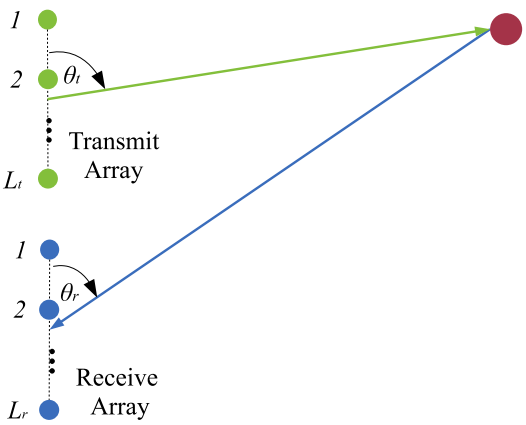

Figure 2.14: Transmitter and receiver location parameters.

A steering vector can be generated to model the effect of the different path lengths from each element in the transmitter array, to the target with location parameter θ. It will be given by

$$\mathbf{a}_t(\theta) = \begin{bmatrix} e^{j2\pi f_0 \tau_1(\theta)} \\ e^{j2\pi f_0 \tau_2(\theta)} \\ \vdots \\ e^{j2\pi f_0 \tau_{L_t}(\theta)} \end{bmatrix} \tag{2.93}$$

where f_0 is the radar's carrier frequency, and τ_i is the time taken for the signal to travel from the ith transmitter element to the reflecting object. The steering vector has L_t entries. This steering vector will have the form given in 2.24 if the transmitter array is a ULA.

Then, the signal which arrives at the reflecting object is given by

$$\mathbf{a}_t^H(\theta)\mathbf{S}. \tag{2.94}$$

The signal is reflected by a target and is received at the receiver. The steering vector, composed of the phase information of the signals propagating from the reflecting target to each element of the receiver is given by

$$\mathbf{a}_r(\theta) = \begin{bmatrix} e^{j2\pi f_0 \tilde{\tau}_1(\theta)} \\ e^{j2\pi f_0 \tilde{\tau}_2(\theta)} \\ \vdots \\ e^{j2\pi f_0 \tilde{\tau}_{L_r}(\theta)} \end{bmatrix} \tag{2.95}$$

where $\tilde{\tau}_i$ is the time taken for the signal to travel from the reflecting object to the ith receiving element. The receiver steering vector has L_r elements.

Thus, the received signal can be represented by

$$\mathbf{X} = \mathbf{a}_r^*(\theta)\beta(\theta)\mathbf{a}_t^H(\theta)\mathbf{S} + \mathbf{Z} \tag{2.96}$$

where $\beta(\theta)$ is the complex amplitude proportional to the radar cross section of the reflecting target which is dependent on the orientation of the target. $\mathbf{Z}$ is the additive interference and noise that will be seen at the receiver. $\mathbf{X}$ and $\mathbf{Z}$ both have dimensions L_r-by-N.

The received MIMO signal can be further generalised to the case of multiple reflecting targets. Consider that there are K targets which reflect the signal. Then, the

received signal will be given by

$$\mathbf{X} = \sum_{k=1}^{K} \mathbf{a}_r^*(\theta_k)\beta(\theta_k)\mathbf{a}_t^H(\theta_k)\mathbf{S} + \mathbf{Z}. \tag{2.97}$$

$\hat{\mathbf{R}}_X$ is an estimate of the covariance matrix of $\mathbf{X}$ and is given by

$$\hat{\mathbf{R}}_X = \frac{1}{N}\mathbf{X}\mathbf{X}^H. \tag{2.98}$$

2.8 MIMO Techniques for Parameter Estimation

When each transmitter antenna transmits independent waveforms, algorithms which provide estimation of target location θ and amplitude $\beta(\theta)$ can be applied. The Capon algorithm discussed in Section 2.3.2.4 can be extended for MIMO radar to include an estimation for $\beta(\theta)$. Also, two additional spectral algorithms, the Amplitude and Phase Estimation (APES) algorithm and a Generalised Likelihood Ratio Test (GLRT), are presented. These methods are based on those of Xu et al. [32] and Li and Stoica [40]. Lastly, the Capon Approximate Maximum Likelihood (CAML) technique, a parametric method to estimate $\beta(\theta)$, which uses a spectral estimate of θ, is presented.

For all of these algorithms, it is assumed that the range of the targets is known. Therefore, the received signal is only the signal for the "range bin" of interest, where a "range bin" is a segment of the signal starting at the exact moment that an echo from a target at a certain range is received, and of length equal to the transmitted signal length. In addition, all of the algorithms require the transmitted signals to be known.

2.8.1 Capon

Recall the Capon optimisation given in Equation (2.71) and the weights solving this optimisation given in Equation (2.72). These equations are restated to include the MIMO notation. The Capon optimisation is

$$\begin{aligned} &\min_{\mathbf{W}} \mathbf{w}^T\hat{\mathbf{R}}_X\mathbf{w}^* \\ &\text{subject to } \mathbf{w}^T\mathbf{a}_r(\theta) = 1 \end{aligned} \tag{2.99}$$

and the optimum weights are

$$\mathbf{w}_{Capon}(\theta) = \frac{\hat{\mathbf{R}}_X^{-1}\mathbf{a}_r^*(\theta)}{\mathbf{a}_r^T(\theta)\hat{\mathbf{R}}_X^{-1}\mathbf{a}_r^*(\theta)}. \tag{2.100}$$

The Capon estimates of $\beta(\theta)$ are obtained by the minimisation of the least squares difference between the weighted received signal, and the product of the transmitted signal and the complex amplitude at location θ [32, 40]. This is

$$\min_{\beta(\theta)} \left\| \mathbf{w}^H\mathbf{X} - \beta(\theta)\mathbf{a}_t^H\mathbf{S} \right\|^2. \tag{2.101}$$

The Capon estimate of $\beta(\theta)$, which is derived in Section D.1 in Appendix D, is

$$\hat{\beta}_{Capon}(\theta) = \frac{\mathbf{a}_r^T(\theta)\hat{\mathbf{R}}_X^{-1}\mathbf{X}\mathbf{S}^H\mathbf{a}_t(\theta)}{N\left[\mathbf{a}_r^T(\theta)\hat{\mathbf{R}}_X^{-1}\mathbf{a}_r^*(\theta)\right]\left[\mathbf{a}_t^H(\theta)\hat{\mathbf{R}}_S\mathbf{a}_t(\theta)\right]}. \tag{2.102}$$

2.8.2 Amplitude and Phase Estimation (APES)

The APES algorithm is a spectral analysis method which provides more accurate estimates of $\beta(\theta)$ than the Capon method [32, 40]. The optimisation for the APES method is

$$\begin{gathered}\min_{\mathbf{w}\beta(\theta)} \left\| \mathbf{w}^T\mathbf{X} - \beta(\theta)\mathbf{a}_t^H(\theta)\mathbf{S} \right\|^2 \\ \text{subject to } \mathbf{w}^T\mathbf{a}_r(\theta) = 1.\end{gathered} \tag{2.103}$$

Therefore APES is the minimisation, in the LS sense to determine the values of $\mathbf{w}$ and $\beta(\theta)$ which result in the received signal being closest to the target signal. The constraint is the same as that used by the Capon beamformer, and ensures unity weighting in the "look direction".

By first minimising with respect to $\beta(\theta)$, and then $\mathbf{w}$, the optimum weights can be found to be

$$\mathbf{w}_{APES}(\theta) = \frac{\hat{\mathbf{Q}}^{-1}\mathbf{a}_r^*(\theta)}{\mathbf{a}_r^T(\theta)\hat{\mathbf{Q}}^{-1}\mathbf{a}_r^*(\theta)} \tag{2.104}$$

and the estimate of $\beta(\theta)$ is

$$\hat{\beta}_{APES}(\theta) = \frac{\mathbf{a}_r^H(\theta)\hat{\mathbf{Q}}^{-1}\mathbf{X}\mathbf{S}^H\mathbf{a}_t(\theta)}{N\left[\mathbf{a}_r^T(\theta)\hat{\mathbf{Q}}^{-1}\mathbf{a}_r^*(\theta)\right]\left[\mathbf{a}_t^H(\theta)\hat{\mathbf{R}}_S\mathbf{a}_t(\theta)\right]} \tag{2.105}$$

where

$$\hat{\mathbf{Q}} = \hat{\mathbf{R}}_X - \frac{\mathbf{X}\mathbf{S}^H\mathbf{a}_t(\theta)\mathbf{a}_t^H(\theta)\mathbf{S}\mathbf{X}^H}{N^2\mathbf{a}_t^H(\theta)\hat{\mathbf{R}}_S\mathbf{a}_t(\theta)}. \tag{2.106}$$

A full derivation of APES is given in Section D.2 in Appendix D.

2.8.3 Generalised Likelihood Ratio Test (GLRT)

The Capon and APES methods both work well to locate targets and estimate their complex amplitudes. However, when there is a jammer in the vicinity of the radar system, neither of these algorithms are able to differentiate between the target returns and the jammer signal. The GLRT, applied to MIMO, is a radar imaging technique which is able to locate targets, while rejecting the influence of a jammer [32, 40]. The GLRT does not locate the targets with a resolution as fine as that of the Capon and APES methods, but can be used together with one of these methods to verify which peaks in the spectrum are targets, and which are jammers.

For the GLRT, it is assumed that the columns of the residual term $\mathbf{Z}$ are i.i.d. complex Gaussian random variables, with unknown covariance matrix $\mathbf{\Psi}$. The GLR optimisation is

$$\rho = 1 - \left[\frac{\max_{\mathbf{\Psi}} f(\mathbf{X}|\beta = 0, \mathbf{\Psi})}{\max_{\beta,\mathbf{\Psi}} f(\mathbf{X}|\beta, \mathbf{\Psi})} \right]^{\frac{1}{N}} \tag{2.107}$$

where

$$f(\mathbf{X} \mid \beta, \mathbf{\Psi}) = \pi^{-NL_r} \left|\mathbf{\Psi}\right|^{-N} \mathrm{e}^{-\operatorname{tr}(\mathbf{\Psi}^{-1}(\mathbf{X}-\mathbf{a}_r^*\beta\mathbf{a}_t^H\mathbf{S})(\mathbf{X}-\mathbf{a}_r^*\beta\mathbf{a}_t^H\mathbf{S})^H)} \tag{2.108}$$

is the PDF of the observed data matrix $\mathbf{X}$, given parameters β and $\mathbf{\Psi}$.

If there is a target at a location θ, then the maximisation on $f(\mathbf{X}\,|\beta, \mathbf{\Psi}\,)$ is much greater than that on $f(\mathbf{X}\,|\beta = 0, \mathbf{\Psi}\,)$ and ρ approaches one. On the contrary, if there is no target at location θ, both of the maximisations will have similar values, and ρ will have a value close to zero.

The method for evaluating the GLR is given in Section D.3 in Appendix D. The GLRT finally evaluates to

$$\rho(\theta) = 1 - \frac{\mathbf{a}_r^H(\theta)\hat{\mathbf{R}}_X^{-1}\mathbf{a}_r(\theta)}{\mathbf{a}_r^H(\theta)\hat{\mathbf{Q}}^{-1}\mathbf{a}_r(\theta)} \tag{2.109}$$

where $\hat{\mathbf{Q}}$ is as defined in Equation (2.106).

2.8.4 Capon Approximate Maximum Likelihood (CAML)

All of the methods presented so far estimate the target parameter $\beta(\theta)$ at each angular location θ. The Approximate Maximum Likelihood (AML) method, however, estimates the complex amplitudes of all of the targets jointly, given estimates of the target locations, which can provide improvements in the accuracy of the estimates.

Because the Capon technique has the highest resolution, it is combined with the GLRT to obtain estimates of the target locations. Hence the CAML is constructed.

Assume that there are K targets, where K is known (it can be determined by the GLRT). Then, the Capon estimator is used to determine estimates of the target locations $\{\hat{\theta}_k\}_{k=1}^{K}$. Define the matrices

$$\mathbf{A}_t = \left[\begin{array}{cccc} \mathbf{a}_t(\hat{\theta}_1) & \mathbf{a}_t(\hat{\theta}_2) & \dots & \mathbf{a}_t(\hat{\theta}_K) \end{array} \right], \tag{2.110}$$

$$\mathbf{A}_r = \left[\begin{array}{cccc} \mathbf{a}_r(\hat{\theta}_1) & \mathbf{a}_r(\hat{\theta}_2) & \dots & \mathbf{a}_r(\hat{\theta}_K) \end{array} \right] \tag{2.111}$$

and

$$\beta = \left[\begin{array}{c} \beta(\hat{\theta}_1) \\ \beta(\hat{\theta}_2) \\ \vdots \\ \beta(\hat{\theta}_K) \end{array} \right]. \tag{2.112}$$

The received signal model given in Equation (2.97) can then be written in matrix form as

$$\mathbf{X} = \mathbf{A}_r^* \mathbf{B} \mathbf{A}_t^H \mathbf{S} + \tilde{\mathbf{Z}} \tag{2.113}$$

where $\mathbf{B} = \text{diag}(\beta)$ and $\tilde{\mathbf{Z}}$ is the residual term with columns which are i.i.d. circularly symmetric complex Gaussian random vectors. This new form is a Diagonal Growth Curve (DGC) model [41]. The AML is used in place of the Maximum Likelihood (ML) method, which cannot produce a closed form estimate of β. The AML is asymptotically equivalent to the ML for a large number of data samples N.

The AML estimate of β is

$$\hat{\beta}_{AML} = \frac{1}{N} \left[(\mathbf{A}_r^T \mathbf{T}^{-1} \mathbf{A}_r^*) \odot (\mathbf{A}_t^T \hat{\mathbf{R}}_S^* \mathbf{A}_t^*) \right]^{-1} \text{vecd}(\mathbf{A}_r^T \mathbf{T}^{-1} \mathbf{X} \mathbf{S}^H \mathbf{A}_t) \tag{2.114}$$

where $\odot$ is the Hadamard product, vecd$(\cdot)$ is the column vector formed from the diagonal elements of a matrix and

$$\mathbf{T} = N\hat{\mathbf{R}}_X - \frac{1}{N} \mathbf{X} \mathbf{S}^H \mathbf{A}_t (\mathbf{A}_t^H \hat{\mathbf{R}}_S \mathbf{A}_t)^{-1} \mathbf{A}_t^H \mathbf{S} \mathbf{X}^H. \tag{2.115}$$

A detailed derivation of the AML can be found in [41], and its application to MIMO can be found in [36] and [40].

2.9 Probing Signal Design

The independent waveforms transmitted by a MIMO radar make a new type of beamforming possible. This is known as transmit beamforming and is the generation of an optimal beampattern by the selection of signals to be transmitted.

Recall from Equation (2.94) that the signal, at a location θ is given by

$$\mathbf{a}_t^H(\theta)\mathbf{S}. \tag{2.116}$$

The signal power is proportional to the average of the square of the signal above. Therefore, the spatial spectrum of the signal power at location θ can be given by

$$P(\theta) = \mathrm{E}\left[\mathbf{a}_t^H(\theta)\mathbf{s}(t)\mathbf{s}^H(t)\mathbf{a}_t(\theta)\right] = \mathbf{a}_t^H(\theta)\mathbf{R}_S\mathbf{a}_t(\theta) \tag{2.117}$$

where $\mathrm{E}[\cdot]$ is the statistical expectation, $\mathbf{R}_S = \mathrm{E}[\mathbf{s}(t)\mathbf{s}^H(t)]$ is the transmitted signal covariance matrix and $\mathbf{s}(t)$ is a column of $\mathbf{S}$. This spatial spectrum is named the transmit beampattern.

This section discusses how transmitter beamforming can be performed, by designing a covariance matrix $\mathbf{R}_S$ to obtain an optimum transmit beampattern. The signal set to be transmitted, $\mathbf{S}$, can be synthesized from $\mathbf{R}_S$. The simplest way to achieve this is to generate a set of signals $\mathbf{W} = [\mathbf{w}_1 \ \ldots \ \mathbf{w}_N]$ where each $\mathbf{w}_i$ is an i.i.d. random vector with zero mean and covariance matrix of $\mathbf{I}$. Then, the set of signals for transmission is given by

$$\mathbf{S} = \mathbf{R}_S^{\frac{1}{2}}\mathbf{W}. \tag{2.118}$$

The ith base signal $\mathbf{w}_i$ can be a Quadrature Phase Shift Keying (QPSK) sequence where each element takes its values from the set $\{\pm\frac{1}{\sqrt{2}} \pm \frac{1}{\sqrt{2}}j\}$ [36].

There are some constraints on $\mathbf{R}_S$ that are common to all of the beampattern designs. Firstly, a power constraint is required. In the designs below either the elemental power constraint or the total power constraint is used. The elemental power constraint ensures that each element transmits a signal of equal power. It is given by

$$R_{S,ll} = \frac{p}{L_t}, \quad l = 1, \ldots, L_t \tag{2.119}$$

where p is the total power to be transmitted and $R_{S,ll}$ is the lth element of the main diagonal of $\mathbf{R}_S$.

The total power constraint allows the power transmitted by each element to be varied, but fixes the total transmitted power to p. It is given by

$$\mathrm{tr}\{\mathbf{R}_S\} = p \tag{2.120}$$

where tr is the trace of a matrix which is the sum of the elements on the main diagonal.

The elemental power constraint is more practical in most cases because it is likely that all transmitter elements will be identical. The most economical performance for a given system will be obtained by transmitting close to the maximum power on all transmitters at all times.

The second constraint is that $\hat{\mathbf{R}}_S$ must be a positive semi-definite matrix so that physically realisable signals can be generated. This is denoted by $\hat{\mathbf{R}}_S \geq 0$.

Different approaches can be taken to design an optimal waveform. However, the principal goal is that the power transmitted in the direction of target locations should be maximised in some way. In addition, the concept of a cross-correlation beampattern is introduced. In order to be able to apply adaptive algorithms, such as Capon, APES and GLRT, it is necessary that the waveforms reflected from different targets are linearly independent of one another. The cross-correlation beampattern is defined as the covariance between the probing signals at locations θ and $\bar{\theta}$ and is given by $\mathbf{a}_t^H(\theta)\hat{\mathbf{R}}_S\mathbf{a}_t(\bar{\theta})$, for $\theta \neq \bar{\theta}$. The performance of adaptive MIMO algorithms decreases as the cross-correlation beampattern increases. Therefore, it is also desirable to minimise the cross-correlation beampattern.

The sections below describe different criteria and optimisation problems for the design of waveforms. The formulations above and the sections below are based on the methods of Stoica et al. [36].

2.9.1 Waveform Design for Unknown Target Locations

With no knowledge of the target locations, the covariance matrix $\mathbf{R}_S$ must be chosen to maximise the reflected power in the worst case scenario. It is intuitive that in these circumstances an omnidirectional signal should be transmitted. Therefore, using the elemental power constraint given in Equation (2.119), the optimum covariance matrix is

$$\mathbf{R}_S = \frac{p}{L_t}\mathbf{I}. \tag{2.121}$$

A more detailed description of this derivation is given by Stoica et al. [36].

Thus, with no knowledge of the target locations, each transmitter's waveform is orthogonal to every other waveform. The resulting signal is spatially white and has

constant power at every location θ.

2.9.2 Maximum Power Waveform Design for Localised Targets

Assume that estimates of the target locations of interest are known. With this knowledge, it is possible to perform transmit beamforming such that maximum power from the target locations is returned. Recall the model from Equation (2.97), and assume that estimates of $\tilde{K}$ ($\tilde{K} \leq K$) target locations $\{\hat{\theta}_k\}_{k=1}^{\tilde{K}}$ are available. From [36] the power from the known target locations is then given by

$$P_{\tilde{K}} = \sum_{k=1}^{\tilde{K}} \mathbf{a}_t^H(\hat{\theta}_k)\mathbf{R}_S\mathbf{a}_t(\hat{\theta}_k). \tag{2.122}$$

By defining

$$\hat{\mathbf{B}} = \sum_{k=1}^{\tilde{K}} \mathbf{a}_t(\hat{\theta}_k)\mathbf{a}_t^H(\hat{\theta}_k) \tag{2.123}$$

Equation (2.9.2) becomes

$$P_{\tilde{K}} = \mathrm{tr}\left\{\mathbf{R}_S\hat{\mathbf{B}}\right\}. \tag{2.124}$$

For maximum power to be transmitted in the directions of the targets, the optimisation problem is

$$\begin{aligned} &\max_{\mathbf{R}_S} \mathrm{tr}\left\{\mathbf{R}_S\hat{\mathbf{B}}\right\} \\ &\text{s.t } \mathrm{tr}\{\mathbf{R}_S\} = p \\ &\mathbf{R}_S \geq 0. \end{aligned} \tag{2.125}$$

Note that the total power constraint is used in place of the uniform power constraint to simplify computation.

Evaluating the objective of the maximisation gives

$$\begin{aligned} \mathrm{tr}\left\{\mathbf{R}_S\hat{\mathbf{B}}\right\} &= \mathrm{tr}\left\{\mathrm{E}\left[\mathbf{s}(t)\mathbf{s}^H(t)\right]\hat{\mathbf{B}}\right\} \\ &= \mathrm{E}\left[\mathrm{tr}\left\{\mathbf{s}(t)\mathbf{s}^H(t)\hat{\mathbf{B}}\right\}\right] \\ &= \mathrm{E}\left[\mathbf{s}^H(t)\hat{\mathbf{B}}\mathbf{s}(t)\right] \end{aligned} \tag{2.126}$$

where $\mathbf{s}(t)$ is a column of $\mathbf{S}$ and the cyclic property of the trace was used. A linear algebra matrix inequality states that

$$\mathbf{s}^H(t)\hat{\mathbf{B}}\mathbf{s}(t) \leq \lambda_{max}(\hat{\mathbf{B}})\mathbf{s}^H(t)\mathbf{s}(t) \tag{2.127}$$

where $\lambda_{max}(\hat{\mathbf{B}})$ is the maximum eigenvalue of $\hat{\mathbf{B}}$.

Therefore, the inequality evaluates to

$$\begin{aligned} \mathrm{tr}\{\mathbf{R}_S\hat{\mathbf{B}}\} &\leq \mathrm{E}\left[\lambda_{max}(\hat{\mathbf{B}})\mathbf{s}^H(t)\mathbf{s}(t)\right] \\ &\leq \lambda_{max}(\hat{\mathbf{B}})\,\mathrm{E}\left[\mathbf{s}^H(t)\mathbf{s}(t)\right] \\ &\leq \lambda_{max}(\hat{\mathbf{B}})\,\mathrm{tr}\left\{\mathbf{R}_S\right\}. \end{aligned} \tag{2.128}$$

Then, due to the total power constraint, the inequality can be rewritten as

$$\mathrm{tr}\left\{\mathbf{R}_S\hat{\mathbf{B}}\right\} \leq p\lambda_{max}(\hat{\mathbf{B}}). \tag{2.129}$$

It can be shown that the inequality achieves its maximum value when

$$\mathbf{R}_S = p\mathbf{u}\mathbf{u}^H \tag{2.130}$$

where $\mathbf{u}$ is the unit-norm eigenvector associated with $\lambda_{max}(\hat{\mathbf{B}})$.

It is relatively easy to compute the covariance matrix for the maximum power waveform design. The design however has deficiencies. Because the total power constraint is used, each transmitter might not be used to its full potential, as the power transmitted by each might vary widely. Secondly, the power at each target location is not specified and might also vary more than desired. Finally, the design does not control the cross-correlation beampattern, and thus the signals received from any two targets can be coherent, degrading the system performance.

2.9.3 Beampattern Matching Design

To improve on the above design, the beampattern matching design is formulated. Let $\phi(\theta)$ represent the desired beampattern which specifies the desired power in directions which lie in the set of locations $\{\mu_q\}_{q=1}^{Q}$. This set of grid points should contain good approximations of the target locations. Let $\{\hat{\theta}_k\}_{k=1}^{\tilde{K}}$ be initial estimates of the target locations.

The optimisation problem is to determine $\mathbf{R}_S$ so that it approximates the desired pattern $\mu(\theta)$ in a LS sense over the points $\{\mu_q\}_{q=1}^{Q}$, and so that it minimises the cross-correlation beampattern $\mathbf{a}_t^H(\theta)\mathbf{R}_S\mathbf{a}_t(\bar{\theta})$ in a LS sensed over the estimated target

locations $\{\hat{\theta}_k\}_{k=1}^{\tilde{K}}$ Stoica et al. [36]. This is expressed as

$$\begin{aligned} \min_{\alpha,\mathbf{R}_S} \quad & \left\{ \frac{1}{Q}\sum_{q=1}^{Q} w_q \left[\alpha\phi(\mu_q) - \mathbf{a}_t^H(\mu_q)\mathbf{R}_S\mathbf{a}_t(\mu_q)\right]^2 \right. \\ & \left. + \frac{2w_c}{\tilde{K}^2 - \tilde{K}} \sum_{k=1}^{\tilde{K}-1} \sum_{p=k+1}^{\tilde{K}} \left|\mathbf{a}_t^H(\hat{\theta}_k)\mathbf{R}_S\mathbf{a}_t(\hat{\theta}_p)\right|^2 \right\} \\ \text{s.t} \quad & R_{S,ll} = \frac{c}{L_t}, \quad l = 1, \ldots, L_t \\ & \mathbf{R}_S \geq 0 \end{aligned} \tag{2.131}$$

where w_q is a weight for the qth location, w_c is a weighting for the cross-correlation term and α is scaling factor for the desired beampattern. These weights are chosen to prioritise the importance of matching the desired beampattern at each location μ_q, and minimising the cross-correlation pattern.

The optimisation can be changed into the form of a semi-definite quadratic program (SQP) which is an optimisation problem with quadratic constraints as well as a constraint requiring a matrix to be positive semi-definite. The form of the optimisation problem is altered for solution with a tool such as SeDuMi ([42] and [43]).

In order to reformulate the problem, we define the operation vec$(\cdot)$ which transforms an A-by-B matrix into an $A \times B$ dimensional vector by stacking the columns of the matrix on top of one another. Due to the Hermitian symmetry of $\mathbf{R}_S$, the following can be defined

$$\text{vec}\left(\mathbf{R}_S\right) = \mathbf{J}\mathbf{r} \tag{2.132}$$

where $\mathbf{r}$ is a L_t^2 dimensional vector composed of $\{R_{S,ll}\}_{l=1}^{L_t}$ and then the real parts followed by the imaginary parts of $\{R_{lp}\}_{l=1,p>l}^{L_t}$. $\mathbf{J}$ is a matrix of constants with the values $(0, 1, \pm j)$. An example and a generalised algorithm for generating $\mathbf{J}$ is given in Appendix E.

The vector $\mathbf{r}$ will be used to solve the optimisation problem. Given the new format of the optimisation variable, it is necessary to reformulate the objective function. Noting that vec$(\cdot)$ operates on a scalar without altering it, and using the property $\text{vec}\left(\mathbf{X}_1\mathbf{B}\mathbf{X}_2\right) = \left(\mathbf{X}_2^T \otimes \mathbf{X}_1\right)\text{vec}(\mathbf{B})$, the following simplifications can be made

$$\begin{aligned} \mathbf{a}_t^H(\mu_q)\mathbf{R}_S\mathbf{a}_t(\mu_q) &= \text{vec}\left(\mathbf{a}_t^H(\mu_q)\mathbf{R}_S\mathbf{a}_t(\mu_q)\right) \\ &= \left(\mathbf{a}_t^T(\mu_q) \otimes \mathbf{a}_t^H(\mu_q)\right)\mathbf{J}\mathbf{r} \\ &= -\mathbf{g}_q^T\mathbf{r} \end{aligned} \tag{2.133}$$

where

$$\mathbf{g}_q = -\left[\left(\mathbf{a}_t^T(\mu_q) \otimes \mathbf{a}_t^H(\mu_q)\right)\mathbf{J}\right]^T. \tag{2.134}$$

Similarly,

$$\begin{aligned} \mathbf{a}_t^H(\hat{\theta}_k)\mathbf{R}_S\mathbf{a}_t(\hat{\theta}_p) &= \left(\mathbf{a}_t^T(\hat{\theta}_k) \otimes \mathbf{a}_t^H(\hat{\theta}_p)\right)\mathbf{J}\mathbf{r} \\ &= \mathbf{d}_{k,p}^H\mathbf{r}. \end{aligned} \tag{2.135}$$

where

$$\mathbf{d}_{k,p} = \left[\left(\mathbf{a}_t^T(\hat{\theta}_k) \otimes \mathbf{a}_t^H(\hat{\theta}_p)\right)\mathbf{J}\right]^H \tag{2.136}$$

Substituting Equation (2.133) and Equation (2.135) back into the objective function of Equation (2.131) reformulates the problem to

$$\begin{aligned} &\frac{1}{Q}\sum_{q=1}^{Q} w_q\left[\alpha\phi(\mu_q) + \mathbf{g}_q^T\mathbf{r}\right]^2 + \frac{2w_c}{\tilde{K}^2 - \tilde{K}}\sum_{k=1}^{\tilde{K}-1}\sum_{p=k+1}^{\tilde{K}}\left|\mathbf{d}_{k,p}^H\mathbf{r}\right|^2 \\ &= \frac{1}{Q}\sum_{q=1}^{Q} w_q\left\{\begin{bmatrix} \phi(\mu_q) & \mathbf{g}_q^T \end{bmatrix}\begin{bmatrix} \alpha \\ \mathbf{r} \end{bmatrix}\right\}^2 + \frac{2w_c}{\tilde{K}^2 - \tilde{K}}\sum_{k=1}^{\tilde{K}-1}\sum_{p=k+1}^{\tilde{K}}\left|\begin{bmatrix} 0 & \mathbf{d}_{k,p}^H \end{bmatrix}\begin{bmatrix} \alpha \\ \mathbf{r} \end{bmatrix}\right|^2 \\ &= \rho^T\mathbf{\Gamma}\rho \end{aligned} \tag{2.137}$$

where

$$\rho = \begin{bmatrix} \alpha \\ \mathbf{r} \end{bmatrix} \tag{2.138}$$

which is a real vector. Also

$$\begin{aligned} \mathbf{\Gamma} = \; & \frac{1}{Q}\sum_{q=1}^{Q} w_q\begin{bmatrix} \phi(\mu_q) \\ \mathbf{g}_q \end{bmatrix}\begin{bmatrix} \phi(\mu_q) & \mathbf{g}_q^T \end{bmatrix} + \\ & \frac{2w_c}{\tilde{K}^2 - \tilde{K}}\sum_{k=1}^{\tilde{K}-1}\sum_{p=k+1}^{\tilde{K}}\begin{bmatrix} 0 \\ \mathbf{d}_{k,p} \end{bmatrix}\begin{bmatrix} 0 & \mathbf{d}_{k,p}^H \end{bmatrix}. \end{aligned} \tag{2.139}$$

Therefore, finally in SQP form, the optimisation problem can be written as [44]:

$$\begin{aligned} &\min_{\delta,\rho}\delta \\ &\text{subject to } \left\|\mathbf{\Gamma}^{\frac{1}{2}}\rho\right\| \leq \delta \\ &R_{S,ll} = \frac{c}{L_t},\ l = 1\ldots L_t \\ &\mathbf{R}_S \geq 0 \end{aligned} \tag{2.140}$$

where $\mathbf{R}_S$ and ρ are linearly dependent on one another due to the relationship between $\mathbf{R}_S$ and $\mathbf{r}$.

2.10 Transmitter Beamforming on Reception (TBR)

When a set of orthogonal MIMO signals is transmitted, the transmitter pattern is omnidirectional. However, on reception, by applying a bank of L_t filters to each of the L_r received signals, the signal received on each transmitter can be split into the L_t transmitted signals. This allows an omnidirectional beam to be transmitted, and a "transmitter beampattern" to be formed on reception. A receiver beampattern can then be formed in addition to the transmitter beampattern. Techniques of transmitter beamforming on reception have been discussed by Frazer et al. [31], Hassanien and Vorobyov [45] and Qu et al. [46] and the formulation below is based on this work, although it excludes the Doppler analysis presented in [31].

TBR is illustrated for a single channel in Figure 2.15. Assume that the ith received signal $\mathbf{x}_i$ and the jth transmitted signal $\mathbf{s}_j$ both have N time samples. This would be true if the received signal was for a particular range bin, in which at least one target is known to be located. The matched filter operation of the jth transmitted signal on the ith received signal can then be given by

$$\tilde{x}_{ij} = \frac{1}{\sqrt{N}} \mathbf{x}_i \mathbf{s}_j^H. \tag{2.141}$$

where the division by $\sqrt{N}$ is included to ensure that the signal energy remains constant before and after matching [46].

This can be written in matrix notation where $\tilde{x}_{ij}$ is the entry in position (i, j) of the matrix given by

$$\tilde{\mathbf{X}} = \frac{1}{\sqrt{N}} \mathbf{X}\mathbf{S}^H. \tag{2.142}$$

This operation produces the cross-correlation matrix of the transmitted and received signals and is a matrix of dimensions L_r-by-L_t.

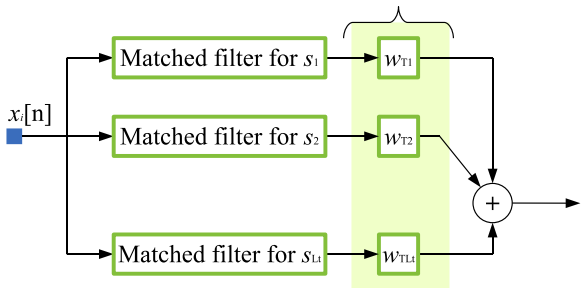

Figure 2.15: Transmitter beamforming on reception (TBR).

Then, substituting the expression for the received signal matrix from Equation (2.97) into Equation (2.142) above gives

$$\begin{aligned} \tilde{\mathbf{X}} &= \frac{1}{\sqrt{N}} \sum_{k=1}^{K} \mathbf{a}_r^*(\theta_k)\beta(\theta_k)\mathbf{a}_t^H(\theta_k)\mathbf{S}\mathbf{S}^H + \mathbf{Z}\mathbf{S}^H \\ &= \frac{1}{\sqrt{N}} \sum_{k=1}^{K} \mathbf{a}_r^*(\theta_k)\beta(\theta_k)\mathbf{a}_t^H(\theta_k) + \tilde{\mathbf{Z}} \end{aligned} \tag{2.143}$$

where the term $\mathbf{S}\mathbf{S}^H = \mathbf{I}$ due to the orthogonal transmitted signals and $\tilde{\mathbf{Z}}$ is white noise which has a Gaussian distribution. Therefore, by applying the matched filtering operation, the target information can be extracted.

If the columns of the matrix $\tilde{\mathbf{X}}$ are stacked to form an $L_t \times L_r$ dimensional vector $\tilde{\mathbf{x}}$, then transmitter and receiver beamforming can be implemented by applying a weight vector

$$\tilde{\mathbf{w}} = \mathbf{w}_T \otimes \mathbf{w}_R \tag{2.144}$$

where $\otimes$ is the Kronecker product [46].

Transmitter and receiver beamforming on reception is then given by

$$y = \tilde{\mathbf{w}}^T \tilde{\mathbf{x}}. \tag{2.145}$$

2.11 Analyses of MIMO Radar

Some concerns as to the real benefits of MIMO have been voiced. MIMO radar systems have increased cost and complexity when compared to phased array systems and the newness results in greater risk in the implementation of MIMO algorithms, when compared to phased array. Below, a summary of the research on the advantages and disadvantages of MIMO radar, mostly with reference to simpler phased array systems, are discussed.

2.11.1 Practical Applications of MIMO Radar

Daum and Huang [10] have raised concerns that in many applications, phased arrays can offer equal if not better performance when compared to a MIMO radar system, with particular reference to radar tracking. The paper discusses two fundamental flaws of MIMO radar which are the loss in SNR and range-Doppler space, and a number of areas where MIMO radar techniques have been suggested, and in some

instances, could realistically provide benefits. The paper is mainly focussed on comparing phased array and MIMO radar in a tracking radar context. The findings are summarised below. Some comments from other sources are included.

Loss in Transmitter Gain and SNR: The measured power at a given range is approximately equal in any direction when orthogonal waveforms are transmitted. When phased array waveforms are transmitted, the measured power is high in the pointing direction of the beam but low in all other directions. Therefore, the unprocessed SNR at a target location will be significantly lower for an omnidirectional MIMO radar system than a phased array system with an equal number of antennas. In fact, it can be shown that the SNR for a phased array will be proportional to L^3 whereas that for MIMO will only be proportional to L^2.

Loss in Range-Doppler Space: The maximum range-Doppler area which can be observed without any ambiguity is unity for phased array and $1/L$ for MIMO [47]. Ambiguity is defined as aliasing of the Doppler-frequency or range which is known as "range-folding". This penalty has worse effect on microwave radars than High Frequency (HF) radars, and therefore, MIMO techniques are seen as most feasible for application to HF radars.

Robustness to Multipath: MIMO radar could prove useful for increasing radar robustness to multipath. However, phased array techniques such as frequency agility or wideband signals to resolve the multipath returns, and non-linear filtering to estimate the reflection coefficient are potentially equally as useful. For example, Smit et al. [48] have shown that UWB radar signals can be used to resolve the direct signal component and multipath components when a target is present in sea surface type environments.

Nulling Jammers in the Main-beam: MIMO could prove more cost effective for nulling jammers in the radar main beam when compared to phased arrays, due to their improved angular resolution and the ability to adapt the transmitted pattern.

Nulling Jammers in the Side Lobe: Phased array techniques for nulling jammers in the side beams are well established and effective, and MIMO does not offer much improvement. However, in some instances, the use of MIMO radar with Space Time Adaptive Processing (STAP) on airborne radars might be beneficial for the suppression of clutter, electronic counter measures (ECM) and radio frequency interference (RFI) at the same time.

Increasing Signal-To-Clutter Ratio: MIMO has shown potential to reduce the signal-to-clutter ratio dramatically. This is of most use for over-the-horizon (OTH) HF radars, where the bandwidth is limited, immense levels of ionospheric multipath and spread Doppler clutter are present and the angular resolution is poor. Preliminary experimentation has shown good potential. Research by Forsythe et al. [38] have shown that using adaptive processing, side lobe reduction can be obtained with sparse array MIMO systems that offer a much larger physical aperture which helps to suppress clutter. Also, in the context of Ground Moving Target Indicator (GMTI) radar, research has shown that approximately 15 dB improvement in signal to interference and noise ratio (SINR) can be obtained with MIMO radar compared to phased array [12], [49].

Search and Track: Theoretically, MIMO radar has been shown to have higher single dwell detection probability at SNRs above 12 dB than phased array radar. The converse is true at SNRs below 12 dB. However, in reality, a sequence of dwells is used in radar search procedures. Forsythe et al. [38] points out that a phased array will have a beam size of approximately $1/L_t^{\text{th}}$ of a MIMO system which transmits L_t uncorrelated waveforms. The search rate is proportional to the beam size and inversely proportional to the number of pulses in the coherent processing interval, and therefore, a MIMO system can use L_t more pulses than the phased array system and still achieve equivalent search rates. In addition, the increased number of pulses will ensure that the phased array and MIMO systems have equal integrated SNRs.

In general [10] states that phased array radar systems are currently a better option than MIMO radar systems. Often, the performance of phased array radar and MIMO radar systems is not fairly compared, resulting in skewed results of comparisons which often blow the benefits of MIMO radar out of proportion. However, for some systems, such as HF OTH or GMTI radars, MIMO radar might be of use.

2.11.2 Beamforming

Hassanien and Vorobyov [45] and Qu et al. [46] have both compared the beampatterns that can be obtained with phased array radars and MIMO radars, and introduced a technique which was called “phased-MIMO radar” and “partial MIMO” in the papers respectively, which attempts to attain the best of MIMO and phased array techniques. It will be referred to as partial MIMO here. The technique is to partition the transmitter array into sub-arrays, and coherently transmit orthogonal waveforms from each sub-array. If the number of sub-arrays is equal to the number

of elements in the array, the system is a MIMO system. Alternatively if the number of sub-arrays is equal to one, the system is a phased array system.

Both of the papers found that by applying TBR to a MIMO system with a given number of transmitters and receivers, the theoretical array pattern which can be obtained is identical to the phased array pattern.

The partial MIMO radar was found to have a reduced gain in [46]. Hassanien and Vorobyov [45] found that the partial MIMO gave an increased signal to interference and noise ratio on the output of the beamformer compared to both the MIMO and phased array results.

Chapter 3

Project Motivation and Objectives

With the insight obtained from the theoretical background presented in the literature review in Chapter 2, the project can be placed in context. In this chapter the project motivation, its objectives and the project deliverables are formalised.

3.1 Project Motivation

The project was formed to fill three gaps identified from a review of past projects and the literature. As stated in the introduction, the CSIR has run projects in which acoustic phased array receivers have been designed and built to illustrate phased array radar principles [7, 8]. To complete the acoustic model of a radar system, the logical extension is to include a phased array transmitter. Thus, the design of the hardware phased array transmitter fills this first gap.

From a review of the literature, it is clear that while many papers have been published on MIMO radar, the concept has not been sufficiently investigated in hardware systems. With the inclusion of a phased array transmitter to the acoustic radar simulator, only slight modifications are required in order to use the hardware system in a MIMO configuration, allowing for experimental verification of MIMO techniques. Therefore, the second gap that can be filled by this project, is the verification of MIMO techniques in hardware.

The third space identified for additional research was the comparison of phased array and MIMO techniques. Papers such as those of Daum and Huang [10], Hassanien and Vorobyov [45] and Qu et al. [46] have begun to investigate and compare phased array techniques to the more complex MIMO techniques. However, much room

remains for more comparison of the techniques, particularly when implemented in hardware.

Thus, the project titled "The Design and Implementation of an Acoustic Phased Array Transmitter for the Validation of MIMO Radar Techniques" came to be.

3.2 Project Objectives

Based on the project motivation, the objectives to be achieved by the project are formulated. They are:

- To implement an array of transmitters to complement the array of receivers constructed by the CSIR. The arrays will be used to model a radar system in the acoustic frequency domain. The system should be low cost, should operate in the audible frequency range and should function in a classroom sized room.
- To implement phased array beamforming and location estimation techniques on signals generated and captured using the hardware platform.
- To implement and validate MIMO beamforming and target parameter estimation techniques on signals generated and captured using the hardware platform.
- To compare phased array techniques to MIMO techniques using the results obtained from suitable tests on the hardware platform.

3.3 Project Deliverables

To achieve the project objectives set out above, deliverables are required. These have been split into algorithm, simulation, hardware and software deliverables. The specifications of each of these deliverables is formulated and described in more detail below.

3.3.1 Algorithms

Many phased array and MIMO techniques for beamforming and parameter estimation were presented in Chapter 2. These techniques are implemented in MATLAB.

In addition, models and algorithms to allow the presented phased array and MIMO target parameter identification techniques to be applied to wideband signals must be derived and presented as a deliverable.

3.3.2 Simulation

Simulations should be performed to test the methods presented in Chapter 2. These will serve to investigate the intricacies of the different phased array and MIMO techniques. The same algorithm implementations can be applied to both the simulated data and the measured data. Therefore, the simulation results can also be referred to for explanations of the performance of the hardware system. In addition, simulations will be used to verify the algorithms formulated for wideband techniques. Therefore, simulations are a necessary deliverable as a stepping stone to the implementation of the radar techniques in hardware.

3.3.3 Hardware System

The hardware system, to be built with analogue components and digital devices, is responsible for implementing an acoustic phased array and MIMO radar simulator. The requirements of the system are:

- The phased array receiver module designed by Stanton [8] should be used as the radar receiver.
- The available Xilinx Virtex 5 FPGA board should be used to control the hardware system.
- To keep the system cost low, the transmitter should make use of generic, low cost speakers and electronic components.
- For maximum effect as an "audio-visual" educational tool, the hardware system should transmit and receive signals in the acoustic range of 20 Hz to 20 kHz.
- The hardware system should have a sample frequency of at least 40 kHz, which is twice the maximum operational frequency of the system.
- The hardware system should be able to detect a target which is a corner reflector of dimensions 100 mm $\times$ 100 mm $\times$ 100 mm.

- The hardware system should be able to detect targets at ranges between approximately 2.5 m, allowing a transmitted signal length of approximately 10 ms, and 5 m.
- The hardware system should be able to detect targets with a DOA between $-60°$ and $60°$, the general usable field of regard for a phased array radar [50].
- The hardware system should be able to transmit a different waveform selected in software on each channel, to be used in MIMO configuration.
- The hardware system should be able to send the received signals from all receiver channels, in real time, to a device where they will be processed.

3.3.4 Software Applications

Software applications are required to configure the hardware system and to process the received signals. The FPGA will be responsible for synchronising the transmitter and receiver, and implementing communication between the hardware and a PC. The PC is used to perform most of the signal processing to extract beampatterns or target location estimates from the received signals. The software is split into the embedded application, and the PC application.

Embedded Application

- The embedded application should accept waveforms from the PC and send the appropriate one to each transmitter channel to start transmission.
- The embedded application should start reception at a determined time after transmission, and pass the signals received by the array to the PC.

PC Application

- The PC application should apply design algorithms to generate phased array and MIMO waveforms which give the desired transmitter beampatterns.
- The PC application should send the signals for transmission to the hardware system.
- The PC application should accept signals received by the hardware array and sent to the PC by the embedded software.

- The PC application should plot the transmitted beampatterns from the set of received signals obtained from measurements at constant angular intervals as the transmitter array is rotated.
- The PC application should apply phased array and MIMO target parameter estimation algorithms to the received data to provide estimates of target range and angular location.

Chapter 4

Narrowband Simulations

Simulations were performed in MATLAB to investigate and highlight the strengths and weaknesses of phased array and MIMO algorithms using the narrowband model. Parameter estimation and beamforming techniques were investigated for phased array and MIMO radar and the MIMO technique of TBR was also simulated. The simulation of the various algorithms was the foundation for the development of realistic experiments to test the performance of the hardware system. The MATLAB implementations of the parameter estimation were applied directly to the hardware received data. The beamforming algorithms used in these simulations are the same ones that were used to generate signals for transmission on the hardware system.

4.1 Phased Array Simulations

Phased array techniques for parameter estimation were presented in Section 2.4 and simulations of these techniques are presented below. The aim was to compare the performance of the different techniques under different conditions. Beamforming design techniques were also simulated, and the results are included below. Simulations of the LCMV method presented in Section 2.3, are discussed. The development and simulation results of a second beamforming technique, the beampattern matching design, are also presented.

4.1.1 Simulation Parameters

For all of the simulations, the number of elements in the arrays was $L = 10$. The simulated signals contained $N = 256$ samples and were sampled at a frequency of

50 kHz. The power of the transmitted signals, given by the variance, was equal to one. The carrier frequency used for modulation was 10 kHz and the array elements were separated by 17 mm which is equal to half the wavelength corresponding to the carrier frequency. Unless otherwise stated, all of the simulations were performed with an SNR of 0 dB on the received signal before any processing.

4.1.2 Phased Array Techniques for Parameter Estimation

Simulations were performed to illustrate the conventional, Capon and MUSIC spectral techniques presented in Section 2.4.1. Three sources transmitted three narrowband, non-coherent signals. A source at $-40°$ transmitted a 1 kHz baseband sinusoid, a source at $0°$ transmitted a 2 kHz baseband sinusoid, and a source at $40°$ transmitted a 3 kHz baseband sinusoid. The simulations were performed in baseband.

The signal received by the array was constructed using the narrowband phased array model presented in Section 2.2. Figure 4.1 shows the conventional, Capon and MUSIC spectrums which all have a measurement resolution of $0.1°$. It can clearly be seen that the conventional beamformer has the poorest target identification resolution, and the MUSIC spectrum has the best. However, the amplitude of the peaks in the MUSIC spectrum at the three source locations is not equal, whereas it is similar for the conventional and Capon techniques.

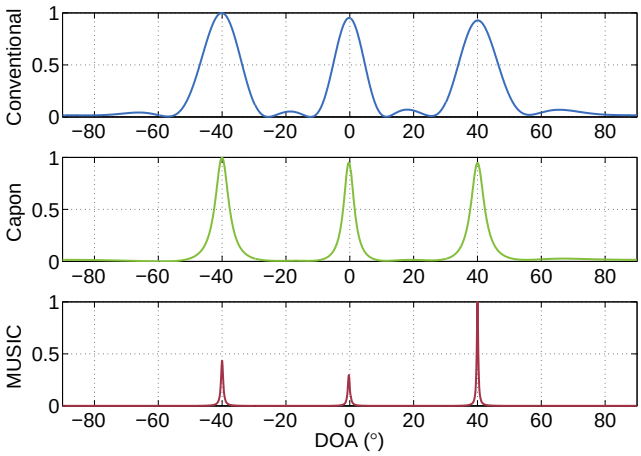

Figure 4.1: The normalised conventional, Capon and MUSIC spectrums for a noise level of 0 dB.

Figure 4.2 shows the Mean Square Errors (MSEs) in the estimations of the DOA of the target at $\theta = 0°$ for 100 trials. It includes the MSE for θ calculated by the DML which was initialised with the Capon target angle estimates. The curves for the targets at $-40°$ and $40°$ are similar to Figure 4.2. The lower the MSE, the better the accuracy of the angle estimates given by the spectrum.

The maximum MSE of 1137 for the conventional beamformer at a reciprocal noise level of -30 dB corresponds to an average absolute error of 33.7°. It can be seen that there is a sharp increase in the accuracy of the estimations as the reciprocal noise level increases (i.e. noise level decreases). At reciprocal noise levels of 20 dB and 30 dB, the Capon and MUSIC spectrums estimated the location of the source with an accuracy better than the machine precision (approximately 10^{-16}) for the 100 trials.

At reciprocal noise levels of -30 dB and -20 dB the spectrums were erratic as shown by the high MSEs, making it difficult to meaningfully compare the performance of the four techniques. At -10 dB the conventional and MUSIC techniques provided better DOA estimates than the DML technique. This indicates that the Capon and DML techniques do not perform well under conditions of high noise. At 0 dB and 10 dB, the DML outperformed the other techniques.

Figure 4.3 shows the conventional, Capon and MUSIC spectrums when the signals transmitted from each source were the same. This means that the signals received at the array were perfectly coherent for the sources located at $-40°$ and $40°$, as

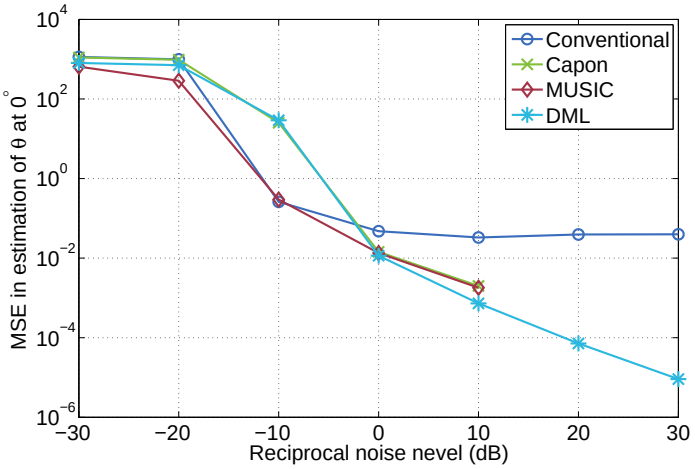

Figure 4.2: The MSEs in estimates of θ in degrees for the target at 0° with 100 trials as the reciprocal noise level varies.

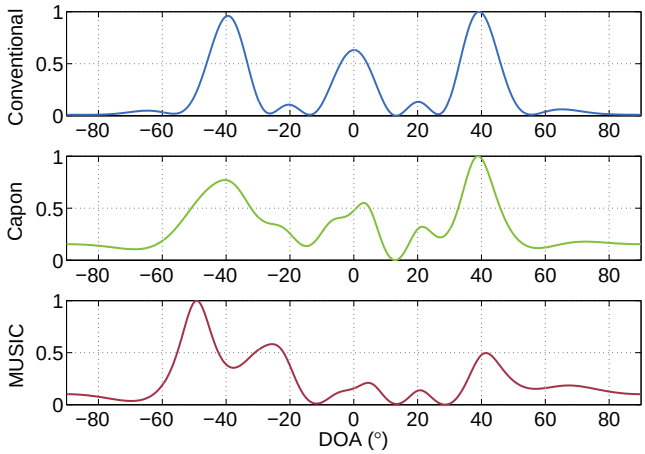

Figure 4.3: The normalised spectrums when the three sources transmit coherent signals.

the time delay between transmission and reception was equal. The signal from the source at 0° will be close to coherent but will have a slight phase shift relative to the signals from −40° and 40°. The conventional spectrum is shown to be the spectrum least affected by coherent signals, although its resolution decreases. The Capon and in particular the MUSIC spectrums are distorted when the signals received from multiple sources were coherent. In reality, it is unlikely that the target echoes will be coherent. In the case that they are, the DML should still provide good target location estimates.

Figure 4.4 shows the MSE curves for the conventional, Capon, MUSIC and DML

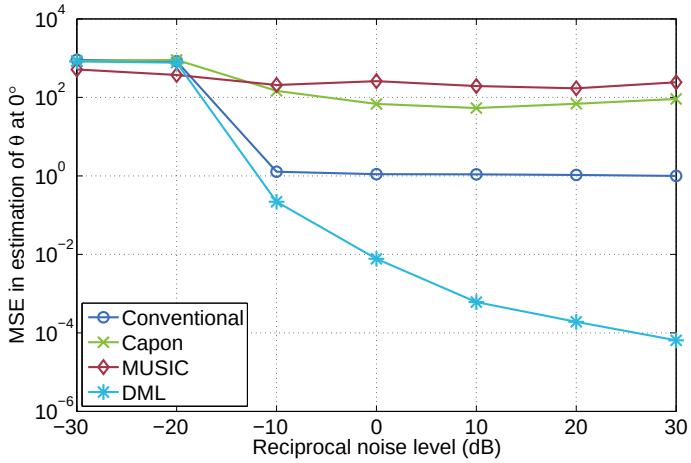

Figure 4.4: The MSEs in estimates of θ in degrees for the target at 0° with 100 trials as the noise level varies when the transmitted signals are coherent.

techniques when the transmitted signals from all directions were identical. The DML was initialised by the conventional estimate. It can be seen that the best estimates of θ were obtained with the DML technique, as was expected for coherent signals. The accuracy of the conventional technique was degraded, but it still provided good enough estimates to initialise the DML. The estimates obtained with the Capon and MUSIC techniques were severely degraded by the coherent signals.

4.1.3 Beampattern Design

Phased array methods for designing transmitter beams which focus energy in one direction are well defined, but methods for designing beampatterns which transmit energy in more than one angular direction are researched less. This is probably because phased array transmitters are usually used to form very high resolution beams with a single main lobe, which are scanned to locate or track targets. Beampatterns with multiple mainlobes are not usually required. Techniques to generate multiple lobed patterns could however be useful if multiple targets are of interest. Also, because MIMO is often used to form versatile, multi-lobed patterns, it is essential to investigate similar techniques for phased array for a fair comparison of phased array and MIMO.

In this section, simulations of methods for designing beampatterns with multiple main lobes are presented. The LCMV beamforming technique and a beampattern matching method which ensures unity amplitude weights are presented.

4.1.3.1 LCMV Beampattern Matching Design

The LCMV was presented in Section 2.3.2.4. This method can be reformulated to match the generated beampattern to a desired beampattern. The development of this technique and simulation results are presented below.

Formulation of the LCMV Beampattern Matching Technique

A desired beampattern $\phi(\theta)$ is defined over a grid of DOA values $\{\theta_i\}$. We then assign this desired beampattern to the LCMV constraint vector

$$\mathbf{f} = \boldsymbol{\phi} \tag{4.1}$$

where $\boldsymbol{\phi}$ is the vector of $\phi(\theta)$ across all grid elements $\{\theta_i\}$.

The constraint matrix $\mathbf{C}$ has i^{th} column equal to the steering vector for grid point θ_i.

LCMV Simulations

A grid of 1° increments from −90° to 90° was used. A desired beampattern, with mainlobes at −40°, 0° and 40°, each of beam width 10° and magnitude one within the beam width and zero beyond was generated. The desired beampattern, together with that designed by the beampattern matching LCMV method is given in Figure 4.5. The simulation parameters described in Section 4.1.1 were used and the phased array signal was a chirp of bandwidth 4 kHz around the carrier.

The beampattern in Figure 4.5 matches the desired beampattern well although the peak amplitudes at −40° and 40° are reduced. The disadvantage of using this technique is that the magnitudes of the weights, shown in Table 4.1, are not unity. Only two of the ten antennas were driven close to their full power. The third antenna's output power was so attenuated by the gain that it was practically switched off. These weights result in reduced transmitter power, which leads to a reduced SNR on reception.

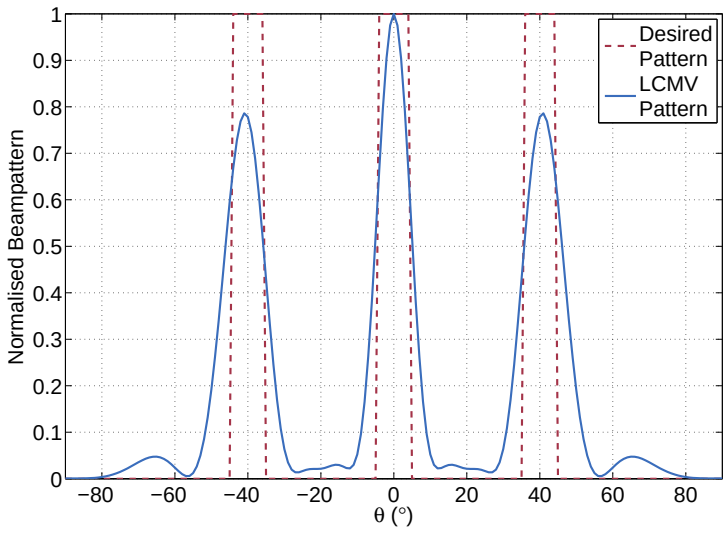

Figure 4.5: Desired and LCMV beampattern matching design generated patterns with mainlobes at −40°, 0° and 40°.

Table 4.1: Absolute value of the weights applied to the phased array signals to generate a pattern with three mainlobes with the LCMV design.

Channel	1	2	3	4	5	6	7	8	9	10
$\lvert\mathbf{w}\rvert$	0.99	0.18	0.02	1.00	0.23	0.12	0.75	0.26	0.18	0.38

4.1.3.2 Beampattern Matching Design

Based on the MIMO beamforming method presented in Section 2.9.3, a technique for beampattern matching with a phased array was devised. No literature has been found on this method. The development of the technique and simulation results are presented and discussed below.

Formulation of the Beampattern Matching Design

The beampattern matching design method optimises the phased array weights by minimising the MSE between the desired pattern and the pattern formed by weighting the signals. This problem can be expressed as

$$\min_{\boldsymbol{\psi}} \frac{1}{K} \sum_{k=1}^{K} \left(P_d(\theta_k) - \mathbf{a}^H(\theta_k) \hat{\mathbf{R}}_S \mathbf{a}(\theta_k) \right) \tag{4.2}$$

where $\hat{\mathbf{R}}_S = \frac{1}{\mathbf{S}_{bf}} \mathbf{S}_{bf} \mathbf{S}_{bf}^H$,

$$\mathbf{S}_{bf} = \begin{bmatrix} w_1 \mathbf{s} \\ w_2 \mathbf{s} \\ \vdots \\ w_{L_t} \mathbf{s} \end{bmatrix} \tag{4.3}$$

and the beamforming weights are $w_i = \mathrm{e}^{j\psi_i}$, with i^{th} phase shift ψ_i. The advantage of this method over the LCMV method is that it forces the magnitude of the weights to be one, which means that the transmitters all transmit at maximum power.

Beampattern Matching Design Simulations

Figure 4.6 shows a beampattern designed by the beampattern matching method with three mainlobes positioned at $-40°$, $0°$ and $40°$. It matches the desired pattern well, but the side lobe levels are higher than those of the LCMV pattern, and the main lobe at $-40°$ is more attenuated.

Further analysis of the beampattern matching design method shows that the method is unable to generate a pattern with mainlobes at $-40°$ and $40°$, without adding

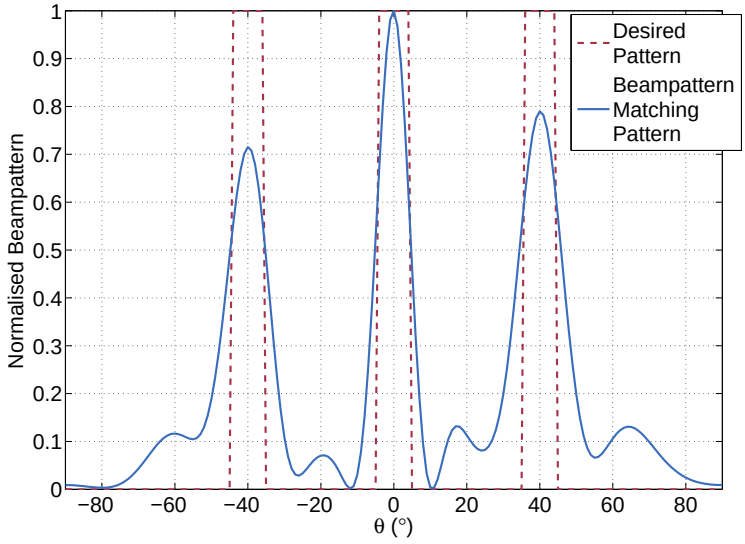

Figure 4.6: Desired and beampattern matching generated pattern with mainlobes at $-40°$, $0°$ and $40°$.

another peak at $0°$. Nonetheless, the method could still be useful in many circumstances.

The limitation of this method is that it requires much longer computation time than other methods such as the LCMV where the beamforming weights are found deterministically. This algorithm requires the implementation of numerical optimisation methods. It is however comparable to MIMO beamforming techniques.

4.2 MIMO Simulations

Simulations of the MIMO parameter estimation, beampattern design, and TBR algorithms presented in Sections 2.8, 2.9 and 2.10 are discussed in this section. Based on the beampattern design algorithms already discussed, a new method for designing patterns is also introduced and investigated in simulation. The simulation parameters are defined, and the results of each of the simulations are presented and analysed in the sections below.

4.2.1 Simulation Parameters

For all of the simulations below, the transmitter array had $L_t = 10$ antennas and the receiver array had $L_r = 10$ antennas. The transmitter and receiver antennas were co-located and therefore, the number of array element number parameter $L = 10$ was used for the transmitter and receiver arrays. The transmitters transmitted QPSK waveforms scaled to meet the uniform elemental power constraint and with $N = 256$ symbols. The total power was limited to 1. The SNR at the receiver was 0 dB. Three targets with $\beta = 1$ were located at angles, θ, of $-35°$, $0°$ and $35°$. A jammer with an amplitude of 1000 and an unknown signal waveform, which was uncorrelated to the transmitted signal waveforms was located at $25°$. These parameters were used for all of the simulations below, unless stated otherwise.

4.2.2 MIMO Techniques for Parameter Estimation

Parameter estimation techniques were applied to a simulated MIMO radar system. With the signal parameters described above, the transmitted pattern is omnidirectional. The Capon and APES estimations of the complex amplitude and the GLRT spectrum are plotted in Figure 4.7. The resolution of the spectrums is $0.1°$, and the true target locations are shown with vertical lines.

The spectrums display the characteristics of the different parameter estimation

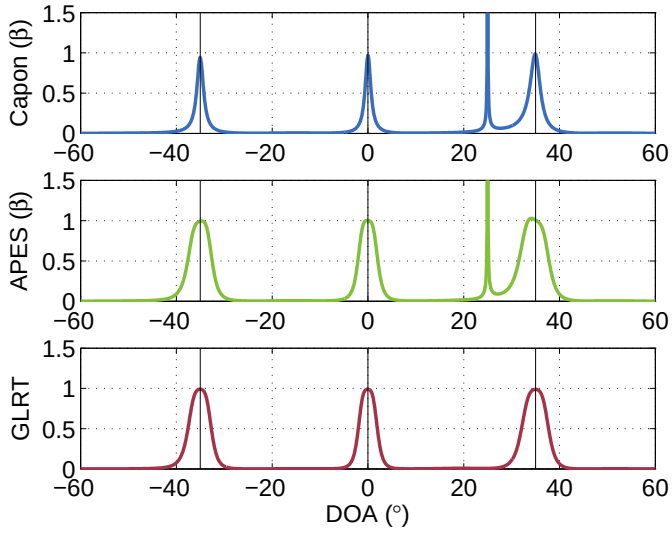

Figure 4.7: MIMO parameter estimation spectrums.

techniques. All of the spectrums clearly identify the three target locations but the Capon and APES spectrums have high peaks at the jammer location. For the target closest to the jammer, the Capon technique gives a more accurate estimate of the DOA than the APES method. The APES spectrum shows distortion in the peak associated with the target closest to the jammer. However, the GLRT effectively rejects the jammer, although its resolution is lower than the Capon spectrum which has the highest resolution.

The means and standard deviations of the estimates of the target locations θ and complex amplitudes β for 100 trials are given in Tables 4.2 and 4.3. The values of θ and β were found by locating the position and amplitude of the maximum in the β spectrum. The GLRT was used to reject the estimate that would be obtained at the jammer location for the Capon and APES estimates. The Capon estimates $\hat{\theta}_k$ were used for the CAML method.

Table 4.2 shows that the Capon method gives more accurate estimates of the target location than the APES method. In Table 4.3, the Capon β estimates are slightly lower than the true complex amplitudes. The APES method gives more accurate estimates at the first two target locations but does not estimate β well for the target located closest to the jammer. The CAML technique clearly gives the best estimates of β.

Table 4.2: Mean and standard deviation of estimates of θ (°)

	$\bar{\theta}$	σ_θ
Capon	-35.00	0.0008
	0.00	0.0006
	34.97	0.0013
APES	-34.88	0.0038
	-0.04	0.0040
	34.03	0.0020

4.2.2.1 Effect of Correlated Transmit Signals

MIMO parameter estimation techniques can be applied to MIMO radar systems due to the linear independence of the transmitted, and consequently the received signals [11]. Therefore, it is expected that if the transmitted waveforms show some

Table 4.3: Mean and standard deviation of estimates $\beta(\theta)$ (The magnitude of the complex value is given in brackets. The standard deviation is for the magnitude.)

	$\bar{\beta}$	σ_β
Capon	0.96 (0.96)	0.012
	0.96 (0.96)	0.014
	$0.96 - j0.01$ (0.96)	0.014
APES	$1.00 + j0.05$ (1.00)	0.005
	$0.99 - j0.02$ (1.00)	0.005
	$0.94 - j0.39$ (1.03)	0.010
CAML	1.00 (1.00)	0.004
	1.00 (1.00)	0.004
	$1.00 - j0.01$ (1.00)	0.005

dependence on one another, the performance of the estimation algorithms will be degraded.

Simulations, with the same parameters as above, were performed to investigate the effect of dependence between transmitter waveforms. Initially, a set of 10 orthogonal (and therefore linearly independent) waveforms was transmitted. To introduce linear dependence between the waveforms, the same signal was transmitted on multiple antennas. Figures 4.8 to 4.10 show a graphical representation of the covariance matrices of the transmitted signals, and the imaging spectrums obtained from the received signals for different numbers of linearly independent transmitted signals.

In the plots of the covariance matrices, a white block indicates high correlation between the ith and j^{th} transmitted signals marked on the x and y-axis. The black blocks indicate low correlation. Therefore, a diagonal white stripe in the centre of the plot indicates that the transmitted signals are orthogonal to one another.

The graphs show that the lower the number of independent signals, the worse the performance of the Capon, APES and GLRT techniques.

Figures 4.9(b) and 4.10(b) show that as the number of independent signals decreased, the amplitude of the Capon β spectrum at the target locations drops. However, the Capon method estimates the target DOA even when only four waveforms are independent (figure not shown).

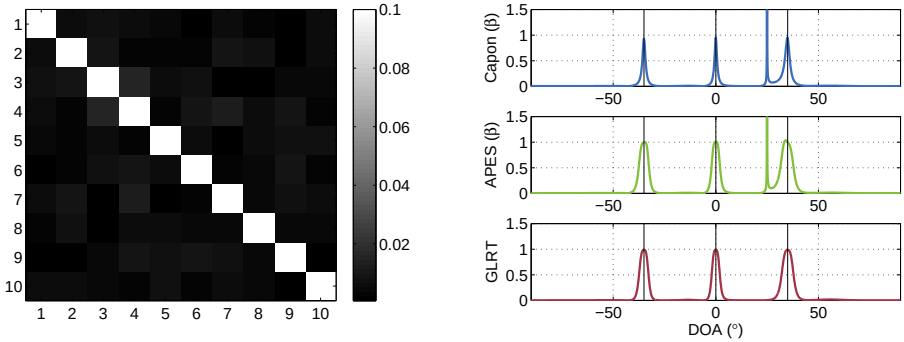

(a) $\mathbf{R}_S$. (b) Target parameter estimation spectrum.

Figure 4.8: Ten independent waveforms.

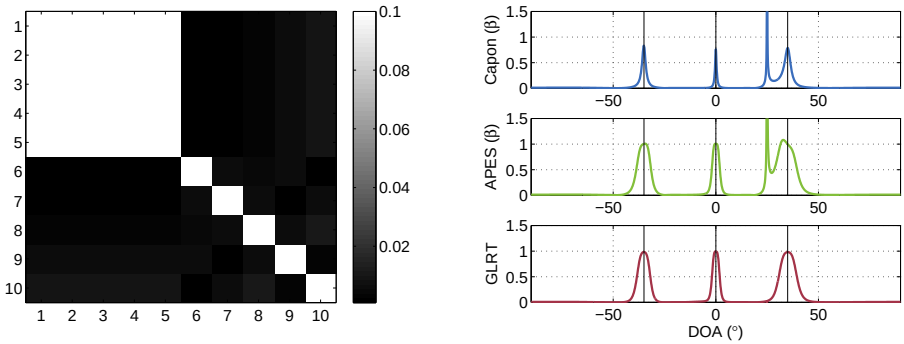

(a) $\mathbf{R}_S$. (b) Target parameter estimation spectrum.

Figure 4.9: Six independent waveforms.

The APES spectrum loses resolution in the DOA estimates as the number of independent transmitted waveforms was decreased and is particularly badly effected close to the location of the jammer. The amplitude estimates of the APES technique at the target location remain fairly accurate no matter how many dependent waveforms were transmitted.

The GLRT spectrum shows a reduced resolution as the number of independent waveforms decreases. The amplitude of the peaks in the spectrum at $-35°$ and $35°$ are worse affected than that at $0°$. This is explained by considering that as the number of independent transmitted waveforms decreases, the MIMO system assumes the behaviour of a phased array and the transmitted pattern becomes directional. In Figure 4.10(b), when only 2 independent waveforms were transmitted, the MIMO system would have had a broadside pattern and the outer two targets cannot be well identified.

Figure 4.11 shows the Capon, APES and GLRT spectrums when all ten transmitted

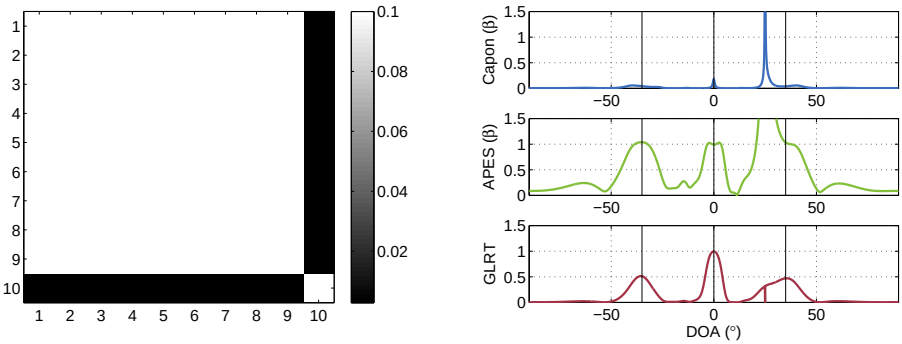

(a) $\mathbf{R}_S$. (b) Target parameter estimation spectrums.

Figure 4.10: Two independent waveforms.

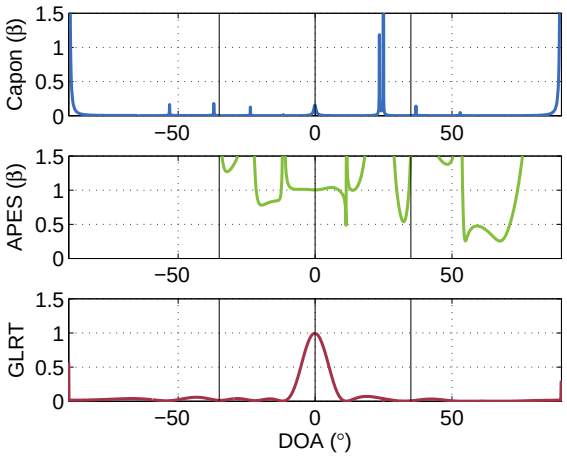

Figure 4.11: Spectrums when all transmitted waveforms are dependent.

waveforms were the same. In this case, the system has been reduced from MIMO to phased array. The Capon spectrum shows a high amplitude peak at the jammer location, as well as peaks at $-90°$ and $90°$, which cannot be explained. The APES estimates of β have high amplitudes at all angles with many erroneous peaks. The APES spectrum does therefore not give accurate estimations of either θ or β. The GLRT shows no peaks at $-35°$ and $35°$ but still identifies the target located at $0°$. This figure makes it clear that MIMO techniques cannot be applied to phased array systems.

These results show that the more linearly independent signals there are the better the Capon, APES and GLRT techniques are able to predict θ and β. However, as long as there are two or more independent signals, the methods continue to work to some extent.

4.2.2.2 Dependence on Range Estimation

In real radar systems, it is likely that neither the DOA nor the range of targets are known. In this case, the receivers will receive for an extended period of time so that target echoes from all ranges of interest are received. All of the previous simulations assumed that the received data was for a single range bin, corresponding to the targets' range, and that the transmitted and received signals were of equal length. The use of the parameter estimation techniques when the target range has to be determined is investigated in this section.

The simulation parameters described in Section 4.2.1 were used except that the jammer was excluded. The received signal was ten times the length of the transmitted signal. The target echo signal was superimposed on a background of Gaussian i.i.d. noise such that the SNR was 0 dB, at a time which gives the target's range.

Figure 4.12(a) shows the Capon, APES and GLRT spectrums when the target range was correctly determined and the correct segment of the received signal was used in the parameter estimation techniques. It can be seen that all three methods identify the target DOAs of $-35°$, $0°$ and $35°$ and Capon and APES give good estimates of β which has an actual value of one.

Figure 4.12(b) shows the same simulation when the segment of the received signal used in the parameter estimation techniques was shifted by one sample period. In this figure, the amplitude of the spectrums is significantly reduced and the GLRT does not even identify the target locations. These results suggest that the MIMO

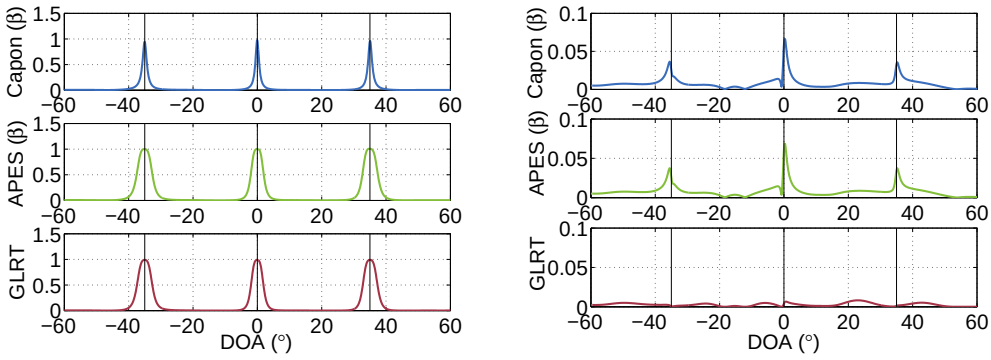

(a) Start time of the received signal correctly matches the return trip time of the transmitted signal.

(b) Start time of the received signal is shifted by one sample period.

Figure 4.12: Spectrums illustrating the dependence on correct range estimations.

parameter estimation spectrums will only give good estimates of the target locations if an accurate range estimate is available.

This sensitivity might make the MIMO parameter estimation techniques difficult to implement in a real system. In the simulations, the travel time of the signal in its journey towards and away from the target is a multiple of the sample period. However, this will not necessarily be true in a real system. The counter-argument is that in simulation the target was modelled as a point. In reality, the target will have some three dimensional physical size, and therefore the echoes received from the target will be a more complex sum of the transmitted signals than in simulation. The signal processing will also spread a point target in range. Therefore, the spectrums might be less sensitive to small delays in reality than in simulation.

4.2.3 Probing Signal Design

Simulations were performed to illustrate the methods of probing signal design discussed in Section 2.9. Results of the unknown target location, maximum power and beampattern matching designs are given below, and a new design based on the maximum power design is introduced and simulated. The simulation parameters presented in Section 4.2.1 were used unless otherwise stated.

4.2.3.1 Omnidirectional Probing Signals

The results obtained when an omnidirectional pattern was transmitted have already been discussed in Section 4.2.2. They were obtained by transmitting the set of orthogonal QPSK signals, with covariance matrix $\mathbf{R}_S = \frac{p}{L}\mathbf{I}$. Figure 4.13(a) shows the covariance matrix $\mathbf{R}_S$ obtained with this set of signals. The diagonal line indicates the orthogonality of the signals.

Figure 4.13(b) shows the normalised omnidirectional beampattern. The pattern does deviate slightly from a truly omnidirectional pattern, but the amount of power transmitted in any direction does not deviate by more than 22.6% across the full 180° for which the pattern is plotted.

The spectrums obtained when an omnidirectional pattern was transmitted were given in Figure 4.7 and discussed in Section 4.2.2.

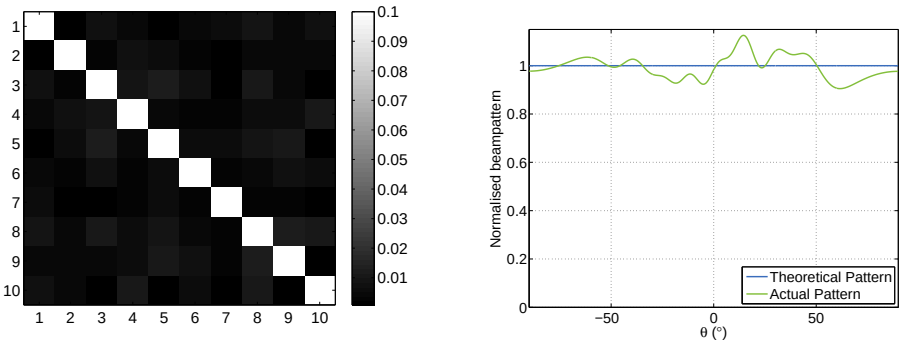

(a) Covariance matrix.

(b) Theoretical and actual beampatterns.

Figure 4.13: The covariance matrix and beampattern for the omnidirectional beampattern design.

4.2.3.2 Maximum Power Probing Signal Design

To simulate the maximum power probing signal design, the covariance matrix $\mathbf{R}_S$ which was defined in Equation (2.130) was generated using the Capon target angle estimates. The magnitude of the covariance matrix is illustrated in Figure 4.14(a). The centre diagonal represents the power transmitted by each transmitter element and the figure illustrates clearly that it varies widely from element to element. This was expected because the total power constraint was used and it does not specify the power on individual transmitters. The uneven distribution of power across the transmitter elements is undesirable in a real system because if all transmitters are identical, maximum power is not transmitted. It can also be seen that there is a very high correlation between some of the transmitted signals, for example between signal pairs one and three. This is expected to result in degradation of the target parameter estimations from the received signal.

Figure 4.14(b) shows the transmitter beampattern generated by the maximum power design. The theoretical pattern was obtained from the designed covariance matrix $\mathbf{R}_S$. The actual beampattern was obtained from the covariance matrix of the set of transmitted signals $\mathbf{R}_S^{\frac{1}{2}}\mathbf{W}$ where each column of $\mathbf{W}$, $\mathbf{w}_i$ is an i.i.d. QPSK sequence with zero mean and covariance matrix $\mathbf{I}$ as in Equation (2.118). The patterns show two distinct peaks at $-35°$ and $35°$, but none at $0°$. One disadvantage of the maximum power design that was stated in Section 2.9.2 is that there are no constraints to equalise the power transmitted to each target location. This led to the pattern seen in Figure 4.14(b), where the optimum solution was obtained by transmitting power in only two of the three target directions. This means that no parameters for the third target can be determined by transmitting this signal.

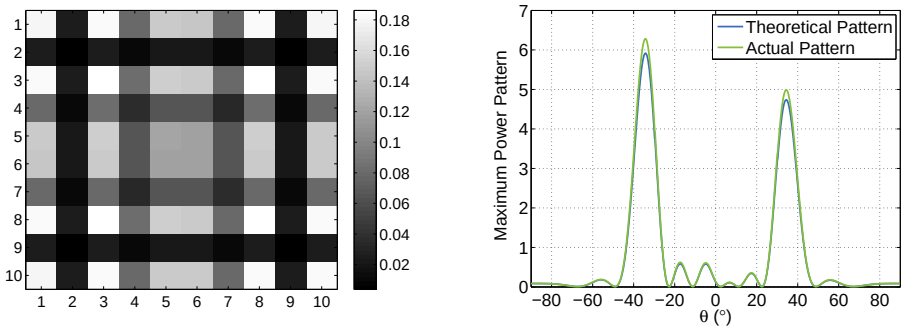

(a) Covariance matrix.

(b) Theoretical and actual beampatterns.

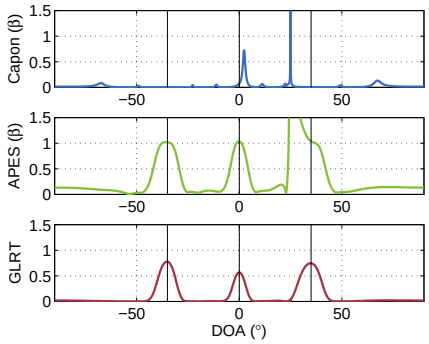

(c) Capon, APES and GLRT spectrums.

Figure 4.14: The covariance matrix, beampattern and received signal spectrums for the maximum power beampattern design.

Similar simulation results with targets at $-40°$, $0°$ and $-40°$ were presented by Stoica et al. [36] in the paper in which the maximum power technique was introduced. With the slightly different target locations, the beampattern transmitted power in all directions almost equally. The authors did not draw attention to the possibility of unequal power distribution as revealed in Figure 4.14(b).

The Capon, APES and GLRT parameter estimation techniques were applied to the received signal, when a pattern generated by the maximum power design was transmitted, and the spectrums are shown in Figure 4.14(c). Improved resolution and accuracy of the estimates at $-35°$ and $35°$ was expected when the maximum power pattern was transmitted compared to an omnidirectional pattern because more power is transmitted in the direction of the targets.

No obvious improvement in the spectrums was found. Initially, the Capon and APES spectrums showed many erroneous peaks, and no peaks at the target locations. In an attempt to explain this poor performance, the transmitted signal covariance matrix $\mathbf{R}_S$ was analysed. The eigenvalue spread of the covariance matrix was in the order of

10^{18} indicating ill-conditioning [51]. This would result in extremely large elements in the inverse $\mathbf{R}_S^{-1}$ and explains the poor performance of the Capon and APES techniques. Conditioning can be performed on the covariance matrix by scaling it by

$$\tilde{\mathbf{R}}_S = 0.99\mathbf{R}_S + 0.01\frac{p}{L}\mathbf{I}. \tag{4.4}$$

This does not alter the transmitted signal set $\tilde{\mathbf{S}} = \tilde{\mathbf{R}_S}^{\frac{1}{2}}\mathbf{W}$ significantly but reduces the eigenvalue spread of $\mathbf{R}_S$ to the order of 10^3.

The spectrums plotted in 4.14(c) are for simulations in which Equation (4.4) was applied. The performance of the APES technique is greatly improved and the spectrum shows peaks at the correct target locations, although the resolution is poor. The Capon spectrum, however, does still not show peaks at the target locations. The GLRT shows peaks at the targets located at $-35°$ and $35°$, and a lower amplitude peak at $0°$. The loss of target information at $0°$ is attributed to the beampattern which does not have a main lobe at $0°$.

The maximum power design does not provide results which improve on the unknown target location probing signal design. In fact, information about the target at $0°$ is lost, and the Capon technique ceases to provide any estimates of the target parameters. Based on the findings of these simulations, it can be concluded that the maximum power design is poor, and when transmitted, the target parameter estimation results will also be unsatisfactory.

4.2.3.3 Pascale's Probing Signal Design

This design was conceived by Pascale Jardin, of ESIEE, Paris, on analysis of the maximum power design technique and its failures. Therefore, it uses much the same formulation as the maximum power technique.

Consider assigning

$$\mathbf{R}_S = \mathbf{a}_t(\hat{\theta}_k)\mathbf{a}_t^H(\hat{\theta}_k). \tag{4.5}$$

Then, the power spectrum is

$$P(\theta) = \mathbf{a}_t^H\mathbf{a}_t(\hat{\theta}_k)\mathbf{a}_t^H(\hat{\theta}_k)\mathbf{a}_t, \tag{4.6}$$

and will have peaks in the direction of θ_k.

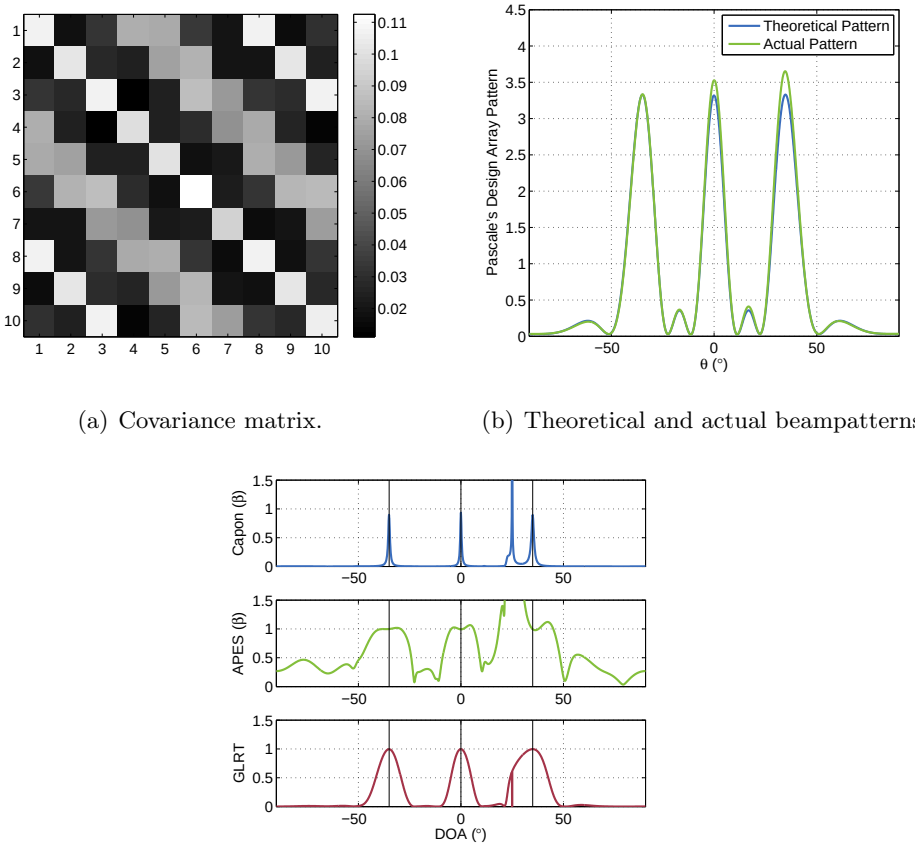

(a) Covariance matrix.

(b) Theoretical and actual beampatterns.

(c) Capon, APES and GLRT spectrums.

Figure 4.15: The covariance matrix, beampattern and received signal spectrums for Pascale's beampattern design.

To transmit power in the direction of all $\tilde{K}$ targets of interest, it seems logical to define the covariance matrix as

$$\mathbf{R}_S = \frac{\hat{\mathbf{B}}}{\mathrm{tr}\{\hat{\mathbf{B}}\}} \tag{4.7}$$

where $\hat{\mathbf{B}}$ is as defined in Equation (2.123).

Figure 4.15 shows the simulation results when this technique was used. The equal amplitude of the diagonal elements of the covariance matrix in Figure 4.15(a) shows that each transmitted signal has approximately equal power.

The beampattern in Figure 4.15(b) shows that three mainlobes of approximately equal power and beam width are generated in the three directions of interest. This is a great improvement on the maximum power design.

The Capon and GLRT spectrums in Figure 4.15(c) also show better results than

those obtained with the maximum power transmitted beampattern. The APES spectrum does show peaks close to the required location, but the resolution of the peaks is large, and there appear to be local minima in the peaks at the true target location.

Thus, the simulations of Pascale's design indicate that a beampattern which better matches the desired pattern and improved target parameter estimates can be obtained when it is transmitted, compared to when the maximum power pattern is transmitted.

4.2.3.4 Beampattern Matching Probing Signal Design

The beampattern matching design was expected to improve on the maximum power design by imposing the elemental power constraint. By minimising the cross-correlation beampattern, the beampattern matching design was also expected to give improved results compared to the maximum power design and Pascale's design due to lower correlation between the signals incident at the target.

The beampattern matching design was presented in SQP form in Equation (2.140) in Section 2.9.3. Appendix E describes in detail how to use the SeDuMi toolbox for MATLAB to solve the SQP problem to obtain the covariance matrix $\mathbf{R}_S$ for the beampattern matching design. Simulations were performed, using this technique, and are presented below. The beam width, Δ, of the desired pattern was 20°.

The beampattern matching design covariance matrix is shown in Figure 4.16(a). Analysis of the matrix shows that, as expected, the power of each signal is approximately equal. Also, the correlation between different transmitted signals is lower than the maximum power design or Pascale's design. The eigenvalue spread of this covariance matrix is 10^8, which is still higher than that of the conditioned maximum power design, so Capon and APES spectrums of reduced quality were expected.

Figure 4.16(b) shows the desired beampattern, and the theoretical beampattern generated from $\mathbf{R}_S$ and the actual pattern obtained by transmitting $\mathbf{R}_S^{\frac{1}{2}}\mathbf{W}$. The amplitude of the pattern in the direction of each target is approximately equal.

Figure 4.16(c) shows the Capon, APES and GLRT spectrums for the received signal. The Capon spectrum identifies the target location with three high resolution peaks. The APES spectrum shows very narrow erroneous peaks of which those at -20° and 20° are the most notable, but it also clearly identifies the three target locations. The

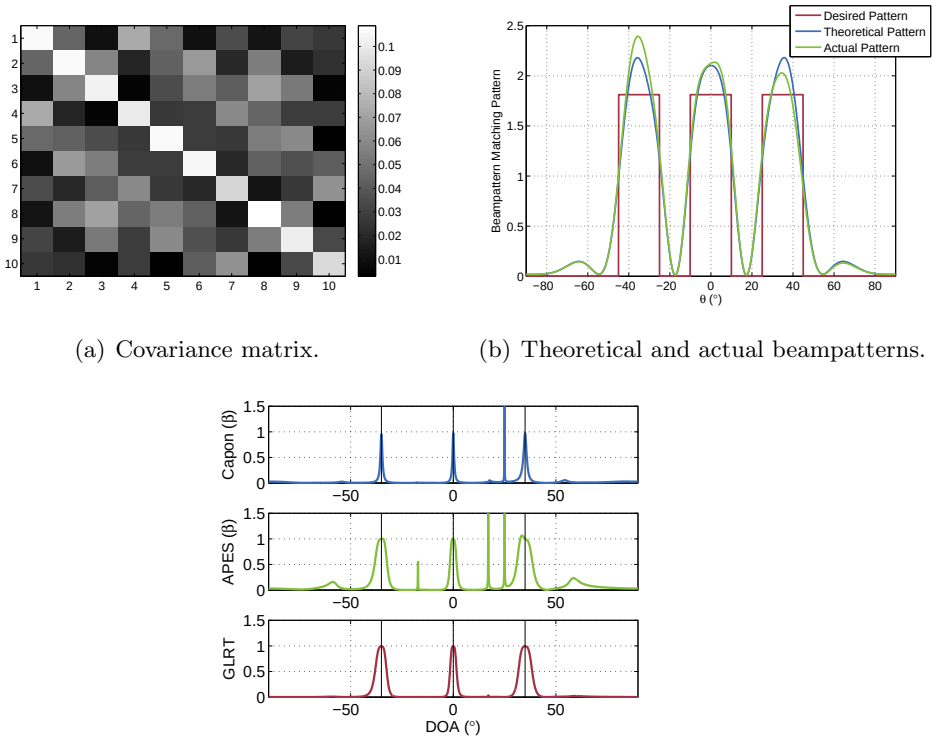

(a) Covariance matrix.

(b) Theoretical and actual beampatterns.

(c) Capon, APES and GLRT spectrums.

Figure 4.16: The covariance matrix, beampattern and received signal spectrums for the beampattern matching design

slightly degraded APES spectrum was attributed to the ill conditioned transmitted signal covariance matrix. The GLRT also correctly identifies each of the target locations and rejects the jammer.

The pattern generated by the beampattern matching design shows improved performance over the maximum power design. It also gives better parameter estimation spectrums than both the maximum power design and Pascale's design. However, it does not appear to improve the results obtained from the parameter estimation spectrums in comparison to an omnidirectional transmitted pattern. The results in the following section illustrate that beamforming does in fact offer improvements to the results although it is not visually apparent in the spectrums.

4.2.3.5 Improvements Offered by Beamforming

In a typical situation, an omnidirectional MIMO beampattern is transmitted and parameter estimation techniques are performed to determine if any targets are present, and to calculate estimates of their locations. With these initial estimates,

beampatterns are designed with mainlobes in the directions of targets. Parameter estimation techniques are applied a second time to better estimate the target parameters. This section presents simulations which were preformed to determine the improvement in θ and β estimates that can be achieved with beamforming.

Three targets were located at $-40°$, $0°$ and $40°$. Note that these angles are different to those used in the MIMO simulations in the above section, and were chosen for comparison to the results in Stoica et al. [36]. The reciprocal noise level was varied from -20 dB to 20 dB, and at each noise level, 100 simulations were performed. For each trial, a new set of MIMO signals was generated. The MIMO signals were selected to give an omnidirectional pattern, a pattern formed by the maximum power design, a pattern formed by Pascale's design, and a pattern formed by the beampattern matching design. Random noise at the appropriate level was added to the modelled, received signals.

Figure 4.17 shows the MSE in θ (in degrees) for the target at $-40°$ when the Capon, APES and GLRT techniques were used to estimate the target location. The targets at $0°$ and $40°$ have similar curves. The Capon and GLRT MSEs at a noise level of 20 dB for all beampatterns except the maximum power pattern, disappear, because the techniques estimated the target location with an accuracy better than the machine precision.

Figure 4.17 shows that the GLRT is the best performing technique, particularly when the noise level is high. This is surprising because simulations in Section 4.2.2 showed that the GLRT's resolution is inferior to the Capon spectrum's. The APES technique gives the poorest results. This is assumably because the APES technique is the worst affected by correlation between the transmitted signals as found in Section 4.2.2.1. This is confirmed by noting that the lowest MSEs are obtained using the APES technique when orthogonal signals (an omnidirectional pattern) was transmitted and correlation between target echoes is thus minimised.

If the MSEs in θ in Figure 4.17 are compared, it is found that the lowest accuracy, by two degrees of magnitude, is obtained when the pattern generated by the maximum power design is transmitted and the Capon or GLRT technique is used for angle estimation. This was noted in Section 4.2.3.2 where Figure 4.14(c) shows that the Capon and GLRT spectrums are unsatisfactory when the transmitted signals are selected by the maximum power design. The MSEs obtained from omnidirectional, Pascale's and beampattern matching patterns are similar for the Capon and GLRT techniques but at higher reciprocal noise levels Pascale's technique provides the best

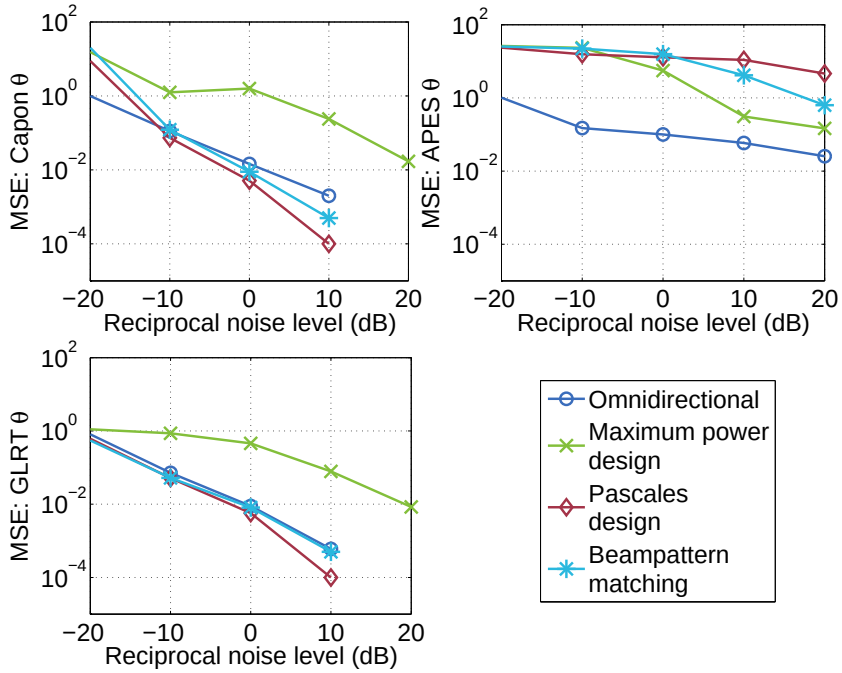

Figure 4.17: The MSE in θ for 100 trials as the reciprocal noise level was varied. θ was estimated by the Capon, APES and GLRT spectrums, and omnidirectional, maximum power, Pascale's and beampattern matching patterns were transmitted.

estimates of θ, giving about 7 dB improvement over any of the other techniques.

Figure 4.18 shows the MSE in β for the target at $-40°$ when the Capon, APES and CAML techniques were used. The targets at $0°$ and $40°$ gave similar results.

The CAML reliably provided the best estimates of β regardless of the transmitted beampattern. Again, APES was the poorest of the methods, and performed best on an omnidirectional pattern. The results obtained from the maximum power transmitted signal with the Capon and CAML techniques were also poor, as for estimates of θ. In the estimation of β, the best results with the Capon method, were obtained for the beampattern matching design signals. The best results with the CAML method, were obtained with Pascale's beampattern, but were almost matched by those from the beampattern matching pattern and were only slightly better than the omnidirectional results.

These MSE curves differ to the ones presented by Stoica et al. [36], where the improvement offered by beamforming for the estimation of θ and β was approximately 10 dB when the CAML technique was used and beamforming was performed by the beampattern matching design. The simulations above show that the Capon estimates of θ and the CAML estimates of β only offered maximum improvements

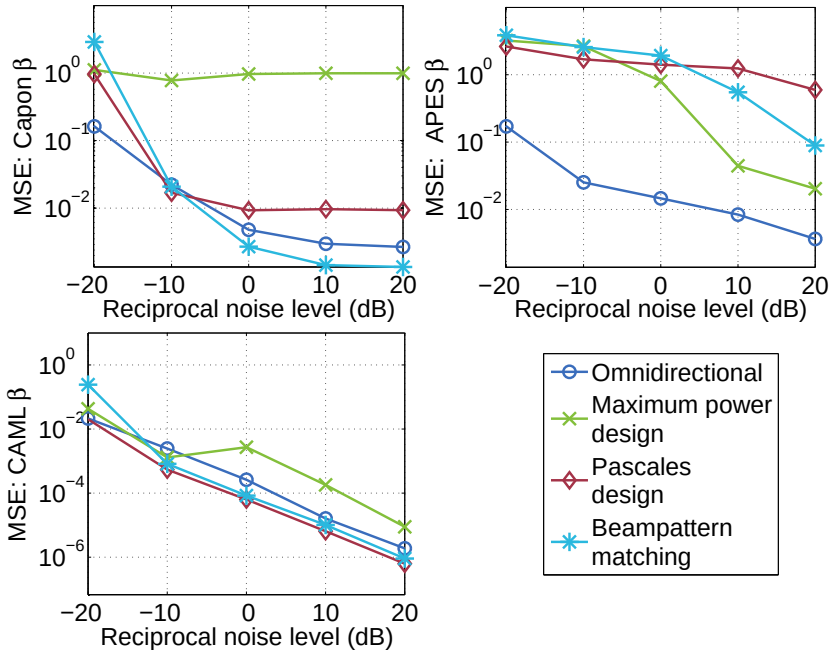

Figure 4.18: The MSE in β for 100 trials as the reciprocal noise level is varied. β was estimated by the Capon, APES and GLRT spectrums, and omnidirectional, maximum power, Pascale's and beampattern matching patterns were transmitted.

of 6.0 dB and 4.8 dB respectively at a reciprocal noise level of 20 dB. However, confidence is held in the results presented in Figures 4.17 and 4.18, as the code has been thoroughly checked. In addition, the code used by Stoica et al. [36], which was kindly made available, has been studied in an attempt to find the source of the discrepancy. However, the differences have not been resolved.

From these results it can be deduced that the APES technique does not estimate θ or β as well as the other spectral techniques. The best results were obtained by estimating θ with the GLRT, and β with the CAML when a transmitter pattern formed by Pascale's design was transmitted.

4.2.4 Transmitter Beamforming on Reception (TBR)

The narrowband model was used to simulate TBR. The simulation parameters presented in Section 4.2.1 were used except that no jammer was included. An omnidirectional pattern, as presented in Section 4.2.3.1 was transmitted. Instead of using the received data to plot the Capon, APES and GLRT spectrums, TBR was applied.

The output of TBR is a scalar. By varying the angle θ for which the weights are calculated, the magnitude of the beamformer output varies. It is largest when a target is present at the DOA θ and is small otherwise. The power of the output can be calculated and plotted as angle varies to give a spectrum from which the target location can be determined.

Figure 4.19 shows the spectrum obtained from TBR compared to the MIMO Capon β spectrum. Both spectrums are plotted in decibels. The Capon β spectrum is the same as that generated when transmission of an omnidirectional beampattern was simulated in Section 4.2.3.1. The weights for the TBR spectrum were calculated by the Capon technique.

This Capon β spectrum has poor resolution, and high side lobe levels in comparison to the spectrum obtained from performing TBR. The side lobes of the TBR spectrum are approximately 20 dB below the Capon β spectrum side lobes.

This simulation indicates that higher resolution estimates of the target locations can be obtained by applying TBR instead of the MIMO spectral techniques. It must not however be neglected that the Capon and APES β spectrums estimate the complex amplitude of the target in addition to the DOA, and the GLRT can be effectively used to reject jammers. Therefore, an analysis of the conditions under which targets must be identified, and of the important parameters is necessary before the optimum method can be selected.

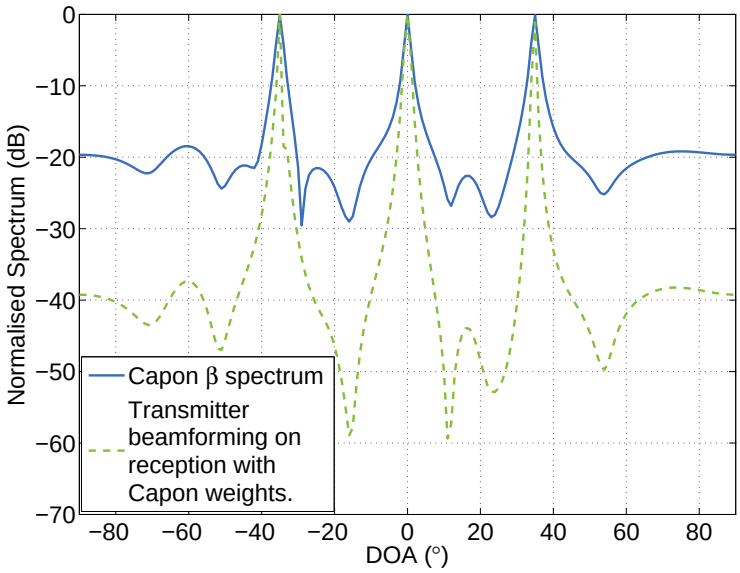

Figure 4.19: Normalised spectrums obtained with and without TBR.

4.3 Summary

In this section, the simulation results of phased array and MIMO techniques for target parameter estimation and beampattern design were presented.

The conventional, Capon, and MUSIC angle estimation techniques for phased array were shown to perform well, provided that the received signals from multiple angles are not coherent. The DML was shown to be more resistant to coherence.

Two beampattern design methods were also simulated. The LCMV beampattern design method was shown to generate the desired beam but to reduce the transmitted signal power due to weights of amplitude less than unity. The beampattern matching design method, which was introduced in this chapter, was shown in simulation to generate beampatterns of similar shape to the LCMV method, but with higher power.

Simulations of the MIMO Capon, APES and GLRT algorithms highlighted the high resolution of the Capon spectrum and good jammer rejection capabilities of the GLRT. The effect of linear dependence in the set of transmitted signals was simulated, and all techniques were shown to provide target angle and complex amplitude estimates provided at least two signals were linearly independent, although the quality of the estimations decreased. The dependence of good quality angle estimates on a correct range estimate was also uncovered with simulations.

The versatility of beampattern design which is available with a MIMO system was explored in simulation, and it was shown that an omnidirectional or directional pattern can be transmitted by selection of the transmitter signal set. The maximum power probing signal design was shown to be flawed as the power to be transmitted in each target direction cannot be specified. However, Pascale's probing signal design was introduced to improve on the maximum power design.

TBR was shown in simulation to give high resolution angular spectrums. Using Capon weights, the side lobe levels of the TBR spectrum were 20 dB below the Capon β spectrum.

The simulations presented in this section were performed at baseband on narrowband signals. It remains necessary to investigate the performance of phased array and MIMO techniques when the signals are wideband. The following chapter discusses wideband beamforming techniques, and presents wideband simulation results.

Chapter 5

Wideband Beamforming Techniques and Simulations

The acoustic radar hardware system requires wideband transmitted signals. Therefore, to maintain the accuracy of the target parameter estimates, wideband processing techniques are required. This chapter explains the breakdown of the narrowband assumption, and details the derivation of two wideband beamformers. The results of wideband phased array and MIMO simulations are presented to illustrate the effect of wideband signals, and to investigate the performance of the wideband beamformers.

5.1 Breakdown of the Narrowband Assumption

Consider an L element ULA. Using the narrowband model, the elements of the array's steering vector are given by Equation (2.24) and are

$$a_i(\theta) = e^{j2\pi f_0 \tau_i} = e^{j\pi(i-1)sin\theta} \tag{5.1}$$

where $i = 1 \dots L$ and τ_i is the time delay between the signal arriving at the first receiver element and that arriving at the ith element. Therefore, the expression for the incremental delay used by the model is

$$\tau = \frac{1}{2f_0} sin(\theta). \tag{5.2}$$

Consider an acoustic system where f_0 is 10 kHz, and the DOA of the signal is 40°. The delay will then be $\tau = 38$ μs. The period of a 10 kHz sine wave is 100 μs, so the incremental delay between consecutive channels will cause a phase shift of 136.8°. Now let the signal also contain components at 8 kHz and 12 kHz. The

period of these additional components is 125 μs and 83.3 μs respectively. Therefore, the 136.8° phase shift that is applied to the signals by the steering vector, is actually equivalent to delays of 47.5 μs and 31.7 μs and results in errors of 25.0% and 16.6% respectively. The phase shifts for a given value of τ as the frequency varies are illustrated for different DOAs, θ, in Figure 5.1. The gradient of the lines indicates that the phase error increases as the DOA moves further from 0°. This discrepency between time delay and phase shift causes errors in the estimation of the target location θ when narrowband assumptions are used. Therefore, a set of wideband techniques is required.

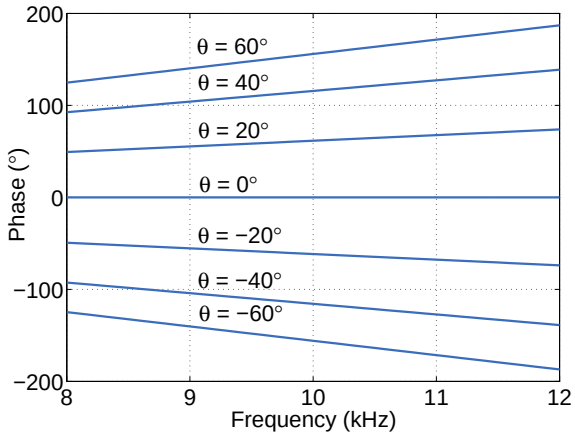

Figure 5.1: The phase difference caused by time delay τ as signal frequency varies for different DOAs θ.

5.2 Time Delay Wideband (TDWB) Beamformer

A delay-and-sum beamformer [13], which is the simplest implementation of a beamformer was discussed in Section 2.2.5. The output of the beamformer was given in Equation (2.46) and is

$$y(t) = \frac{1}{L}\sum_{i=1}^{L} w_i x_i(t - \tau_i). \tag{5.3}$$

Under the assumptions of the narrowband model, the delay τ_i is implemented on the ith received signal by modelling it as a phase shift as described above. To avoid the errors introduced by modelling the time delay as a phase shift, a fractional delay (FD) filter can be used to implement the delay. This implementation of a wideband beamformer will be referred to as a time delay wideband (TDWB) beamformer throughout the rest of this dissertation.

An FD filter generates samples of the original analogue signal at offset sampling instances in a restricted frequency band. If the signal is a real-valued, band-limited baseband signal, the ideal impulse response of the filter is

$$h[n] = \frac{\sin(\pi[n - \tau_{frac}])}{\pi[n - \tau_{frac}]} = \text{sinc}[n - \tau_{frac}] \tag{5.4}$$

where τ_{frac} is the fractional delay that is desired, and $n \in (-\infty, \infty)$ [52]. If the signal is complex two filters would be required where one would be for the real component and the other for the imaginary component. This filter is an approximation of a linear-phase all-pass filter with a constant group delay equal to τ_{frac}.

The FD filter can be implemented with an $N+1$ length FIR filter, by truncating the ideal filter response to $N+1$ terms. However, truncation of the filter impulse response results in ripple in the magnitude response due to the Gibbs phenomenon [52]. To reduce the ripple, a window can be applied to the impulse response. Therefore, the windowed FIR filter impulse response to implement an FD filter is

$$h[n] = \begin{cases} W[n - \tau_{frac}]\,\text{sinc}[n - \tau_{frac}] & \text{for } 0 \leq n \leq N \\ 0 & \text{otherwise} \end{cases}. \tag{5.5}$$

This fractional delay filter can easily be implemented in MATLAB and used to create a wideband delay-and-sum beamformer. To point the receiver beam in direction θ, the ith received signal is delayed by

$$\tau_i = \frac{(i-1)d}{c}\sin(\theta). \tag{5.6}$$

The delay is multiplied by the sample frequency to be given in terms of the number of samples. If the delay is larger than one sample, it is split into the fractional delay component τ_{frac} and the "whole delay" component which contains the portion of the delay which is an integer multiple of the sampling period. The whole delay is implemented by padding the signal with zeros on either side, and then shifting the signal. The fractional delay is implemented with the FD filter given in Equation 5.5. A similar wideband beamformer was implemented by Tang et al. [53].

5.3 Filter and Weight Wideband (FWWB) Beamformer

A wideband beamformer was introduced in Section 2.5. Instead of applying a multiplicative coefficient to each received signal, like a narrowband beamformer, the proposed wideband beamformer applies a filter on each channel to reduce

the bandwidth of the signal while including compensation for the delays between channels. Restating what was presented in Section 2.5, the output of the J tap beamformer is given by

$$\begin{aligned} y[n] &= \sum_{j=0}^{J-1}\sum_{i=1}^{L_r} w_{ji}^* x_i[n-j] \\ &= \bar{\mathbf{w}}^H \bar{\mathbf{x}}[n] \end{aligned} \tag{5.7}$$

where the wideband weight vector is

$$\bar{\mathbf{w}} = \begin{bmatrix} w_{01} & \dots & w_{0L_r} & \dots & w_{(J-1)1} & \dots & w_{(J-1)L_r} \end{bmatrix}^T \tag{5.8}$$

and the wideband received signal vector is

$$\bar{\mathbf{x}} = \left[x_1[n] \ \dots \ x_{L_r}[n] \ \dots \quad x_1[n-(J-1)] \ \dots \ x_{L_r}[n-(J-1)] \right]^T . \tag{5.9}$$

Suppose that the filter applied to each channel is identical. Then, $\bar{\mathbf{w}}$ can be reformulated as

$$\bar{\mathbf{w}} = \begin{bmatrix} h_0\boldsymbol{\alpha}^T & h_1\boldsymbol{\alpha}^T & \dots & h_{J-1}\boldsymbol{\alpha}^T \end{bmatrix}^T \tag{5.10}$$

where $\boldsymbol{\alpha} = \begin{bmatrix} \alpha_1 & \dots & \alpha_{L_r} \end{bmatrix}^T$ is equivalent to the set of weights for a narrowband beamformer and $\mathbf{h} = \begin{bmatrix} h_0 \dots h_{J-1} \end{bmatrix}^T$ is the set of coefficients of the impulse response of the filter which is applied to each channel. This reformulation of the beamformer is illustrated in Figure 5.2.

Equation (5.7), the output of the beamformer, becomes

$$\begin{aligned} y[n] &= \sum_{j=0}^{J-1}\sum_{i=1}^{L_r} (h_j\alpha_i)^* x_i[n-j] \ = \ \sum_{i=1}^{L_r} \alpha_i^* \tilde{\mathbf{x}}_i[n] \\ &= \boldsymbol{\alpha}^H \tilde{\mathbf{x}}[n] \end{aligned} \tag{5.11}$$

where $\tilde{\mathbf{x}}_i[n] = \mathbf{h}^H \begin{bmatrix} x_i[n] & \dots & x_i[n-(J-1)] \end{bmatrix}^T$ and $\tilde{\mathbf{x}}[n] = \begin{bmatrix} \tilde{\mathbf{x}}_1^T[n] & \dots & \tilde{\mathbf{x}}_{L_r}^T[n] \end{bmatrix}^T$.

By choosing the filter implemented by $\mathbf{h}$ to be a low-pass filter, the wideband signal $\mathbf{x}$ will be reduced to a narrowband steering vector and the phased array and MIMO parameter estimation methods presented in Sections 2.4 and 2.8 can be applied to the received signal $\tilde{\mathbf{x}}[n]$. This wideband beamformer is referred to as a filter and weight wideband (FWWB) beamformer throughout the rest of this dissertation.

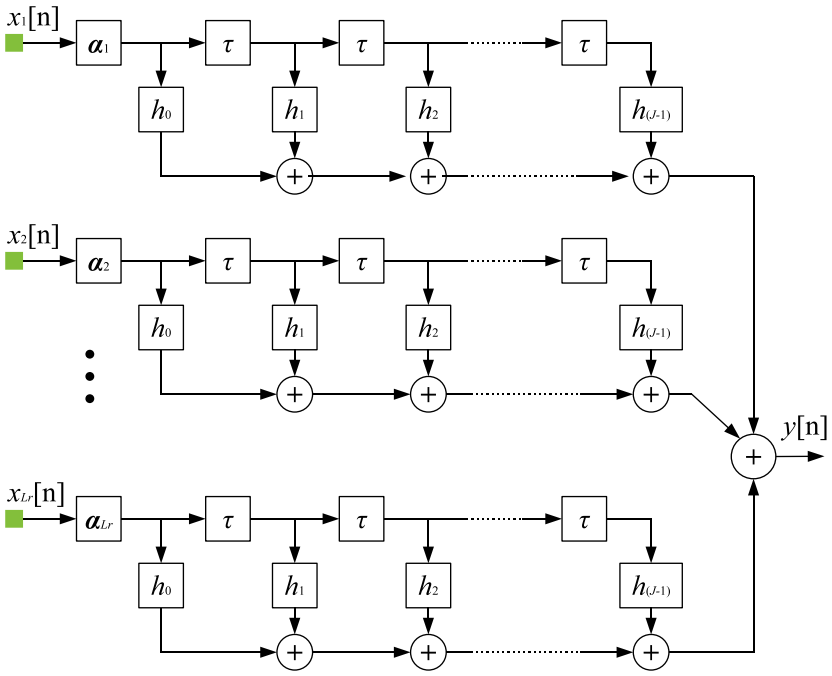

Figure 5.2: A filter and weight wideband (FWWB) beamformer.

5.4 Phased Array Simulations

The effect of wideband signals, and the performance of the wideband beamformers was simulated for a phased array system. In the sections below the effect of wideband signals on phased array beampatterns is presented first. A method for modelling wideband signals is then introduced followed by simulations of the TDWB beamformer. Finally, the simulation results obtained with an FWWB beamformer and wideband phased array signals are presented.

5.4.1 Wideband Beampatterns

What is the effect of wideband chirp signals on the transmitted pattern? To investigate this, simulations were performed to determine the phased array beampattern when wideband signals are transmitted, without the use of the narrowband model.

When an acoustic signal is transmitted from a point source, it can be assumed that all signal components will travel at the speed of sound, c. To realistically determine the array beampattern, a grid of points was defined on a circle so that all were equidistant from the centre of the array. Assuming that each transmitter was perfectly omnidirectional, the signal at each grid point was calculated, by combining

L signals delayed by a time calculated by

$$\tau_{ij} = \frac{R_{ij}}{c} \tag{5.12}$$

where R_{ij} is the distance from the ith point-source transmitter element to the jth grid point. Because the time delay was not necessarily an integer multiple of the sample frequency, the signal was up-sampled by a factor of 32 and then re-sampled back to the sample frequency taking the delay into account.

Figure 5.3 shows phased array beampatterns with different signal bandwidths. The separation between the antennas was equal to half a wavelength of the 10 kHz

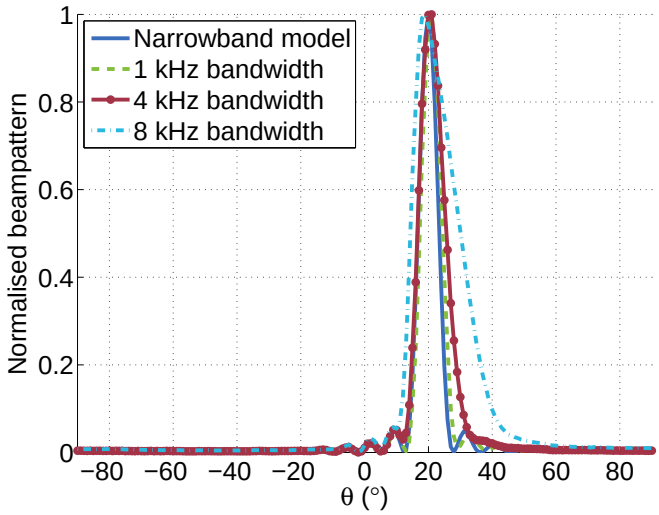

(a) Normalised patterns.

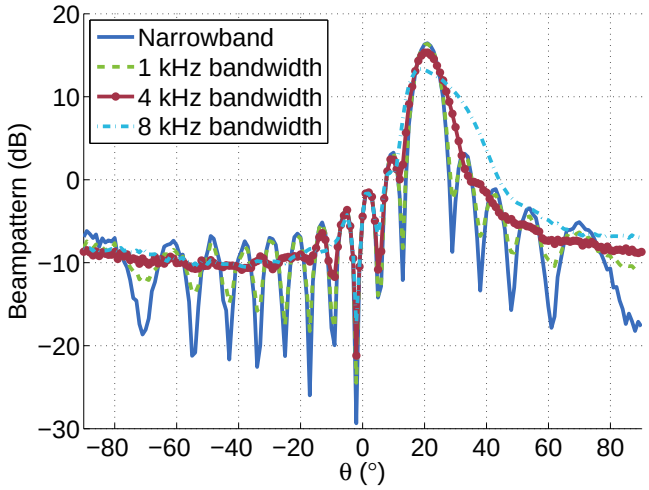

(b) Patterns plotted in decibels.

Figure 5.3: Phased array patterns generated with transmitted signals of different bandwidths.

centre frequency. Each of the beampatterns was weighted so that the main lobe was directed at 20°. Figure 5.3(a) shows the normalised patterns, and illustrates that the pattern generated with the narrowband model has the narrowest beam width. As the signal bandwidth increases (the centre frequency is fixed) the beam width of the main lobe also increases. With a bandwidth of 1 kHz, the change in beam width is negligible, but the nulls in the side lobes are not as deep. However, with a bandwidth of 8 kHz, the beam width approximately doubles.

Figure 5.3(b) shows the four patterns plotted in decibels and illustrates that as the bandwidth increases, the peak amplitude of the patterns decreases. For the pattern generated with signals of 4 kHz bandwidth, the amplitude of the peak decreases by approximately 1 dB, and by a further 2 dB for an 8 kHz bandwidth. This will reduce the SNR of the received signal.

Simulations also showed that the further the main lobe was from 0°, the wider the beam of a pattern generated with a given signal bandwidth. This is a well known array antenna principle that as the projected area of the aperture decreases, the beam width increases [54]. When the main lobe is at 0°, almost no beam width widening is noted, regardless of the bandwidth.

In summary, these simulation results show that as the bandwidth is increased, the beampattern widens, and the amplitude of the main lobe decreases. However, the majority of the power is still transmitted in the desired direction.

5.4.2 Wideband Simulation Method

To simulate wideband operation, the narrowband model could not be used as it was for the narrowband simulations in Section 4.1. A technique for simulating wideband signals was required. The flow of the wideband simulation method used is summarised in Figure 5.4. The set of real passband signals $\mathbf{S}$ was formulated. The signal at the target was then constructed by

$$\tilde{x}(t) = \sum_{i=1}^{L} s_i \left(t - \tau_i(\theta)\right). \tag{5.13}$$

As for the beampatterns, the delay $\tau_i(\theta)$ is not necessarily an integer multiple of the sample period, and therefore, the signal is sampled up by a factor of 32, and then re-sampled to the original frequency incorporating the delay $\tau_i(\theta)$.

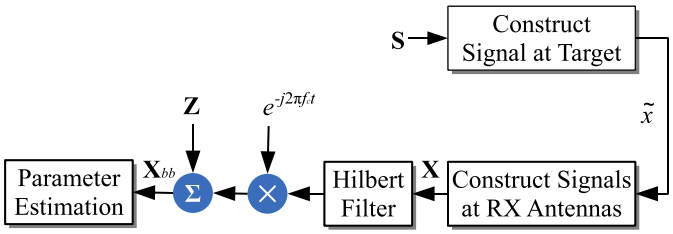

Figure 5.4: Illustration of a wideband phased array simulation method which does not use the narrowband model.

The signals received by the array are then calculated by

$$x_i(t) = \tilde{x}\left(t - \tau_i(\theta)\right). \tag{5.14}$$

Again, the signal is sampled up by a factor of 32 for the calculation of the received signals to increase the simulation accuracy. The received signal was then passed through a Hilbert filter and demodulated before the wideband beamformer and parameter estimation techniques were performed.

For the simulations below, the sample frequency f_s was 40 kHz. The transmitted signal was a chirp signal which was weighted by the delay-and-sum beamforming technique (Section 2.3) such that the main lobe pointed in direction 20°. A target was assumed to be located a distance $R = 3$ m from the transmitter array at an angle of 20° relative to the array.

5.4.3 TDWB Beamformer

The wideband simulations illustrated in Figure 5.4 can also be used to test techniques to determine range. Range-angle charts can be plotted to obtain range and DOA estimates from the simulated received data. In this section, beamforming was applied to the real, passband received signal matrix $\mathbf{X}$. The output of the beamformer was then cross correlated with the transmitted signal. The angle θ for which beamforming was applied, was varied. A peak in the cross correlation is obtained at the range and angle of the target location. In the simulations below, chirp signals with a bandwidth of 4 kHz centred at 10 kHz were used.

Figure 5.5(a) and 5.5(b) show the range-angle charts when beamforming was applied using a narrowband beamformer with Capon weights and a TDWB beamformer respectively. A comparison of the two charts shows that the NB beamformer gives a better angle resolution, but a poorer range resolution than the TDWB beamformer.

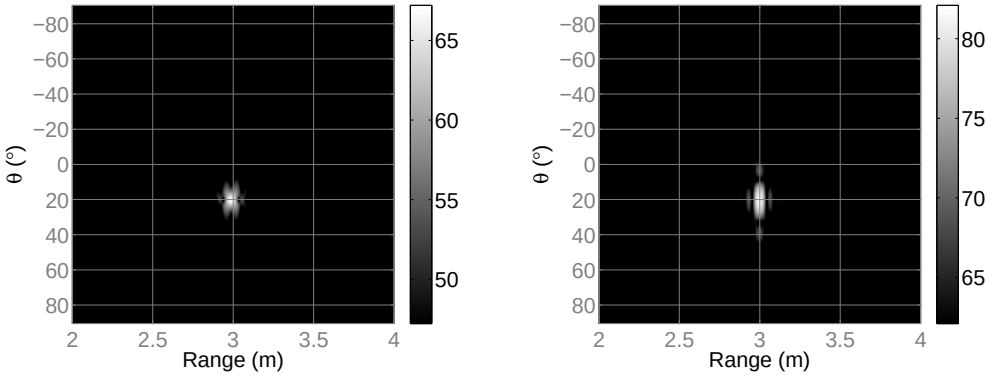

(a) NB beamformer with Capon weights.

(b) TDWB beamformer.

Figure 5.5: Range-angle charts.

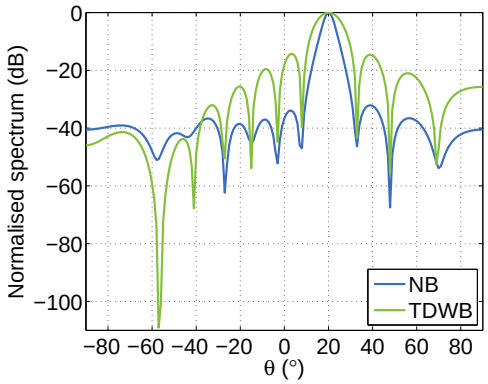

Figure 5.6: Spectrums obtained at the estimated range from NB beamforming and TDWB beamforming.

Figure 5.6 shows the power spectrum obtained from plotting the power in the cross correlations at the estimated target range. This confirms that the NB beamformer with Capon weights gives a higher resolution angle estimate than the TDWB beamformer. These results show that although the signals were wideband, higher resolution angle estimates can be obtained with a narrowband beamformer than a TDWB beamformer, for a phased array.

5.4.4 FWWB Beamformer

Using the wideband simulation model in Figure 5.4, simulations were performed to test the performance of the FWWB beamformer. Each channel of the beamformer therefore included an FIR filter which is shown in Figure 5.7, when the tap variable J was five, ten and twenty. A Hamming window based FIR filter design method was

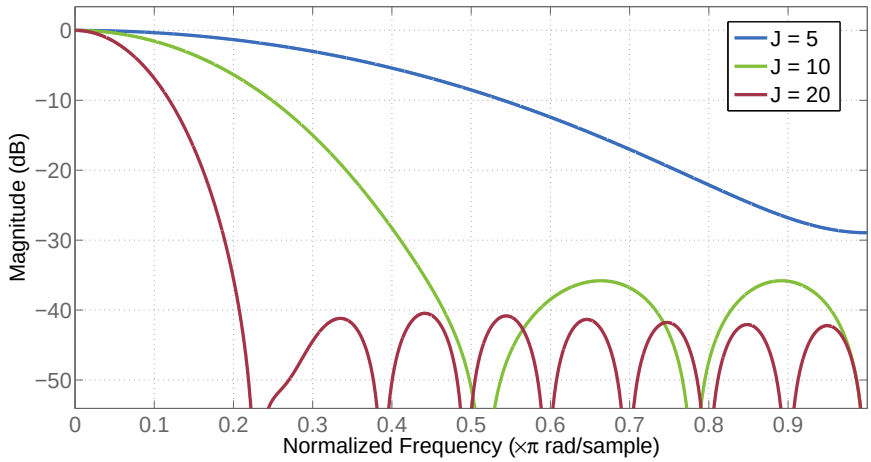

Figure 5.7: FIR filter responses with a cutoff frequency of 40 Hz for a sample frequency of 40 kHz, with 5, 10 and 20 taps.

used (MATLAB function `fir1`). The filter's normalised cutoff frequency was 0.001, which corresponds to 40 Hz, with a sample frequency of 40 kHz.

The transmitted signal was a chirp signal with a 10 kHz centre frequency and a variable bandwidth. To determine the performance of the FWWB beamformer, and to determine the number of taps that are necessary, 50 trials were performed at bandwidths from 100 Hz to 10 kHz, with 1 to 20 FWWB beamformer taps (where 1 tap corresponds to a narrowband system). The MSE of the estimation of the target angle was then determined using the conventional spectrum, Capon and MUSIC spectrums and the DML. The results are plotted in Figure 5.8.

The MSEs obtained with narrowband processing remained smaller than 0.016 for all methods as the signal bandwidth was increased from 100 Hz to 1 kHz. From 2 kHz onwards the MSEs increased regardless of the number of taps. For all of the estimation techniques the FWWB beamformers had little effect on improving the estimation accuracy at bandwidths below 5 kHz, except for the Capon technique which gave improved estimates when the FWWB was implemented from 3 kHz. For all of the techniques at bandwidths of 5 kHz and 10 kHz, the FWWB beamformers improved the estimations by up to 20 dB over the narrowband beamformer.

This illustrates that a FWWB beamformer can improve the results for bandwidths of 3 kHz and above. For bandwidths below 3 kHz, FWWB beamforming has no effect. Table 5.1 shows the empirically selected tap variables which are believed to give optimum results. A tap variable $J = 1$ corresponds to narrowband processing.

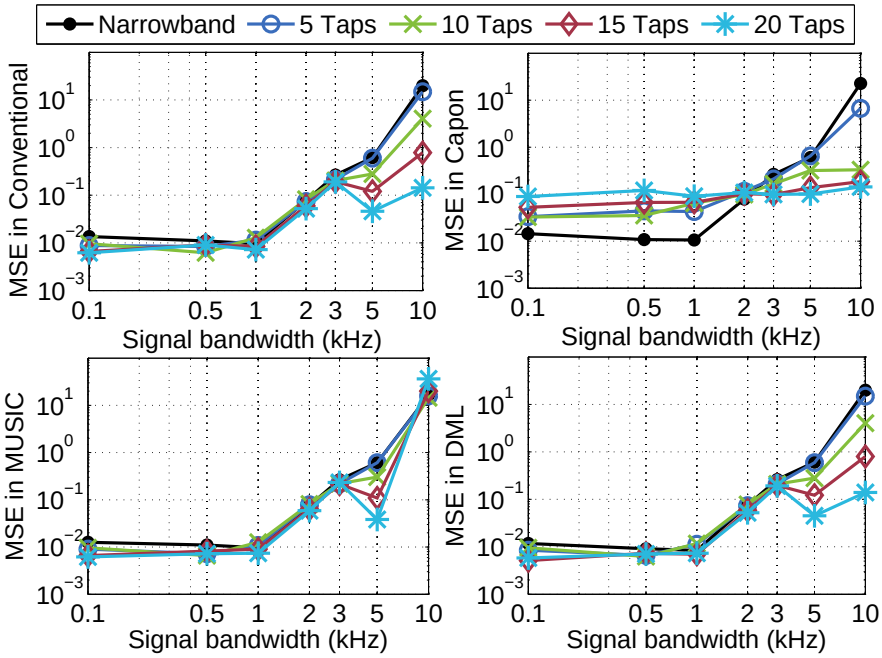

Figure 5.8: The MSE in target location estimations obtained with the conventional, Capon and MUSIC spectrums and the DML technique, as the signal bandwidth is varied, and the tap variable J of the FWWB beamformer is increased.

Table 5.1: The empirically selected phased array tap variables.

B (kHz)	0.1	0.5	1	2	3	5	10
J	1	1	1	1	20	20	20

5.5 MIMO Simulations

Wideband simulations were performed in MATLAB to test wideband MIMO systems and wideband beamformers. Firstly, the effect of wideband signals on the beampatterns is presented. The method for performing wideband simulations is then demonstrated. Simulations investigating TBR and the TDWB beamformer are discussed next and the section is ended with a simulation analysis of MIMO parameter estimation techniques with the FWWB beamformer.

For all of the simulations in this section, the number of transmitter and receiver antennas was $L_t = L_r = 10$ and they were in a ULA configuration, separated by half the wavelength of the carrier frequency, $f_c = 10$ kHz.

5.5.1 Wideband Beampatterns

To investigate the effect of wideband signals on MIMO beampatterns, the beampattern generated by the beampattern matching design to have main lobes at $-40°$, $0°$ and $40°$ was plotted with varying transmitted signal symbol frequency.

To determine the wideband pattern, the amplitude of the summed transmitter signals was calculated at different points on a circle surrounding the array. This is the same technique that was used for the phased array patterns in Section 5.4.1.

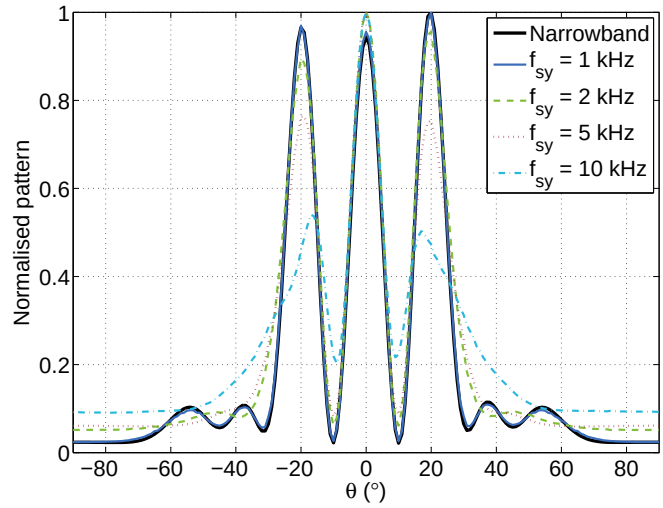

(a) Linear patterns

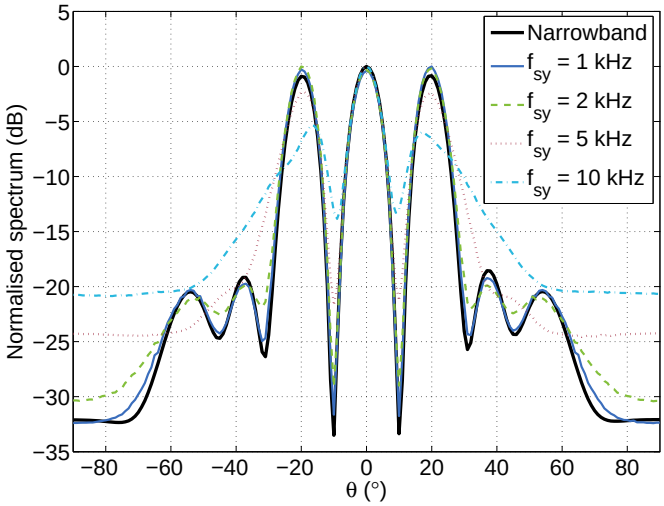

(b) Patterns in decibels.

Figure 5.9: Beampatterns generated by the beampattern matching design to have mainlobes at $-20°$, $0°$ and $20°$ as symbol frequency is varied.

Figure 5.9 shows the beampatterns calculated using the narrowband model and using the wideband technique at symbol frequencies between 1 kHz and 10 kHz. As the signal symbol frequency was increased, the magnitude of the main lobes at $-20°$ and $20°$ decreased. However, the width of the lobes remained constant. Also, as the symbol frequency increased, the side lobe level increased. The signal with a 10 kHz symbol frequency has a side lobe level almost 10 dB higher than the 1 kHz signal.

5.5.2 Wideband Simulation Method

The flow of the wideband simulation method is shown in Figure 5.10. Figures 5.11(a) to 5.11(g) show the real components of the signals at the different stages of the simulations which are marked A to G on the flow diagram. The set of orthogonal QPSK signals with 256 samples at a symbol frequency f_{sy} was scaled by the covariance matrix $\mathbf{R}_S$ according to Equation (2.118), sampled at $f_s = 50$ kHz and filtered by a square root Nyquist transmitter filter (TX Filter) before modulation. The signal at the target was constructed by

$$\tilde{x}(t) = \sum_{i=1}^{L_t} s_i \left(t - \tau_i(\theta)\right) \tag{5.15}$$

and those at the receiver were calculated by

$$x_i(t) = \tilde{x}\left(t - \tau_i(\theta)\right). \tag{5.16}$$

As for the phased array, to simulate these two equations, the signals were up-sampled by a factor of 32 (to get delays that were integer multiples of the sample period). After demodulation, the received signals were filtered by Nyquist receiver filters (RX Filter). A complex Gaussian i.i.d. noise matrix $\mathbf{Z}$, with a noise level of 0 dB, was then added to the signal matrix. Finally, the signal was decimated to f_{sy}. The wideband beamformers described in this chapter, and the target parameters

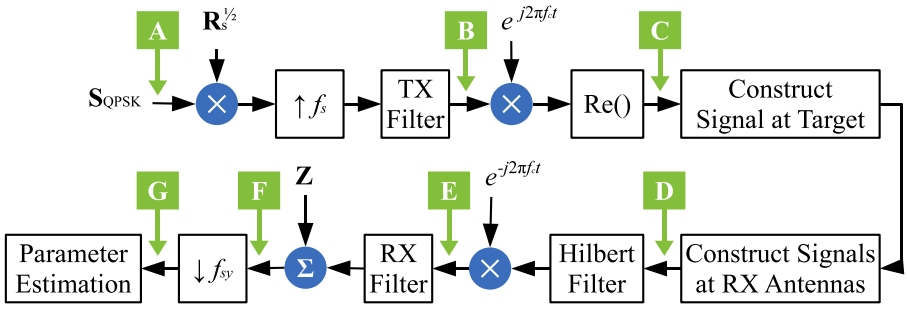

Figure 5.10: Flow diagram of the wideband simulations.

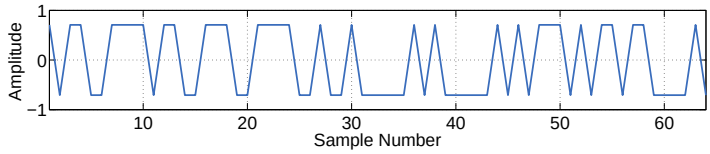

(a) A: QPSK symbols.

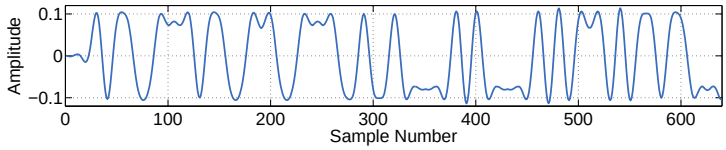

(b) B: Transmitter signal on Channel 1 after transmitter Nyquist filter.

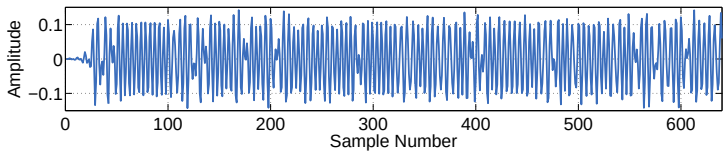

(c) C: Transmitter signal on Channel 1 after modulation.

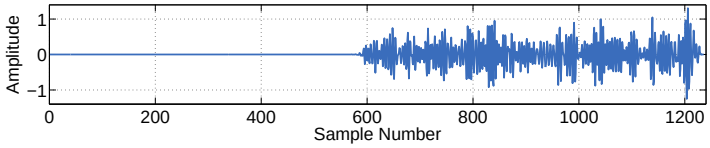

(d) D: Received signal on Channel 1.

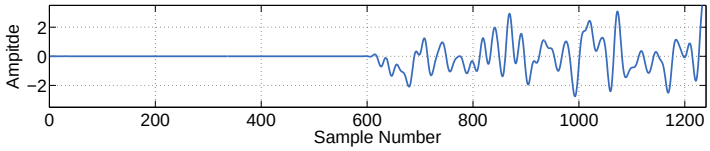

(e) E: Received signal on Channel 1 after demodulation and receiver Nyquist filter.

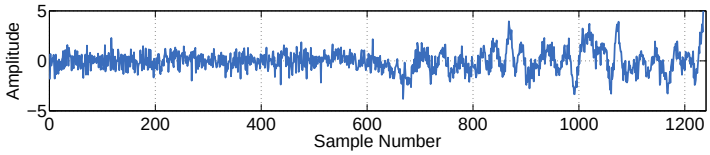

(f) F: Received signal on Channel 1 with noise added.

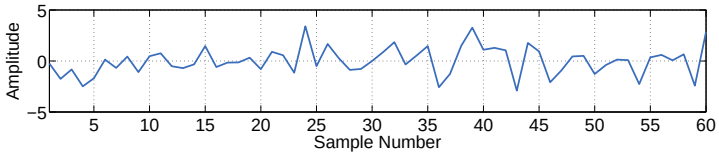

(g) G: Received symbols on Channel 1.

Figure 5.11: The transmitted and received signals at different points in the simulation.

estimation techniques that were described in Section 2.8 can then be applied to the simulated data.

5.5.3 TDWB Beamformer

The received signals from the wideband simulations illustrated in Figure 5.10 contain more samples than the transmitted signals due to the delays implemented to account for the different array element locations and the distance travelled by the signal to and from the target. Therefore, to apply TBR, as presented in Section 2.10, the range of the target must first be determined. With small modifications, TBR can be used to estimate the target range as well as angle.

Figure 5.12 shows the generalised implementation of TBR. Firstly, receiver beamforming is applied by multiplying the signal received on the ith receiver element with a complex weight w_{Ri}. All of the weighted received signals are then summed, to give one signal. A matched filter for each of the transmitted signals is then applied to the output of the receiver beamformer, increasing the number of signals to L_t. Each of these signals is then weighted with a complex weight w_{Ti} and summed, to apply transmitter beamforming.

If the target range is unknown, the implementation of matching by calculating the cross correlation matrix of all transmitted and received signal combinations, as given in Equation (2.142), can be modified. Instead, the cross correlation of the output of the receiver beamformer $x_R[n]$, and the ith transmitted signal $s_i[n]$ can be calculated as a function of time delay, which is given by

$$\tilde{\mathbf{x}}_i[k] = \sum_{n=1}^{N_X} x_R[n] s_i^*[n+k] \quad k \in [-N_S, N_X]. \tag{5.17}$$

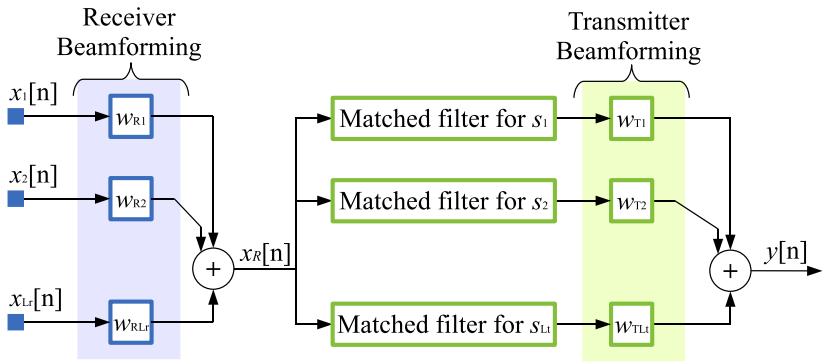

Figure 5.12: Simulation technique for TBR.

where N_S is the number of time samples of the transmitted signal and N_X is the number of samples of the received signal. The $N_S + N_X - 1$ time samples obtained from this matched filtering operation form the ith row of the matrix $\tilde{\mathbf{X}}$.

Transmitter beamforming is then performed by multiplication with a vector of weights, $\mathbf{w}_T$, which is selected by any of the beamforming methods presented in Section 2.3. The output of TBR is then

$$\mathbf{y} = \mathbf{w}_T^T \tilde{\mathbf{X}}. \tag{5.18}$$

The vector $\mathbf{y}$ can be calculated as the DOA θ for which the weights are calculated is varied. It will have peaks when θ corresponds to the DOA of a target and when the time delay of the cross correlation corresponds to the range of the target. Therefore, target angle and range can be determined.

TBR was simulated using different beamforming techniques to select the weight vectors $\mathbf{w}_R$ and $\mathbf{w}_T$. The simulation parameters were as described in Section 5.5.2, and a symbol frequency of 5 kHz was used. Range-angle charts were generated by plotting the matrix whose rows are made up of the vector $\mathbf{y}$, as θ was changed.

Figure 5.13 shows the range-angle chart when Capon weights were used to implement TBR, and no wideband compensation was implemented. The amplitude is in decibels. This simulation was performed at baseband, but at the sample frequency because the range of the target is needed before down-sampling the signal to the symbol frequency. Therefore, TBR is performed at the point marked F in Figure 5.10.

The long length of the stripes identifying the targets at $-40°$ and $40°$ in Figure 5.13(a) shows that the angular and range resolution is poor and this is confirmed in Figure 5.13(b), where the range of the target is magnified at the target location. The spectral peaks at these two target locations are almost $30°$ and 100 mm in size. The angular and range resolution for the target at $0°$ is good. This suggests that the effect of wideband signals is more detrimental to parameter estimation the further a target is from $0°$ and is also shown in Section 5.5.4.3.

TBR was then performed with the beamforming implemented by the TDWB beamformer and is shown in Figure 5.14. The amplitude is in decibels. The MATLAB implementation of the FD filter had $n \in [-100, 100]$. A Blackman window was used but it was not shifted by τ_{frac} as described in Equation 5.5. The filter and windows

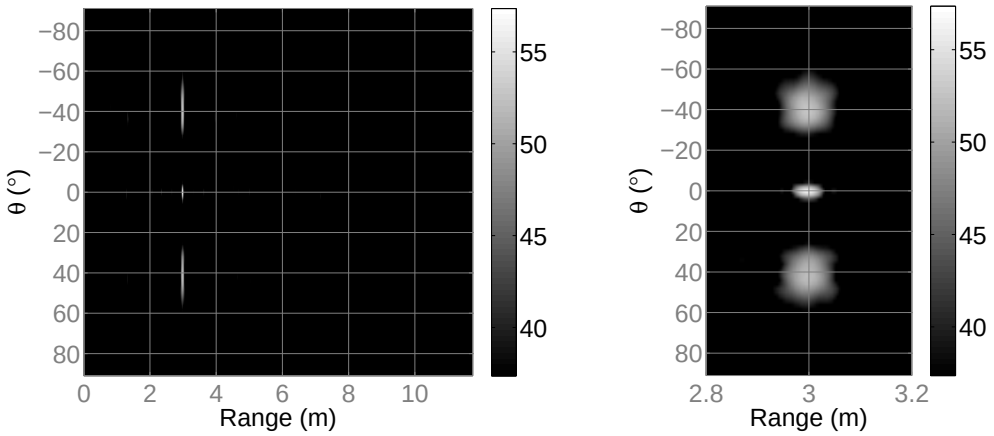

(a) The full range-angle chart. (b) Target range magnified.

Figure 5.13: Range-angle charts when TBR is performed with the narrowband beamformer and Capon weights.

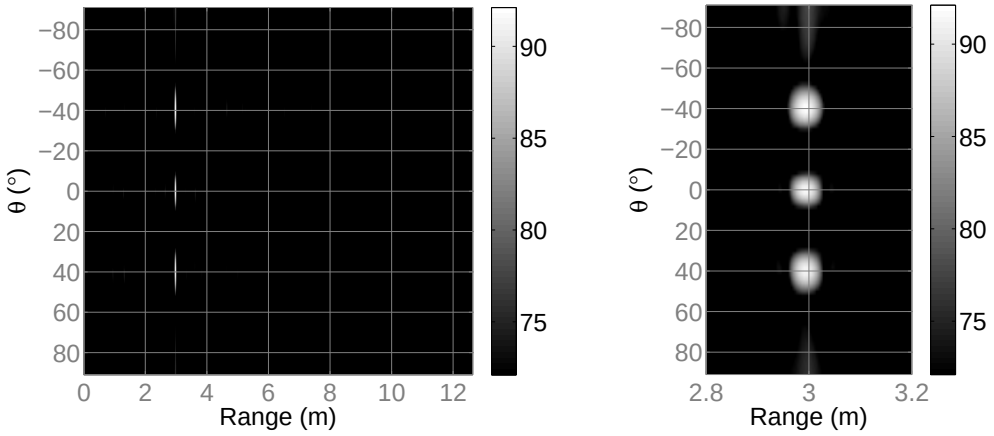

(a) The full range-angle chart. (b) Target range magnified.

Figure 5.14: Range-angle charts when TBR is performed with the TDWB beamformer.

were long (100 samples), so this inaccuracy has little effect. The TDWB beamformer was applied to the baseband sampled signals at point F in Figure 5.10.

The full range chart in Figure 5.14(a) clearly identifies three targets located at a range of approximately 3 m and with angles of about $-40°$, $0°$ and $40°$, as was simulated. The angular and range resolution of the spectrum is the same at all three target locations, with the peaks having main lobes of about $20°$ and 70 mm. Therefore, the targets at $-40°$ and $40°$ are identified with better resolution, and that at $0°$ with worse resolution compared to the spectrums obtained from the narrowband beamformer.

Figure 5.15 shows the spectrums obtained from TBR, when different beamformers were implemented. For the narrowband and FWWB beamformers, Capon weights were used. The spectrums were obtained by calculating the power in the cross correlation at the estimated target range as the DOA θ was varied. The spectrums are therefore effectively cross sections of the range-angle chart at the target range. This is equivalent to implementing transmitter beamforming as it was first introduced in Section 2.10.

When beamforming was performed by the narrowband beamformer, the three target locations are clearly identified but the resolution of the spectral peaks far from 0° is poor.

When the TDWB beamformer was used, the averaged spectrum has improved resolution at $-40°$ and $40°$. However, this spectrum has the poorest resolution of all the spectrums at 0°. Also, it has the highest side lobe levels, which are less than 15 dB below the main peak.

The best results were obtained when beamforming was performed by the FWWB beamformer with 8 taps. This method applied to MIMO is described in the following section. The range estimation obtained from the narrowband beamformer with Capon weights was used to down-sample the signal before the FWWB beamformer was applied. The FWWB beamforming spectrum shows the best combination of high resolution and low side lobe levels. Although its highest side lobe is at approximately -17.5 dB compared to -29 dB for the narrowband spectrum, its

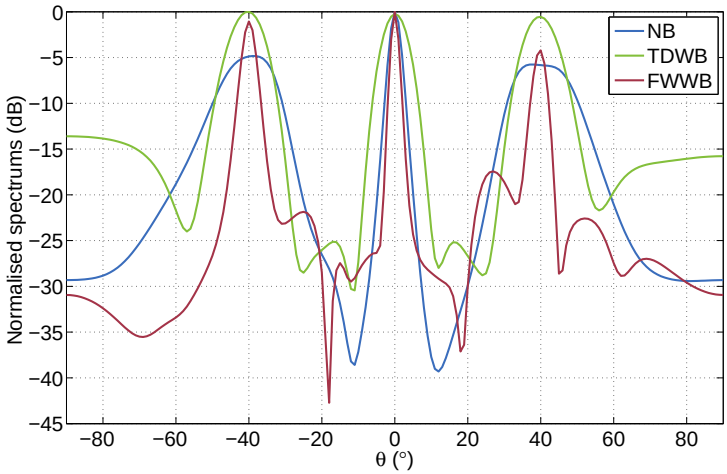

Figure 5.15: Spectrums for TBR with beamforming implemented by a narrowband, TDWB, and FWWB beamformer.

resolution is significantly better at -40° and 40°.

These results show that the estimates obtained from TBR techniques are improved when the TDWB and FWWB beamformers are used in comparison to a narrowband beamformer. The TDWB beamformer is best used for determining the range of the target. With the range estimate the FWWB beamformer can be implemented to obtain a high resolution angular spectrum giving the target angle.

5.5.4 FWWB Beamformer

Unlike the TDWB beamformer, the FWWB beamformer can be used with the MIMO wideband parameter estimation techniques. Three sets of simulations were performed to determine the optimum number of wideband taps, illustrate the parameter estimation spectrums and determine the improvements that can be offered by wideband processing.

5.5.4.1 Optimum Number of Taps

To determine the optimum number of taps, the tap variable J was varied from one to ten at five different symbol frequencies. The MSE of 100 estimations of θ and $\beta(\theta)$ at each target location was calculated for each value of J, with an omnidirectional pattern and a pattern obtained from the beampattern matching design. The optimum tap variable which gives the lowest MSE was then selected from each curve. The results are given in Table 5.2.

It is apparent that many more taps are required to give an optimal estimation of $\beta(\theta)$ than θ. For the target at 0°, the best result was almost always obtained with $J = 1$ i.e. with no taps and therefore narrowband beamforming. However, the MSE at 0° did not increase much as the number of taps increased or as the symbol frequency increased. Although the optimum tap variable differed with target location and depending on the parameter being estimated, it is desirable to only use one beamformer configuration to estimate θ and $\beta(\theta)$. Table 5.3 shows the chosen tap variables for each symbol frequency that were used to obtain the results that follow.

Table 5.2: Optimum values of J, for estimating $\beta(\theta)$ and θ at different frequencies for the three targets.

		Omnidirectional Pattern					***Beampattern Design***				
f_{sy} (kHz)		0.5	1	2	5	10	0.5	1	2	5	10
$-40°$	β	1	2	5	8	10	1	2	8	8	10
	θ	1	1	2	2	10	1	1	2	2	2
$0°$	β	1	1	1	1	1	1	1	1	1	2
	θ	1	1	1	1	1	1	1	1	1	1
$40°$	β	1	2	8	8	10	1	2	8	8	10
	θ	1	1	2	2	10	1	1	2	2	2

Table 5.3: Empirically selected values of J, which compromise well between θ and $\beta(\theta)$ estimations at different values of f_{sy}.

f_{sy} (kHz)	0.5	1	2	5	10
J	1	2	5	8	10

5.5.4.2 Capon and GLRT Plots

The improvement of the Capon and GLRT spectrums with FWWB processing is shown in Figure 5.16. The spectrums were obtained for a symbol frequency of 5 kHz and a tap variable of eight. It can be seen that the FWWB beamformer offered little improvement for the target at 0°. The resolution and accuracy of the Capon and GLRT spectrums were however greatly improved with FWWB beamforming at $-40°$ and 40°. Close analysis of Figure 5.16 shows that the side lobe levels of the spectrum are slightly increased after applying the FWWB beamformer. This highlights a weakness of the FWWB technique. Because the received signal is filtered, only part of it is to generate the spectrums and the received signal SNR is reduced. This results in higher side lobe levels.

5.5.4.3 Comparison of Wideband and Narrowband Results

Using the optimum tap variable calculated in Section 5.5.4.1, the performance of a FWWB beamformer was investigated. The symbol frequency was varied and

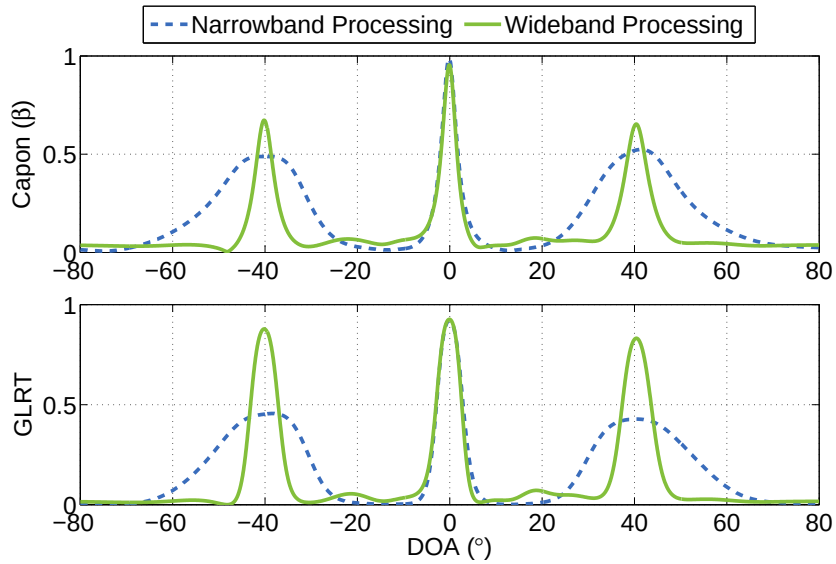

Figure 5.16: The Capon and GLRT spectrums for a symbol frequency of 5 kHz and with an omnidirectional transmitted beampattern with narrowband and wideband processing.

the GLRT and AML were used to estimate θ and $\beta(\theta)$ respectively. The GLRT estimates were used to initialise the AML. The MSE for 100 trials at each symbol frequency was calculated for omnidirectional beampatterns, and for those formed by the beampattern matching design, with and without FWWB processing. The results are shown in Figures 5.17 to 5.19.

Figure 5.17 shows the MSE in the estimation of θ for the target at $-40°$. It shows that at symbol frequencies below 2 kHz the performance of the FWWB and narrowband beamformers is similar. However, as the symbol frequency increases, the FWWB beamformer outperforms the narrowband beamformer. At a symbol frequency of 10 kHz, the MSE of the omnidirectional signal processed by the FWWB beamformer is almost 1000 times less than that processed by the narrowband beamformer. The figure also shows that when FWWB processing is applied, the benefit of transmitter beamforming decreases as the symbol frequency increases.

Despite the improvement offered by FWWB processing as the symbol frequency increases, the MSE of the results also increases. The use of a wideband signal with an FWWB beamformer does not provide better results than the use of a narrowband signal and beamformer. However, in scenarios when a wideband signal is unavoidable, Figure 5.17 illustrates that FWWB beamforming does offer improvements.

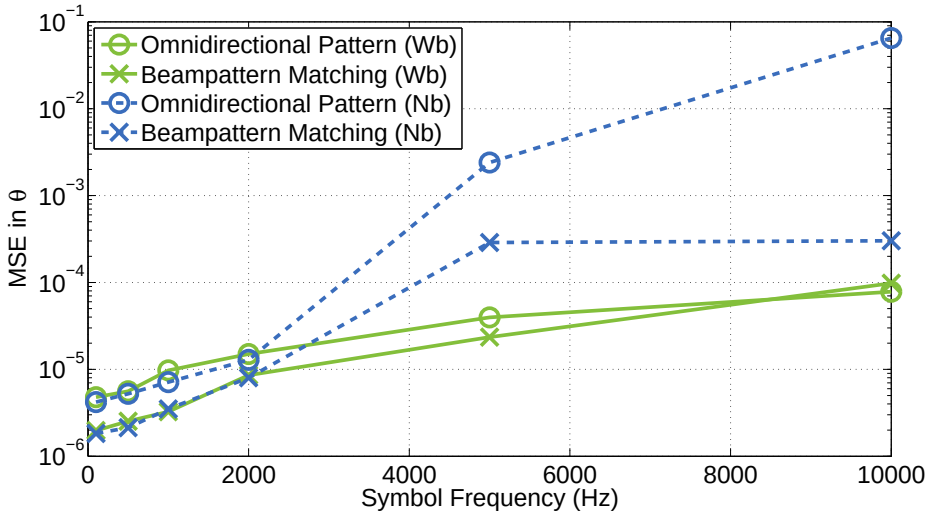

Figure 5.17: MSEs in θ for the target at $-40°$ for 100 trials as the symbol frequency is varied.

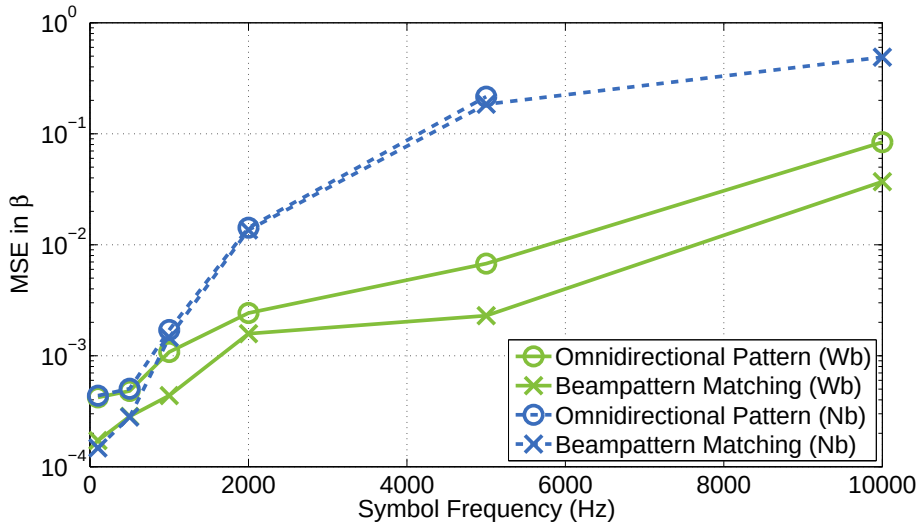

Figure 5.18: MSEs in $\beta(\theta)$ for the target at $-40°$ for 100 trials as the symbol frequency is varied.

Figure 5.18 shows similar trends in the estimation of $\beta(\theta)$ at $-40°$. However, the FWWB beamformer offers improvements at an earlier frequency of 1 kHz. The narrowband estimator was unable to estimate $\beta(\theta)$ at a symbol frequency of 10 kHz when an omnidirectional pattern was transmitted. However, the FWWB beamformer provides this estimate, with an MSE smaller than 0.1.

Figure 5.19 shows the MSE in the estimation of θ for the target at $0°$. The deterioration in the accuracy of the results as the frequency is varied is not as severe

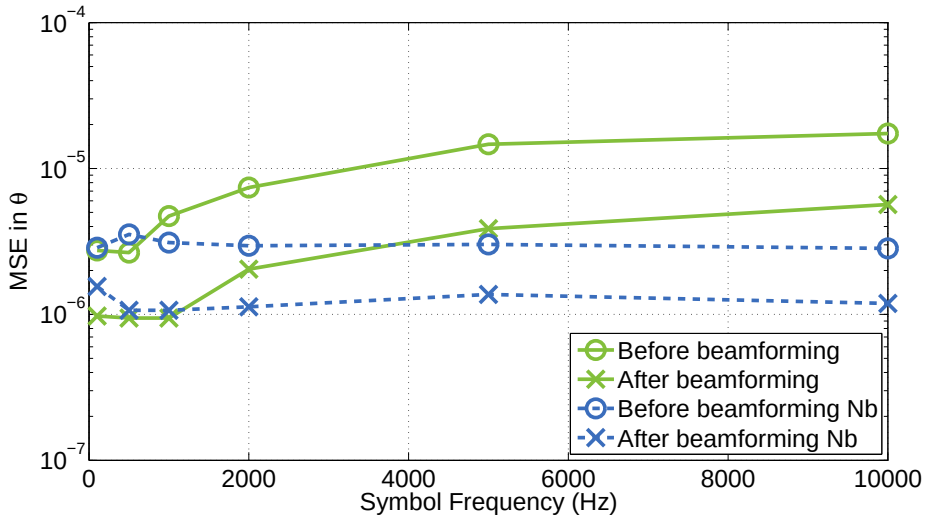

Figure 5.19: MSEs in θ for the target at 0° for 100 trials as the symbol frequency is varied.

as that seen for the target at $-40°$ regardless of the beamformer used. Contrary to the results seen for the target at $-40°$, the narrowband beamformer is, on average, better able to estimate the target location than the FWWB beamformer but the results are not very different for either.

Similar observations can be made from the estimations of $\beta(\theta)$ at 0°. Also, the curves for the target at 40° closely resemble those at $-40°$.

These simulations illustrate that applying a FWWB beamformer when wideband signals are transmitted is better than using a narrowband beamformer. The improvement is most noticeable for very wideband signals and for targets far from 0°. However, the results obtained with a wideband signal and FWWB beamformer are never better than those obtained in a narrowband scenario. So the presented FWWB beamformer is only of benefit in cases where wideband signals are unavoidable. Under these circumstances, the FWWB beamformer significantly improves the accuracy of target parameter estimations.

5.6 Summary

In this chapter two methods to take wideband signals into account so that phased array and MIMO techniques can be applied to wideband systems were presented. The TDWB beamformer requires a true time delay to be applied to the transmitted

and received signals if they are wideband, instead of a phase shift. This avoids the inaccuracies introduced by modelling the time delay as a phase shift when the radar signals are wideband. The second method allows wideband signals to be transmitted, but an FIR filter is applied on reception to reduce the bandwidth of the signals, so that narrowband processing can be applied.

Wideband simulations were then performed on phased array and MIMO systems. When the transmission of wideband phased array signals was simulated, the beam width of the beampatterns generated was found to increase, and the amplitude difference between the main lobe peaks and the side lobes was found to decrease. For MIMO patterns, the amplitude of the side lobes for targets far from 0° also decreased significantly. However, the beam width of the main lobes did not increase much.

The TDWB beamformer applied to phased array was shown in simulation to give higher target range resolution, but lower target angular resolution than the Capon method. When applied to MIMO radar, simulations showed that the TDWB beamformer gives higher angular resolution estimates than a narrowband Capon beamformer at angles far from zero, but lower angular resolution estimates close to zero. In addition, with the TDWB beamformer, the amplitude of all peaks was close to equal, as desired for identical targets, whereas the targets at -40° and 40° had lower amplitude compared to that at 0° with the Capon beamformer. Therefore, the TDWB is more robust than the narrowband Capon method when applied to wideband MIMO systems.

Wideband phased array simulations showed that the FWWB beamformer could improve the accuracy of the angle estimates from signal bandwidth to centre frequency ratios greater than 3:10. The FWWB beamformer was also shown to improve the accuracy of MIMO techniques for estimating target angle and complex amplitude at a bandwidth to centre frequency ratio greater than 1:5, compared to narrowband techniques. The higher the bandwidth, the greater the improvement.

In this chapter, the simulation conditions were similar to the conditions that apply to the hardware system. It has been shown, that with some extra processing, the phased array and MIMO techniques that were developed for narrowband systems can also be applied to wideband systems. Therefore, all of the theory required to implement phased array and MIMO techniques has been presented. In the following chapter, the hardware on which these techniques were implemented is described.

Chapter 6

Hardware System Design

A hardware system was designed to test the theoretical principles described in Chapter 2 and simulated in Chapters 4 and 5. Figure 6.1 shows a diagram of the hardware modules used to implement the system. The system consists of an acoustic phased array transmitter and receiver, which are controlled and interfaced with a Master Control Unit (MCU) implemented on an FPGA. The MCU is connected to a PC, which controls the hardware.

In this chapter, the hardware system design is discussed. Firstly, the system design parameters are defined. The receiver which was designed by the CSIR and the additions and modifications made to it are described next. The transmitter design is then detailed and this is followed by the architecture and functionality of the MCU. Finally, the PC applications are presented.

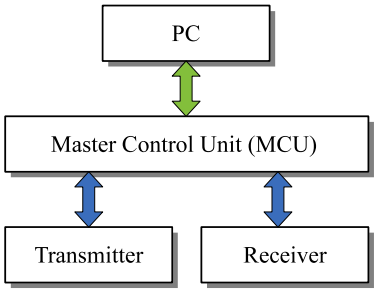

Figure 6.1: The hardware system.

6.1 System Design Parameters

The design parameters were central to many of the design decisions made and described throughout the rest of this chapter. The parameters of the hardware system are:

- **Supply Voltage:** The supply voltage is a dual-polarity supply of ±5 V. In addition, 2.5 V and 3.3 V voltage supplies are available.
- **Number of Channels:** 16 speakers and 16 microphones are used in the transmitter and receiver arrays respectively.
- **Sample Frequency:** The system sampling frequency is 40 kHz, which is the minimum permitted sampling frequency specified in Section 3.3.3. A higher frequency was not used due to limitations introduced by the use of serial peripheral interface (SPI) for communication between the MCU, and the transmitter and receiver boards.
- **Operating Frequency:** The bandwidth of the signals is 4 kHz centred around a carrier frequency of 10 kHz. This band is a compromise between the required inter-element spacing of the array elements, and the measured frequency response of the elements available. This is discussed in more detail in Section 6.2.1.

6.2 Receiver Array

Stanton [8], in association with the CSIR, designed and built a 16-by-16 rectangular acoustic phased array receiver with 16 analogue boards that each condition the signal for 16 channels. For this project, one of the analogue boards was used and a ULA of 16 microphones was built.

The receiver analogue board biases the microphones, implements an amplifier and a low-pass filter for anti-aliasing, and converts each signal from analogue to digital. Figure 6.2 shows a block diagram of the receiver as designed by Stanton [8] and Figure G.3(c) in Appendix G shows a photograph of the board.

Preliminary measurements on the receiver board showed that the gain was too low. The gain-bandwidth product of the amplifier was also already close to its limit.

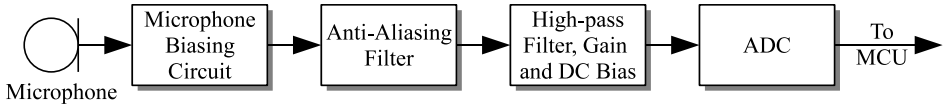

Figure 6.2: Block diagram of the phased array receiver.

Therefore an add-on amplifier board was necessary. It was built to connect between the microphone, and the microphone biasing circuit on Stanton's board.

Each module on the analogue receiver board and the additional amplifier board are described in the following sections.

6.2.1 Microphones

16 F6035AU back electret condenser microphones were arranged in a ULA configuration. The frequency response of the microphones is approximately flat from 20 Hz to 20 kHz, with ripple below 2 dB between approximately 5 and 10 kHz. The frequency response, taken from the data sheet [55], is shown in Figure 6.3.

The spacing between each of the microphones is critical as it determines the signal frequency for which the array is effective. To avoid aliasing in the spatial frequency domain, the microphones must be separated by at least half a wavelength of the highest frequency component [13]. Simulations however showed that if the antenna separation corresponded to $\frac{\lambda}{2}$ for the centre frequency component, no grating lobes occurred, and the beampattern could be centred at the desired angle. Other antenna separations resulted in off-centre beampatterns when the array was steered away from zero. Therefore, for the centre frequency f_c of 10 kHz, the speaker separation

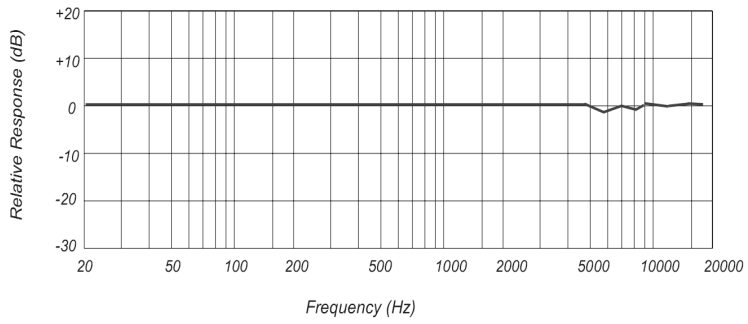

Figure 6.3: The frequency response of the microphones [55].

was

$$\frac{\lambda}{2} = \frac{c}{2f_c} = 17 \text{ mm}. \tag{6.1}$$

The microphones were mounted on a printed circuit board (PCB). This was based on findings by [7] and [8], that the rigidity provided by the PCB allows accurate placement of the microphones. The design of the PCB is discussed in Appendix H, and a photograph of the microphone board is included in Figure G.3(a) in Appendix G.

6.2.2 Microphone Biasing Circuit

Back electret condenser microphones require a biasing power supply due to the presence of a small preamp which is part of the microphone. The biasing circuit used is shown in Figure 6.4. The 2.5 V supply is used to bias the amplifiers, and results in the microphone signals having a 2.5 V DC component.

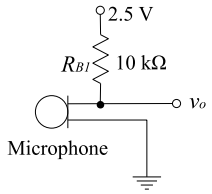

Figure 6.4: Microphone biasing circuit.

6.2.3 Anti-Aliasing Filter

An anti-aliasing filter is required because the signals received by the microphone are sampled by an analogue to digital converter (ADC). The anti-aliasing filter has the added benefit of filtering out any noise at frequencies above the upper frequency of the signal. A sixth order Type I Chebyshev filter was chosen, and implemented with the Sallen-Key topology. The filter circuit diagram is shown in Figure 6.5.

The sampling frequency of Stanton's system was 62.5 kHz. The filter was designed by Stanton [8] to have a stop-band rejection of at least -74 dB (equal to the 12-bit ADC noise floor) at this sampling frequency and an attenuation of 81.5 dB was achieved. To meet these requirements, the filter corner frequency is 16 kHz, and a maximum of 0.1 dB passband ripple is allowed. However, the requirement should

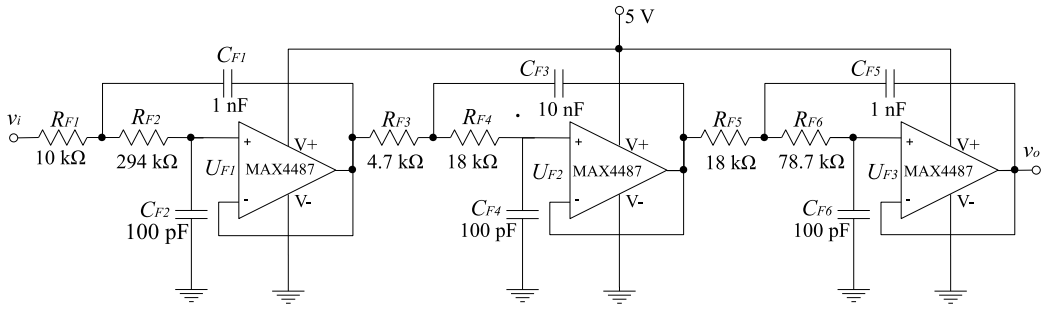

Figure 6.5: Sixth order Type I Chebyshev anti-aliasing filter on the receiver.

be that the cutoff is equal to the ADC noise floor at the Nyquist frequency, and not the sampling frequency. Therefore, for this project, the ideal anti-aliasing filter has 74 dB attenuation at the Nyquist frequency of 20 kHz. With the implemented filter, the Nyquist frequency cutoff is below 40 dB. This is regrettably above the noise floor of the ADC and will result in the received signals having a higher noise level. Fortunately, microphones also have low-pass filter characteristics with a cutoff close to 20 kHz, and therefore, the actual attenuation at the Nyquist frequency will probably be lower. Therefore, Stanton's filters were used, without any modifications.

6.2.4 High-pass Filter, Gain and DC Bias

Filtering, biasing and amplification are accomplished by the circuit shown in Figure 6.6.

A high-pass filter is required to remove the DC bias introduced by the microphone biasing circuit. This filter has the additional functionality of removing 50 Hz noise. A first order passive filter with a cutoff at 486 Hz and an attenuation of 20 dB at 50 Hz was used. The signal is biased again, so that it is centred around 2.5 V as the

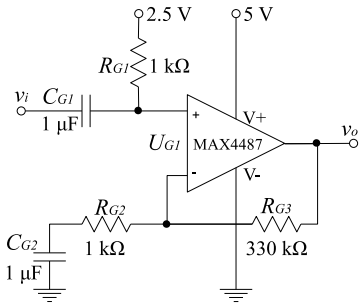

Figure 6.6: Receiver high-pass filter and amplifier with DC bias.

ADC requires the signal voltages to be between 0 V and 5 V.

Finally, the signal is amplified so that it takes on values covering the full range of the ADC, to give maximum dynamic range. A feedback resistor R_{G3} of 330 kΩ is used with a 1 kΩ resistor to ground, R_{G2}, which gives a voltage gain of approximately 330 (50 dB). This gives a gain bandwidth product of 6.6 MHz (calculated with a conservative maximum bandwidth of 20 kHz), which is below the 7 MHz gain-bandwidth product of the amplifiers used. Early testing found the gain to be insufficient. The gain of the amplifier implemented in Figure 6.6 could not be increased, because the amplifier operates close to its gain-bandwidth product limits. Therefore, an additional gain stage was added.

6.2.5 Analogue to Digital Converter (ADC)

A single AD7490 ADC was used for all 16 receiver channels. It is a 16 channel, 1 Mb/s and 12 bit ADC which can be connected to the FPGA with an SPI interface. The ADC samples each channel sequentially and sends the received data to the FPGA as a serial stream. At 1 Mb/s, each channel can be sampled at a maximum frequency of 62.5 kHz. The delay introduced between channel samples by the sequential sampling has the effect of beamforming. The effect of this delay, and a method of compensating for it are discussed in Section 6.2.5.1 below.

6.2.5.1 ADC Sampling Error

Sequential sampling of the receiver channels has the effect of beamforming, because a time delay is added to each channel. Given the system sampling frequency of 40 kHz, each channel is sampled every 25 μs. This means that the delay between sampling adjacent channels is one sixteenth of this, which is approximately 1.56 μs. At a centre frequency of 10 kHz and for a true DOA of 0°, this corresponds to an error in beamforming angle of 1.79°. As the DOA angle increases, the beamforming error also increases and at a DOA of 40°, the error in beamforming angle is 2.38°.

This can be corrected by up-sampling and interpolating the signals to a frequency 16 times higher than the original sampling frequency. The signals are then re-sampled, with a delay which compensates for that introduced by the ADC. In the case of 16 channels, channel one is re-sampled with a delay of 15 sampling periods, channel two with a delay of 14 sample periods and so on.

6.2.6 Receiver Board Power Supply

The receiver board power supply is shown in Figure 6.7. In addition to the capacitors C_{P1} and C_{P2}, a 2200 μF capacitor was connected across the power supply. The circuit diagram of the voltage regulator used to supply 2.5 V is given in Figure 6.8. The regulator was not implemented on the receiver boards, but was included on the additional amplifier PCB described in Section H.2 of Appendix H.

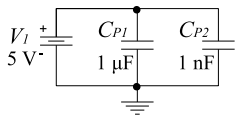

Figure 6.7: Receiver power supply.

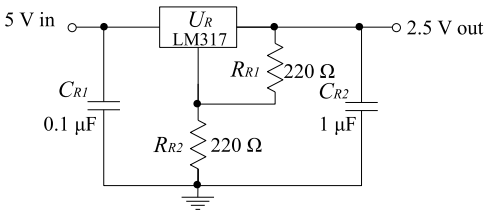

Figure 6.8: Regulator to convert 5 V to 2.5 V.

6.2.7 Additional Amplifier Stage

Testing showed that the amplifier on the receiver analogue electronics board did not amplify the signal sufficiently. Therefore, an additional amplifier stage had to be designed. Because the receiver analogue electronics described in Sections 6.2.2 to 6.2.6 above are all neatly built on a single board, the most accessible point to amplify the signal is between the microphone and the microphone biasing circuit.

A single channel of the additional amplifier is shown in Figure 6.9. A non-inverting amplifier with a dual supply and a gain of 23 was implemented with a TL074CN amplifier. The total gain of the receiver analogue circuitry is therefore 7590 (78 dB). The output of the amplifier is AC coupled.

As the microphones need to be biased, this circuit also includes a microphone biasing circuit identical to that in Section 6.2.2 which is implemented with the 2.5 V supply

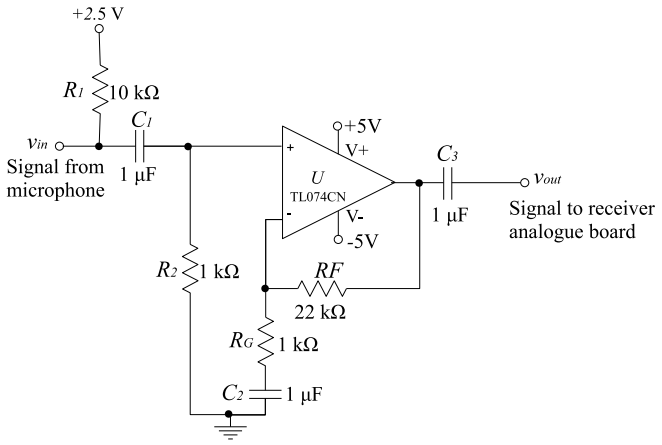

Figure 6.9: Additional receiver amplifier stage.

and R_1. This renders the second biasing circuit, described in Section 6.2.2, useless and it could be omitted in future versions. The microphone acts as a low-pass filter because its frequency response drops off after 20 kHz. A high-pass filter, implemented with C_1 and R_2, was also included to remove the DC bias introduced by the microphone biasing circuit before amplification of the signal.

The amplifier circuit was replicated for all 16 transmitter channels, and implemented on a PCB which was manufactured by chemical etching of a copper-clad board. The board design and manufacture method is given in Appendix H.2 and Figure G.3(b) in Appendix G is a photograph of the implemented board.

6.3 Transmitter Array

Transmitter analogue circuitry is required to convert a digital signal into an analogue one which can be transmitted on the speaker. Figure 6.10 is a block diagram of the transmitter. A DAC converts the signal sent by the MCU from digital to analogue. A reconstruction filter removes high frequency components of the signal that arise due to the conversion. The signal is then amplified so that it can be transmitted on

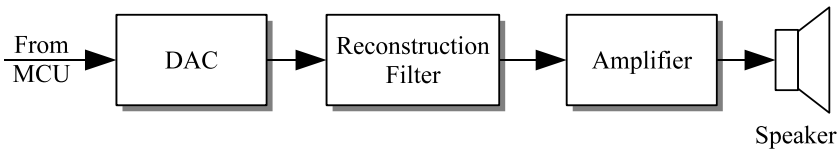

Figure 6.10: Block diagram of the phased array transmitter.

the speakers at maximum power.

Each channel has its own reconstruction filter, amplifier and speaker. However, only two Digital to Analogue Converters (DAC) are used for all 16 channels. All of the transmitter circuits were implemented on a PCB which is photographed in Figure G.2(a) in Appendix G. The speakers were mounted on a PCB which is also shown in Appendix G in Figures G.2(b) and G.2(c). The design of these PCBs, is presented in Appendix H. The components of the transmitter are described below.

6.3.1 Digital to Analogue Converter (DAC)

The MAX5306 DAC was selected. It is an 8 channel 12 bit DAC, with a 15 MHz SPI interface which can be connected to the MCU. The DAC has a voltage settling time of 5 μs and therefore, the maximum sampling frequency is 200 kHz, which is well above the 40 kHz used.

Two DACs are required for the 16 channels, and they are driven in parallel from separate, but synchronised, SPI lines. This enables higher speeds if necessary. The data from eight channels is transmitted serially within a single sample period with 16 bits transmitted for each channel. Therefore, to ensure a system sampling frequency of 40 kHz, a clock frequency of at least 5.8 MHz must be used, which is well below the maximum rated frequency. The DAC has synchronous update and thus, all of the outputs can be updated at the same time which ensures that the transmitter DAC is not afflicted by the same sampling error as the receiver ADC.

The DAC output voltage varies between approximately 0 V and 3.3 V. The circuit diagram of one of the transmitter module DACs is shown in Figure 6.11. The inputs

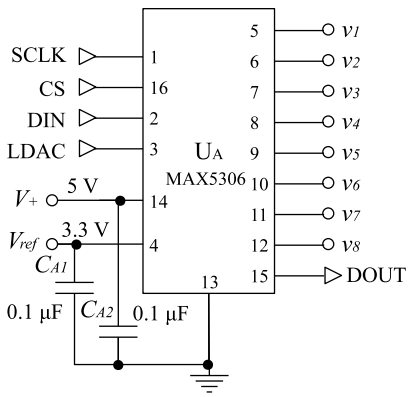

Figure 6.11: DAC on the transmitter.

SCLK to CS on the left are driven by the FPGA and will be discussed in Section 6.4.2.

6.3.1.1 DAC SNR

The ideal SNR of the DAC can be calculated, in the same way as for an ADC [56]. This gives the best noise level that the DAC can attain. The root mean square (RMS) powers are used to derive the SNR. The RMS of the full range signal output by the DAC, provided that the signal is sinusoidal, is given by

$$V_{signal} = \frac{2^{N-1}q}{\sqrt{2}}$$

where q is the voltage of the least significant bit and N is the number of bits. The DAC has an uncertainty which is given by $\pm 1/2$ the value of a bit. This uncertainty can be assumed to have a triangular response across the analogue input signal, and therefore has an RMS value of

$$V_{noise} = \frac{1}{2}\frac{q}{\sqrt{3}} = \frac{q}{\sqrt{12}}.$$

The best signal to noise ratio that can be achieved with the DAC is therefore given by

$$\text{SNR} = 20\log\frac{V_{signal}}{V_{noise}} = 20\log\frac{2^{N-1}q}{\sqrt{2}}\frac{\sqrt{12}}{q} = 6.02N + 1.76 \text{ dB}, \tag{6.2}$$

and for a 12 bit DAC, the ideal signal to noise ratio is 74 dB.

6.3.2 Reconstruction Filter

The DAC's output is a series of steps that must be passed through a low-pass filter to remove the higher frequency harmonics and reconstruct a smooth analogue signal. The ideal reconstruction filter allows the signal to pass with constant phase delay and a flat frequency response up to the Nyquist frequency, and has a zero frequency response beyond the Nyquist frequency.

In practice, because the DAC SNR is inherent, it is sufficient for the attenuation of the reconstruction filter to be less than or equal to the DAC SNR at the Nyquist frequency f_N. Thus, the reconstruction filter should have at least 74 dB of attenuation at $f_N = 20$ Hz.

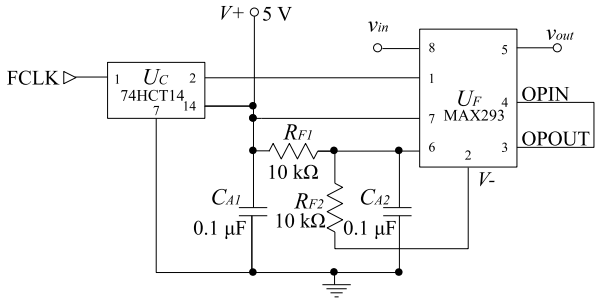

Figure 6.12: The reconstruction filter with TTL to CMOS conversion of the filter clock.

The reconstruction filter circuit diagram is shown in Figure 6.12. A MAX293 eighth order elliptic low-pass switched capacitor filter was chosen to implement the reconstruction filter. Elliptic filters have ripple in the pass-band and the stop-band but the MAX293 has a maximum ripple amplitude of 0.15 dB which is sufficiently low.

The MAX293 has a 1.5 transition ratio and a stop-band attenuation of 80 dB so at frequencies higher than 1.5 times the corner frequency, the attenuation will be at least 80 dB. For the stop-band to begin at f_N the corner frequency required is

$$f_c = \frac{20}{1.5} = 13.33 \text{ kHz}\,. \tag{6.3}$$

To simplify the clock generation as will be described in Section 6.4.2.4, f_c is chosen to be 15 kHz. This theoretically gives an attenuation of at least 50 dB at 20 kHz, which is less than ideal. This might result in the transmitted signal having slightly higher noise levels, but the speaker will also have some low-pass properties thus reducing the attenuation at the Nyquist frequency.

The corner frequency of the filter assumes a value equal to one hundredth the frequency of FCLK (Filter Clock). Therefore, FCLK is required to have a frequency of 1.5 MHz.

The clock input to the filter uses CMOS +5 V logic. However, the FPGA signals use TTL logic and have a maximum logic level of 3.3 V. Therefore the FPGA clock signal requires a TTL to CMOS level adjustment. This is performed with a 74HCT14 inverting Schmitt trigger which, due to its hysteresis also cleans the clock signal. The inversion of the clock signal does not have an effect, since it is only used to set the corner frequency of the filter. A photograph of the Schmitt trigger circuit is shown in Figure G.2(e) in Appendix G.

The DAC output signal is the input to the filter, and can vary from approximately 0 V to 3.3 V. Testing showed that filter output was clipped if the input signal was below approximately 400 mV. Therefore, the DAC signal had an offset of 400 mV added to it. The maximum voltage that can be supplied on the output of the MAX293 is 4 V, and thus no clipping occurred at the signal's maximum voltage.

6.3.3 High-pass Filter and Amplifier

The output signal of the filter varies between 0.4 V and 4 V. It is optimised for transmission by the speakers by removing the DC offset, amplifying the voltage and amplifying the power. The circuit that achieves this is shown in Figure 6.13.

To remove the DC offset, a first order passive high-pass filter with a cutoff at approximately 350 Hz was implemented. The reconstruction filter can drive a minimum load of 20 kΩ, and therefore the high-pass filter resistor R_{HF} is 22 kΩ. The capacitor is chosen by

$$C_{HF} = \frac{1}{2\pi f R_{HF}} \tag{6.4}$$

and is 21 nF.

A Class AB audio amplifier, which provides voltage and power amplification to optimise the output signal for driving the speakers, was implemented. A MAX4495 general purpose operational amplifier was chosen as it can be powered by a dual supply. It also has Total Harmonic Distortion (THD) below 0.006% for signals in the frequency band of interest. The slew rate of the amplifier is 3 V/μs.

The maximum RMS voltage that can be applied to the speakers is calculated in Equation (6.8) which follows and is approximately 2.5 V RMS. Therefore, by limiting

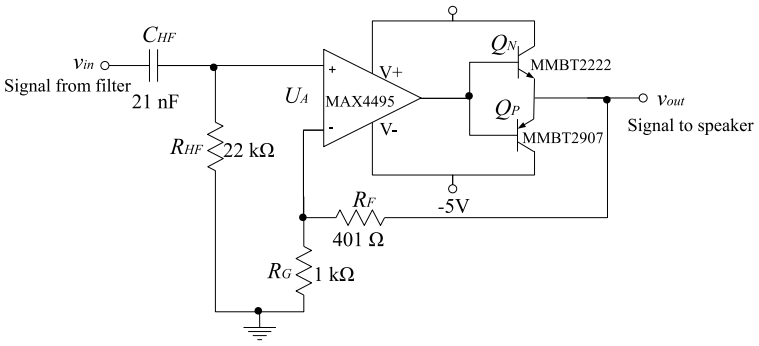

Figure 6.13: Transmitter high-pass filter and amplifier.

the output of the amplifier to 5 V peak to peak, the speaker's maximum power is not exceeded. The maximum peak-to-peak output voltage of the filter is 3.6 V so amplification is necessary.

The required gain is

$$G = \frac{V_{out}}{V_{in}} = 1.39. \tag{6.5}$$

A non-inverting amplifier which has gain

$$G = \left(1 + \frac{R_F}{R_G}\right) \tag{6.6}$$

was selected. R_G was set to be 1 kΩ, so R_F must be approximately 400 Ω. Resistors of 386 Ω were used for R_F.

To amplify the signal's power, a push-pull pair of Bipolar Junction Transistors (BJT), Q_N and Q_P were used. They have a voltage gain of one but a high current gain. On its own, a push-pull transistor pair suffers crossover distortion because the turn-on voltage of a typical BJT is 0.7 V. Therefore, if the input signal to the push-pull pair is between -0.7 and +0.7 V, the output is 0 V. Using the configuration in Figure 6.13, crossover distortion is minimised by connecting the output of the amplifier to the input of the push-pull pair, and the feedback resistor to the output of the push-pull pair. The amplifier then compensates for the cross-over distortion provided that its slew rate is high enough.

The transmitter high-pass filter and amplifier circuit was simulated in ORCAD Capture CIS Demo version 16.2. The PSpice model for the MAX4495 amplifier was downloaded and added to the project. The input signal was a 0.4 V to 4 V 8 kHz sinusoid to simulate the output of the filter. The simulated signals at the input and the output of the amplifier were plotted in MATLAB and are shown in Figure 6.14(a). As desired, the output signal varies from approximately -2.5 V to 2.5 V and appears undistorted. When the signals are magnified at the zero crossover point, as shown in Figure 6.14(b), distortion is visible. For approximately 1 μs, the output remains at zero while the input increases to approximately 150 mV. The output signal then corrects itself. Therefore, despite the correction circuitry, some crossover distortion is still present.

To further analyse the effect of the crossover distortion, Figure 6.14(c) which shows the power spectrum of the amplifier output with a sampling frequency of 1 MHz is included. Harmonics are visible at odd multiples of the signal frequency. The harmonics have a maximum amplitude 20 dB below the main harmonic. In the hardware system, these components will be filtered more by the speaker, which acts

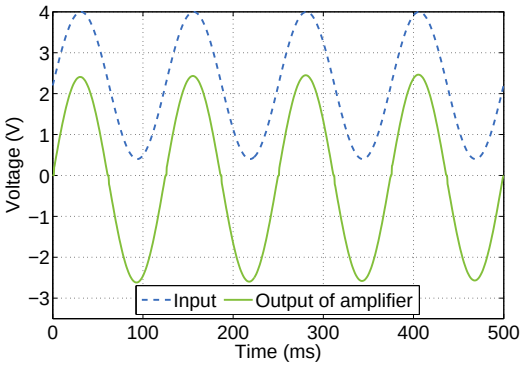

(a) Voltage response of the high-pass filter and amplifier circuit.

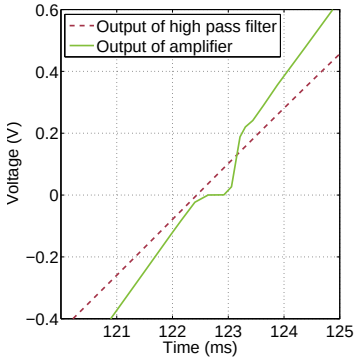

(b) Crossover distortion in the amplifier circuit.

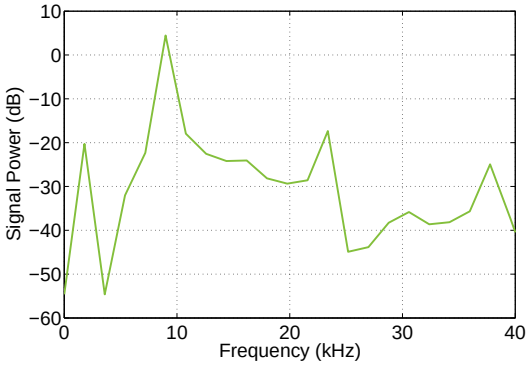

(c) Power spectrum of the amplifier output.

Figure 6.14: Voltage response and power spectrum of the high-pass filter and amplifier circuit simulated in Orcad with an 8 kHz sine wave input.

as a low-pass filter with cutoff at 20 kHz. The THD and maximum power output of this circuit and a number of other circuits designed to reduce the crossover distortion were investigated and are presented in Appendix F. The findings of this investigation were that the circuit in Figure 6.13 gave the best overall performance.

Figure 6.15 shows the simulated frequency response of the high-pass filter and amplifier circuit. The magnitude response is approximately flat over the band of interest and low frequency signals are attenuated, with DC offsets being completely removed and any 50 Hz noise being attenuated by approximately 13.5 dB.

6.3.4 Speakers

As for the receiver, the required spacing between the transmitter speakers was 17 mm. RM-1332-NL speakers from Regal Electronics have a diameter of 13 mm

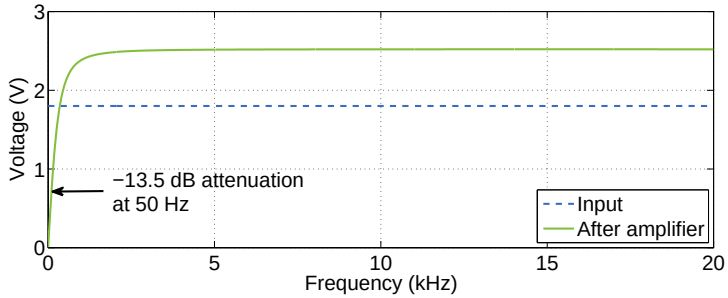

Figure 6.15: Frequency response of the high-pass filter and amplifier circuit as simulated in ORCAD.

and are therefore suitable. The speakers are shown in Figure G.2(d) in Appendix G Their electrical response is:

- Frequency range : 500 Hz to 20 kHz,
- Nominal power input : 0.5 W,
- Maximum power input : 0.8 W,
- Input impedance : 8 Ω,
- Resonant frequency : 1200 Hz.

The impedance of the speakers was measured as a function of frequency by connecting the speaker in series with a resistor $R = 436.5$ kΩ and measuring the input voltage and the voltage across the speaker as the frequency of the applied signal was increased. This setup is illustrated in Figure 6.16. The speaker impedance, Z is calculated by

$$V_{out} = \frac{R}{R+Z} V_{in}. \tag{6.7}$$

Figure 6.17 shows the impedance of the speaker across its rated frequency range. A spike in the impedance is observed at around 1.1 kΩ. This confirms that the resonant frequency of the speaker is in the region of 1.2 kHz as stated in the electrical

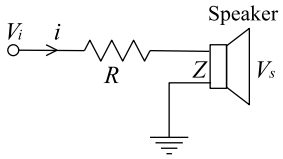

Figure 6.16: Circuit to measure the speaker impedance.

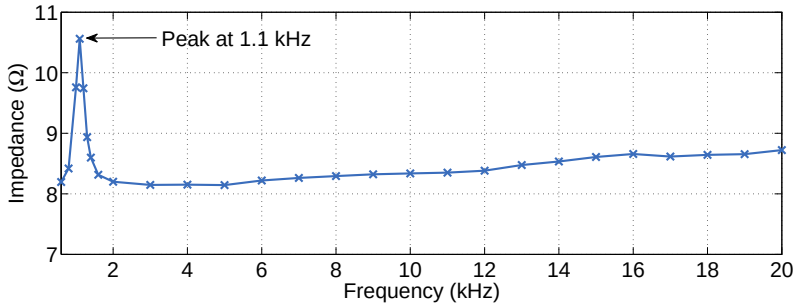

Figure 6.17: The impedance of the speaker as a function of frequency.

characteristics of the speaker. The graph shows that although the impedance of the speaker does vary with frequency, it does not deviate significantly from the 8 Ω input impedance specified on the data sheet.

Using the minimum value of this impedance over the frequency range of interest, which is approximately 8 Ω, the maximum RMS voltage that can be applied to the speakers is

$$V = \sqrt{P_{max} Z} = \sqrt{0.8 \times 8} = 2.52 \text{ V}. \tag{6.8}$$

Figure 6.18 shows a characterisation of the speakers. It was difficult to obtain an accurate characterisation, since a microphone was required to record the signal transmitted by a speaker. Therefore, the response of the speaker and the microphone are determined as a pair. The measurements shown in Figure 6.18 were taken by connecting a RM-1332-NL speaker to a PC and transmitting a chirp signal which was recorded with a F6035AU microphone. The chirp signal frequency was swept linearly from 600 Hz to 20 kHz in a time of 100 ms, covering the full specified frequency band of the speaker. The characterisation graph was obtained by taking a fast Fourier transform (FFT) of the received audio signal and plotting the result in decibels. A sample rate of 44.1 kHz was used. The response is not very flat, and peaks at approximately 8.5 kHz.

Over the chosen frequency band of 8 kHz to 12 kHz, the frequency response of the speaker-microphone pair varies by over 5 dB. This is significantly more than desired. However, provided that the variation is the same from channel to channel, it does not affect the array performance significantly. After construction, the frequency response of each of the channels was tested and calibrated to compensate for differences where necessary.

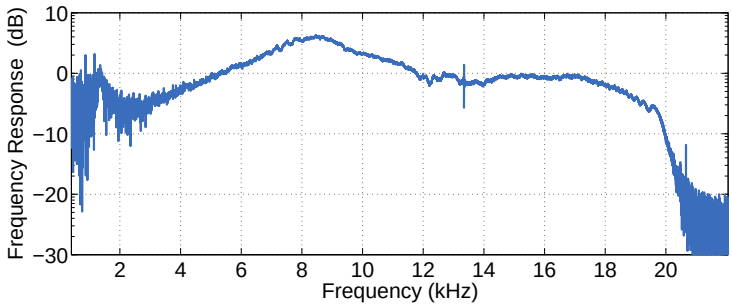

Figure 6.18: The frequency response of a typical microphone-speaker pair.

6.3.5 Transmitter Board Power Supply

The transmitter board power supply is shown in Figure 6.19. The voltages were fed onto the transmitter analogue PCB where the capacitors were placed. The 5 V V_{CC} supply was shared with the receiver board power supply. As for the 5 V supply, a 2200 μF capacitor was also soldered directly across the -5 V V_{EE} supply.

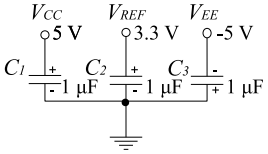

Figure 6.19: Transmitter power supply.

6.4 Master Control Unit (MCU)

The MCU was implemented on an FPGA. Its primary responsibilities are to synchronise the transmitter and the receiver and to interface a PC to the transmitter and receiver analogue electronics. Figure 6.20 is a block diagram of the hardware system, highlighting the communications interfaces of the MCU. It is connected to a PC by Ethernet, and to the ADC and DAC of the receiver and transmitter respectively by SPI. In the sections below, the MCU architecture and the functions that it performs are described.

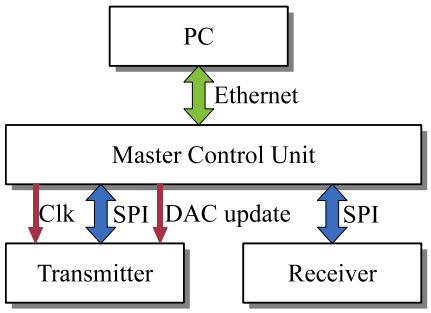

Figure 6.20: MCU interfaces to a PC, transmitter and receiver.

6.4.1 MCU Platform

A Xilinx Virtex 5 XC5VLX50T-1FFG1136 on an ML505 evaluation platform [57] was used to implement the MCU. A photograph of the ML505 is included in Figure G.1 in Appendix G. Many features were available on the platform, including a tri-speed Ethernet PHY transceiver that supports MII, GMII, RGMII and SGMII, which eased the development of the MCU.

The software packages used for developing the MCU are included in the Xilinx ISE Design Suite 10.1 and are:

- Xilinx ISE Version 10.1i for coding the VHDL modules,
- Xilinx Platform Studio (XPS) Version 10.1 (nt) for generating and instantiating the system and
- Xilinx Platform Studio (XPS) Software Development Kit (SDK) Version 10.1.0 for writing the software.

6.4.2 MCU Architecture and Modules

The system architecture is illustrated in Figure 6.21. A MicroBlaze processor was instantiated on the FPGA and was used to control four peripheral Intellectual Property (IP) modules which are responsible for Ethernet and SPI communications and the visual interface. A low level description of the MCU architecture is given in Appendix I.1 and each module is described in more detail in the sections below.

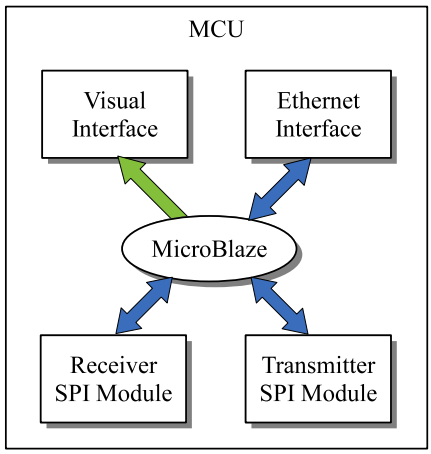

Figure 6.21: Top level MCU modules.

6.4.2.1 Visual Interface Module

The visual interface module allows the internal state of the FPGA to be easily displayed. Text indicating whether tasks performed by the MCU are a success or failure is displayed on the LCD screen. The code used to display text on the screen is heavily based on that by Johnson [58]. In addition, LEDs form part of the visual interface module, and are flashed by the various IPs to indicate their internal state.

6.4.2.2 Ethernet Interface

Figure 6.22 explains the Ethernet communications between the MCU and the PC. The PC transmits signals to the MCU, which are then sent to the DACs of the transmitter board to be transmitted on the speakers. The MCU sends the received data from the receiver ADC back to the PC where it is processed.

Only the Ethernet transmission of the received radar signals from the MCU to the PC was implemented, although simple tests of Ethernet reception on the FPGA

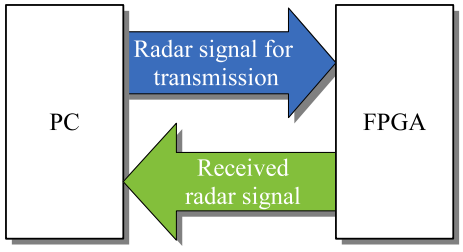

Figure 6.22: Ethernet interface.

were successful. The PC to MCU Ethernet connection was bypassed by storing the signals for transmission in the MicroBlaze application as static variables.

C code was written for the PC to receive the Ethernet packet, and is described in Section 6.5. The implementation of the Ethernet interface on the FPGA is described in detail in Appendix I.2.

6.4.2.3 Receiver SPI Interface

The FPGA was connected to the receiver's ADC with a standard SPI interface. It requires four connections between the MCU and the receiver which are shown in Figure 6.23. The SPI interface allows the MCU to receive signals from the 16 receiver channels in digital form. This data is received as a serial stream of 16 bit words, consisting of 4 bits specifying the channel, and 12 bits giving the voltage reading on that channel. This data is then transmitted by Ethernet to the PC for further processing.

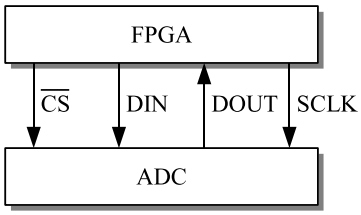

Figure 6.23: SPI interface between FPGA and receiver.

The maximum SPI clock frequency of the ADC is 20 MHz and was chosen as the receiver SPI clock frequency. SCLK (Serial Clock) period T_{SCLK} is therefore 50 ns and the time to sample one channel is

$$T_{channel} = 16 \times T_{SCLK} = 800 \text{ ns}. \tag{6.9}$$

Also, the ADC requires a "quiet time" of at least 50 ns between conversions. Consider having a "quiet time" of two clock cycles. Therefore, the minimum time in which all 16 channels can be sampled is

$$T_{all} = (T_{channel} + 2T_{SCLK}) \times 16 = 14.4 \ \mu\text{s}. \tag{6.10}$$

This gives a maximum sampling frequency for each channel of

$$f = \frac{1}{T_{all}} = 69.4\,\text{kHz}\,. \tag{6.11}$$

This sample time could not be realised because the FPGA has tasks to perform in between sampling. It firstly transfers each sampled value to a data structure that can be transmitted by Ethernet after each channel has been sampled. After all 16 channels have been sampled, the set of data for the channel is transmitted by Ethernet to a computer. Therefore, due to these added operations, the maximum sampling frequency that could be achieved was 40 kHz.

The SPI read and write cycles are controlled by a VHDL module which was added as a peripheral to the MicroBlaze processor. A detailed description of the receiver SPI read and write process, and the implementation of the VHDL module which controls them is given in Appendix I.3.

6.4.2.4 Interface between Transmitter and MCU

The connections between the transmitter and the MCU are shown in Figure 6.24. The connections CS (Chip Select), DIN (Data In) and SCLK make up the SPI connection between the FPGA and the DAC, and are duplicated for the two 8 channel DACs. The connection $\overline{\text{LDAC}}$ (Load DAC) is a connection between the FPGA and DAC and carries the instruction for the DAC outputs to be updated on the pins. FCLK is the clock signal for the reconstruction filters.

Both DAC's are controlled in parallel. SCLK is driven at the maximum specified frequency of 15 MHz which gives a period T_{SCLK} of 66.7 ns. The time to load data into the conversion register for one channel is therefore

$$T_{channel} = 16 \times 66.7 = 1.067\ \mu\text{s}. \tag{6.12}$$

The maximum sampling frequency, taking into account the "quiet time" between

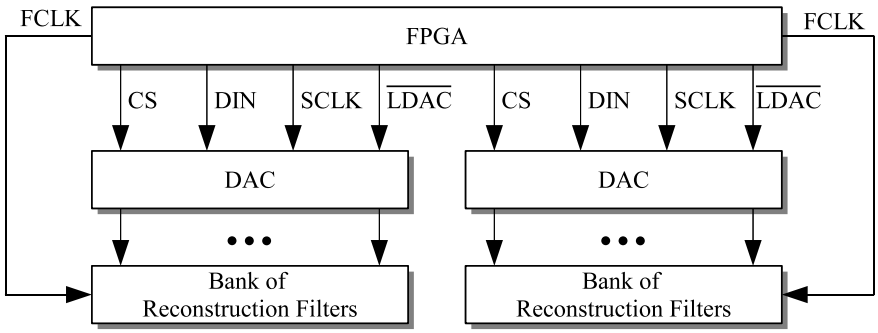

Figure 6.24: Connections between MCU and transmitter.

transmissions when CS is low (T_{CS}), is

$$f_{max} = \frac{1}{(8)(T_{channel} + T_{CS})} = 115 \text{ kHz}, \tag{6.13}$$

Because the receiver uses a sampling frequency of 40 kHz, this is chosen as the transmitter sampling frequency too. Therefore, although all of the DAC conversion registers are loaded much faster, the channels are only updated at the sampling frequency controlled by driving $\overline{\text{LDAC}}$ with a 40 kHz clock. The DAC conversion registers are only updated again, after the $\overline{\text{LDAC}}$ clock has been driven low. FCLK is the clock for the switched capacitor reconstruction filter. As described in Section 6.3.2, this clock requires a frequency of 1.5 MHz which can be obtained by dividing down the 15 MHz SPI clock. It is important that the DAC clock and the filter clock are synchronised to prevent beat frequencies which can alias into the passband.

The required SPI operation for the transmitter, as well as the VHDL module which controls it are described in Appendix I.4.

6.5 The PC

The PC is used to receive data from the hardware system, to perform signal processing, and to display the results. The task of receiving Ethernet packets from the FPGA is implemented with a C application. The signal processing is all performed in MATLAB. The C and MATLAB applications are described below.

6.5.1 C Application to Receive Ethernet Packets

The library WinPcap [59] was used by the application to receive Ethernet packets sent by the FPGA. The example file `basic_dump` can receive packets from any of the network interface devices on a PC and is part of the WinPcap download. It was used as a base for the C application, and extended to perform the required functions.

The application receives N (which can be adjusted depending on how many samples are required) packets, and writes them to a file `ReceivedData.txt` in hexadecimal format. Each packet has the form of the transmitted packet shown in Figure I.2 but the Preamble and start of frame delimiter (SFD) are removed by the Ethernet MAC on the PC and replaced by a single byte. Also, the cyclic redundancy check (CRC) is automatically removed by the PC's Ethernet MAC.

Once all of the packets transmitted by the FPGA have been received, the application decodes the packets. The application reads one line of the `ReceivedData.txt` file at a time. First, it checks that the first two bytes of the destination address are correct to confirm that the received packet was sent by the FPGA to the PC, and is not a generic communications packet. The first 30 characters, which represent the device addresses and data length field are then ignored. Starting from the 31st character, the text symbols are converted into the decimal numbers that they represent. Every fourth symbol represents a channel and the following three symbols represent the ADC conversion value for that channel. Therefore, if a symbol corresponds to a channel number i, the corresponding file for that channel `outi.txt` is opened. The decimal conversion of the following three symbols is then written into the file.

The above application is illustrated in the flow chart in Figure 6.25. 16 text files are generated by running the application and they are processed by MATLAB from this point onwards.

6.5.2 MATLAB Application for Signal Processing

Many different MATLAB applications were required, depending on whether the array was used in phased array or MIMO radar mode, and whether calibration, beampattern measurements or target detection was being performed. However, regardless of the final purpose, there are functions common to all of the applications that will be described here.

The MATLAB application reads the 16 files representing the 16 received signals into a vector $\mathbf{x}_i$. Each vector element, which is the decimal representation of the 12 bit ADC code of the received signal is scaled to represent the measured voltage by

$$\mathbf{x}_i = 5\frac{\mathbf{x}_i}{2^{12}}. \tag{6.14}$$

It is then centred around zero by

$$\mathbf{x}_i = \mathbf{x}_i - \text{ave}(\mathbf{x}_i). \tag{6.15}$$

The vectors are then combined as the rows of a matrix $\mathbf{X}$ containing all of the received signals.

The signal matrix is filtered by an eighth order Butterworth band-pass filter with a lower cutoff frequency at 7.6 kHz and an upper cutoff frequency at 12.4 kHz to remove any noise outside the band of interest. If calibration is being performed, or

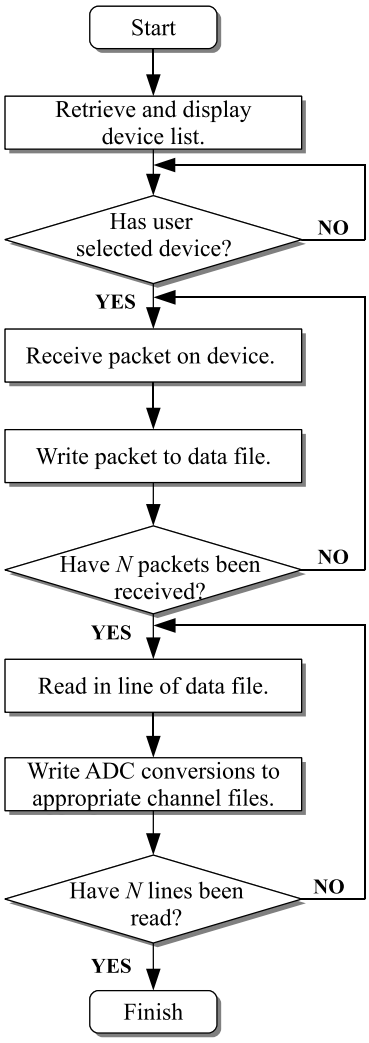

Figure 6.25: Flowchart of the C application to receive and process data sent from the FPGA to a PC.

beampatterns are being plotted, no more processing is performed. If target parameter estimation is being performed, the signal is filtered by a Hilbert filter before demodulation. In addition, the signal is filtered by an eighth order Butterworth low-pass filter with a cutoff frequency at 2.2 kHz.

Finally, due to the sampling error introduced by the ADC and described in Section 6.2.5.1, correction is implemented. The signal on each channel is up-sampled by a factor of 16, and then re-sampled with an appropriate delay to remove the effect of the ADC sampling.

The power received on a single receiver can then be calculated to plot the beampattern, or receiver calibration can be performed and the radar algorithms can be applied to the data matrix $\mathbf{X}$ just as they were applied to simulated data.

6.6 Summary

In this chapter, the design of the hardware system was specified. The receiver array and electronics were mostly designed by Stanton [8], and this design was summarised together with descriptions of the added amplifier stage. The transmitter array and electronics were designed from scratch, and the final design of all components was given in this chapter, with reference to the appendices. An MCU was also implemented on an FPGA, to control the receiver and transmitter and allow communication between them and a PC. An overview of the MCU realisation was given. The theory and hardware have now both been presented. In the following chapter, the calibration and tests applied to the hardware, based on phased array and MIMO theory, are introduced.

Chapter 7

System Calibration and Testing

In this chapter, the methods used to calibrate and test the hardware system are introduced and explained. Test protocols for the application of these methods are also presented.

7.1 Calibration

The operation of a phased array or MIMO radar relies on the intricate relationship of phase between the array channels. The phase differences, which can be exploited to perform beamforming, occur because of the spatial separation of the channels. Information about the radar's environment, such as the location and properties of any targets present, is then extracted from the received signals.

Therefore, to obtain accurate results from a radar system, it is important that the amplitude, and in particular, the phase responses of each transmitter and receiver element, are as close to identical as possible, across all frequencies of interest. Slight amplitude and phase differences arise mainly due to tolerances on the components making up the transmitter and receiver amplifiers, filters, and speakers and microphones, as well as PCB layout and cables. Therefore, it is necessary to have a technique to measure the response of each channel on the transmitter and receiver, and to calibrate each channel to compensate for any variations.

In the sections below, a study on the necessity of calibration is presented. Methods which can be used to calibrate phased array transmitters and receivers are then introduced. Finally, a calibration protocol to be used on the hardware transmitter is defined.

7.1.1 The Effect of Calibration Errors

Before a method of calibration was selected, simulations were performed to analyse how calibration errors effect the performance of an array antenna. To illustrate the effect of amplitude and phase errors between channels, the beampattern of a 16 element beamformer was simulated over the interval $-90°$ to $90°$ in increments of $5°$, in the presence of random amplitude and phase calibration errors of varying magnitude. The mean absolute deviation, and the maximum absolute deviation of each pattern with calibration errors from the ideal pattern was then calculated.

Table 7.1 shows the deviations in the normalised beampattern due to random amplitude variations between 0% and α% for 100 trials. Also, Figure 7.1 shows an example of a beampattern obtained (simulated in increments of $1°$) when the amplitude varies randomly between 0% and 100% of the maximum. It can be seen that even with large variations in the transmitter amplitudes, the width of the main lobe is maintained, although the side lobe levels are slightly elevated.

Table 7.1: The average and maximum absolute beampattern deviation for random variations in the amplitude of phased array elements of up to α% when a phased array beam is steered to $40°$.

α	*Average Deviation*	*Maximum Deviation*
50	0.0072	0.0243
100	0.0452	0.1452

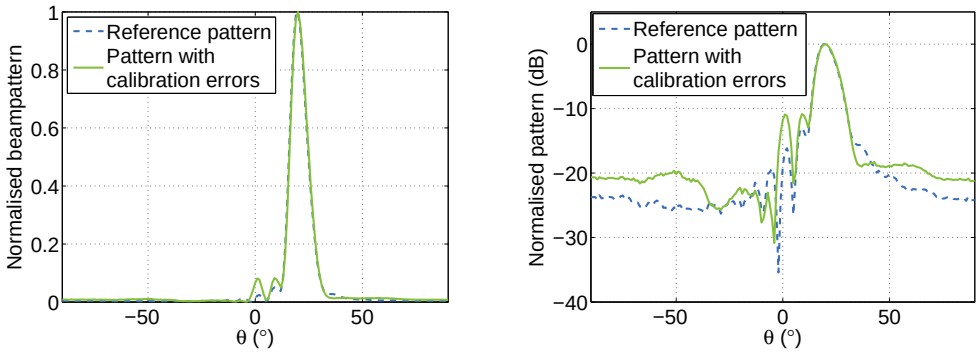

(a) Linear beampattern.

(b) Beampattern in decibels.

Figure 7.1: Ideal beampattern and that obtained with a random amplitude variation of up to 100% of the maximum on each transmitter channel when the beam is steered to $20°$.

Figure 7.2 shows the simulated beampatterns obtained when phase calibration errors are present in the phased array. In Figures 7.2(a) and 7.2(b), when the phase varies up to a maximum of $\pm 5^\circ$, the beampattern is only slightly affected in the side lobes. However, when phase calibration variations up to $\pm 20^\circ$ are present, as shown in Figures 7.2(c) and 7.2(d), the beampattern consistently becomes heavily disfigured, with false peaks forming.

Figure 7.3 shows the maximum and average absolute deviations from the ideal beampattern for 100 trials, as the phase calibration error varies randomly to a positive or negative maximum marked on the x-axis when a phased array pattern is steered to 0° and 40°. The ideal pattern and the pattern obtained with calibration errors are both normalised and therefore their magnitudes vary between 0 and 1. When the phase error varies to a maximum of $\pm 8^\circ$, the average pattern deviation is already 10%, and calibration becomes necessary. Also, the further that the beam is steered from 0°, the larger the errors caused by calibration.

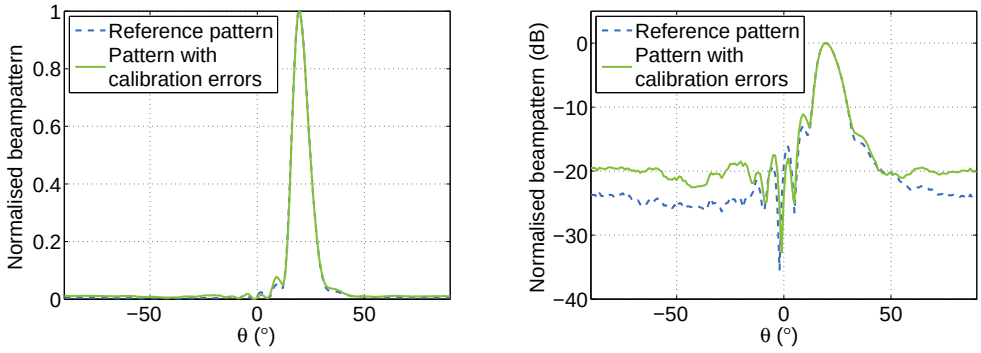

(a) Linear beampattern with phase calibration error varying randomly between $\pm 5^\circ$.

(b) Beampattern in decibels with phase calibration error varying randomly between $\pm 5^\circ$.

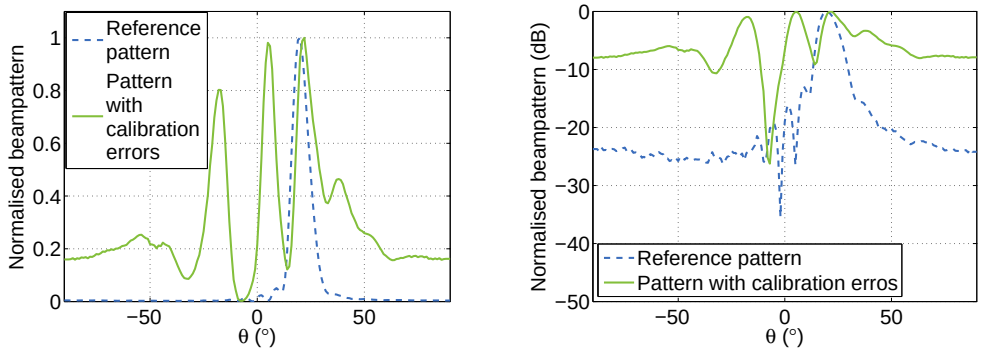

(c) Linear beampattern with phase calibration error varying randomly between $\pm 20^\circ$.

(d) Beampattern in decibels with phase calibration error varying randomly between $\pm 20^\circ$.

Figure 7.2: Ideal beampattern and that obtained with phase calibration errors when a phased array beam is steered to 20°.

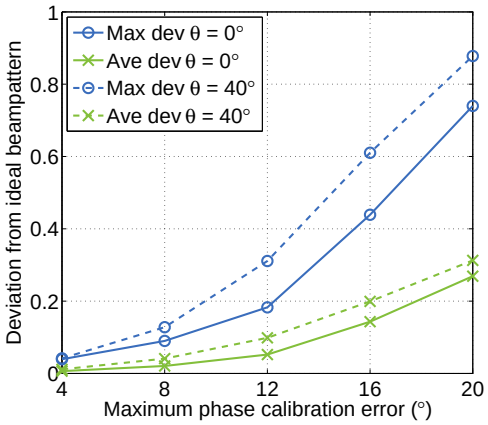

Figure 7.3: Average and maximum pattern deviation as a function of maximum phase variation for a phased array beam steered to 0° and 40°.

These results illustrate that variations in the amplitude response have little effect on the beampattern generated by an array. Amplitude variations are still undesirable, as maximum SNR can only be achieved when all of the speakers transmit at maximum amplitude which is the same across all elements. If the phase varies slightly, the deviation in the beampattern from the ideal is also small. However, for large phase variations, calibration becomes critical, to avoid immense distortion of the array's beampattern. As a result of this investigation, calibration will only be performed to equalise the phase response across all of the transmitter and receiver channels.

This investigation into the effect of calibration errors was performed in the narrowband domain. In the wideband case, the amplitude and phase response of the array elements has an extra degree of freedom and can potentially vary across the frequency band of interest from channel to channel. Therefore, in performing calibration, a method to equalise the channels over frequency is required if the frequency response varies from channel to channel. Two calibration methods are presented in the sections below.

7.1.2 FIR Filter Calibration Method

Consider a receiving array. When a signal from a point source at 0° in the far-field of the array is received, the signal on each channel should be in phase across the whole frequency band of interest. This is since the path length travelled by the signal received on each element is approximately equal. If the received signal is

not in phase on any channel and at any frequency, this can only be due to variable phase responses on the receiving elements of the array. The phase response can be corrected by selecting a single channel as a reference, and applying an FIR filter to each of the remaining channels, to match the phase to that on the reference channel.

To synthesize a suitable FIR filter for each channel, the signal received by each of the receiving elements is measured when sinusoidal signals, at a selection of frequencies across the band of interest, are transmitted. The signals received from transmission of all the transmitted sinusoids is combined into one signal per channel. An FIR filter is then designed for each channel (excluding the reference channel) such that the output approximates the desired signal on the reference channel, in an LS sense.

This method is more suited to the receiver, but can be extended to the transmitter if a single receiver, located in the far-field of the transmitter array at location 0°, receives the signals from each of the transmitters which transmit individually. The phase-correcting FIR filters for each of the transmitter channels can then be generated. These can then be applied to the transmitter signals before transmission.

7.1.3 Transmitter Beampattern Calibration Method

Consider a transmitting array. The sole reason for using an array to transmit in a radar system is so that beamforming can be performed and power can be transmitted in the directions in which it is desired, and not in those where it is not desired. Therefore, the performance of a transmitting array can be graded by evaluating the accuracy with which the measured pattern matches the theoretical pattern.

If phase errors are present in the transmitter, then the beampattern deviates from the ideal pattern as shown in Section 7.1.1. By matching a simulated beampattern to the measured beampattern with the addition of phase shifts to each channel, the calibration error on each channel can be found. The error can then be compensated for. This method is not a wideband method, as a single phase shift independent of frequency is used to correct each channel. However, if the deviation in frequency across the channels is not large, this method can still be used for successful calibration of the transmitter array.

Consider the measured pattern given by P_m, and the simulated pattern P_s. Then, the phase shift vector $\boldsymbol{\phi}$ containing elements representing the phase shift ϕ_i on the

i^{th} channel can be found by

$$\min_{\phi} \frac{1}{K}(P_m - P_s)^2 \tag{7.1}$$

where K is the number of points at which the pattern is defined.

P_s is calculated from $\bar{\mathbf{S}}$ which has rows $\bar{\mathbf{s}}_i = \mathrm{e}^{j2\pi\phi_i}\,\mathbf{s}_i$ and $\mathbf{s}_i$ is the ideal transmitted signal.

Compensation for the phase shifts can then be performed to obtain the calibrated signals for transmission by the multiplication

$$\tilde{\mathbf{s}}_i = \mathrm{e}^{-j2\pi\phi_i}\,\mathbf{s}_i. \tag{7.2}$$

7.1.4 Calibration Test Protocol

The protocol to test the uniformity of the phase of the transmitter and receiver arrays and calibrate the elements, if necessary, is detailed below. The FIR filter method is the preferred method for calibration. However, if it does not result in successful calibration of the transmitter array, the beampattern phase calibration method is used.

Protocol 1: Receiver Calibration

1. The receiver array is placed at one end of an anechoic chamber. A single transmitter is placed at the opposite end, a distance of 4.5 m from the receiver array. This setup ensures that the transmitted signal is received by the array 13.1 ms after transmission starts and therefore 3.1 ms after transmission ends. Also, it ensures that the receiver is in the far-field of the array, by the definition given in Section 2.1.3, which evaluates to a far-field distance of $D \geq 3.8$ m. See Figure 7.4 for this setup.
2. The transmitter transmits a 10 ms snippet of an 8 kHz sinusoidal wave.
3. As soon as transmission is complete, the receiver array measures the 16 received signals for a duration of 20 ms and sends them to the PC over Ethernet.
4. Steps 2 and 3 are repeated for sinusoidal signals of frequencies 9 kHz, 10 kHz, 11 kHz and 12 kHz.
5. The set of signals is scaled, shifted, demodulated and filtered and compensation for the ADC sampling delay is performed as described in Section 6.5.2. The received signals are plotted.

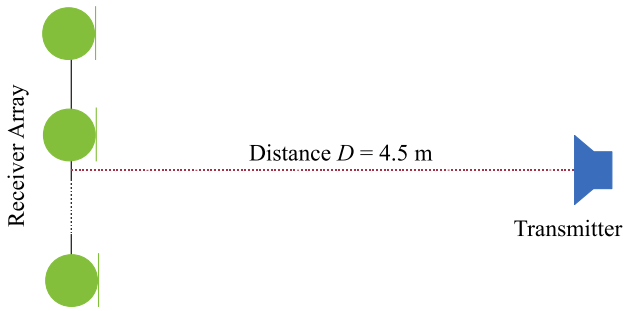

Figure 7.4: Experimental setup for receiver calibration.

6. In the case that the phase responses do not deviate significantly from channel to channel, calibration is not required and steps 6 and 7 are ignored. Else, calibration should be performed and the subsequent steps followed.

7. FIR filter phase calibration is performed, as outlined in Section 7.1.2.

8. The signal received on each channel is filtered by the appropriate FIR filter determined in Step 6 for all tests to follow.

Protocol 2: Transmitter Calibration

1. The transmitter array is placed at one end of an anechoic chamber. A single receiver is placed at the opposite end, a distance of 4.5 m from the transmitter. As for the receiver, this results in the signal being received 13.1 ms after transmission starts, and ensures that the receiver is in the far-field of the array. See Figure 7.5 for this setup.

2. The first transmitter transmits a 10 ms snippet of an 8 kHz sinusoidal wave.

3. As soon as transmission is complete, the receiver measures the received signal for a duration of 20 ms and sends it to the PC over Ethernet.

4. Steps 2 and 3 are repeated for sinusoidal signals of frequencies 9 kHz, 10 kHz, 11 kHz and 12 kHz.

5. Steps 2, 3 and 4 are repeated for the other 15 transmitter elements.

6. The set of signals is scaled, shifted, demodulated and filtered as described in Section 6.5.2 and plotted.

7. In the case that the phase responses do not deviate significantly from channel to channel, calibration is not required and Steps 8 to 11 are ignored. Else calibration should be performed and the subsequent steps followed.

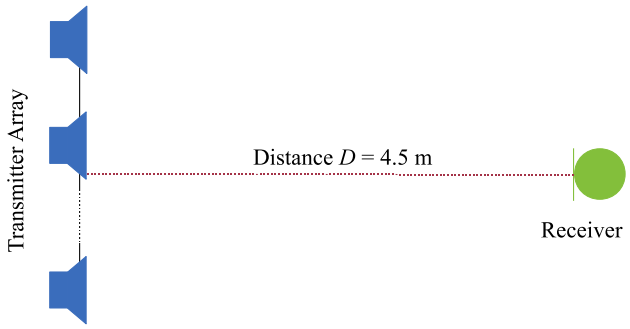

Figure 7.5: Experimental setup for transmitter calibration.

8. FIR filter phase calibration is performed, as outlined in Section 7.1.2.

9. In the case that calibration corrects the phase deviations between channels sufficiently, calibration is complete and all signals to be transmitted are first filtered by the appropriate FIR filter. Else, Steps 10 to 12 are followed.

10. A beampattern is transmitted as described in Protocol 3 for beampattern testing.

11. If the measured pattern deviates significantly from the theoretical and simulated patterns, beampattern phase calibration is performed, as outlined in Section 7.1.3.

12. In further tests, the ith signal is multiplied by the phase factor ϕ_i calculated in Step 11 before transmission.

7.2 System Testing

The aim of the project was to compare MIMO radar algorithms to traditional phased array algorithms. Two main aspects were of interest. The first, is the design of beampatterns. Phased array beamforming methods and MIMO beampattern design methods will be tested so that an analysis of the two techniques can be performed. Secondly, target parameter identification is of interest. The range of targets will be estimated by cross correlation and compared when the system operates in phased array and MIMO configuration. Also, different techniques for target angle detection that can be applied to phased array and MIMO systems will be tested so that the results can be compared to one another to determine if MIMO processing methods offer benefits over phased array methods.

7.2.1 Beampattern Design

Three test scenarios were developed to test and compare phased array beamforming to MIMO beampattern design. The beampatterns of interest, are an omnidirectional pattern, a pattern with a single main lobe, and a pattern with multiple mainlobes.

For all of the beampatterns, the baseband signal bandwidth is 2 kHz, giving a passband bandwidth of 4 kHz. The transmitted signals are of duration 10 ms, which at a sample frequency of 40 kHz, gives $N = 400$ samples. The MIMO signals are composed of 40 QPSK symbols. A Nyquist filter is used to interpolate the signals to increase the number of samples to the required 400 as in the simulations in Section 5.5.2 .

A phased array is not capable of transmitting an omnidirectional pattern. Therefore, only the MIMO transmitter configuration is used to test an omnidirectional pattern. The theoretical pattern, obtained with the set of experimental signals is shown in Figure 7.6.

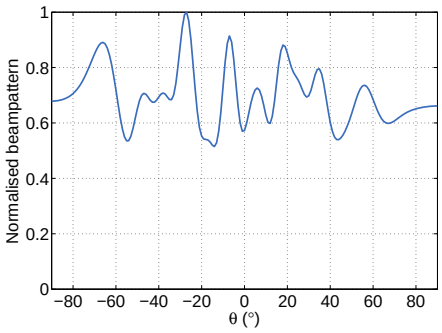

Figure 7.6: MIMO omnidirectional pattern generated with 16 MIMO signals of 40 symbols and 400 samples.

For the second scenario, a pattern with a single main lobe in the direction 20° is generated for a phased array system and a MIMO system. This experiment is of importance to test if MIMO beamforming techniques can deliver as much power in a required direction, when compared to phased array beamforming techniques. Therefore, the measured received power will be analysed. Three beampatterns are generated for this experiment. The first is a phased array pattern, where the signal on each channel is delayed so the combined pattern has a main lobe at 20°. The other two beampatterns are MIMO patterns generated by Pascale's design described in Section 4.2.3.3 and the beampattern matching design introduced in Section 2.9.3.

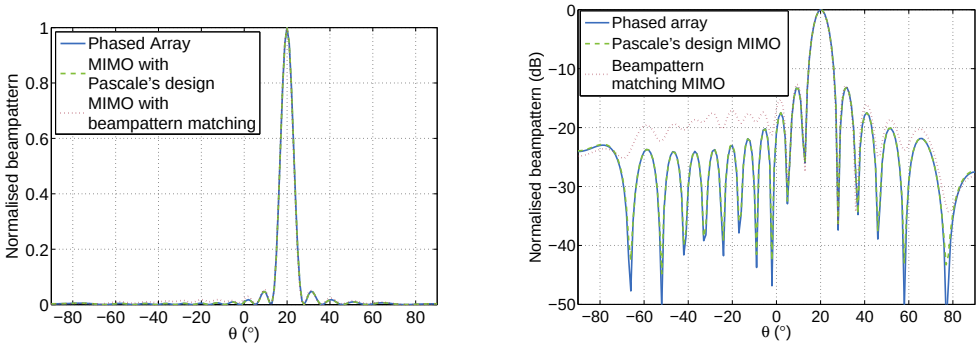

(a) Patterns. (b) Patterns in decibels.

Figure 7.7: Normalised beampatterns with mainlobes at 20° generated with 16 signals with phased array and MIMO techniques. Each signal has 400 samples, and each MIMO signal is generated from 40 symbols.

All three theoretical patterns are shown on a linear axes in Figure 7.7(a) and in decibels in Figure 7.7(b).

Finally, beams with multiple side lobes are tested in the last scenario. The desired beampattern has mainlobes at $-20°$, $0°$ and $20°$. Two phased array beamforming techniques, the LCMV technique and the beampattern matching technique, which are presented in Section 4.1.3, are used. The MIMO beampatterns are generated using Pascale's design and the beampattern matching technique. The four beampatterns are shown in Figure 7.8(a) on a linear axes and in Figure 7.8(b) in decibels.

The test protocol, to measure the beampatterns is the same for all of the patterns, and is described below.

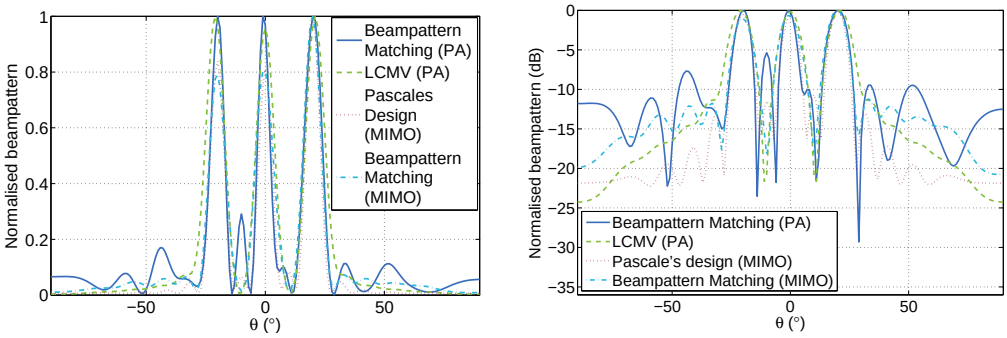

(a) Patterns on linear axes. (b) Patterns in decibels.

Figure 7.8: Normalised beampatterns with mainlobes at $-20°$, $0°$ and $20°$ generated by 16 signals with phased array and MIMO techniques. Each signal has 400 samples, and each MIMO signal is made up from 40 symbols.

Protocol 3: Beampattern Measurement

1. As for the transmitter calibration experiment, the transmitter array is placed at one end of an anechoic chamber. A single receiver is placed at the opposite end, a distance of 4.5 m from the transmitter array so that it is in the far-field. See Figure 7.5.

2. The transmitter array is rotated to point in direction $-90°$. Angles are defined in Figure 7.9.

3. The transmitter array transmits a set of signals of duration 10 ms which have been chosen to give the desired beampattern.

4. As soon as transmission finishes, the receiver measures the received signal for a duration of 20 ms and sends it to the PC over Ethernet.

5. The power of the received signal is calculated, after the signal has been scaled, shifted, demodulated and filtered as detailed in Section 6.5.2.

6. The array is rotated in increments of 5° up until 90° and steps 2 to 5 are repeated at each angle.

7. The measured beampattern is determined by plotting the power calculated in step 5 against the array angle.

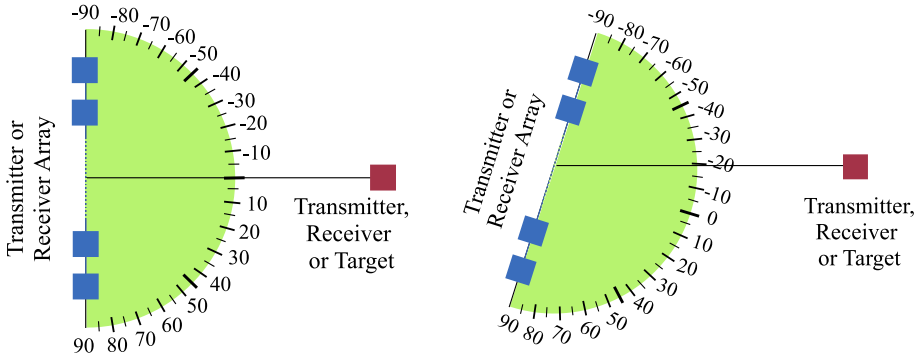

(a) Target at 0° relative to the array. (b) Target at $-20°$ relative to the array.

Figure 7.9: Definition of the array DOA angles.

7.2.2 Target Parameter Estimation

Three experiments were designed to characterise the performance of the phased array and MIMO systems in terms of target angle and range detection. The complex amplitude of the target is not of interest in these experiments, as no method is available for determining the true β-value of the targets for comparison to the estimated values. The experiments test the parameter estimation in the presence of one target, three targets, and two closely spaced targets. The beampatterns measured in the above section are the same beampatterns which are transmitted to investigate target parameter estimation. Each of the experimental scenarios is described below.

For the first experiment, a single target is placed at an angle of 20° relative to the arrays, as shown in Figure 7.10. Four tests are performed in this configuration. Firstly, target angle and range detection is performed with a phased array system and with beamforming on the transmitter so that the main lobe is centred at 20°. For the other three tests, MIMO target parameter estimation techniques are applied to the received signal when an omnidirectional MIMO beampattern and MIMO patterns with a single main lobe at 20° designed by Pascale's design and the beampattern matching design are transmitted. See figures 7.6 and 7.7 for the omnidirectional and directional patterns respectively.

This test is primarily included to evaluate the performance of the phased array, which should perform well under these conditions. It will also indicate if MIMO can offer any improvements to phased array, when only one target is present.

The second experiment requires that 3 targets are placed at −20°, 0° and 20° relative to the arrays as illustrated in Figure 7.11. Then parameter identification techniques are performed when the phased array transmitted signals are those determined by

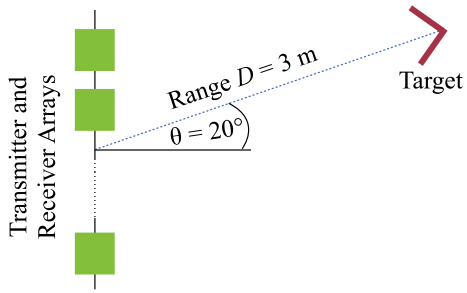

Figure 7.10: Experimental setup with a single target.

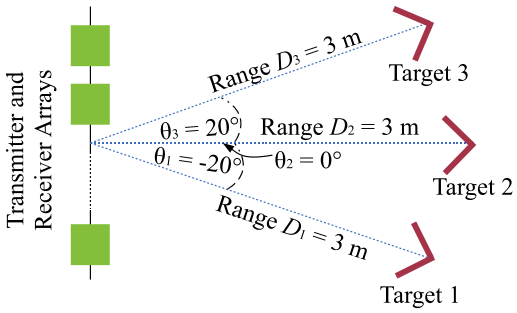

Figure 7.11: Experimental setup with three targets.

the beampattern matching design and the LCMV to have mainlobes pointing at the three targets as shown in Figure 7.8. MIMO target parameter estimation is applied when an omnidirectional pattern (Figure 7.6), a pattern with mainlobes in each of the target directions designed by Pascale's design and another designed by the beampattern matching design (Figure 7.8) are transmitted.

This experiment pushes the boundaries of how phased array is usually used. When phased array signals are transmitted, there is a risk that the reflections received from the targets will be coherent. In particular, since the path distance from the targets at $-20°$ and $20°$ to the centre of the array will be equal, the echoes will be coherent if the targets are accurately placed. Three of the four phased array techniques do not perform well when the target echo signals are coherent as discussed in Section 4.1.2 and illustrated in Figure 4.3. Therefore good target angle estimation is not expected from the phased array patterns. In the case of MIMO transmitted signals, the target echoes should be linearly independent, so better estimation is expected.

For the final experiment, the capability of the detection techniques at resolving closely spaced targets is investigated. Therefore, a target is placed at 17°, and a second at 23° as illustrated in Figure 7.12. Target detection is then performed with the four sets of signals used in the first experiment.

Once again, phased array angle detection techniques are not expected to perform well due to the risk of coherence of the transmitted signals. The target echoes received in the MIMO case should again be linearly independent and therefore, better target parameter estimation should be obtained from the MIMO techniques.

The protocol followed for three parameter identification experiments is described below.

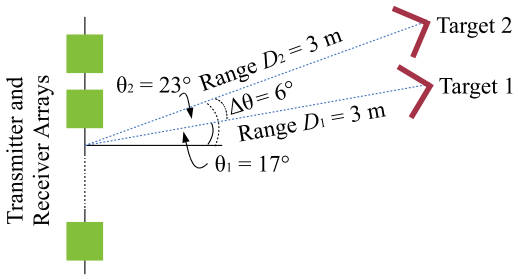

Figure 7.12: Experimental setup with two closely spaced targets.

Protocol 4: Target Parameter Estimation

1. The receiver array is placed above or below the transmitter array, so that the two arrays are as close to co-located as possible. A target or multiple targets is/are placed a distance of 3 m from the arrays at the specified angles. The return signal path from transmitter array to receiver array is therefore 6 m. The setup is illustrated for the three tests in Figures 7.10, 7.11 and 7.12.

2. The transmitter array transmits the specified signals to give a required beampattern, for a duration of 10 ms.

3. Immediately after transmission is complete, the receiver array measures the received signal for a duration of 40 ms and sends it to a PC over Ethernet.

4. Signal processing to scale, shift, filter and demodulate the signal is performed as described in Section 6.5.2.

5. Target range estimation is performed. The method for range detection is described in Section 8.3.1.

6. Target angle estimation is performed. When phased array signals are transmitted, the conventional, Capon, MUSIC and DML techniques, described in sections 2.4.1 and 2.4.2, are used. When MIMO signals are transmitted, the Capon, APES and GLRT techniques, presented in Section 2.8, and TBR presented in Section 2.10 are used.

7.3 Summary

In this chapter, the necessity of calibration was investigated. Simulations showed that amplitude differences between channels have little effect, but that phase differences between channels can lead to significant distortion of the array beampatterns.

Based on this, two methods for calibrating the phase of the arrays were presented, and protocols for transmitter and receiver calibration were specified. Tests to determine the beampatterns that can be transmitted were then defined, and this was followed by tests for phased array and MIMO target detection.

In the chapter that follows, the results of the calibration procedures defined in this chapter are presented. The beampattern and target detection results obtained with the hardware array when the specified tests are performed are also detailed in the following chapter.

Chapter 8

Results and Analysis

This chapter presents the results obtained when the methods described in Chapter 7 were implemented. The results of calibrating the receiver and transmitter arrays are presented first. This is followed by the presentation and discussion of the measured beampatterns. The parameter estimation test results are then included. An analysis of all of the results is given with reference to the simulation results.

8.1 Calibration

Two calibration techniques were introduced in Section 7.1. In this section, the measurements used to determine the calibration errors, and the implementation of the calibration techniques as defined in the protocol in Section 7.1.4 are presented. The improvement offered by calibration is highlighted. Receiver calibration is discussed first, followed by transmitter calibration.

8.1.1 Receiver Calibration

Receiver calibration was performed by the FIR filter calibration technique described in Section 7.1.2. The calibration signal received on one channel is shown in Figure 8.1. This signal was constructed by transmitting five sinusoidal signals at 8 kHz, 9 kHz, 10 kHz, 11 kHz and 12 kHz of 10 ms duration as described in the receiver calibration protocol in Section 7.1.4.

Figure 8.2(a) shows the raw received signal on the 16 receiver channels for the time period 50 to 51.25 ms, which corresponds to a section in the time during which

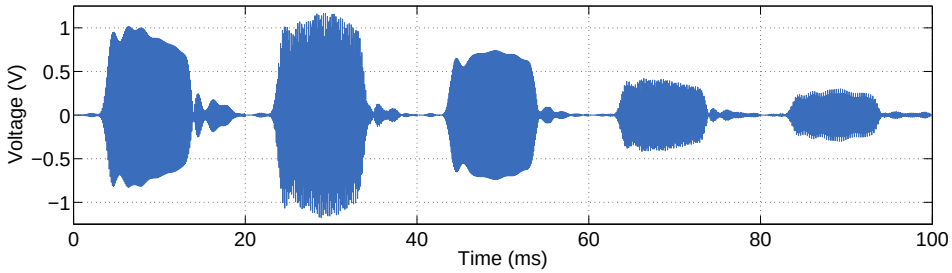

Figure 8.1: The calibration signal received on Channel 1.

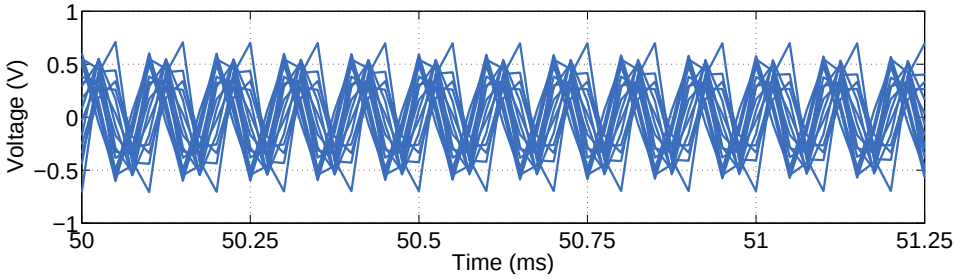

(a) Raw received signals.

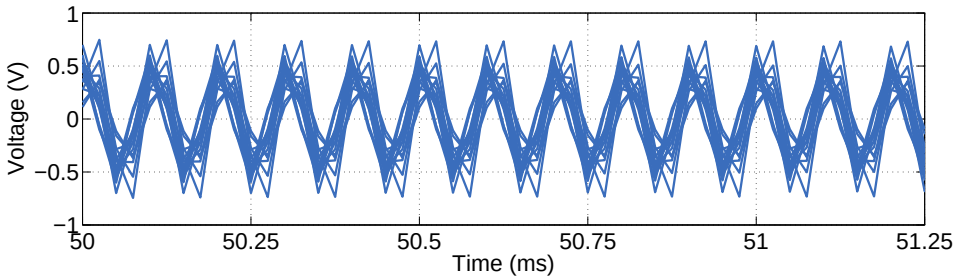

(b) Signals with compensation for sampling delays.

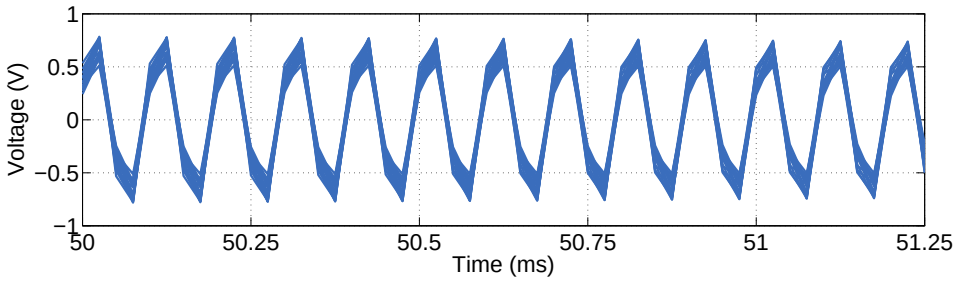

(c) Signals after calibration.

Figure 8.2: A segment of the 16 received signals before and after calibration.

the 10 kHz sinusoidal signal was received. The signals at different frequencies were similar. It can be seen that the phase of the received signals deviates significantly from channel to channel and confirms that calibration is required.

Figure 8.2(b) shows the same 10 kHz signals after compensation for the ADC sampling delays has been performed as outlined in Section 6.2.5.1. The deviation in phase between the different channels is reduced but still varies and can be further improved by calibration.

Figure 8.2(c) shows the same segment of the received signals after calibration has been implemented on each channel. The signals appear to be in phase after being filtered by the appropriate FIR filters with real coefficients.

The magnitude responses and group delays of the FIR filters which were successful in calibrating the receiver are shown in Figure 8.3. The magnitude responses are given in Figure 8.3(a) and the group delays in Figure 8.3(b). In the frequency band of interest between 8 kHz and 12 kHz, the magnitude response varies between -3.5 dB and 6.7 dB. The group delay of the filters varies by less than 4 samples across the frequency band of interest, and illustrates the equalising phase compensation applied to each channel.

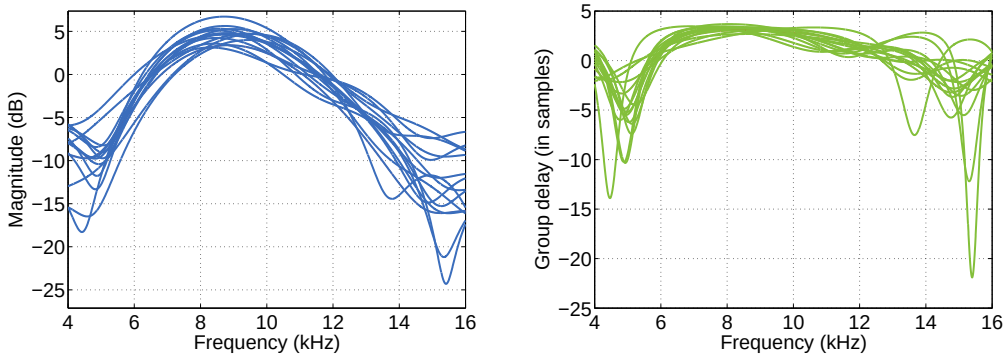

(a) Magnitude responses.

(b) Group delays.

Figure 8.3: Frequency responses of the receiver calibration FIR filters.

To confirm that the calibration technique performed well over the frequency band of interest, it was applied to the received signals when a random signal band-limited between 8 kHz and 12 kHz was transmitted. Figure 8.4(a) and Figure 8.4(b) show the same segment of the 16 received signals before and after the application of the FIR calibration filters respectively. The narrower line of the signal after calibration shows that the phase deviations between the different receiver channels was reduced and

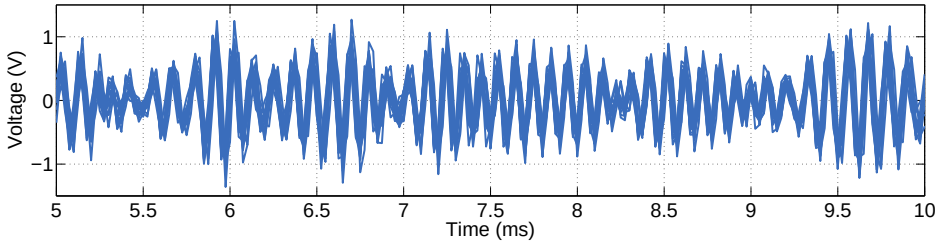

(a) Before calibration.

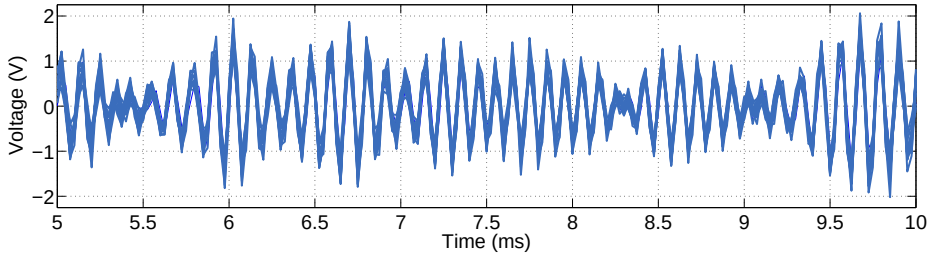

(b) After calibration.

Figure 8.4: An 8 kHz to 12 kHz band-limited random signal received on the 16 receiver channels.

therefore, the calibration technique does improve the response of the system. Similar results were obtained when an 8 kHz to 12 kHz chirp signal was transmitted and receiver calibration was performed. Therefore, the calibration of the received data using the FIR filter method successfully compensates for phase variations present between channels.

8.1.2 Transmitter Calibration

The transmitter was more difficult to calibrate than the receiver. Initially, the FIR filter method was used, as defined in the protocol in Section 7.1.4. After the poor performance of the FIR filter method, the beampattern calibration method was applied. In the sections below, a description of the results of the two calibration techniques, and the results of an investigation into the reasons for the poor response of the transmitter to calibration are given.

8.1.2.1 FIR Filter Calibration

The 16 received signals which were constructed from the individual transmission of each transmitter channel, look the same as those used for receiver calibration in

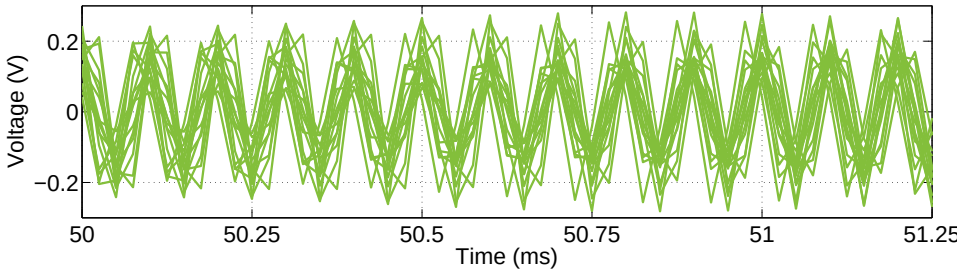

(a) Raw received signals.

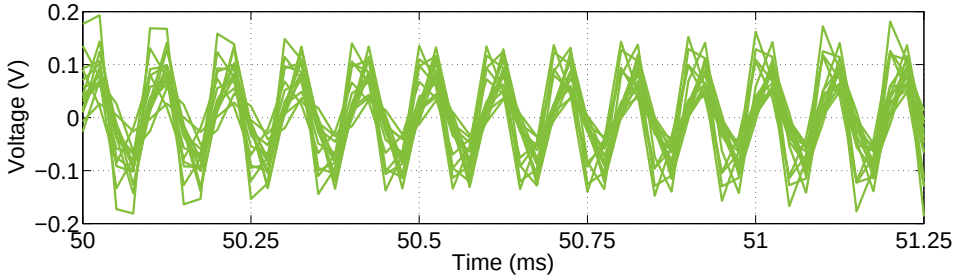

(b) Calibrated received signals.

Figure 8.5: Received signals before and after calibration when a 10 kHz sinusoid is transmitted by each transmitter channel.

Figure 8.1. Figure 8.5(a) shows a segment of the 10 kHz sinusoidal signals received from transmissions on each channel. The phase deviation from transmitter channel to channel is similar to that seen across the receiver channels in Figure 8.2(a).

Figure 8.5(b) shows the received signals after calibration was applied. The signals were filtered on reception, to determine the filters required on each transmitter channel. Analysis of the calibration results shows that the phase variation between channels was reduced, but still occurs. In addition, a relatively large variation in signal amplitude from channel to channel was introduced by the calibration filters. Because the peak transmission amplitude is fixed, the variations introduced by calibration can only result in reduced power being transmitted on some channels which has the undesirable effect of reducing the SNR at the target.

To illustrate that the FIR calibration method does not correct the phase variations on the transmitters as well as it does on the receivers, Figure 8.6 is included. Figure 8.6(a) shows the signals received when an 8 kHz to 12 kHz linear chirp signal was transmitted on each transmitter and no form of calibration was performed.

Figure 8.6(b) shows the same signals after the generated FIR filters have been applied to the signal received from transmission of each channel. Calibration can be seen

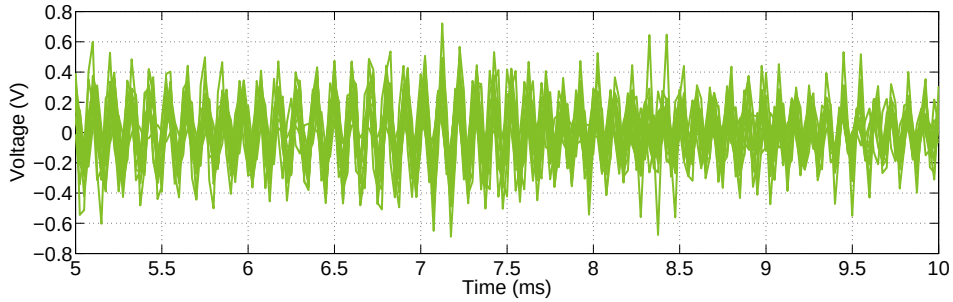

(a) Uncalibrated.

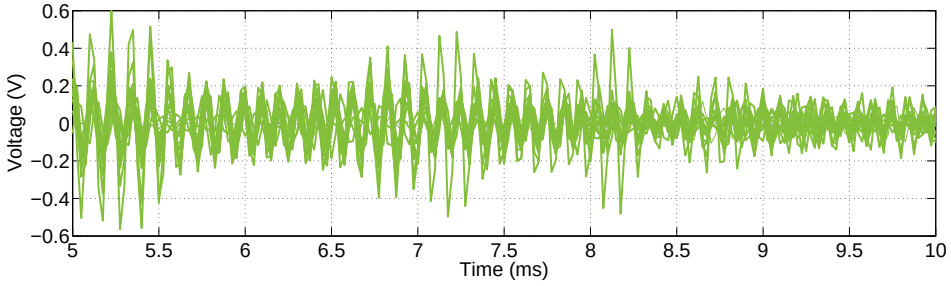

(b) Calibrated on reception.

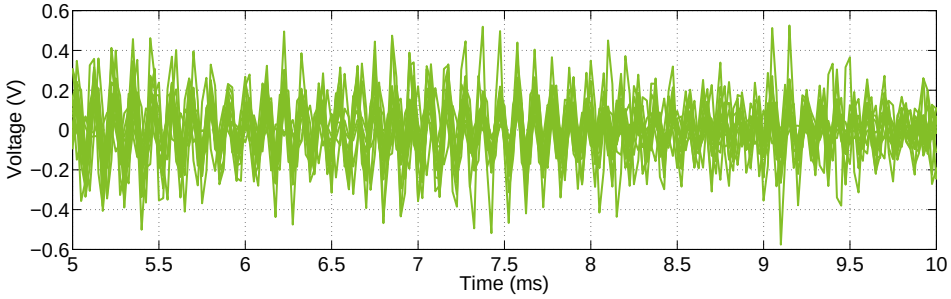

(c) Calibrated before transmission.

Figure 8.6: Received signals when an 8 kHz to 12 kHz chirp signal is transmitted by each transmitter channel with and without calibration.

to have provided some improvement in the phase variation from channel to channel. However, it also increased the amplitude variation with frequency and from channel to channel, which is undesirable.

Figure 8.6(c) shows the received signals when the transmitted signals were filtered by the set of FIR filters before transmission. It can be seen that in some periods, such as the 0.5 ms around 7.5 ms, the calibrated signal shows reduced phase variation between channels. However, in most other periods the calibration results in similar phase variation between channels as seen in the uncalibrated signals in Figure 8.6(a). Therefore, the FIR calibration method does not improve the results sufficiently.

8.1.2.2 Beampattern Calibration Method

Due to the inefficiency of the FIR filter calibration method in compensating for the phase differences between transmitter channels, the beampattern calibration method was applied, as defined in the transmitter calibration protocol in Section 7.1.4.

The beampattern generated by Pascale's design with a single main lobe at 20° was chosen arbitrarily to be used for calibration, but any of the patterns would have been suitable. Figure 8.7 shows three figures comparing the theoretical pattern with the uncalibrated measured pattern, the pattern calibrated by the beampattern method and, the pattern calibrated by the FIR filter method.

Except for a slightly wider beam width, the measured pattern and theoretical pattern agree well in the main lobe at 20° without any calibration. However, the measured pattern shows an undesired peak at 5°, and a smaller one at −10°. In addition, the side lobe levels of the measured pattern are significantly higher than those of the theoretical patterns.

The beampattern measured when beampattern calibration was implemented shown in the centre plot of Figure 8.7 better matches the desired pattern between −20°

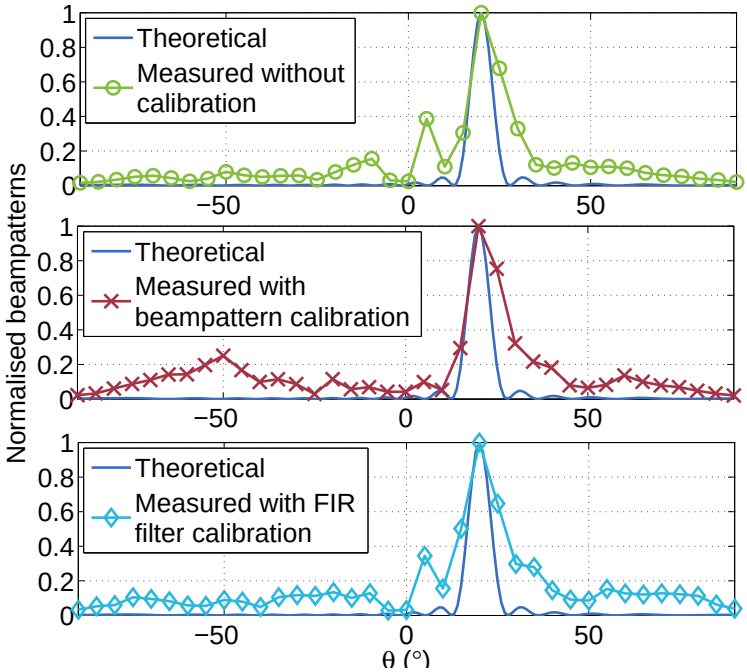

Figure 8.7: Beampatterns obtained from theory, simulation and measurement, showing the effect of calibration.

and 50°. However, an undesired peak appears in the pattern at −50°. Nonetheless, beampattern calibration improves the pattern in general.

The beampattern measured after transmitter calibration by the FIR filter method is shown in the bottom plot of Figure 8.7. This beampattern closely resembles the pattern measured when no calibration was performed but the side lobe levels are increased at some angles. This confirms that the FIR filter calibration method does not improve the results that can be achieved with a transmitting array.

Analysis of the different calibration methods shows that the beampattern method performs slightly better than the FIR filter method. The benefit of beampattern calibration was not, however, obvious so calibrated and uncalibrated patterns are used for the beampattern and parameter estimation tests in Sections 8.2 and 8.3 below.

8.1.2.3 Transmitter Array Properties

The high side lobe levels of the measured patterns visible in Figure 8.7, and the difficulty experienced in calibration, led to an investigation of the transmitting properties of the array. To better understand the transmitter array, the beampatterns of a selection of individual speaker making up the array were measured. The beampatterns, shown in Figure J.1 in Appendix J, were found to vary significantly for each speaker and for each frequency transmitted. After an in-depth investigation which is described in detail in Appendix J, the findings were:

- The speakers used in the array were expected to have a cardioid-shaped pattern with a maximum value at 0°, and nulls at −90° and 90° instead of the omnidirectional pattern assumed in simulations. This was found to be true, with the amplitude at 0° approximately 10 dB higher than that at −90° and 90°. However, the pattern was found to contain ripples of up to 5 dB, which varied with speaker and frequency.
- There was found to be coupling between the speakers and the PCB of the transmitter array which resulted in the entire PCB transmitting.
- When the speakers were mounted on a stiffer material, for example a wooden board, this coupling was found to be reduced or possibly even eliminated.

- The coupling of the speaker array reduces the quality of the beampattern that can be transmitted by the array, but the general form of the pattern is unaffected.

Therefore, the difficulty experienced in calibrating the transmitter array can almost certainly be attributed to the inconsistent beampatterns of the speaker elements and the coupling of the speakers to the transmitter board. Nevertheless, the transmitter array functioned sufficiently well to illustrate phased array and MIMO beamforming and parameter estimation principles to meet the objectives of the project.

8.2 Beampatterns

In the sections below, the results obtained from the measurement of the eight transmitter beampatterns described in Section 7.2.1 are plotted. For each beampattern, the theoretical, simulated and measured patterns are presented. The theoretical beampatterns were obtained using the narrowband expression for power given by

$$P(\theta) = \mathbf{a}^H(\theta)\hat{\mathbf{R}}_S\mathbf{a}(\theta).$$

The simulated beampatterns were plotted to give a more realistic representation of the expected beampatterns taking the wideband transmitted signals into account. The patterns were simulated as described in Section 5.4.1. Finally, the measured beampatterns are presented with and without calibration. An analysis of each of the beampatterns is given together with the graphs.

8.2.1 Omnidirectional MIMO Pattern

Figure 8.8 shows the linear and decibel omnidirectional MIMO beampatterns. The theoretical, simulated and measured omnidirectional MIMO patterns show significant variation of power with direction which can be explained by evaluating the orthogonality of the transmitted signals. Figure 8.9 shows the auto and cross correlations of the transmitted signals which should be orthogonal to each other to give an omnidirectional pattern. The autocorrelations only peak 10 dB above the level of the cross correlations. Therefore, the orthogonality of the transmitted signals is relatively poor and the "omnidirectional" pattern deviates from a constant power as angle changes.

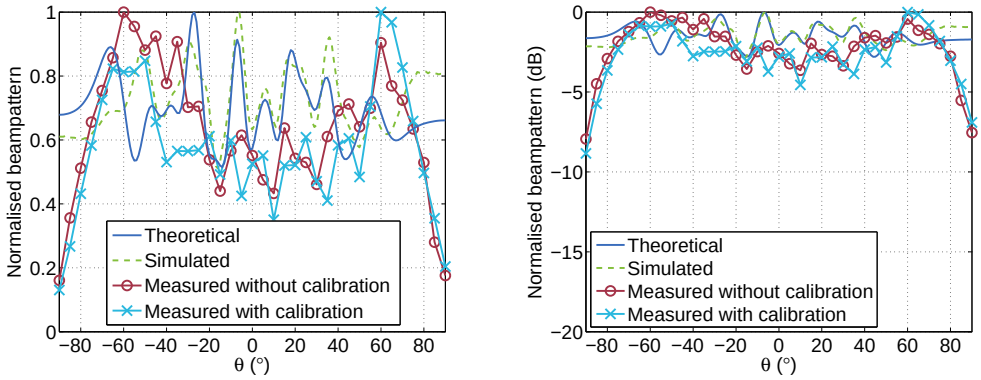

(a) Linear Scale.

(b) Decibel Scale.

Figure 8.8: Omnidirectional MIMO beampatterns.

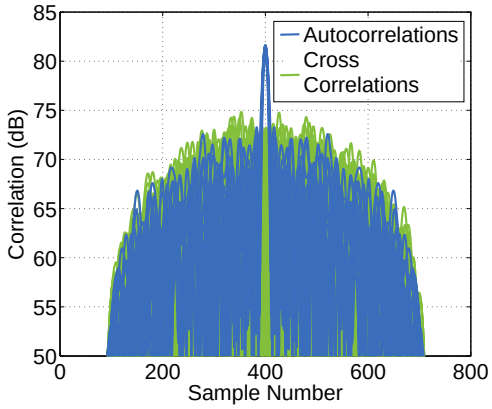

Figure 8.9: Auto correlations and cross correlations of the omnidirectional transmitted signals.

The orthogonality of the transmitted signal set could be increased, thus reducing the angular power variations, by increasing the number of QPSK symbols used to generate the pattern. This could be achieved by increasing the duration of the transmitted signals or the system sampling frequency. Figure 4.13 in the MIMO simulation section, is a better omnidirectional pattern that was generated with 256 symbols in comparison to the 40 used for the patterns in Figure 8.8. The use of orthogonal codes could also provide better omnidirectionality with the same number of symbols.

The theoretical and simulated beampatterns in Figure 8.8 deviate from each other because of the theoretical assumption that the signal is narrowband. The simulated pattern is a better representation of the expected measured wideband pattern.

The measured patterns also deviate from the simulated ones. Both the uncalibrated

and calibrated patterns have a "bowl-like" shape between $-60°$ and $60°$, dropping to less than half the maximum power in the centre. Also, the patterns drop off significantly at angles less than $-60°$ and greater than $60°$. The patterns take this form because they are affected by the patterns of the speakers making up the array. Each individual speaker element was not omnidirectional as was assumed in the simulations, but had nulls at $-90°$ and $90°$ which were 10 dB below the maximum at $0°$. This accounts for the nulls at $-90°$ and $90°$ in the omnidirectional pattern. The transmission of the speaker PCB due to the speakers coupling to it resulted in the measured patterns of some speaker elements having peaks at approximately $-60°$ and $60°$, particularly at 8 kHz and 10 kHz as can be seen in Figure J.1 in Appendix J. This was the cause of the peaks that appeared in the omnidirectional pattern.

Regardless, the variation in the omnidirectional pattern in Figure 8.8 is less than 5 dB between $-80°$ and $80°$, and therefore this pattern is significantly more omnidirectional than any of the patterns that will be presented in the sections to follow.

8.2.2 Patterns with a Single Mainlobe

Figure 8.10 shows the three measured patterns with a single main lobe at $20°$ without transmitter calibration in decibels. The power of the phased array pattern is about 7 dB greater than the power of the MIMO patterns in all directions. This power discrepancy was also noted in simulations which predicted that the phased array pattern would have power over 10 dB greater than the MIMO patterns in most directions.

This power variation is entirely due to the nature of the signals. The PDFs, averaged for the 16 transmitted signals over their 10 ms duration, are shown for the omnidirectional pattern in Figure 8.11(a) and the patterns with one main lobe generated with phased array signals and by Pascale's MIMO design in Figures 8.11(b) and 8.11(c) respectively. The PDF for the signals generated by the MIMO beampattern matching design for a single main lobe pattern was almost identical to that generated by Pascale's design.

Analysing Figure 8.11(b) shows that the chirp signals transmitted by the phased array have a high probability of having values close to the minimum and maximum voltage at any point in time. The randomly generated set of MIMO signals have PDFs in Figure 8.11(c) which are approximately triangular in shape with a peak

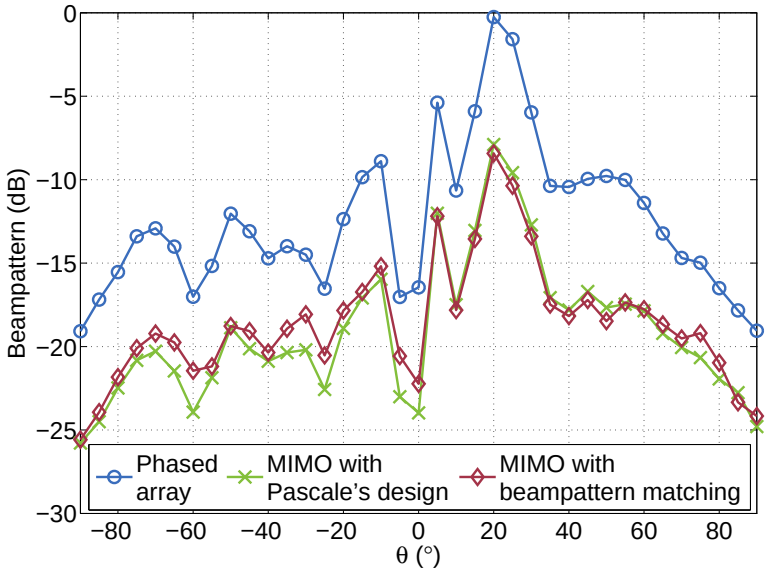

Figure 8.10: Measured patterns with a main lobe at 20° in decibels.

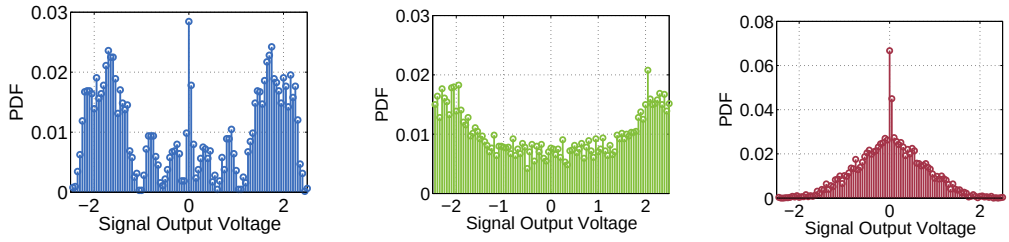

(a) Omnidirectional. (b) Phased array. (c) Pascale's design.

Figure 8.11: PDFs of the averaged transmitter signals for different beampatterns.

at zero and are therefore more likely to have voltages close to zero at any moment. Therefore, the phased array signals inherently have a higher peak to average power ratio (PAPR) compared to the MIMO directional signals used in this project. The PDFs of the omnidirectional MIMO signals show that the orthogonal signals have higher PAPR than the directional MIMO signals.

Disregarding the amplitude differences, the three beampatterns are close to identical. In the field of radar signal processing, the maximisation of SNR is of immense importance and the phased array pattern is therefore the most attractive of the three patterns as its power is significantly higher than that of the MIMO patterns.

In the sections that follow, the three normalised patterns with main lobes at 20° are compared to the theoretical and simulated patterns, and discussed in more detail.

8.2.2.1 Phased Array Pattern

The phased array patterns with a main lobe at 20° are shown in Figure 8.12. The simulated pattern matches the theoretical pattern closely, except that the beam width is slightly wider when the transmitted signal bandwidth is taken into account.

The measured beampatterns clearly have a main lobe at 20° as required. The uncalibrated pattern has a peak at 5°, which was successfully removed by calibration, but in the process, another peak was introduced at −50°. The measured patterns also show high side lobe levels in comparison to the theoretical and simulated patterns. The normalised maximum side lobe level of the theoretical and simulated beampatterns is 0.045 (-13.46 dB), whereas the maximum levels of the measured patterns are 0.3 (-5.23 dB) and 0.23 (-6.38 dB) for the uncalibrated and calibrated patterns respectively. As described in Section 8.1.2, the high side lobe levels are probably a result of the irregular speaker beampatterns and coupling between the speakers and the transmitter array board.

Even with the undesired peaks in the patterns and the high side lobe levels, the phased array effectively transmits the majority of the signal power in the desired direction when beamforming is implemented. Therefore, these patterns illustrate how beamforming can be achieved with a phased array transmitter.

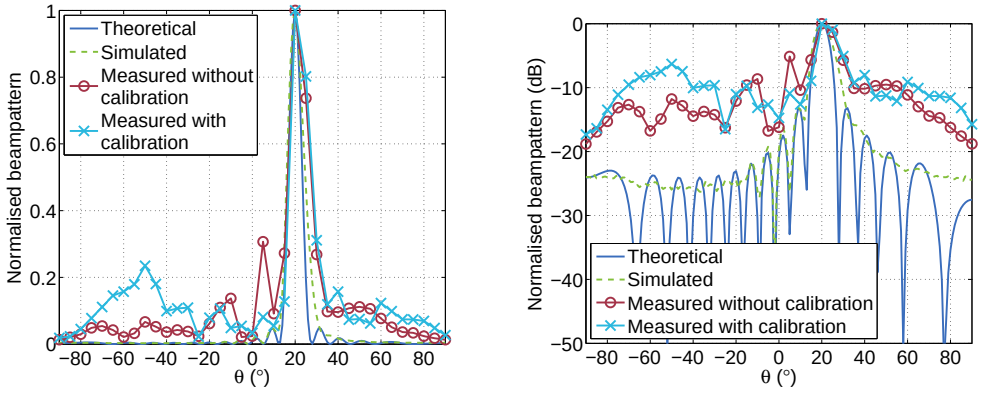

(a) Linear Scale.

(b) Decibel Scale.

Figure 8.12: Phased array patterns with a main lobe at 20°.

8.2.2.2 MIMO Pattern Generated by Pascale's Design

The MIMO patterns generated using Pascale's design are shown in Figure 8.13. The theoretical, simulated and measured patterns are all remarkably similar to the phased array patterns. Therefore, everything said with reference to the phased array patterns applies here.

However, as shown in Figure 8.10, the power of the MIMO pattern generated by Pascale's design was significantly reduced in comparison to the power of the phased array pattern. The loss of SNR is expected to have a negative effect on parameter estimation despite the existence of advanced MIMO methods.

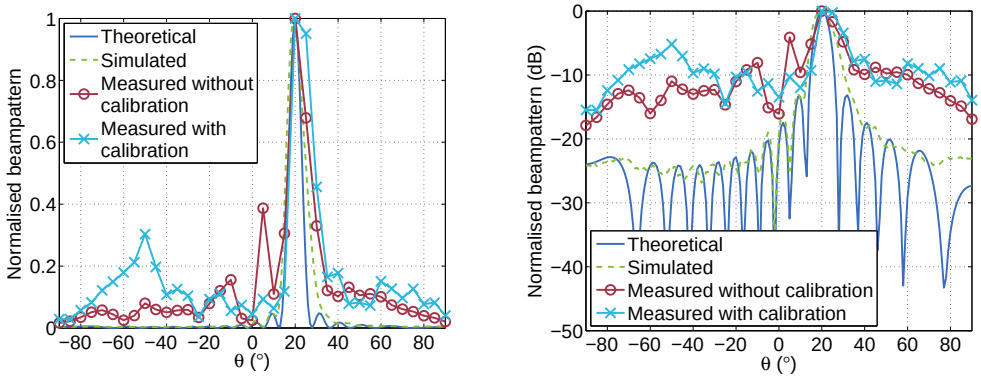

(a) Linear Scale.

(b) Decibel Scale.

Figure 8.13: MIMO patterns generated by Pascale's design with a main lobe at 20°.

8.2.2.3 MIMO Pattern Generated by Beampattern Matching

The MIMO patterns generated using the beampattern matching design are shown in Figure 8.14. The theoretical, simulated and uncalibrated measured patterns are again very similar to the patterns achieved with a phased array. The main lobe of the calibrated signal peaks at 25° rather than 20°. It is possible that this error can be attributed to inaccuracies in the measurement, as the calibrated pattern designed by the beampattern matching design was re-measured due to an error in the original measurement. The power of the single-lobed pattern generated by the beampattern matching design was similar to the power of the pattern generated by Pascale's design, as shown in Figure 8.10. This results in a reduced SNR of any target reflections when the beampattern matching pattern is used for parameter estimation.

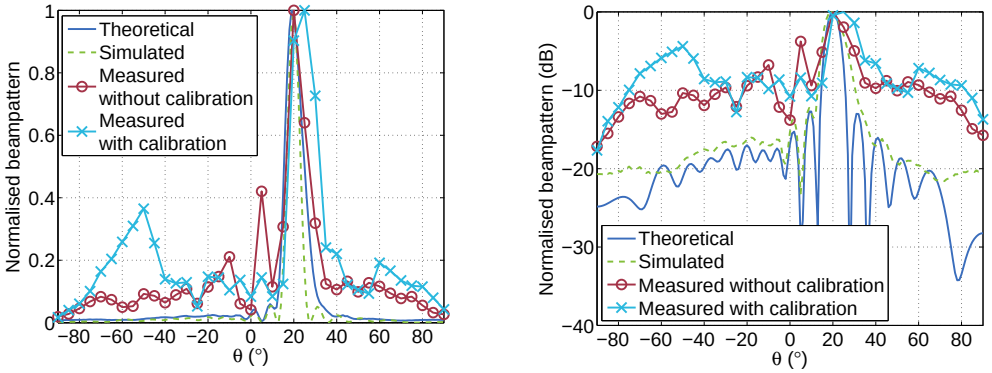

(a) Linear Scale.

(b) Decibel Scale.

Figure 8.14: MIMO patterns generated by beampattern matching with a main lobe at 20°.

8.2.3 Patterns with Three Mainlobes

Figure 8.15 shows the uncalibrated measured patterns with three main lobes at −20°, 0° and 20°. The phased array pattern generated by beampattern matching has the highest power. The phased array pattern designed with the LCMV has the lowest power, due to the varying amplitude of the weights generated by the method. Like the low-powered MIMO single main lobe patterns, the MIMO multiple-lobed patterns also show lower power compared to the phased array pattern designed by

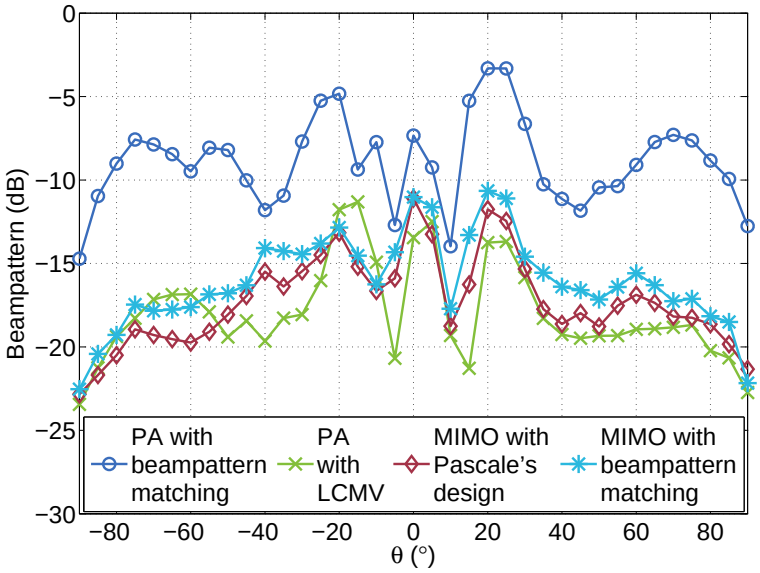

Figure 8.15: Patterns with main lobes at −20°, 0° and 20° in decibels.

beampattern matching. Again, lower pattern amplitude leads to reduced SNR at the target and consequently parameter estimations of reduced accuracy are expected.

Each of the normalised beampatterns with three lobes are presented and discussed below.

8.2.3.1 Phased Array Pattern Generated by Beampattern Matching

The phased array patterns generated by the beampattern matching method with three main lobes at $-20°$, $0°$ and $20°$ are shown in Figure 8.16. The theoretical pattern shows three main lobes of equal power and a high side lobe at $-10°$ which also appears in the measured patterns. The simulated pattern indicates that the two outer main lobes will have slightly reduced amplitude when compared to the centre one, but the opposite is seen in the measured patterns. The uncalibrated measured pattern has two dominant peaks at $-20°$ and $20°$. The main lobe at $0°$, although it is present, is of almost equal amplitude to the side lobe at $10°$, and others at $-70°$, $-55°$ and $75°$. When the pattern was calibrated, the two main lobes at $-20°$ and $0°$ show up well. However, the main lobe at $20°$ disappears and three high amplitude side lobes appear. Calibration therefore worsens this beampattern.

The measured patterns obtained from the phased array beampattern matching method are the poorest at matching the desired pattern of all the beampatterns with three main lobes. However, they have the maximum power, and therefore the parameter estimation accuracies obtained with these pattern might still be better

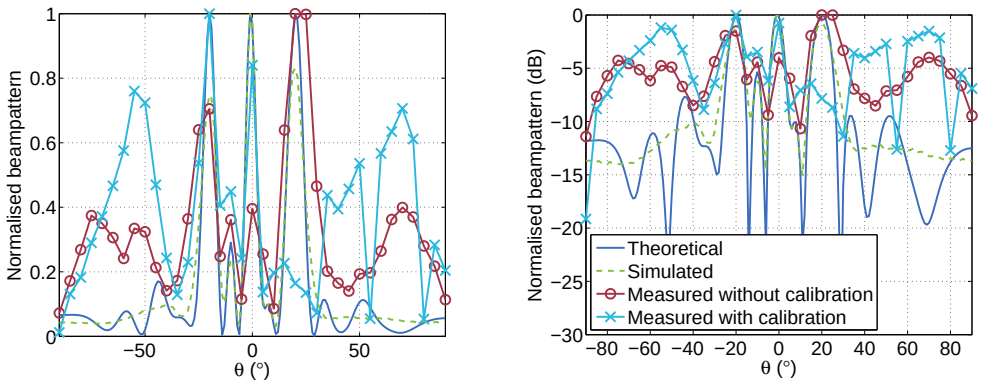

(a) Linear Scale. (b) Decibel Scale.

Figure 8.16: Phased array patterns generated by beampattern matching with main lobes at $-20°$, $0°$ and $20°$.

than that achieved with the others, due to the higher SNR at the target that will be achieved.

8.2.3.2 Phased Array Pattern Generated by LCMV

Figure 8.17 shows the phased array beampatterns with main lobes at −20°, 0° and 20° generated by the LCMV method. The theoretical and simulated patterns have lower side lobes than the phased array pattern generated using the beampattern matching method. The measured side lobe levels are still, at their worst, 15 dB above the simulated levels. This is once again due to the poor speaker beampatterns and coupling of the speakers to the transmitter board.

The two measured patterns show three clear peaks at the desired locations. The amplitudes of the main lobes at 0° and 20° are reduced for the uncalibrated pattern but the matching of the amplitudes at the three peaks is improved by calibration. Between −30° and 35°, the calibrated pattern matches the simulated pattern remarkably well. However, the side lobe levels are increased at angles less than −30° and greater than 35°, when compared to the theoretical, simulated and uncalibrated measured pattern.

This phased array pattern effectively transmits power in the three desired directions but has the lowest power of all of the patterns with three main lobes. The improvement in the pattern shape comes at the cost of power when compared to the phased array pattern generated by the beampattern matching method.

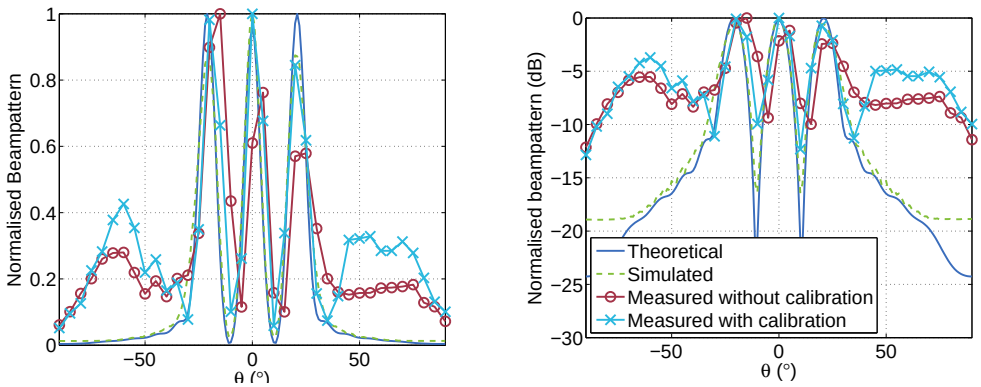

(a) Linear Scale. (b) Decibel Scale.

Figure 8.17: Phased array patterns generated by LCMV with main lobes at −20°, 0° and 20°.

8.2.3.3 MIMO Pattern Generated by Pascale's Design

The MIMO beampattern generated by Pascale's design with main lobes at $-20°$, $0°$ and $20°$ is shown in Figure 8.18. The pattern measured without calibration shows peaks at the desired angles. The measured pattern after calibration has lower side lobe levels at most angles but the main lobe at $20°$ has reduced amplitude. The measured patterns generated by Pascale's design have the lowest side lobe levels of all of the three-lobed patterns.

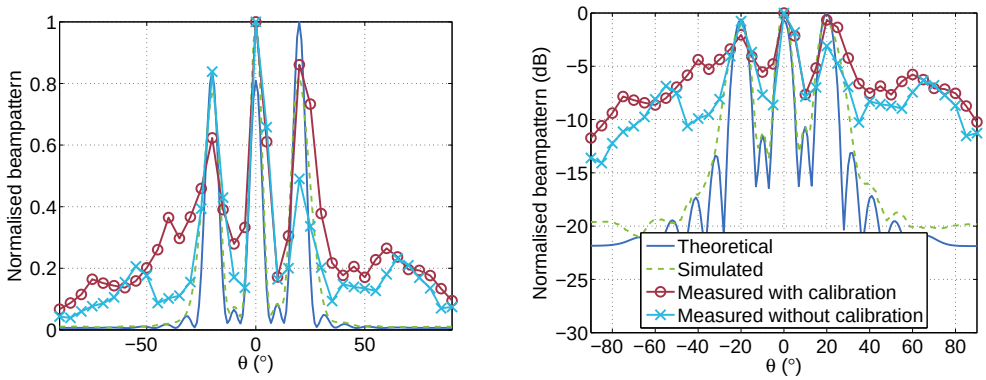

(a) Linear Scale.

(b) Decibel Scale.

Figure 8.18: MIMO patterns generated by Pascale's design with main lobes at $-20°$, $0°$ and $20°$.

8.2.3.4 MIMO Pattern Generated by Beampattern Matching

Figure 8.19 shows the MIMO beampattern with three main lobes at $-20°$, $0°$ and $20°$. The theoretical and simulated patterns show a main lobe of decreased amplitude at $-20°$ and the measured results concur with this. With the implementation of calibration, the side lobe levels are reduced. However, as with the MIMO beampattern generated with Pascale's design in Figure 8.17, the main lobe at $20°$ also has reduced amplitude.

8.2.4 Analysis of Beampattern Results

To analyse the different beampatterns, three characteristics were compared. These are the transmitted power, the pattern quality and the independence of the transmitted signals.

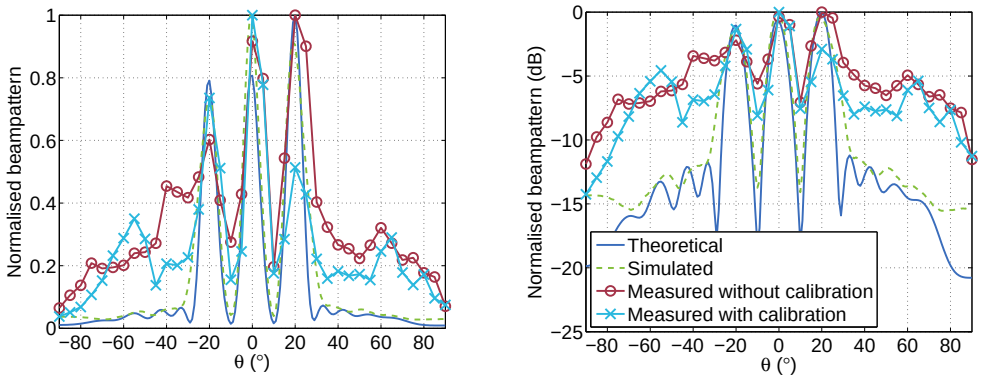

(a) Linear Scale.

(b) Decibel Scale.

Figure 8.19: MIMO patterns generated by beampattern matching with main lobes at $-20°$, $0°$ and $20°$.

To evaluate the transmitted power, the SNR of the received signal at the angle in which the most power was transmitted was calculated. To quantify the beampatterns' quality, the mean square deviation between the simulated pattern and the measured pattern was calculated. Finally, to analyse the independence of the transmitted signals, the condition number of the matrix of transmitted signals was calculated. All of these measures are given in Table 8.1 for each of the beampatterns. The acronyms used to describe the patterns are explained in Appendix K. An analysis of the results is given below.

Table 8.1: Comparison of the transmitted beampatterns.

	Without Calibration		With Calibration		
Pattern	SNR	Matching	SNR	Matching	Condition
OMNI	26.712	0.0649	27.201	0.0834	2.16E+00
PA1	32.279	0.0081	33.851	0.0137	1.43E+04
MIMOPD1	24.643	0.0098	26.447	0.0219	1.88E+02
MIMOBM1	24.106	0.0116	25.272	0.0386	5.07E+03
PABM3	29.225	0.0582	28.732	0.1246	1.66E+04
PALCMV3	21.224	0.0489	22.703	0.0432	9.04E+03
MIMOPD3	21.427	0.0355	23.003	0.0214	2.91E+02
MIMOBM3	21.887	0.0428	23.793	0.0281	3.80E+03

8.2.4.1 Transmitted Power

The SNR was the measure chosen to compare the power of the different patterns. It was calculated at the angle in which the maximum power was transmitted using the signal power and the power measured when no signal was transmitted. In the case of the signal with one main lobe, this gives the SNR of the received signal at 20° and for the three-lobed signals, the SNR is for the peak with the maximum power at either −20°, 0° or 20°. For the omnidirectional signal the maximum SNR was selected, but the SNR only varies by approximately 5 dB regardless of the angle between −80° and 80°.

The more focussed the pattern, the higher the SNR. Therefore, the omnidirectional signal which transmits power in all directions was expected to have the lowest maximum power as the power is distributed across all angles. The patterns with a single main lobe were expected to have the highest maximum power. The three-lobed patterns which share the power in three directions were expected to have slightly lower maximum power. In addition, the phased array patterns were expected to have a higher average power in all directions, compared to the MIMO patterns (except for the LCMV phased array pattern) due to the higher PAPR of the phased array transmitted signals.

The results in Table 8.1 show that the uncalibrated and calibrated phased array patterns with a main lobe at 20° do have the highest maximum power. Therefore, in terms of maximising the SNR at the target location, these are the optimum patterns.

The power of the directional patterns followed the expected trends, but the omnidirectional pattern was found to have a higher maximum power than the MIMO directional patterns. This discrepancy was also noted in simulations. It is explained by comparing the PDF for the omnidirectional signals in Figure 8.11(a) to that for the directional MIMO signals optimised by Pascale's design in Figure 8.11(c) and noting that the omnidirectional signal set will have a higher PAPR than the directional MIMO signals.

The power results also show that with only one exception, the calibrated patterns had higher maximum SNRs than the uncalibrated patterns. This was not true for the phased array pattern designed by beampattern matching with three main lobes, where the results of calibration were notably poor. This indicates that, in general, calibration improves the pattern results.

8.2.4.2 Beampattern Quality

The mean square deviation between the normalised simulated and measured beampatterns lies between 0.01 and 0.09 for 13 of the 16 beampatterns. The best matching was achieved with an uncalibrated phased array pattern with a single main lobe at 20°, which had a deviation of 0.0081.

The patterns with a main lobe at 20° all match the theoretical patterns better than the patterns with three main lobes, regardless of whether the patterns were calibrated or not. The omnidirectional measured patterns matched the theoretical patterns worst, of all the pattern types.

The matching figures in Table 8.1 show that calibration improved the shape of the patterns for the LCMV phased array and the two MIMO patterns with main lobes at three locations. However, in all other cases, better matching was obtained without calibration.

8.2.4.3 Independence of Signals

The rank of all of the phased array and MIMO transmitted signal sets was calculated to be 16 which indicates that the signals in each set are linearly independent. However the unweighted phased array transmitted signal matrix has a rank of one, and the correlation between the weighted signal is high. This information is not captured by the measure of rank, which makes it an insufficient measure of the independence of the signals.

The transmitted signal sets can be further characterised in terms of how independent they are. The condition number of a matrix is defined as the ratio of its largest to smallest singular values. If a matrix has any linearly dependent rows the condition number is infinite, as the smallest singular value will be zero. In the case of perfectly orthogonal transmitted signals the condition number is one. For any other matrix, the condition number gives a measure of the linear independence between the column vectors of the matrix [60]. Therefore, to measure the linear independence of the transmitted signal sets, the condition number of the transposed signal matrix was calculated. The results are shown in Table 8.1.

The lowest singular value of 2.16 was obtained for an omnidirectional pattern because the signals were orthogonal. Because the phased array signals are time shifted

versions of the same signal, the linear independence of the phased array patterns was the poorest, as indicated by the high condition numbers. Comparing the condition numbers for the MIMO pattern designed by Pascale's Design and the beampattern matching design shows that the independence of the signals transmitted by Pascale's design is better by an order of magnitude. The condition numbers of the directional MIMO signal matrices are still large in comparison to the omnidirectional signal matrix which could result in poor performance of the MIMO parameter estimation techniques.

8.2.4.4 Overall Performance

The difference between the signals generated with phased array techniques, compared to those generated by MIMO techniques is small. The phased array patterns (except that designed by the LCMV) transmitted about 7 dB more power in all directions than the MIMO directional patterns, at the cost of having the lowest measure of linear independence. The condition number of the directional MIMO transmitted signal sets shows that they are not significantly more independent than the phased array signals. The patterns all had deviations from the simulated patterns of similar orders of magnitude with neither phased array nor MIMO outperforming the other.

From analysis of the beampatterns, better parameter estimations are expected from the phased array patterns compared to MIMO for a single target, due to the higher SNR. When three targets are present, poor phased array performance is expected due to the low measure of linear independence of the transmitted signals and the risk of signal coherence that this introduces. The MIMO directional patterns are also expected to perform badly when multiple targets are present, as the linear independence of the transmitted signal sets is not much improved, and the SNR is reduced. Due to the good linear independence of the omnidirectional signals, better estimation accuracies are expected from the omnidirectional transmitted signal for multiple targets.

8.3 Parameter Estimation

Parameter estimation was performed when the eight patterns presented above were transmitted, and targets were present in the radar field of view as described in the

test protocol in Section 7.2.2. The results of the parameter estimation tests allow comparison between the different signals and methods available for determining target range and angle. In the sections below, a description of the methods used to obtain the target range and angle estimates is presented. The parameter estimation graphs obtained under different experimental conditions are then presented and where suitable, analysed with reference to the simulation results.

8.3.1 Range Estimation

In radar theory, an important characteristic of a radar system is its range resolution, which gives the minimum distance by which two targets must be separated to still be resolved by the radar [18]. The range resolution is defined as

$$\Delta R = \frac{c}{2B}. \tag{8.1}$$

The bandwidth B of all of the transmitted signals was 4 kHz, giving a range resolution of 42.9 mm. Pulse compression was performed on the phased array by transmitting a chirp signal, and therefore the phased array angular resolution should be better than ΔR.

The target was not a point target as simulated, but had a size of 100 mm × 100 mm in the x-y plane. In all of the target parameter estimation experiments presented below, the corner at which the three surfaces meet was was placed at 3 m. Therefore, range estimates of 2.9 m to 3 m are considered accurate. However, the target is concentrated at the apex of the reflector, since all triple bounce path lengths are equal and so accurate range estimates of 3 m are expected.

Another important property of a radar is its minimum detection range which is

$$R_{min} = c\frac{t_{rx} - t_{tx}}{2} \tag{8.2}$$

where t_{tx} is the time that transmission started, and t_{rx} is the time that reception started. Transmission lasts for 10 ms, and there is a 5 ms dead-time between transmission and reception, so the minimum range R_{min} is 2.57 m. All of the targets were located beyond this minimum at a range of 3 m.

Two methods were used to estimate target range. The first method estimates the target range by cross correlating each of the received signals with the transmitted signal or set of signals. In the case of a phased array system, each transmitter channel transmits the same base signal which is multiplied by a complex weight specific to

the channel. Therefore each of the 16 received signals is cross correlated with the base transmitted signal, giving 16 cross correlations. In the case of a MIMO system, each of the transmitter channels transmits a signal which is ideally uncorrelated to any of the other signals. Therefore, each of the 16 received signals is cross correlated with each of the 16 transmitted signals, giving 256 cross correlations.

Peaks in the cross correlations occur when the received signal is strongly correlated to the transmitted signal and therefore indicate the time at which an echo of the transmitted signal was received. From the time delay t, the range R of a target can be calculated by

$$R = c\frac{t}{2} \tag{8.3}$$

where c is the speed of sound. t is divided by two because the signals travel twice the target range on their path from the transmitter array to the target and then back to the receiver array.

The second method, which gives more accurate results by increasing the SNR, is to perform beamforming on the received signals before cross correlation with the transmitted signal(s). The narrowband beamformer with Capon weights and a TDWB beamformer were used in the tests. The beamforming weights or time delays are calculated for angles between $-90°$ and $90°$ in increments of $1°$. In the case of phased array, the output of the beamformer is cross correlated with the transmitted signal, giving a single cross correlation for each angle. In the case of MIMO, the beamformer output is cross correlated with all 16 of the transmitted signals giving 16 output signals which are weighted or delayed again as for TBR. The result is one cross correlation for each angle.

The cross correlations obtained with both range estimation techniques were plotted to graphically display the range results. A "map" was generated by colouring the blocks in a grid to represent the amplitude of the cross correlations for a particular channel or angle and time delay. The values on the x-axis were marked with range R for both methods. For the first method, the values on the y-axis correspond to the receiver number. For the MIMO systems, each channel block was further split into 16 parts for the 16 unique transmitted signals. This chart is referred to as a range chart. For the second method, the y-axis corresponds to angle, and the plot is referred to as a range-angle chart.

For the first method, estimates of the target range were obtained from the 16 or 256 cross correlation outputs by averaging the location of the peak. For phased array signals, the mean of the peak estimated for each channel was used. For MIMO

signals, where some of the cross correlations give erroneous estimates, the mode of the indices of the cross correlation peaks was used. For the second method, the target range and target angle were estimated by locating the maximum value (or values if there is more than one target) of the range-angle chart.

In the parameter estimation sections below, the range and range-angle charts are plotted for the different scenarios. The range estimates obtained for all of the experiments are given in Tables K.2 to K.14 in Appendix K.

8.3.2 Angle Estimation

Spectral and parametric methods were used to estimate the target angle. The DML, which was the only parametric method and which was used for phased array, directly gave estimates of the target angles. However, the target angle estimates had to be extracted from the spectrums for all of the spectral techniques used for phased array and MIMO. For the phased array systems, the conventional, Capon and MUSIC spectral methods, and the spectrum obtained from the range angle chart were used to determine the angle. For the MIMO systems, the Capon θ, Capon β, APES and GLRT spectral methods and the TBR spectrums, are used to estimate angle. For the MIMO techniques, the range estimate obtained from the first method was used to obtain the time delay at which to sub-sample the baseband received signal to the symbol frequency. For the omnidirectional signals, better range estimates are obtained by using the second method, but the first method was still used for illustrative purposes.

The phased array and MIMO spectrums from which the angle estimates were obtained are plotted and discussed in the sections below. All of the spectrums were calculated from -90° to 90° in increments of 1°. Finer increments add no value, as the angle was only measured to 1° accuracy when the target was placed. The MIMO Capon θ and β spectrums were plotted on the same axes, and the Capon θ spectrum, whose amplitude value has no meaning, was scaled so that its peak value is equal to the peak value of the β spectrum.

To obtain target angle estimates from the spectrums, the maximum value of the spectrum was located and selected as the first target location. All spectrum values adjacent to the first peak that were above a threshold value were set equal to the threshold, to remove its effect from the spectrum. The new maximum was then located, and selected as the second target location estimate. It was assumed that

the number of targets was known, and this process was repeated until all of their angles had been estimated. The value of the threshold used was a fifth of the maximum spectrum amplitude.

All of the angle estimates obtained from the spectral and parametric techniques are presented in Tables K.2 to K.14 in Appendix K. When MIMO processing was performed, the Capon estimates given in the tables in Appendix K were from the Capon β spectrum.

The target used was a corner reflector with dimensions 100 mm $\times$ 100 mm $\times$ 100 mm. Because it deviates from the point target assumed in simulations, the resolution of the angular location of the target is decreased. With the target located 3 m from the arrays, the difference in DOA from one end to the other is up to 2.7° depending on the orientation of the target. The best angular resolution that can be obtained is therefore approximately 3°.

8.3.3 Single Target

A single target was located at 20° at a range of 3 m from the centre of the transmitter and receiver arrays as prescribed in Section 7.2.1. Estimation of the target range and DOA was performed with a phased array pattern, an omnidirectional MIMO pattern and two directional MIMO beampatterns generated with Pascale's and the MIMO beampattern matching design technique. The directional patterns pointed directly at the target at 20°. The parameter estimation results obtained with each of these patterns are presented below.

8.3.3.1 Phased Array

The results obtained when a single target was located at 20° and a phased array beam was pointed at it are shown in Figure 8.20. Clearer range charts and spectrums were achieved when the pattern transmitted was uncalibrated, and therefore, the graphs obtained from the calibrated pattern are not presented.

The range chart in Figure 8.20(a) shows a clear white stripe at approximately 3 m indicating that the peak in the cross correlation on all channels occurs at the time delay corresponding to the true target range. Note the slight slant of the range line

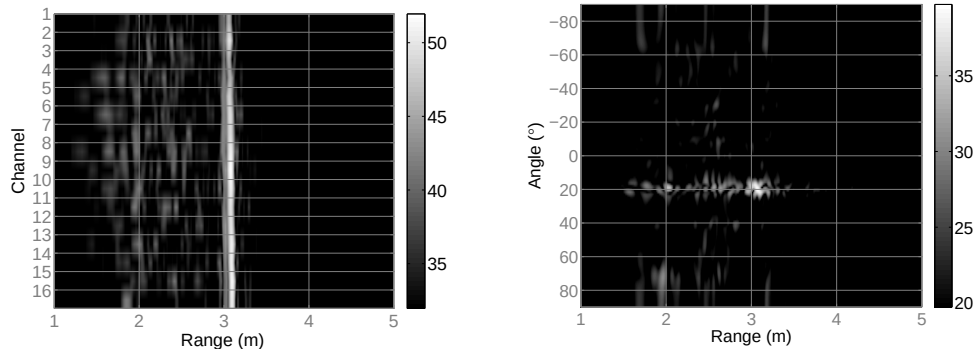

(a) Phased array range chart.

(b) Range-angle chart for narrowband beamformer with Capon weights.

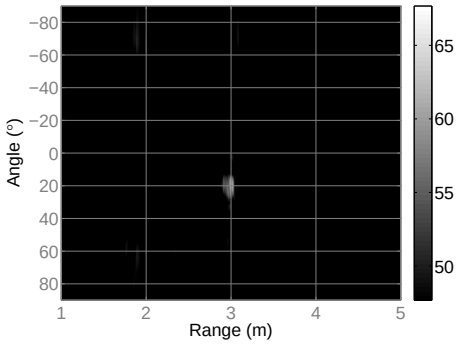

(c) Range-angle chart for TDWB beamformer.

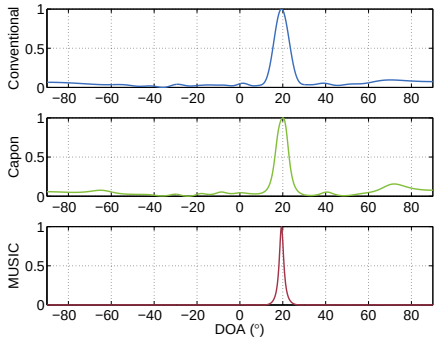

(d) Phased array angle estimation spectrums without FWWB processing.

Figure 8.20: Results obtained when a target was located at 20° and 3 m and an uncalibrated phased array pattern with a main lobe pointed at the target was transmitted.

which occurs because the elements on the one side of the array are slightly closer to the target than those on the other side.

Figure 8.20(b) is the range-angle chart obtained when a narrowband beamformer with Capon weights was used. The target location at 20° and 3 m can clearly be read from the chart. There are some side lobes visible along the range axis and streaks are visible at −80° and 80°, which could be reflections from the walls of the anechoic chamber. Figure 8.20(c) is the range-angle chart when the TDWB beamformer was used. This identifies the target very clearly, with no side lobes above the 20 dB sensitivity of the chart. The TDWB beamformer was found to give better range-angle charts in all scenarios and therefore, it is the only range-angle chart included for the remainder of the tests.

Figure 8.20(d) shows the conventional, Capon and MUSIC spectrums. All of the

spectrums clearly show peaks at 20°, and the spectrums are comparable to the results obtained in narrowband simulations shown in Figure 4.1. FWWB processing was not performed on the phased array results shown, and when it was, the spectrums still gave good estimates of the target location but they were less clean, the resolution was reduced, and in some instances additional peaks appeared. Therefore, FWWB processing does not improve the results for a phased array system with one target.

Table K.2 in Appendix K shows the target range and angle estimates including those obtained when a calibrated signal was transmitted, and when FWWB processing was implemented. The range estimates achieved with and without calibration were within 10 mm of the true range of 3 m.

Table K.2 shows that the angles estimated by the conventional and MUSIC techniques usually give the same estimates, which are also usually the most accurate estimates. The DML gives the least accurate estimates. In the phased array simulation analysis illustrated in Figure 4.2, it was found that at low SNRs, the DML was the least accurate estimation technique. However, simulations showed that from an SNR of 0 dB, the DML technique gave better estimates than the conventional technique. The experimental raw received signal had an SNR of -0.2 dB which is close to the simulated value where DML outperforms all other techniques, and therefore the poor performance of the DML technique cannot be explained.

8.3.3.2 Omnidirectional MIMO Pattern

An omnidirectional MIMO pattern is desirable when nothing is known about the scene which a radar is to probe. Ideally, information about any targets in the radar's field of view can be obtained from a single transmission of an omnidirectional signal. Using this information, beamforming can then be performed, to transmit power in the directions that the omnidirectional estimates show need further investigation.

Figure 8.21 shows the results obtained when the omnidirectional pattern was transmitted and the target was located 3 m from the transmitting and receiving arrays at an angle of 20°. The range chart, in Figure 8.21(a), is noisy and does not identify the target range.

Figures 8.21(b) to 8.21(e) are the MIMO spectrums which reveal some interesting behavioural traits of the omnidirectional pattern and MIMO processing. Figure 8.21(b) shows the spectrum obtained when the range was determined from the range

chart and was estimated to be 2.60 m. Although the spectrums do show peaks of maximum amplitude in the general target direction, they show many peaks at other angles.

Figure 8.21(c) shows the spectrums obtained under the same conditions when the range was chosen manually to be 2.97 m. These spectrums are a significant improvement on those in Figure 8.21(b), as the target location can be identified from each without ambiguity.

The varying spectrums in Figures 8.21(b) and 8.21(c) reveal the sensitivity of the MIMO spectral algorithms to the range estimate. The exact range of the target is required, so that the segment of the received signal used by the algorithms contains an echo of the transmitted signal, reflected by the target. The poor performance of the MIMO algorithms when the range is incorrect was illustrated with simulations in Section 4.2.2.2 and is confirmed by experiment here.

The shape of the target peak in the Capon θ spectrum in Figure 8.21(c) can be directly compared to that for phased array in Figure 8.20(d). The resolution of the peak at 20° is higher when MIMO processing is used. However, even when the range was forced as in Figures 8.21(c) to 8.21(e), the MIMO spectrums are more noisy than the phased array spectrums in Figures 8.20(d) due to the reduced SNR at the target location and increased SNR at all other locations which results in more reflections when an omnidirectional pattern is transmitted. Although the measurements were taken in an anechoic chamber, it was an RF chamber and the walls could still reflect acoustic signals to a certain degree. Also, the walkways were wooden, and would scatter and reflect any incident signals. Table K.1 in Appendix K shows the estimated SNR of the raw received signal to be 12.2 dB, compared to the marginally higher SNR of 12.4 dB for the phased array signal. The noisy omnidirectional spectrums and range chart indicate that the signal components in the received signal which contribute to the high SNR are not all echoes from the target, but include reflections from the walls and walkway of the chamber.

Figures 8.21(d) and 8.21(e) show the target angle spectrums when the calibrated omnidirectional signal was transmitted and the range was fixed to 2.91 m without and with FWWB processing respectively. Peaks are visible at the target location in both of the figures, but FWWB processing can be observed to reduce the level of the noise around the spectral estimate, and to significantly improve the estimates' resolutions.

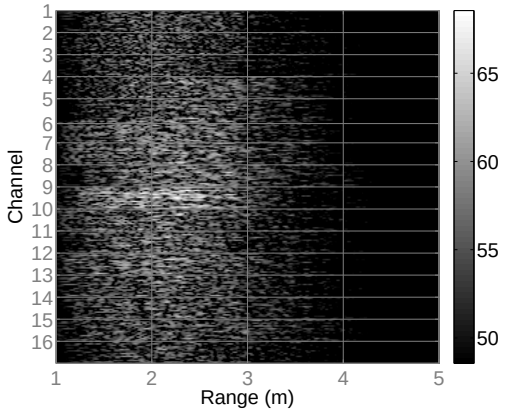

(a) MIMO range chart for uncalibrated signal.

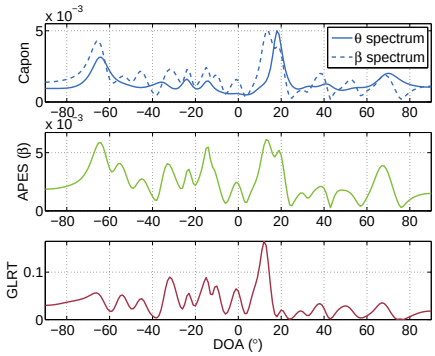

(b) MIMO parameter estimation spectrums for uncalibrated signal with range estimated of 2.60 m.

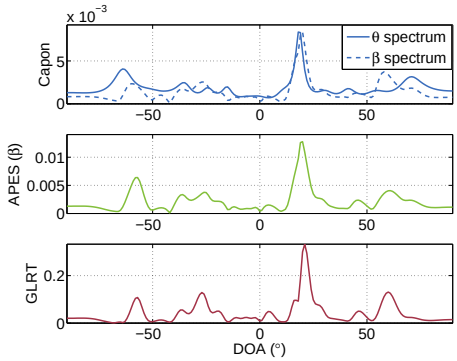

(c) MIMO parameter estimation spectrums for uncalibrated signal with range selected manually to be 2.97 m.

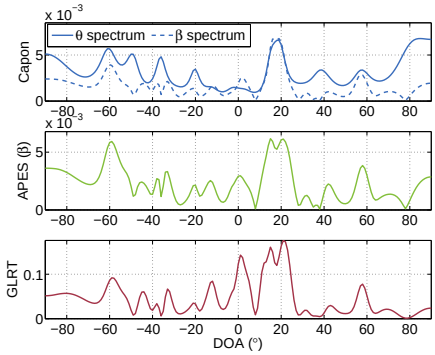

(d) MIMO parameter estimation spectrums for calibrated signal with range selected manually to be 2.91 m.

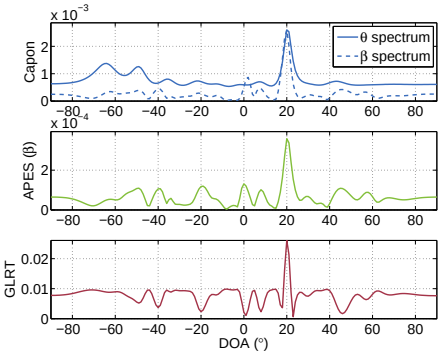

(e) MIMO parameter estimation spectrums for calibrated signal with range selected manually to be 2.91 m and with FWWB processing.

Figure 8.21: Results obtained when a target was located at 20° and 3 m and an omnidirectional pattern was transmitted.

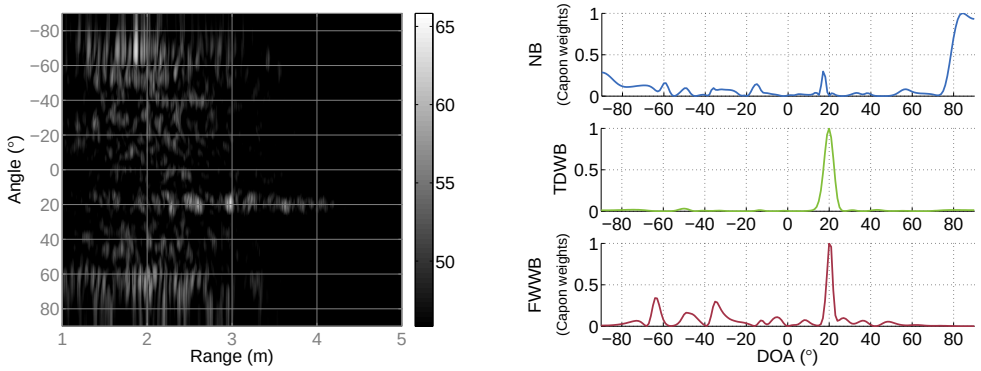

(a) Range-angle chart for TDWB beamformer. (b) Angle estimation spectrums for different beamformers.

Figure 8.22: Results obtained from TBR when a target was located at 20° and 3 m and a calibrated omnidirectional pattern was transmitted.

Figure 8.22 shows the range-angle chart and the spectrums obtained when an omnidirectional pattern was transmitted and TBR was applied. This chart is an improvement on the range chart in Figure 8.21(a), and a high amplitude peak is located at the target location of 20° and 3 m. The chart is however still noisy and has a notable peak of amplitude similar to the target peak at approximately −70° and 2 m. Analysis of the experimental setup showed that the laptop used for receiving the results, and the anechoic chamber light were both located at this approximate angle and range (at different heights) and one or both of these objects are likely to be responsible for the strong peak at this location. The fact that the omnidirectional pattern had peaks at −60° and 60° as seen in Figure 8.8 would have led to higher amplitude reflections from these directions.

The spectrums obtained from TBR in Figure 8.22(b) all show peaks at the target location. When the narrowband beamformer with Capon weights was used, the dominant peak occurred just above 80°, the cause of which is unknown. The TDWB and FWWB beamformers both however give high resolution estimates of the target locations.

Table K.3 in Appendix K summarises the range and angle estimations discussed in the above sections when an omnidirectional MIMO pattern was transmitted. This table clearly shows that better target angle estimates were obtained from the conventional, Capon and MUSIC spectrums when the range was correct. The best range and angle estimates were however found when TBR was performed with a TDWB beamformer with a calibrated or uncalibrated pattern.

8.3.3.3 MIMO Pattern Designed by Pascale's Design

Figure 8.23 shows the results obtained when a single target was located at 3 m and 20° and a MIMO beampattern, designed by Pascale's design to have a main lobe in the target direction, was transmitted.

The range chart obtained with a calibrated signal is shown in Figure 8.23(a) and the target range of 3 m can be read off it. Similar to the omnidirectional range chart in Figure 8.21(a), the received signal on each channel is correlated with each of the 16 transmitted signals. Unlike the omnidirectional range charts that look very speckled vertically across each receiver channel, the range charts here are very smooth. This prompted further analysis of the signals transmitted by Pascale's design, and they are shown in Figure 8.24. It can be seen that the transmitted signals for each channel are phased shifted versions of the same base signal. The optimum signals generated

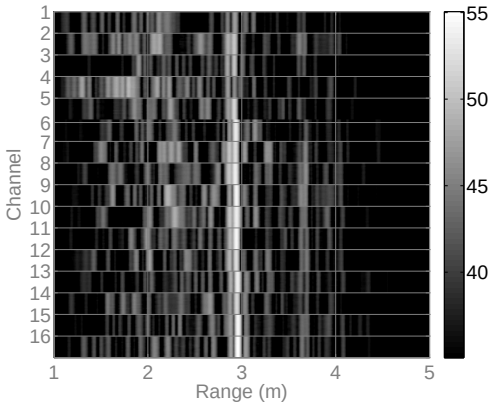

(a) MIMO range chart.

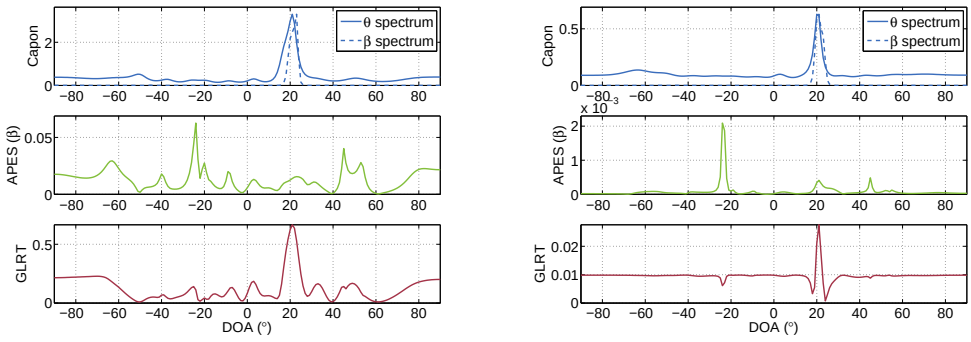

(b) MIMO parameter estimation spectrums.

(c) MIMO parameter estimation spectrums with FWWB processing.

Figure 8.23: Results obtained when a target was located at 20° and 3 m and a calibrated MIMO pattern generated by Pascale's design was transmitted.

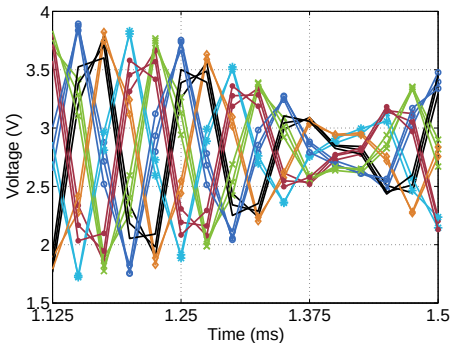

Figure 8.24: The signals transmitted when the beampattern was designed by Pascale's design. The signals have been coloured into groups of overlapping signals, and can be seen to all be time shifted versions of the same base signal.

by Pascales's beamformer are therefore very similar to phased array signals.

Figures 8.23(b) and 8.23(c) show the spectrums obtained when a calibrated set of signals was transmitted without and with FWWB processing respectively. The spectrums in both figures are cleaner in comparison to those obtained with an uncalibrated transmitter signal set. The Capon and GLRT spectrums locate the target correctly in Figure 8.23(b). In Figure 8.23(c), FWWB processing improves the resolution of the spectral peaks, but also increases the side lobe levels. This is because the FWWB beamformer filters the received signals, and therefore only a portion of the target echo signal is used. This has the effect of reducing the SNR of the received signal.

The APES spectrum does not locate the target and identifies a false target at $-20°$. This poor performance can almost certainly be attributed to the phased array-like transmitted signals, and the low measure of linear independence of the signals designed by Pascale's design given by the condition number discussed in Section 8.2.4.3. The simulation results in Section 4.2.2.1 showed that the APES technique was particularly sensitive to dependence between signals.

Figure 8.25 shows the results obtained from the pattern designed by Pascale's design when TBR was performed. In the simulations presented in Section 5.5.3, TBR was only performed when an omnidirectional signal was transmitted. However, even when some beampattern design has been performed on MIMO signals, by Pascale's design or the beampattern matching design, the cross correlation between the transmitted signals should remain low. Therefore, it becomes possible to perform TBR on the received signals, even though transmitter beamforming has already been

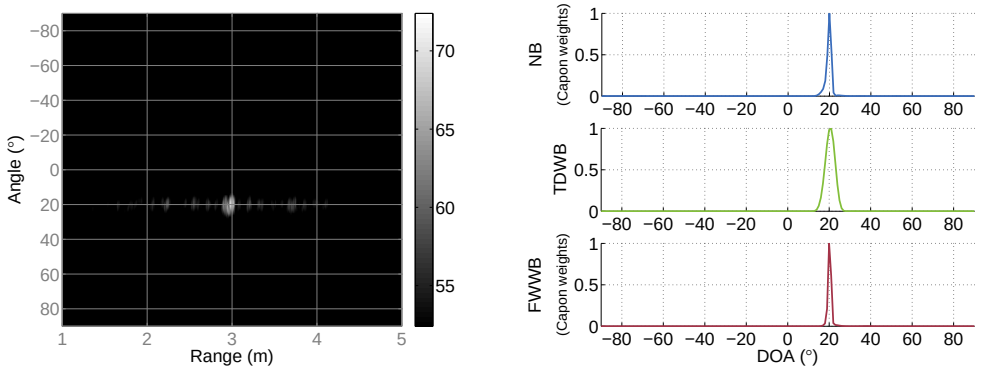

(a) Range-angle chart for TDWB beamformer. (b) Angle estimation spectrums for different beamformers.

Figure 8.25: Results obtained when from TBR when a target was located at 20° and 3 m and a calibrated MIMO pattern generated by Pascale's design was transmitted.

performed at the transmitter.

The range-angle chart in Figure 8.25(a) clearly identifies the target at 20° and 3 m although side lobes are present. The TBR spectrums in Figure 8.25(b) give very high resolution and accurate estimates of the target angle. Therefore, even though the transmitted signals are effectively phased array signals, TBR still performs well.

Table K.4 in Appendix K presents the target range and angle estimates obtained when calibrated and uncalibrated beampatterns generated by Pascale's design were transmitted. The table shows that when excluding the APES target angle estimates, the best results are obtained from the MIMO spectrums when the calibrated pattern was transmitted and FWWB processing was implemented. TBR spectrums give the best estimates when the uncalibrated signal was transmitted.

8.3.3.4 MIMO Pattern Designed by Beampattern Matching

Figure 8.26 shows the results obtained when the transmitted beampattern was designed by the beampattern matching design with a single main lobe at 20°. The range chart in Figure 8.26(a) identifies the target location with a white stripe across all channels at approximately 3 m. The range chart is more speckled than that for a pattern designed by Pascale's design in Figure 8.23(a). This shows that the cross correlation between the signals in the set of transmitted signals was lower than it was for the signals designed by Pascale's design. Vertical lines are still present across some channel blocks, indicating that the correlation is still significantly higher than

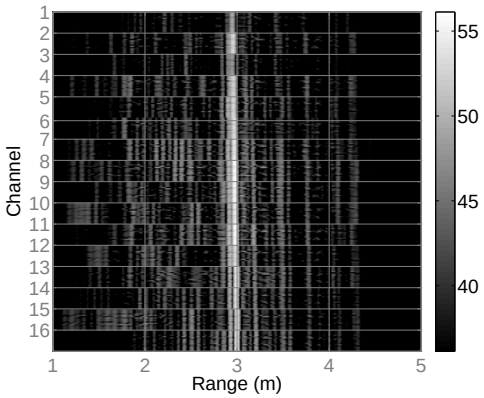

(a) MIMO range chart.

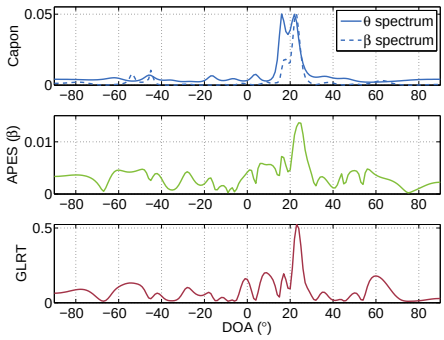

(b) MIMO parameter estimation spectrums.

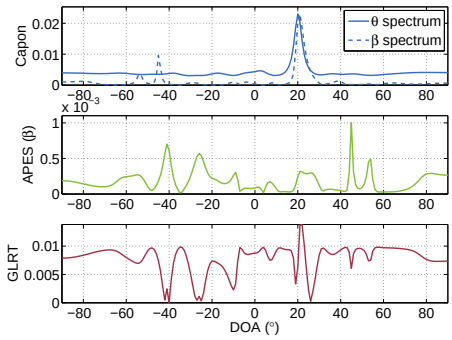

(c) MIMO parameter estimation spectrums with FWWB processing.

Figure 8.26: Results obtained when a target was located at 20° and 3 m and a calibrated MIMO pattern generated by the beampattern matching design was transmitted.

the omnidirectional signals.

Figures 8.26(b) and 8.26(c) show the spectrums obtained when a calibrated pattern was transmitted without and with the implementation of processing by the FWWB beamformer respectively. When no FWWB processing was performed, all of the spectrums give target angle estimates true to the actual target location although they are noisy. The APES spectrum locates the target and this indicates a reduction in the correlations between the transmitted signals compared to the signals of Pascale's design. When FWWB processing was performed, giving rise to the spectrums in Figure 8.26(c), the APES technique no longer gives a good target estimate. The resolution of Capon spectrums improves, and the double-lobed peak reduces to a single lobe. The resolution of the GLRT also improves at the target location but the level of the spectrum at other angular directions increases. This is again attributed to the reduction in the SNR which arises when the FWWB beamformer is implemented.

Figure 8.27 shows the results obtained when the beampattern matching design was used to optimise the transmitted signals and TBR was implemented. The range-angle chart in Figure 8.27(a) identifies the target at 20° and 3 m without any ambiguity. All of the TBR spectrums shown in Figure 8.27(b) have high resolution peaks close to the target location, although their accuracy is not as good as that in Figure 8.25(b) for the pattern designed by Pascale's design.

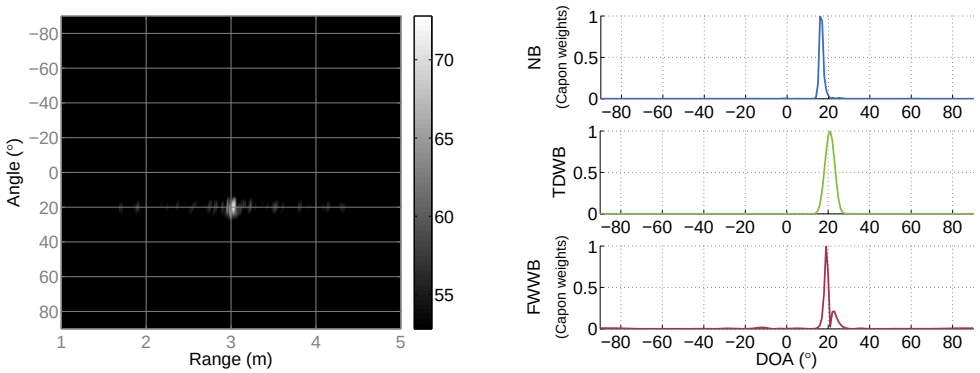

(a) Range-angle chart with TDWB beamformer. (b) Angle estimation spectrums for different beamformers.

Figure 8.27: Results obtained with transmitter beamforming when a target was located at 20° and 3 m and a calibrated MIMO pattern generated by the beampattern matching design was transmitted.

Table K.5, gives the range and angle estimates obtained from the different methods. The results for the beampattern matching design indicate that it is a better MIMO beampattern design technique than Pascale's design, when only one main lobe is required because the cross correlations between the transmitted signals were lower. However, more accurate parameter estimation results (except for the APES technique) were obtained when Pascale's beampattern was transmitted, as can be seen by comparing Tables K.4 and K.5 in Appendix K.

8.3.4 Three Targets

Three targets were located at angular locations $-20°$, $0°$ and $20°$ all with ranges of 3 m from the centre of the array, as prescribed in the protocol in Section 7.2.1. Target parameter estimation techniques were then performed when the omnidirectional pattern and the four patterns with three main lobes presented in Section 8.2 above were transmitted.

8.3.4.1 Phased Array Pattern Designed by Beampattern Matching

Figure 8.28 shows the results when phased array signals designed by the beampattern matching method to have main lobes at $-20°$, $0°$ and $20°$ were transmitted and three targets were present. The target range of 3 m is clearly indicated on the range chart in Figure 8.28(a). Unlike the clean and solid line of the phased array range chart when only one target was present in Figure 8.20(a), this range chart has a second fainter line at a range slightly larger than 3 m. This is because the ranges of the three targets varied slightly around 3 m.

The range-angle chart generated with the TDWB beamformer in Figure 8.28(b) shows peaks at the three target locations. However, the range of the three targets varies slightly, with the target at $-20°$ being almost 100 mm off the desired location. This is most likely due to a true target location which is not exactly 3 m, and not due to inaccuracies in the estimation technique. Also, the peak at $20°$ has the

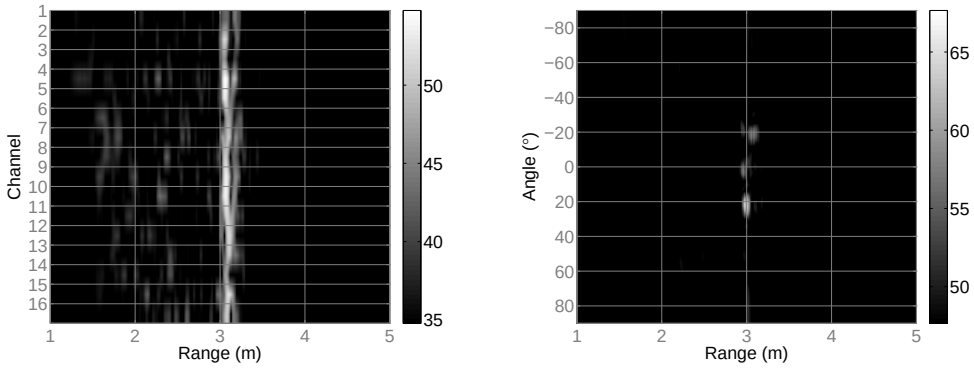

(a) Phased array range chart.

(b) Range-angle chart with TDWB beamformer.

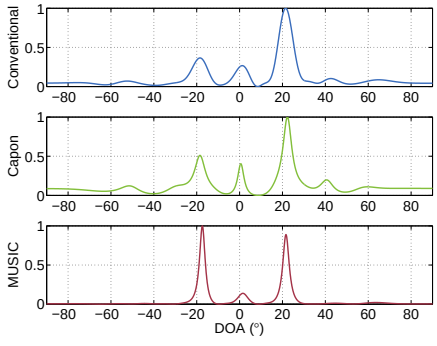

(c) Phased array angle estimation spectrums.

Figure 8.28: Results obtained when three targets were located at $-20°$, $0°$ and $20°$ and range 3 m and an uncalibrated phased array pattern generated by the beampattern matching design was transmitted.

highest amplitude and the peak at 0° has the lowest amplitude. This can possibly be explained by the beampattern in Figure 8.13 where the uncalibrated beampattern transmitted the most power in direction 20° and the least in direction 0°.

Figure 8.28(c) shows the spectrums obtained when an uncalibrated pattern was transmitted. Surprisingly, despite the expected poor performance of the phased array due to the possibility of coherent reflections from the targets, peaks are visible close to the three target locations of −20°, 0° and 20° in all of the spectrums. Coherence was probably not an issue because, as can be seen in the range-angle chart, the range of the target at −20° is slightly longer than that at 20°. Therefore, there would be a time delay between the echoes received from the two targets, and coherence would be reduced.

The target at 20° has the highest peak in all the target angle detection spectrums except for the MUSIC spectrum, where the target at −20° has the highest peak. The target at 0° has the lowest peak as in the range chart. The differing peak amplitudes could possibly also be attributed to the beampattern, as described above.

The calibrated pattern in Figure 8.13 transmitted power almost equally in the directions −20° and 0°, while that transmitted in the direction 20° was significantly reduced. Despite this, the spectrums obtained when calibration was performed were almost identical to those in Figure 8.28(c) when the uncalibrated pattern was transmitted, with peak power being received from 20°. This suggests that the variability of the spectral peaks can rather be attributed to the physical setup of the targets, with the target at 20° reflecting more strongly. This could happen if the orientation of the three targets differed.

Table K.6 in Appendix K shows the estimates of range and target angle obtained when the phased array pattern designed by beampattern matching design was transmitted. The table shows that the results were similar regardless of whether the transmitter pattern was calibrated or not. FWWB processing did not change the results significantly either.

8.3.4.2 Phased Array Pattern Designed by the LCMV

Figure 8.29 shows the results obtained when a phased array pattern designed by the LCMV to have three main lobes at −20°, 0° and 20° was transmitted. The target range of 3 m is correctly determined in the range chart in Figure 8.29(a). However,

the peak amplitude of the cross correlation is almost 10 dB below the peak in the range chart obtained with the beampattern matching phased array pattern in Figure 8.28(a). This is due to the reduced amplitude of the phased array signals designed by the LCMV. Despite the lower SNR of the LCMV pattern, the range chart does not display more noise, indicating that the SNR is below the 20 dB scale of the range chart after cross correlation for both phased array patterns.

The target locations on the range-angle chart in Figure 8.29(b) agree with those obtained when the phased array beampattern matching pattern was transmitted, as shown in Figure 8.28(b). This confirms that the longer range of the target at $-20°$ can be attributed to the physical target placement and not inaccuracies in the estimation. The amplitudes of each of the peaks are similar to one another in the LCMV phased array range-angle chart.

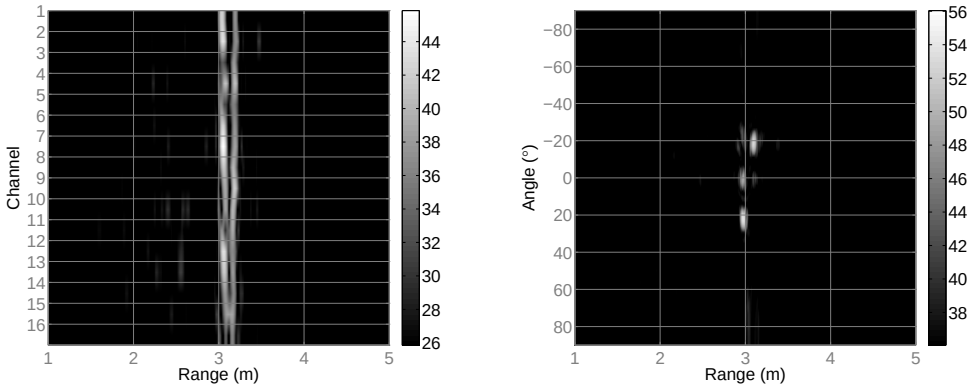

(a) Phased array range chart.

(b) Phased array range-angle chart with TDWB beamformer.

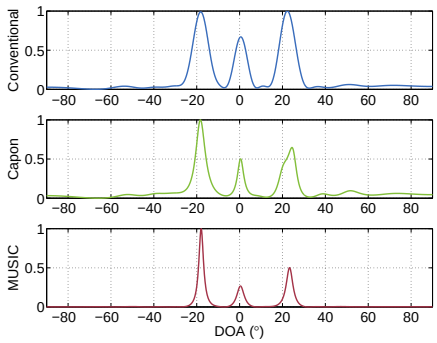

(c) Phased array angle estimation spectrums.

Figure 8.29: Results when three targets were located at $-20°$, $0°$ and $20°$ and range 3 m and an uncalibrated phased array pattern generated by the LCMV was transmitted.

Figure 8.29(c) shows the spectrums obtained for the uncalibrated transmitted pattern. In all of the spectrums, three clear peaks are visible close to the target location. This was again unexpected because high correlation between the echoes received from the three targets was expected resulting in three signals which are close to coherent and thus poor performance from the estimation techniques. All of the spectrums, but particularly the Capon spectrum, show three peaks closer in amplitude when compared to the varying amplitudes obtained with the beampattern matching design in Figure 8.28(c). The results with calibration were very similar to the uncalibrated results displayed in this section.

Table K.7 in Appendix K shows the target range and angle estimations obtained when a phased array pattern with three main lobes designed by the LCMV was transmitted. The Capon spectrum obtained with calibrated transmitted signals and FWWB processed received signals had a target estimate of 60° for the third target, where the spectrum is known to have identified the target. This erroneous estimate is due to the threshold value used in obtaining estimates of the target's angular location from the spectrums. If the threshold value was smaller, this error would not have occurred. However, the chosen threshold was found to be optimum under most conditions.

8.3.4.3 Omnidirectional MIMO Pattern

The results obtained when an omnidirectional MIMO pattern was transmitted are shown in Figure 8.30. The 3 m range of the three targets located in the radar field of view cannot be determined from the uncalibrated range chart shown in Figure 8.30(a) or the calibrated range chart. The range chart appears very noisy. However, the estimated raw SNR of 3.2 dB for the omnidirectional signal was only 0.2 dB below that achieved with three targets when a phased array pattern designed by beampattern matching was transmitted. The poor identification of the target is then almost certainly because of the reflections from all directions from the anechoic chamber walls and walkway which are received when an omnidirectional pattern is transmitted.

When the range was determined by cross correlation the error was large and therefore the spectrums do not identify the target locations of $-20°$, $0°$ and $20°$, regardless of whether FWWB processing is applied or not. These graphs are not shown. Figures 8.30(b) and 8.30(c) show the spectrums obtained when the range estimate was forced to 2.91 m, close to the true target location. Before FWWB processing

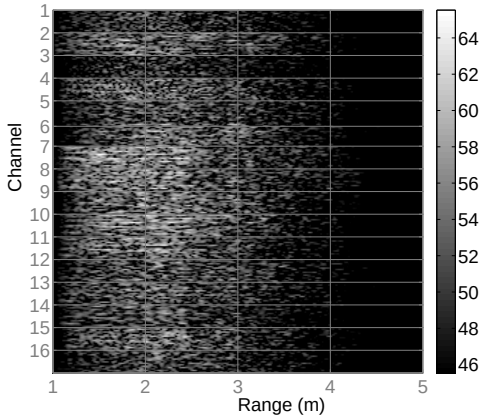

(a) MIMO range chart.

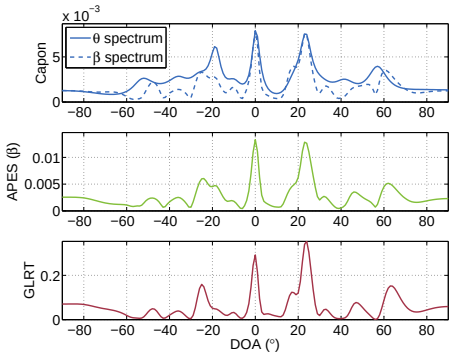

(b) MIMO parameter estimation spectrums obtained when range is manually chosen to be 2.91 m.

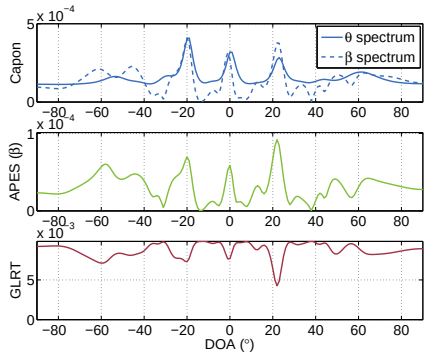

(c) MIMO parameter estimation spectrums obtained when range is manually chosen to be 2.91 m with FWWB processing.

Figure 8.30: Results obtained when three targets were located at $-20°$, $0°$ and $20°$ and range 3 m and an uncalibrated omnidirectional MIMO pattern was transmitted.

was implemented in Figure 8.30(b), all four of the spectrums show peaks close to the target locations. However, the spectrums are not as clean or as accurate as those obtained from the phased array techniques.

When FWWB processing was implemented as shown in Figure 8.30(c), the peaks in the Capon β and APES spectrums are made clearer and shifted slightly closer to the true target locations. The target location estimates in the GLRT are lost. The results obtained when the signal was calibrated were similar.

Figure 8.31 shows the results obtained when TBR was performed. The range-angle chart in Figure 8.31(a) shows many reflections, but the target located at $20°$ and 3 m is distinguishable from the surrounding reflections. There is indication that two other targets are present at $-20°$ and $0°$, but the amplitude of these peaks is similar

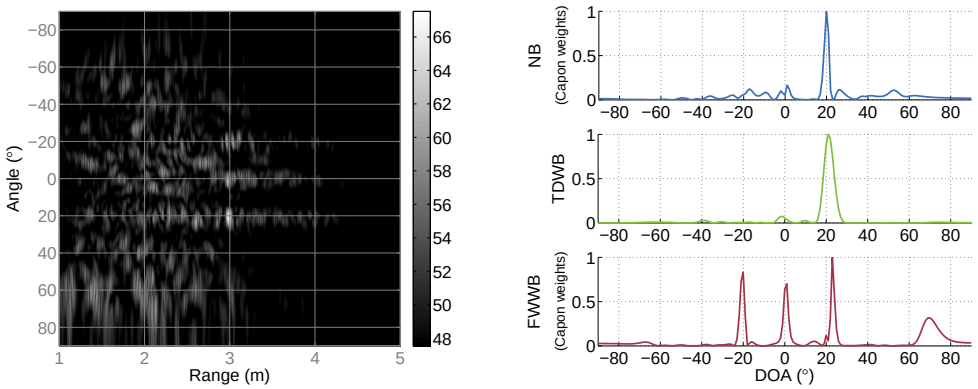

(a) MIMO range-angle chart with TDWB beamformer.

(b) Angle estimation spectrums for different beamformers.

Figure 8.31: Results obtained from TBR when three targets were located at $-20°$, $0°$ and $20°$ and range 3 m and an uncalibrated omnidirectional MIMO pattern was transmitted.

to that of the reflections at $60°$ whose cause is unknown.

Of the three TBR spectrums in Figure 8.31(b), the FWWB beamformer is the only one to locate the three targets, giving high resolution estimates of their locations. The narrowband and TDWB beamformers only estimate the location of the strongest reflecting target at $20°$. The partial estimation of the targets can also be attributed to the unaligned range of the three targets, as the TBR spectrums are effectively cross sections of the range-angle charts.

Table K.8 in Appendix K summarises the estimates of range and target angular location obtained under the different conditions when the omnidirectional pattern was transmitted.

8.3.4.4 MIMO Pattern Designed by Pascale's Design

Figure 8.32 shows the results obtained when a calibrated pattern designed by Pascale's design with three main lobes was transmitted and three targets were present. In the range chart in Figure 8.32(a), a stripe can be made out at approximately 3 m where the three targets were located. The chart does not identify the target range as clearly as it was identified when phased array patterns were transmitted.

The range chart does not have vertical stripes in each channel block as in Figure 8.23(a). This suggests that when multiple main lobes are desired, the optimisation

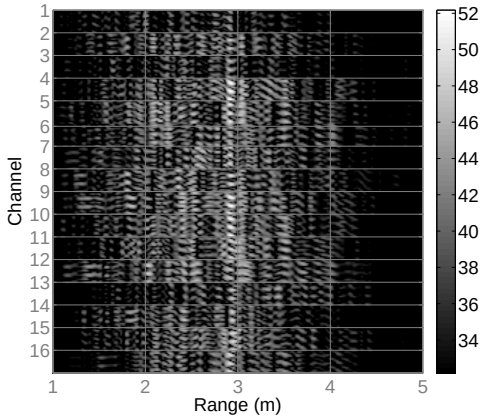

(a) MIMO range Chart.

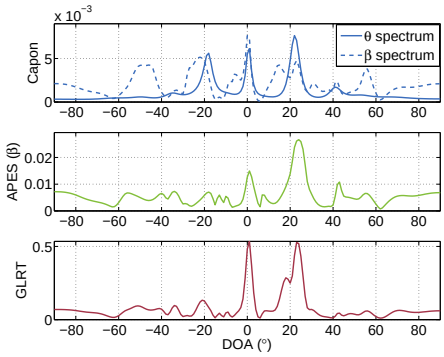

(b) MIMO parameter estimation spectrums.

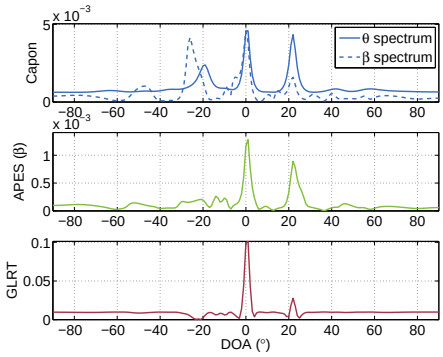

(c) MIMO parameter estimation spectrums with FWWB processing.

Figure 8.32: Results obtained when three targets were located at $-20°$, $0°$ and $20°$ and range 3 m and a calibrated MIMO pattern generated by Pascale's design was transmitted.

of Pascale's design results in a lower cross correlation between the signals in the transmitter signal set compared to when one main lobe is required.

Figures 8.32(b) and 8.32(c) show the spectrums obtained when the transmitted signals were calibrated. The best target angle estimates are obtained with the Capon θ spectrum, with and without FWWB processing. The Capon θ spectrum applied to MIMO signals is identical to that used to determine the Capon spectrum for phased array systems, and therefore no MIMO techniques are in fact implemented. However, the resolution of the spectrums obtained with the Capon θ spectrum applied to MIMO data is better than the resolution of the phased array Capon spectrums in Figures 8.28(c) and 8.29(c).

The Capon β spectrum is a noisy spectrum, which does not clearly identify the

targets. It is cleaned up well by FWWB processing but does still not estimate the target locations accurately. The GLRT and APES spectrums both identify the targets at 0° and 20°, but do not locate the target at −20°. The resolution of these two spectrums is increased and contrary to other findings, the noise level is decreased when FWWB processing was implemented. The results obtained with an uncalibrated signal were similar, except that the APES spectrum did not give any target location estimates, again attributable to the low measure of linear independence of the transmitted signal set.

Figure 8.33 presents the results obtained when a pattern designed by Pascale's design was transmitted and TBR was performed. The three target locations are clearly identified by the range-angle chart in Figure 8.33(a). Because each target's range is slightly different, all of the angle estimation spectrums in Figure 8.33(b) do not identify the three angular target locations. The centre target is well identified by the three techniques. The TDWB beamformer TBR spectrum shows peaks at all three target locations, but the peak amplitudes vary significantly.

Table K.9 in Appendix K show the target range and angle estimates obtained from the results presented above, as well as those obtained from the uncalibrated signal.

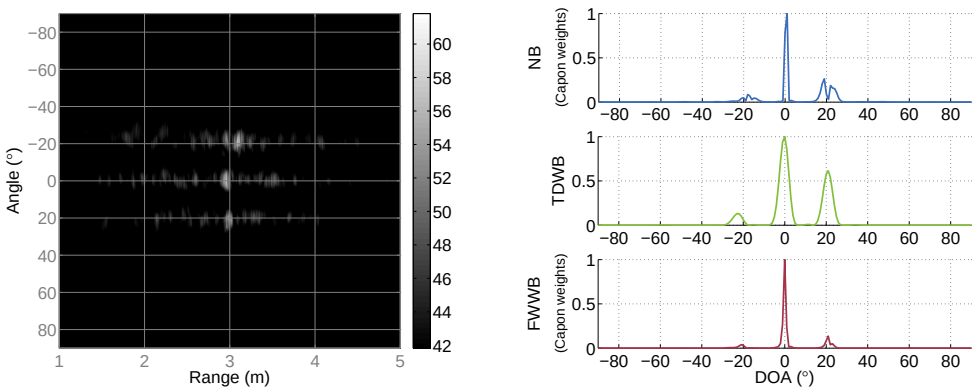

(a) MIMO range-angle chart with TDWB beamformer.

(b) Angle estimation spectrums for different beamformers.

Figure 8.33: Results obtained when three targets were located at −20°, 0° and 20° and range 3 m and a calibrated MIMO pattern generated by Pascale's design was transmitted.

8.3.4.5 MIMO Pattern Designed by Beampattern Matching

Figure 8.34 shows the results obtained when a MIMO pattern designed by the beampattern matching design to have three main lobes was transmitted. In the range chart in Figure 8.34(a), a stripe at close to 3 m can be discerned but the noise level is extremely high.

Figures 8.34(b) and 8.34(c) show the spectrums obtained when uncalibrated signals were transmitted without and with FWWB processing respectively. These spectrums are remarkably similar to those obtained when the MIMO pattern designed by Pascale's design was transmitted, as shown in Figure 8.32.

In Figure 8.34(b), the Capon θ spectrum clearly identifies the three target angles.

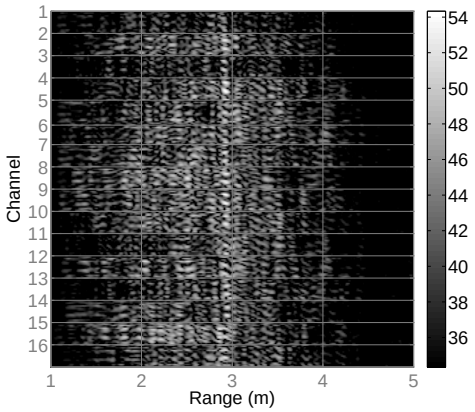

(a) MIMO range chart.

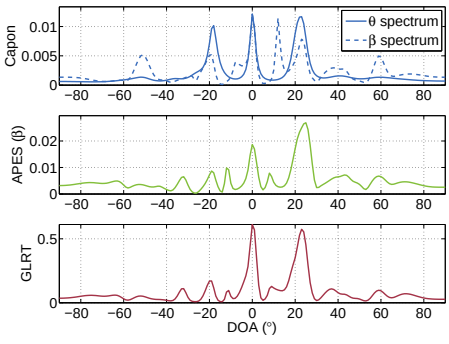

(b) MIMO parameter estimation spectrums.

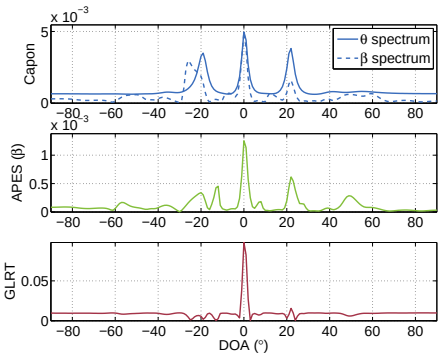

(c) MIMO parameter estimation spectrums with FWWB processing.

Figure 8.34: Results obtained when three targets were located at $-20°$, $0°$ and $20°$ and range 3 m and a calibrated MIMO pattern generated by the beampattern matching design was transmitted.

The targets at 0° and 20° were well identified by the APES and GLRT spectrums but peaks at angles where no targets were present makes it difficult to identify the number of targets. The results of FWWB processing, shown in Figure 8.34(c) give improved target angle estimation for the two Capon spectrums. The APES spectrum was improved by FWWB processing, although erroneous peaks are still present. After FWWB processing, the GLRT only clearly identifies the centre target.

Figure 8.35 shows the results obtained from TBR when a MIMO pattern generated by beampattern matching was transmitted. These results are an improvement on the parameter estimation results in Figure 8.34. The range and angle of each target can be read off the range-angle chart in Figure 8.35(a), although high side lobes are present around the target estimates, with the target at −20° worst affected.

None of the angle estimation spectrums in Figure 8.35(b) clearly identify all three of the targets, but the narrowband spectrum comes the closest. The TDWB and FWWB spectrums do however identify one and two target locations respectively with high resolution and no false peaks.

Table K.10 in Appendix K shows the target location estimates obtained from the results for the MIMO pattern designed by beampattern matching. It can be seen that the best results are obtained when the transmitted signals were calibrated.

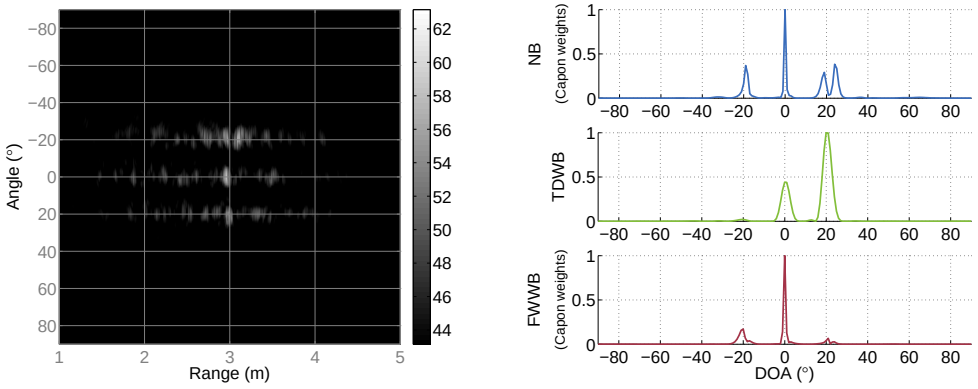

(a) MIMO range-angle chart with TDWB beamformer.

(b) [Angle estimation spectrums for different beamformers.

Figure 8.35: Results obtained from TBR when three targets were located at −20°, 0° and 20° and range 3 m and a calibrated MIMO pattern generated by the beampattern matching design was transmitted.

8.3.5 Two Closely Spaced Targets

Xu et al. [32] claimed that MIMO techniques can be used to obtain high resolution spectrums for target location. To verify if MIMO radar can resolve two closely spaced targets better than phased array, two targets were placed at a range of 3 m separated by 6°, with one target at 17° and the other at 23° as prescribed in the protocol in Section 7.2.2.

The uncalibrated and calibrated omnidirectional pattern, and beampatterns with single main lobes at 20° were transmitted. Only the results from the pattern giving the best target estimations are presented here. The range charts are not presented, as they were similar to those obtained with a single target located at 20°. The spectrums and range-angle charts of interest are included. Tables with the target range and angular location estimates are given in Tables K.11 to K.14 in Appendix K. Because of the proximity of the two targets, the threshold for determining the target angles from the spectrums was reduced to half of the spectrum's maximum value.

8.3.5.1 Phased Array

Figure 8.36 shows the results obtained when two targets were separated by a small angle. The range-angle chart in Figure 8.36(a) has a significantly larger white smear at approximately 20° and 3 m than the range-angle chart for the same transmitted signal when only one target was present as shown in Figure 8.20(c), but it does not differentiate between two distinct targets.

Figure 8.36(b) shows the spectrums obtained when a phased array pattern with a main lobe at 20° was transmitted. The transmitted pattern was uncalibrated, because it led to the MUSIC spectrum giving better results. The other spectrums were almost identical regardless of whether a calibrated pattern was transmitted or not.

The conventional and Capon spectrums do not identify the two targets. However, the MUSIC spectrum does show a peak split into two lobes each peaking at 18° and 21° respectively. Therefore, although the MUSIC spectrum does not clearly resolve the two targets, it is different to that obtained when only one corner reflector was present.

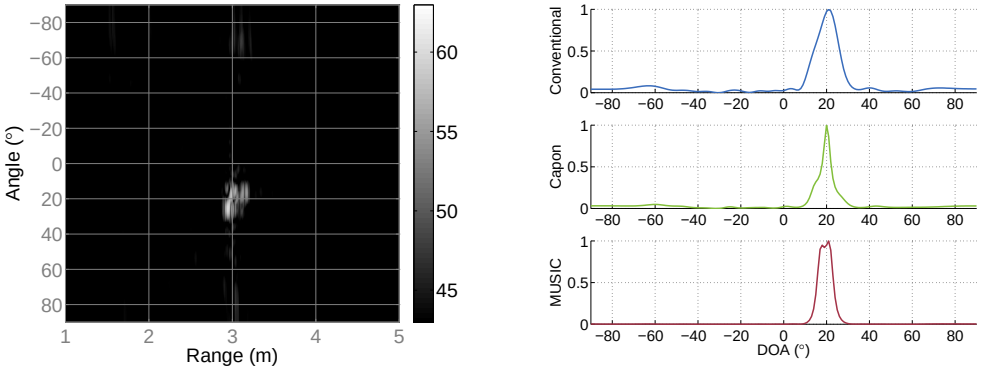

(a) Phased array range-angle chart with TDWB beamformer.

(b) Phased array angle estimation spectrums.

Figure 8.36: Results obtained when two closely spaced targets were present and an uncalibrated phased array pattern was transmitted.

Table K.11 shows the range and angle estimates. The range estimates were all accurate to within 0.02 m. The performance of the angle estimation techniques was poorer, and only the conventional, Capon and range-angle spectrum with a TDWB beamformer estimated the two targets to be located on either side of 20°.

8.3.5.2 Omnidirectional MIMO

The results obtained when an uncalibrated MIMO omnidirectional pattern was transmitted are shown in Figure 8.37.

Figure 8.37(a) shows the spectrums obtained when the target range was identified by cross correlation of the raw received signals. Besides the Capon θ spectrum, all of the spectrums are noisy. A maximum in the Capon β spectrum occurs at 14°, which is 3° from the true target location. The APES and GLRT spectrum both peak at −3°, and have many false peaks of similar amplitude, thus giving no information about the true target location.

Figure 8.37(b) shows the spectrums after FWWB processing was implemented on the received signal which improves the quality of the target angle estimates resulting in all of the spectrums peaking close to the target location. The Capon β and APES spectrums both have peaks on either side of 20°. Table K.12, documents that the Capon β spectrum gives angle estimates of 19° and 26° after FWWB processing, and the APES spectrum estimates 19° and 27°. Since the true target angles were 17° and 23°, the accuracy of the FWWB Capon and APES estimates is not good,

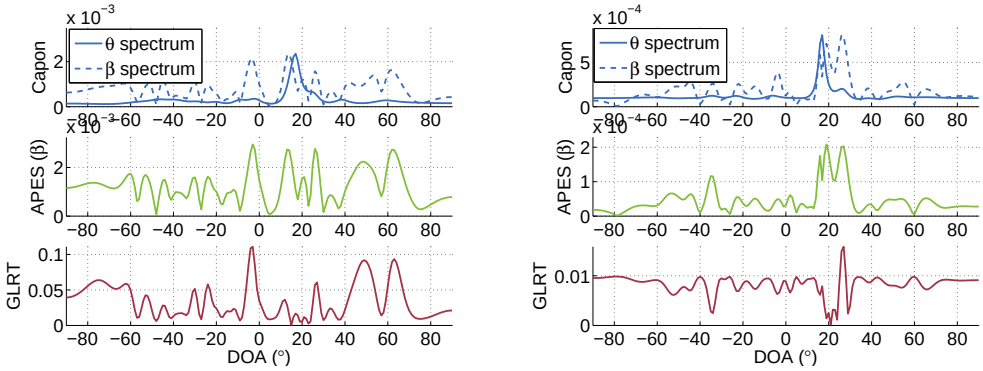

(a) MIMO parameter estimation spectrums.

(b) MIMO parameter estimation spectrums with FWWB processing.

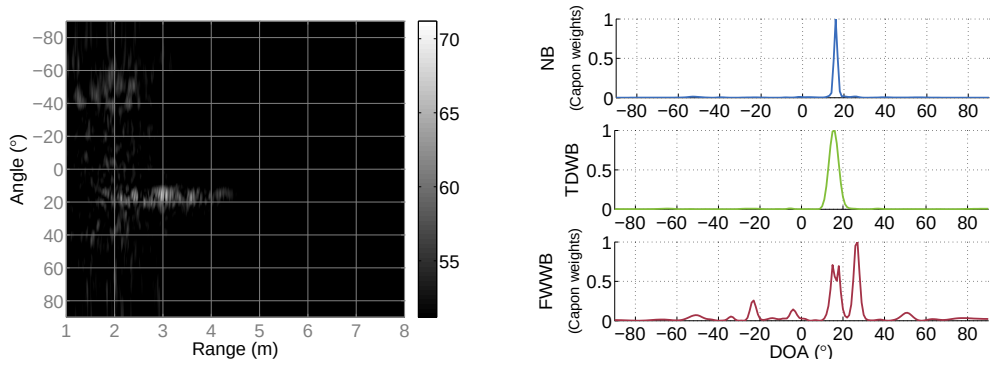

(c) TBR range-angle chart with TDWB beamforming.

(d) TBR angle estimation spectrums with different beamformers.

Figure 8.37: Spectrums obtained when two targets were present and an uncalibrated MIMO omnidirectional pattern was transmitted.

but the techniques do clearly resolve the two targets.

Figure 8.37(c) shows the TBR range-angle chart when the TDWB beamformer was used. The chart clearly identifies a target at approximately 20° but does not resolve it into two targets that were present on either side of 20°. The range of the targets is difficult to determine from this range angle chart, largely due to the presence of high amplitude side lobes in the range-axis. The range-angle chart is, however, cleaner than either of the charts obtained with different target configurations when an omnidirectional pattern was transmitted shown in Figures 8.22(a) and 8.31(a).

Figure 8.37(d) shows the TBR spectrums. The narrowband and TDWB spectrums only locate one of the two targets. The FWWB clearly locates two targets at 15° and 27°, which differ from the true target locations by 2° and 4° respectively.

The range and angle estimates obtained with an omnidirectional signal when two

targets were separated by 6° are given in Table K.12 in Appendix K.

8.3.5.3 MIMO Pattern Designed by Pascale's Design

The results obtained when a calibrated MIMO pattern designed by Pascale's design was transmitted are shown in Figure 8.38. In Figure 8.38(a) the Capon β spectrum can be seen to have a second lobe to its peak at approximately 23°. The APES spectrum contained no useful information, as for a single target in Figure 8.23(b). This is certainly due to the high cross correlation between the signals in the transmitter signal set. The GLRT spectrum has a peak close to 20°, but does not identify that two targets were present.

After FWWB processing, in Figure 8.38(b), the Capon β spectrum shows two peaks of similar amplitude at 17° and 24°. The GLRT shows a wide peak around 20°,

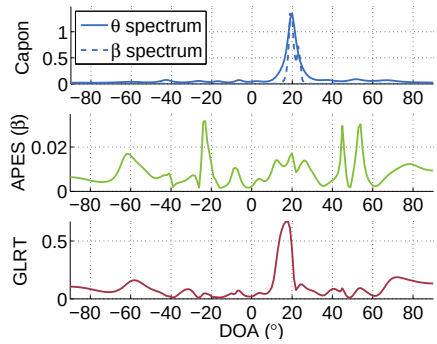

(a) MIMO parameter estimation spectrums.

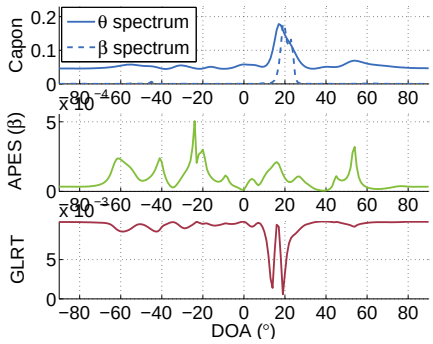

(b) MIMO parameter estimation spectrums with FWWB processing.

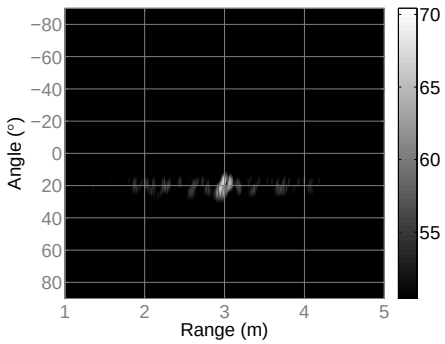

(c) TBR range-angle chart with TDWB beamformer.

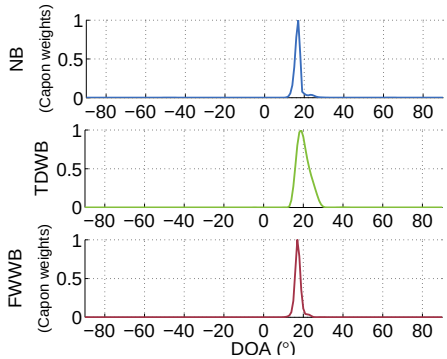

(d) TBR angle estimation spectrums with different beamformers.

Figure 8.38: Results obtained when two closely spaced targets were present and a calibrated MIMO pattern designed by Pascale's design was transmitted.

indicating that the two targets are represented but not resolved, but this information is lost when FWWB processing was implemented and the resolution of the spectrum was decreased.

Figure 8.38(c) is the TBR range-angle chart, which identifies a large target at approximately 20° and 3 m but does not resolve two targets at 17° and 23°. Similarly, the TBR spectrums in Figure 8.38(d) only identify a single target. On close analysis of the narrowband and FWWB spectrums a second peak of less than a tenth of the amplitude of the main peak can be made out at about 23° . Therefore, the narrowband and FWWB spectrums do give some indication of the presence of a second target. The low amplitude of the spectral peak means that most detectors will not, however, pick up the presence of the second target.

The target range and angle estimations are given in Table K.13. The Capon parameter estimation spectrum gives the best angle estimates.

8.3.5.4 MIMO Pattern Designed by Beampattern Matching Design

Figure 8.39 shows the results obtained when a MIMO beampattern generated by the beampattern matching design was transmitted. The Capon β spectrum shows a global maximum at 24° and a local maximum at 19°. The APES spectrum was an improvement on the one obtained from Pascale's pattern and had a peak at 28°. The GLRT has two peaks close to the target locations with one at 17° and a second at 26°.

Once FWWB processing was implemented, shown in Figure 8.39(b), the side lobe levels for all of the spectrums increase, with false peaks unrelated to the target location forming. However, the Capon θ spectrum does begin to resolve the two target locations after FWWB processing was implemented.

Figure 8.39(c) shows the TBR range-angle chart. A target was easily located at 20° and 3 m from this chart, but the technique does not resolve the two targets that were present.

The TBR spectrums in Figure 8.39(d) again locate a target at approximately 20°. The FWWB spectrum has a peak at 24° and a second local maximum at 26° but the other spectrums give no indication that two discrete targets were present in the radar's field of view.

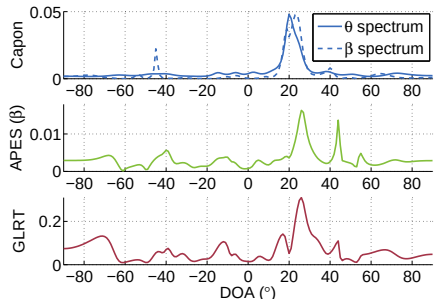

(a) MIMO parameter estimation spectrums.

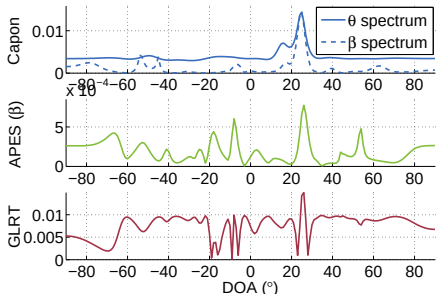

(b) MIMO parameter estimation spectrums with FWWB processing.

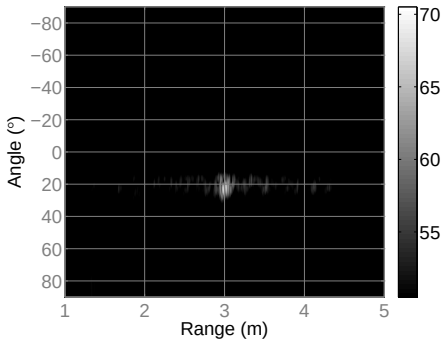

(c) TBR range-angle chart with TDWB beamformer.

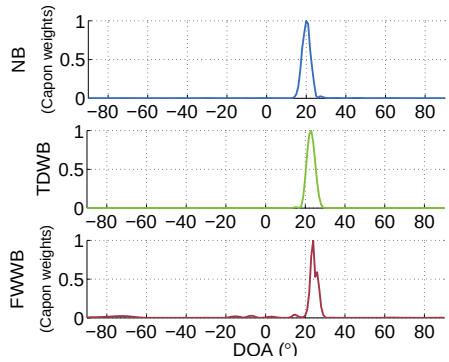

(d) TBR angle estimation spectrums with different beamformers.

Figure 8.39: Spectrums obtained when two closely spaced targets were present and a MIMO pattern generated by the beampattern matching design was transmitted.

Table K.14 in Appendix K gives the estimations obtained for range and angle.

8.3.6 Analysis of Parameter Estimation Results

The objective of building a phased array transmitter was to extend the accuracy of the phased array model of a radar system, to validate MIMO techniques on a hardware system, and to compare phased array and MIMO techniques. The parameter estimation experiments serve to contribute towards the fulfilment of the latter two outcomes. An evaluation of the different parameter estimation techniques, beampatterns and the effect of calibration can be performed with the results obtained. The parameter estimation results are analysed and compared to one another below, with reference to the graphs presented in the above sections, the tables in Appendix K and the simulation results.

8.3.6.1 Phased Array

When only one target was present, simulations showed that phased array techniques can accurately predict the target locations, and this was confirmed in experimentation. The target range was easily and accurately determined with a single target 3 m from the array in the anechoic chamber. The range-angle charts also gave unambiguous estimates of the target range and angle. In the simulations described in Section 4.1 and in the experimental results the conventional spectrum had the lowest resolution, and the MUSIC spectrum had the highest resolution. The DML performed poorly in experimentation compared to simulation. The experimental angle estimations were to within $\pm 2^\circ$ of the true location without any compensation for the wideband transmitted signals except for the DML estimates.

Simulations in Section 5.4 showed that the performance of phased array parameter estimation techniques with wideband signals was relatively robust but with the implemented signal bandwidth of 4 kHz, FWWB beamforming improved the accuracy of the estimations slightly. The more taps, the better the improvement, and the best accuracy was obtained with 20 taps. The phased array experimental results were found to be accurate to within the system uncertainties without any wideband processing. When a 5 tap FWWB beamformer was applied to the experimental received signals, the target angle estimations did not improve and in some cases the estimation accuracy even deteriorated. Wideband processing was, however, found to improve the experimental range-angle chart, which was cleaner when the TDWB beamformer was used compared to the narrowband beamformer with Capon weights. This result was not illustrated by the wideband phased array simulations.

Simulations showed that when multiple coherent signals were received, the phased array radar did not perform well. When multiple targets were placed at equal distances from the centre of the array, the target echoes were expected to be close to coherent. Therefore, for the experiments with multiple targets, the phased array radar was not expected to perform well. Surprisingly, experiments showed that the phased array parameter estimation techniques still provided good estimates of the targets' angular locations when three targets were present. This is probably due to the misalignment of the three targets, resulting lower coherence than expected.

The targets' range was determined accurately to within 0.01 m when the phased array pattern designed by beampattern matching was transmitted. When the lower powered LCMV phased array pattern was transmitted, the range accuracy was lower, with a maximum error of 0.11 m. This suggests that accuracy in range estimation is

heavily dependent on SNR. The experimental target angle estimation appeared less effected by low power, with the pattern designed by beampattern matching giving similar results to that designed by the LCMV. The angle estimates obtained from the spectrums extracted from the range-angle plots were of lower accuracy than the parameter estimation spectrums. This was because the ranges of the three targets were different. Better target angle estimates could have been acquired if they were read straight off the range-angle chart, or if multiple spectrums at each of the target ranges had been extracted from the range-angle chart.

When two targets were only separated by 6°, the conventional and Capon spectrums did not resolve them. However, the high resolution MUSIC spectrum did just resolve the two targets.

Calibration of the transmitter signals had little effect on the phased array results for one, two or three targets.

8.3.6.2 MIMO

MIMO radar was expected to outshine phased array when locating multiple targets and especially those separated by a small distance. When only one target was present, little difference was expected between the phased array and MIMO results. The experiments showed otherwise.

The parameter estimation performance obtained with an omnidirectional MIMO pattern differed significantly to that obtained with directional MIMO patterns. In the case of omnidirectional signals, the range could not be resolved by cross correlating the received signals with the transmitted signals, regardless of whether one, two or three targets were present. This had the knock-on effect of a signal segment which did not contain echoes of the transmitted signal being selected as an input to the parameter estimation algorithms. The MIMO target parameter estimation techniques therefore performed poorly and the target location could not be identified. This problem was identified in simulations in Section 4.2.2.2 and experiments confirmed it.

If the correct signal segment was used, all three spectrums located the target angle with relatively good clarity, although the spectrums were significantly more noisy than the simulated spectrums in Section 4.2.2. For a single target, the angle estimates were accurate to within 1° in most cases. The parameter estimation

accuracy of the Capon, APES and GLRT spectral techniques was similar when an omnidirectional pattern was transmitted and they all had similar resolution, which was higher than the phased array resolution.

In the case of an omnidirectional transmitted pattern, TBR offered remarkable improvement over the parameter estimation spectrums and also allowed range to be estimated. This result was suggested by the TBR simulation in Section 4.2.4. When the TDWB beamformer was used for TBR the range and angle estimates were definitively better than the range estimates obtained with any of the other techniques. The range estimates had a maximum error of 0.02 m, regardless of the number of targets.

When directional patterns were transmitted, the Capon θ spectrum (which is technically not a MIMO technique) was the most robust spectrum and identified the target locations clearly in most cases. The Capon β spectrum was often very noisy but was improved by the implementation of FWWB processing. The APES spectrum was poor, and especially for a single target, often failed to identify the target location. This was probably due to the low measure of linear independence of the transmitted signals as described in Section 8.2.4. The GLRT performed slightly better than the APES method and always located a single target. None of the MIMO techniques reliably identified three targets.

For the directional patterns, TBR gave results which were exceptional in comparison to the parameter estimation spectrums. Even if the parameter estimation spectrums did not identify the target angles, the range-angle chart and spectrums obtained from TBR were able to locate the targets, when one or three targets were present with high resolution and extremely low side lobe levels. When three targets were present, better TBR spectrums could have been obtained by plotting a spectrum at the exact range estimated for each target, instead of only plotting the spectrum at one range, due to the inaccuracies in the target placement.

In general, the effect of FWWB processing was to improve the resolution of the target parameter estimation spectrums. However, it also often increased the side lobe levels seen on the spectrums, because filtering the signal leads to an SNR reduction. These effects of the FWWB beamformer were as predicted in the simulations in Section 5.5.4. When three targets were present, FWWB processing did not appear to increase the side lobe levels. FWWB processing led to the useful angle information displayed in the narrowband spectrums of one or more targets being lost in a number of instances, especially for the APES and GLRT spectrums.

Two closely spaced targets were not clearly resolved by MIMO techniques in most cases. The omnidirectional pattern gave the best results, however, and the Capon β and APES spectrum clearly resolved the two targets after FWWB processing. The TBR FWWB spectrum also clearly identified two targets. The directional patterns did not clearly resolve the targets under any circumstances.

In summary, provided that the range was accurately measured, the best Capon β, APES and GLRT spectrums were obtained when an omnidirectional pattern was transmitted. This is almost certainly due to the high degree of orthogonality of the transmitted signals and therefore also the received target echoes. Improvement in the spectrums and target angle estimations, particularly for the directional patterns, was achieved by calibrating the transmitted pattern. TBR gave exceptionally clean and high resolution target range and angle estimates for all transmitted patterns.

8.3.7 Comparison of MIMO and Phased Array

Target parameter estimation results were rated on the accuracy of the range and angle estimates. The hypothesis before experiments were performed, was that the phased array results would be better when there is only one target in the radar field of view, and that MIMO results would be better for the identification of multiple targets. This was based on the literature review and on simulation results.

Experiments showed that the phased array techniques were more robust than the MIMO techniques, giving good performances when one or three targets were present regardless of the chosen technique. Contrarily, MIMO results varied depending on the technique used, but in most cases TBR gave significantly better results than the Capon β, APES and GLRT spectrums. When two targets were separated by a small angle, an omnidirectional pattern was the only pattern to clearly resolve two targets indicating that the orthogonality of the transmitted signals does provide increased resolution.

Below, three characteristics of the phased array and MIMO beampatterns and parameter estimation techniques that had an effect on the accuracy of the techniques are discussed. These sections are focussed, in particular, on explaining the poor performance of the MIMO Capon β, APES and GLRT spectrums. Finally, the findings of the results are discussed with reference to a real radar system.

8.3.7.1 Power

The power difference between the signals transmitted by the phased array, and those transmitted by the MIMO radar restricts the direct comparison of phased array and MIMO techniques.

In two of the three cases, the phased array signals had much higher average power than the directional MIMO signals. The exception is the phased array beampattern designed by the LCMV, which had the lowest signal power of all of the signals, and yet the results obtained when it was transmitted and three targets were present were still comparable to the results obtained from the significantly higher powered beampattern matching phased array pattern. Therefore, the lower power of the directional MIMO patterns was not the sole cause of the reduced accuracy of the MIMO Capon β, APES and GLRT estimations, although it would have contributed.

The transmission of power in all directions by the omnidirectional pattern also had an effect on the parameter estimation results. Table K.1, which shows the SNR of the received signals when targets were present, shows that the omnidirectional signals had SNRs close to or even higher than the phased array signals. However, Table 8.1 shows that the maximum SNR for the phased array signal was higher than that of the omnidirectional signal. This means that although the SNR of the omnidirectional signal was high, the contributing signal components do not necessarily correspond to target echoes, but also are reflections from "clutter", which hides the target information. A cone in the anechoic chamber which is struck by a normally incident signal could act as clutter. This helps to explain the noisy omnidirectional spectrums, range and range-angle charts.

8.3.7.2 The Reliance of MIMO Techniques on Range Estimates

A second cause of the poor MIMO Capon β, APES and GLRT results was the sensitivity of the spectrums to the range estimate. This shortcoming of the MIMO parameter estimation techniques was uncovered in simulation and verified experimentally. While this is a problem with the MIMO parameter estimation spectrums which is worth noting, even when a good range estimate was available the spectrums were mostly poor in comparison to the phased array spectrums.

8.3.7.3 Linear Independence of the Transmitted Signals

A third cause of the inadequate MIMO Capon β, APES and GLRT results was the low measure of linear independence between the transmitted signals. This was a problem identified for the directional MIMO patterns only, and not for the omnidirectional pattern. The low degree of linear independence is likely to have had a large effect on the Capon β, APES and GLRT algorithms and is probably responsible for having degraded their performance significantly.

Part of the reason for reduced linear independence between the transmitted signals was poor signal orthogonality. The MIMO signals were generated with only 40 symbols which reduced the measure of orthogonality. The number of samples was not increased, due to the restrictions on the duration of the transmitted signal and on the sample frequency. Increasing the number or symbols or better methods for the generation of orthogonal codes could improve the measure of linear independence of the MIMO signals and thus the performance of the MIMO parameter estimation algorithms.

8.3.7.4 Applying the Results to Radar Systems

When phased array is used to search for targets, its narrow beam is swept across the search area. In contrast, an omnidirectional MIMO signal could survey the whole scene with only one transmission. The target parameter estimation results in this section showed that the phased array identified the targets significantly better than the omnidirectional MIMO signal, when the beam was pointed directly at the target. However, the possibility of increasing the number of omnidirectional pulses transmitted, to increase the SNR, as suggested in Forsythe et al. [38] and discussed in Section 2.11.1 has not been investigated. It is possible that, if the number of transmitted omnidirectional pulses was equal to the number of phased array pulses transmitted as the beam is swept, MIMO results comparable to traditional phased array sweeping methods could be obtained.

It was also found that TBR could be applied to a received MIMO signal even after beamforming had been performed on the signal. Therefore, it would be possible to trade-off between scanning with a narrow beam, and detection with a single pulse. For example, a wide beam of beam width 30° could be transmitted and scanned in 30° steps. TBR could then be used within the beam width to locate targets.

When an omnidirectional signal is transmitted, the signal power is spread in all directions, giving the signal a lower power density compared to the main beam of phased array signals with a narrow beam width. Therefore, an omnidirectional signal has lower probability of detection compared to a phased array signal, which might be attractive in many instances.

Once a target has been located, a radar usually tracks it. This requires maximising the target echo, and minimising echoes received from anything that is not the target. The results presented in this dissertation showed that the MIMO TBR results were comparable to phased array results, and in many cases even had higher resolution. However, with the identical phased array and MIMO array configuration and transmitting elements, the simplicity of phased array beampattern synthesis, and the reduced complexity of a phased array system makes a phased array system more suitable to target tracking.

However, if the configuration of the MIMO transmitters was changed, the hardware complexity could be decreased by a MIMO system, while results comparable to phased array could be achieved. For example, a 16-by-16 element square phased array could be replaced with a 16 element transmitter ULA in the horizontal plane and a 16 element receiver ULA in the vertical plane. It would be necessary to increase the power of the transmitter elements in comparison to the phased array transmitters, but the reduced number of elements would significantly decrease the hardware requirements. The signal processing would be more complex, but with the rapid increases in processing power described by Moore's Law, MIMO radar could certainly be feasible.

Therefore, under certain circumstances such as in high clutter scenarios, and with clever configuration, MIMO radar has the potential to provide improved performance in radar search and tracking applications.

Chapter 9

Conclusions and Recommendations

The objective achieved by the project was the design and implementation of an acoustic transmitter array to demonstrate MIMO techniques. On the path to achieving this, phased array and MIMO radar techniques were researched and investigated in simulation. Ultimately, the performance of the two methods was compared to uncover the strengths of MIMO techniques and place them in the context of array signal processing. In the sections below, the conclusions drawn from the achievement of the project objectives are expanded and recommendations for further work are discussed.

9.1 Conclusions

The important project deliverables, outcomes and results are presented below. The hardware system is discussed first, followed by the findings related to phased array and MIMO systems. Finally, phased array and MIMO techniques are compared.

9.1.1 Hardware System

A hardware system modelling an array radar in the acoustic domain was successfully implemented. An acoustic transmitter array was designed and built to operate with an existing acoustic receiver array. The transmitter and receiver electronics used low cost analogue and digital components, and the arrays were each constructed of 16 small speakers and microphones respectively. The transmitter and receiver arrays were interfaced to each other and a PC with an FPGA. The array was designed to operate at a centre frequency of 10 kHz with a signal bandwidth of 4 kHz. The

system sampling frequency was 40 kHz. As required, the transmitter array could transmit different signals on each channel to be used in MIMO configuration.

The receiver array was successfully calibrated by applying an FIR filter to compensate for the phase differences between channels and across the frequency band of interest. The transmitter array was found to be more difficult to calibrate.

Prompted by the problems encountered in calibration, the transmitter array was tested thoroughly to characterise its behaviour. It was found that the beampattern of the individual speakers in the array were not cardioid-shapes as expected. A search for the reasons revealed that the chosen speakers do not have a smooth pattern. Also, measurements indicated that the speakers were coupling to the speaker board, resulting in the entire board vibrating and transmitting the audio signal. Testing showed that despite these flaws, the array behaved approximately as expected. The only visible effect of the less-than-ideal speakers and array construction was the raised side lobe levels of the transmitter array patterns.

Testing of the hardware system confirmed that the transmitter and receiver arrays could identify a $100 \times 100 \times 100$ mm corner reflector target at a range of 3 m, and at angles of between -20° and 20°.

9.1.2 Phased Array

Simulations were performed to investigate the theoretical performance of phased array techniques. The simulation results were then compared to the experimental results of the hardware system. Phased array beampatterns and parameter estimation techniques were of interest.

9.1.2.1 Beampatterns

To compare phased array and MIMO in terms of flexibility of beampattern design, the formation of beams with multiple main lobes was investigated for a phased array system. The LCMV beamformer and a beampattern matching technique were chosen for this purpose. Simulation showed that by using these techniques, multi-lobed transmitter array patterns can be generated with phased array techniques. The disadvantage of the LCMV was that the optimal weights did not have unity magnitude, resulting in variable transmission power from transmitter element to

element and a reduced maximum transmitter power. The beampattern matching technique is more computationally expensive, but maximises transmitter power. These patterns were implemented on the hardware system and effectively transmitted energy in multiple directions. As for all of the beampatterns, the side lobe levels were increased.

Simulations showed that if wideband signals were transmitted, the beam width of the array beampattern increases. The measurement results confirmed this and showed a widening of the expected beampatterns compared to the theoretical patterns.

Therefore, the phased array beampattern simulations and hardware tests show that phased array systems can be used to design more diverse beampatterns.

9.1.2.2 Parameter Estimation

Phased array techniques accurately estimated the range and angle of a single target or three targets in the hardware tests, with results comparable to those obtained in simulation. It was illustrated in simulation that the phased array conventional, Capon and MUSIC techniques do not perform well when the received signals are coherent. When three targets were located at equal range from the receiver array, the reflected signals were expected to be close to coherent, and a degradation in the results of the phased array parameter estimation techniques was expected. However, experimental results showed that the phased array techniques continued to estimate the target range and angles well under these conditions.

Simulations showed the phased array parameter estimation techniques to be robust when the transmitted signals were wideband, and hardware tests confirmed this. Nonetheless, the TDWB beamformer was found to give the cleanest range-angle charts. Simulations indicated that, at bandwidths close to that of the system, an FWWB beamformer could give better estimation accuracy. However, the best phased array results were obtained without FWWB processing.

When two targets were separated by 6°, the phased array conventional and Capon techniques were not able to resolve the targets. However, the high resolution MUSIC technique did just resolve the targets.

Phased array parameter estimation techniques were therefore shown to behave, in most cases, as predicted by theory and simulation.

9.1.3 MIMO Radar

MIMO radar literature claims that MIMO beampattern design and target parameter estimation can provide performance gains over phased array methods. These techniques were investigated in simulation and experiment. The results and findings of the tests are summarised below.

9.1.3.1 Beampatterns

Simulations were performed to investigate the performance of the different beampattern design techniques. These simulations exposed that the maximum power beampattern design which was presented in the MIMO literature does not always result in power being transmitted in all desired directions. The degree of linear independence was also found to be very poor with this design. In response to this, Pascale's beampattern design method, which ensures that power is transmitted equally in all target directions and also reduces the cross correlation between the transmitted signals was presented.

Simulations showed that when wideband signals were transmitted, the beam width of the patterns did not increase significantly, but the amplitude of the peaks at angles greater than or less than zero decreased.

The measured MIMO omnidirectional pattern had peaks at approximately $-60°$ and $60°$ which were not present in the simulated patterns. It also dropped off by almost 10 dB at $\pm 90°$. Analysis of the speaker patterns showed that many speakers exhibited peaks at the same angles and nulls at $\pm 90°$, causing the omnidirectional array pattern to have the same form. Therefore, if transmission of an omnidirectional pattern is required, the beampattern of the array elements becomes important, as the array pattern is only as omnidirectional as the array elements.

The measured directional beampatterns had significantly lower power than the phased array patterns, due to the method of generating MIMO signals. The condition numbers of the directional pattern transmitted signal sets were also high, indicating that the degree of linear independence of the directional patterns was lower. The condition number affected the parameter estimation as discussed in the next section. The shapes of the directional patterns were as expected from simulation, although the side lobes were higher than simulated as for the phased array patterns.

By generating, transmitting and measuring omnidirectional, single-lobed and multi-lobed MIMO beampatterns, the diversity of MIMO beamforming was demonstrated.

9.1.3.2 Parameter Estimation

Simulation and experiments showed that target range and angle can be identified with MIMO techniques, but also highlighted two conditions under which the accuracy of the estimates suffers, or the methods fail.

Simulations showed that the first condition under which the Capon, APES and GLRT spectral parameter estimations fail, is when there is a high degree of correlation between the transmitted signals. When directional MIMO patterns were formed, the correlation between signals increased, and experiments showed that poorer estimates were obtained, particularly from the APES spectrum.

The second failure condition, also uncovered in simulation, was the reliance of the Capon, APES and GLRT spectrums on good availability of range estimates. In hardware testing, accurate range estimates were not obtained when the omnidirectional pattern was transmitted, and the quality of the parameter estimation spectrums decreased significantly.

TBR was found to be resistant to the two failure conditions stated above and gave accurate target range and angle estimations. The resolution of the TBR spectrums was comparable, and in many cases better, than the phased array system resolution.

Wideband techniques were found to improve the results of parameter estimation under some conditions. In general, the FWWB technique improved the resolution of the parameter estimation spectrums but reduced the SNR. When TBR was applied, the best results were mostly obtained when the TDWB was used, instead of a narrowband Capon beamformer.

The experimental results also indicated that orthogonality between the transmitted signals can increase the system resolution. This was best illustrated by the successful identification of two targets separated by 6° when an omnidirectional pattern was transmitted. The directional patterns were not able to resolve the targets.

Therefore, MIMO parameter estimation techniques were demonstrated in hardware. The Capon, APES and GLRT techniques did not perform as well as expected, but reasons for this were identified. MIMO TBR performed exceptionally well.

9.1.4 Comparison of Phased Array and MIMO Radar

The experimental results showed that phased array techniques are more robust than MIMO techniques. The phased array techniques are also simpler to implement, with lower computational complexity. In almost all scenarios, the phased array conventional, Capon and MUSIC spectral parameter estimation techniques outperformed the equivalent MIMO Capon, APES and GLRT techniques. However, TBR resulted in clean, high resolution MIMO spectrums.

When a single target needs to be tracked, the results of this project suggest that a phased array system is optimum. The high resolution beams that can be formed with low computational complexity with a phased array are ideal for target tracking. The increased complexity of a MIMO system, MIMO beamforming techniques and MIMO parameter estimation methods do not improve the performance of the MIMO system sufficiently to make it better than phased array. Even the good results obtained with MIMO systems when TBR was performed, do not make MIMO techniques better for target tracking.

Under some circumstances, there remains the possibility that MIMO techniques will be preferential. For example, when a traditional radar system searches for a target, it sweeps a narrow beam across its field of view. This takes time, and the high SNR within the main lobe leads to a high probability of detection. However, an omnidirectional transmitted signal spreads the transmitted power, which reduces the probability of detection of the radar signal. With the implementation of TBR and by increasing the number of pulses to be equivalent to the number transmitted by the phased array system as it scans, the target SNR can be equal for omnidirectional MIMO search and phased array search. So MIMO techniques might be feasible for radar searches.

9.2 Recommendations

Recommendations for future work that can extend on the foundation laid by this project are presented. Improvements to the hardware system are discussed first, followed by an introduction to avenues of research that were uncovered by the results of this project.

9.2.1 Hardware

To improve beamforming, a new transmitter speaker array should be designed. Preliminary experiments showed that by mounting the speakers on chipboard, the coupling, that resulted in the speaker board transmitting, can be reduced or possibly even eliminated. This will lower the side lobe levels of the transmitted patterns and will make effective calibration of the transmitter array possible. It will also lead to improved parameter estimation results.

Improvement to the accuracy of the results obtained from the hardware system could be obtained by increasing the system sampling rate. This would have multiple benefits, including reducing the requirements of the anti-aliasing and reconstruction filters on the receiver and transmitter, and increasing the number of symbols that could be used to generate MIMO codes.

The hardware system designed and built in this project is only a prototype. Some redesign of the receiver and transmitter boards is recommended, for the delivery of a robust and compact experimental platform. For example, it would be preferable to combine the additional amplifier stage with the receiver analogue board, and thus eliminate the need for two biasing circuits. It would also be desirable to combine the Schmitt trigger, for converting the FPGA clock to a clock suitable to set the transmitter filter corner frequency, onto the transmitter analogue board. Research into a suitable power supply solution would also be advised.

Finally, the FPGA used as the MCU to interface between the transmitter and receiver and a computer was under-utilised. In the future, either more of the signal processing, such as digital filtering and modulation, could be implemented on the FPGA. Alternatively, a simpler device, and more economical solution should be devised.

9.2.2 Research Avenues

This research project, while revealing some properties and clarifying some characteristics of MIMO radar systems and techniques, also uncovered many subjects for future research. These are discussed below.

The MIMO codes used in simulation and hardware experiments were simply randomly selected QPSK codes which are approximately orthogonal to one another.

However, to improve the MIMO results, a theoretical investigation into different codes with better correlation properties is suggested. This would reduce the ripple on omnidirectional MIMO patterns, lower the MIMO directional pattern side lobe levels, and improve the performance of the Capon, APES and GLRT techniques.

In this dissertation, the configuration of the MIMO array was identical to the phased array. However, it was shown in Chapter 2 that by selecting the arrangement of the L_t transmitter and L_r receiver elements, virtual arrays of up to $L_t \times L_r$ virtual elements can be constructed. It would be of great interest to examine the performance of radar techniques with different virtual array configurations. Of particular interest would be the construction of a 2-dimensional virtual array with 1-dimensional transmitter and receiver arrays.

Much of the literature has shown that the best performance benefits of MIMO radar in comparison to phased array radar can be obtained with the use of sparse arrays in environments of high clutter. Therefore to extend on the findings of this project, MIMO sparse array techniques in clutter should be researched. The speakers and microphones of the transmitter and receiver arrays respectively could easily be rearranged in sparse array form. After implementing the hardware and coding improvements mentioned above, MIMO performance in high clutter environments could be investigated.

Appendix A

Mathematical Concepts

An overview of the mathematical concepts and notation used throughout the dissertation are given here. The notation and concepts are mostly based on those of Keener [61].

A.1 Scalar, Vector and Matrix Operations

The following operations are defined:

1. **Complex Conjugate**: The complex conjugate of $\alpha \in \mathbb{C}$ is denoted α^*. If $\alpha = \alpha_I + j\alpha_Q$, then $\alpha^* = \alpha_I - j\alpha_Q$.

2. **Transpose**: The transpose of vector $\mathbf{x}$ is denoted by $\mathbf{x}^T$. If $\mathbf{x} = (x_1\ x_2\ ...\ x_n)$, then $\mathbf{x}^T = \begin{pmatrix} x_1 \\ x_2 \\ \vdots \\ x_n \end{pmatrix}$.
   Similarly, the transpose of matrix
   $$\mathbf{A} = \begin{bmatrix} a_{11} & a_{12} & \dots & a_{1n} \\ a_{21} & a_{22} & \dots & a_{2n} \\ \vdots & \vdots & \ddots & \vdots \\ a_{m1} & a_{m2} & \dots & a_{mn} \end{bmatrix} \quad \text{is} \quad \mathbf{A}^T = \begin{bmatrix} a_{11} & a_{21} & \dots & a_{m1} \\ a_{12} & a_{22} & \dots & a_{m2} \\ \vdots & \vdots & \ddots & \vdots \\ a_{1n} & a_{2n} & \dots & a_{mn} \end{bmatrix}$$

3. **Hermitian Transpose** The Hermitian transpose (or conjugate transpose) of a vector $\mathbf{x}$ is denoted by $\mathbf{x}^H$. The definition is
   $$\mathbf{x}^H = (\mathbf{x}^*)^T.$$

Similarly, the Hermitian transpose of a matrix $\mathbf{A}$ is denoted $\mathbf{A}^H$ and defined as

$$\mathbf{A}^H = (\mathbf{A}^*)^T.$$

4. **Inverse**: The inverse of an $n \times n$ square matrix $\mathbf{A}$ is denoted by $\mathbf{A}^{-1}$ and is of the same size as $\mathbf{A}$ such that

$$\mathbf{A}\mathbf{A}^{-1} = \mathbf{A}^{-1}\mathbf{A} = \mathbf{I}$$

where $\mathbf{I}$ is the $n \times n$ identity matrix.

A.2 Linear Vector Spaces

Many problems require a single solution which satisfies some constraints to be chosen from a large number of contending solutions. The collection of all of the contending solutions can often be represented by a vector space. The operations of addition and scalar multiplication need to be defined in a vector space $\mathbf{S}$. If $\mathbf{x}, \mathbf{y}, \mathbf{z} \in \mathbf{S}$ then the following applies to addition

1. Commutative Law: $\mathbf{x} + \mathbf{y} = \mathbf{y} + \mathbf{x}$
2. Associative Law: $\mathbf{x} + (\mathbf{y} + \mathbf{z}) = (\mathbf{x} + \mathbf{y}) + \mathbf{z}$
3. Additive Identity: If $\mathbf{0} \in \mathbf{S}$, then $\mathbf{0} + \mathbf{x} = \mathbf{x}$
4. Additive Inverse: If $-\mathbf{x} \in S$, then $-\mathbf{x} + \mathbf{x} = \mathbf{0}$

Also, if α and β are elements of the set of scalars, the operation of scalar multiplication has the properties

1. $\alpha(\beta\mathbf{x}) = (\alpha\beta)\mathbf{x}$
2. $(\alpha + \beta)\mathbf{x} = \alpha\mathbf{x} + \beta\mathbf{x}$
3. $\alpha(\mathbf{x} + \mathbf{y}) = \alpha\mathbf{x} + \alpha\mathbf{y}$
4. $1\mathbf{x} = \mathbf{x}$ and $0\mathbf{x} = 0$

Scalars are most commonly the set of real numbers $\mathbb{R}$ or the set of complex numbers $\mathbb{C}$. However, they can also be defined as other sets, such as the binary set $\{0, 1\}$. A linear space can be formed with this set of scalars and with modulo-2 arithmetic operations [62].

Definition A.2.1. Linear Vector Spaces
If $\mathbf{S}$ is a linear vector space then

1. If $\mathbf{x}, \mathbf{y} \in \mathbf{S}$ then $\mathbf{x} + \mathbf{y} \in \mathbf{S}$
2. If $\alpha \in \mathbb{R}$ or $\mathbb{C}$ and $\mathbf{x} \in \mathbf{S}$ then $\alpha\mathbf{x} \in \mathbf{S}$

Definition A.2.2. Linearly Dependent and Independent Sets
If $\mathbf{x}_1, \mathbf{x}_2, ..., \mathbf{x}_n \in \mathbf{S}$ and $\alpha_1, \alpha_2, ..., \alpha_n \in \mathbb{R}$ or $\mathbb{C}$, and the linear combination $\alpha_1\mathbf{x}_1 + \alpha_2\mathbf{x}_2 + ... + \alpha_n\mathbf{x}_n = 0$ does not require all of the scalars α_j to be zero, then the set $\{\mathbf{x}_1, \mathbf{x}_2, ..., \mathbf{x}_n\}$ is linearly dependent. This set is linearly independent if the linear combination can only be equal to zero if all of the scalars α_j are equal to zero.

Thus, a vector in a linearly independent set cannot be written as a linear combination of the other vectors [62].

Definition A.2.3. Spanning Set
A set of vectors $\mathbf{T} \subset \mathbf{S}$ is a spanning set of $\mathbf{S}$ if every $\mathbf{x} \in \mathbf{S}$ can be written as a linear combination of the elements of $\mathbf{T}$.

Definition A.2.4. Span
The span of a set of vectors $\mathbf{T}$ is the collection of all vectors which are linear combinations of the vectors making up $\mathbf{T}$.

Definition A.2.5. Basis
If a spanning set $\mathbf{T} \subset \mathbf{S}$ is linearly independent, then $\mathbf{T}$ is a basis for $\mathbf{S}$. If $\mathbf{T}$ has a finite number of elements, then $\mathbf{S}$ has a finite dimension equal to the number of elements of $\mathbf{T}$.

Definition A.2.6. Vector Norm
The norm, which is also known as the amplitude, magnitude or length of $\mathbf{x}$ where $\mathbf{x} \in \mathbf{S}$, is denoted by $\|\mathbf{x}\|$. It is a function $\|\cdot\| : \mathbf{S} \to [0, \infty)$ and it has the properties:

1. $\|\mathbf{x}\| \geq 0$ if $\mathbf{x} \neq 0$,
2. $\|\mathbf{x}\| = 0$ implies that $\mathbf{x} = 0$,
3. $\|\alpha\mathbf{x}\| = |\alpha| \cdot \|\mathbf{x}\|$ for $\alpha \in \mathbb{R}$ or $\mathbb{C}$,
4. $\|\mathbf{x} + \mathbf{y}\| \leq \|\mathbf{x}\| + \|\mathbf{y}\|$ which is known as the triangle inequality.

The most commonly used norm is the Euclidean norm. It represents the Euclidean length of a vector [15]. For a real vector $\mathbf{x}$, the Euclidean norm is given by

$$\|\mathbf{x}\| = \left[\sum_{i=1}^{N} \mathbf{x}_i^2\right]^{1/2} = (\mathbf{x}^T\mathbf{x})^{1/2} \tag{A.1}$$

In the complex case the Euclidean norm of vector $\mathbf{x}$ is

$$\|\mathbf{x}\| = \left[\sum_{i=1}^{N} \mathbf{x}_i^* \mathbf{x}_i\right]^{1/2} = \left[\sum_{i=1}^{N} |\mathbf{x}_i|^2\right]^{1/2} = (\mathbf{x}^H \mathbf{x})^{1/2} \tag{A.2}$$

If the elements of the vector $\mathbf{x}$ are the elements of a zero mean sequence with N elements, then their standard deviation is $\|\mathbf{x}\| / N^{\frac{1}{2}}$, and their variance is $\|\mathbf{x}\|^2 / N$ [15].

For real or complex continuous signals $x(t)$ defined over the interval T, the norm can be defined as

$$\|\mathbf{x}\| = \left[\int_T |x(t)|^2 \, dt\right]^{\frac{1}{2}} \tag{A.3}$$

This norm is often chosen for signal representation. Physically, the square of this norm can be interpreted as the signal energy. $L^2(T)$ space is then defined as the set of all functions for which the norm in (A.3) is bounded [62].

Definition A.2.7. Inner Product

If $\mathbf{x}, \mathbf{y} \in \mathbf{S}$, the inner product of $\mathbf{x}$ and $\mathbf{y}$ denoted $\langle \mathbf{x}, \mathbf{y} \rangle$ is a function that maps the vectors to the real or complex domain. This is represented as $\langle \cdot, \cdot \rangle : \mathbf{S} \times \mathbf{S} \to \mathbb{R}$ or $\mathbb{C}$. The inner product has the properties

1. $\langle \mathbf{x}, \mathbf{y} \rangle = \overline{\langle \mathbf{x}, \mathbf{y} \rangle}$,
2. $\langle \alpha \mathbf{x}, \mathbf{y} \rangle = \alpha \langle \mathbf{x}, \mathbf{y} \rangle$,
3. $\langle \mathbf{x} + \mathbf{y}, \mathbf{z} \rangle = \langle \mathbf{x}, \mathbf{z} \rangle + \langle \mathbf{y}, \mathbf{z} \rangle$,
4. $\langle \mathbf{x}, \mathbf{x} \rangle \geq 0$ if $\mathbf{x} \neq \mathbf{0}$, $\langle \mathbf{x}, \mathbf{x} \rangle = 0$ if and only if $x = \mathbf{0}$.

The inner product is also known as the scalar product or dot product. There are many forms of the inner product. In $\mathbb{R}^n$, the dot product of two vectors $\mathbf{x} = (x_1, x_2, ..., x_n)$ and $\mathbf{y} = (y_1, y_2, ..., y_n)$ is given by

$$\langle \mathbf{x}, \mathbf{y} \rangle = \mathbf{x}^T \mathbf{y} = \sum_{i=1}^{n} x_i y_i \tag{A.4}$$

This is known as the Euclidean inner product. The Euclidean inner product can be applied to vectors in the complex domain $\mathbb{C}^n$. Also, the Hermitian inner product can be applied to vectors in $\mathbb{C}^n$ [15]. It is defined as

$$\langle \mathbf{x}, \mathbf{y} \rangle = \mathbf{x}^H \mathbf{y} = (\mathbf{x}^*)^T \mathbf{y} = \sum_{i=1}^{n} x_i^* y_i \tag{A.5}$$

Another inner product of interest is that defined in $L^2(T)$ space. It is given by

$$\langle \mathbf{x}, \mathbf{y} \rangle = \int_T x(t) y^*(t) dt \qquad \mathbf{x}, \mathbf{y} \in L^2(T) \tag{A.6}$$

The inner product can be interpreted to give the angular relationship between two vectors. The real angle θ between two vectors is defined as

$$\cos\theta = \frac{\Re \langle \mathbf{x}, \mathbf{y} \rangle}{\|\mathbf{x}\| \, \|\mathbf{y}\|} \tag{A.7}$$

This angular interpretation is most commonly applied to determine if two vectors are orthogonal to each other. If $\langle \mathbf{x}, \mathbf{y} \rangle = 0$, then $\mathbf{x}$ and $\mathbf{y}$ are said to be orthogonal [62].

A.2.1 Gram-Schmidt Orthogonalisation Procedure

It is often desirable to have a set of vectors which are orthogonal to each other. Orthogonal vectors can be used to create an orthonormal basis which has many useful properties [62]. A commonly used procedure to orthogonalise n linearly independent vectors is the Gram-Schmidt orthogonalisation or orthonormalisation procedure. Consider the set of vectors $\{\mathbf{v}_i\}$. n orthogonal vectors can be found by

$$\begin{aligned}
&\mathbf{w}_1 = \mathbf{v}_1 \\
&\mathbf{w}_2 = \mathbf{v}_2 - \langle \mathbf{v}_2, \mathbf{u}_1 \rangle \mathbf{u}_1 \\
&\mathbf{w}_3 = \mathbf{v}_3 - \langle \mathbf{v}_3, \mathbf{u}_2 \rangle \mathbf{u}_2 - \langle \mathbf{v}_3, \mathbf{u}_1 \rangle \mathbf{u}_1 \\
&\vdots \\
&\mathbf{w}_i = \mathbf{v}_i - \sum_{k=1}^{i-1} \langle \mathbf{v}_i, \mathbf{u}_k \rangle \mathbf{u}_k \\
&\vdots
\end{aligned} \tag{A.8}$$

where $\mathbf{u}_i$ is the normalisation of vector $\{\mathbf{w}_i\}$ and is given by

$$\mathbf{u}_i = \frac{\mathbf{w}_i}{\|\mathbf{w}_i\|}; \quad i = 1, 2, ..., n \tag{A.9}$$

The set of vectors $\{\mathbf{u}_i\}$ is then a set of orthonormal vectors. This process is illustrated graphically for a set of two vectors in Figure A.1.

A.3 Matrix Spectral Theory

Suppose that a matrix problem of the form $\mathbf{A}\mathbf{x} = \mathbf{b}$ must be solved. $\mathbf{x}$ and $\mathbf{b}$ are vectors which are expressed relative to some basis. They can easily be transformed

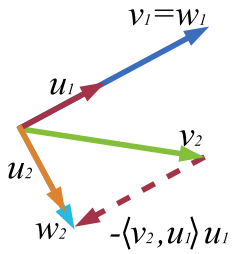

Figure A.1: Two dimensional Gram-Schmidt orthogonalisation.

relative to a new basis so that $\mathbf{x} = \mathbf{C}\mathbf{x}'$ and $\mathbf{b} = \mathbf{C}\mathbf{b}'$. Then, the matrix problem becomes $\mathbf{A}\mathbf{C}\mathbf{x}' = \mathbf{C}\mathbf{b}'$. Rearranging this to its original form gives $\mathbf{C}^{-1}\mathbf{A}\mathbf{C}\mathbf{x}' = \mathbf{b}'$. The transformation $\mathbf{A}' = \mathbf{C}^{-1}\mathbf{A}\mathbf{C}$ is known as a similarity transform. If $\mathbf{A}$ can be transformed to be diagonal, the matrix problem can easily be solved. The process that achieves this is known as the spectral decomposition of $\mathbf{A}$ and is described in the theorems below.

Definition A.3.1. Eigenpairs, Eigenvectors and Eigenvalues
An eigenpair of $\mathbf{A}$ is a pair $(\lambda, \mathbf{x})$ where $\lambda \in \mathbb{C}$ and $\mathbf{x} \in \mathbb{C}^n$ which satisfies

$$\mathbf{A}\mathbf{x} = \lambda\mathbf{x}, \qquad \mathbf{x} \neq \mathbf{0} \tag{A.10}$$

The vector $\mathbf{x}$ is called an eigenvector and λ is called an eigenvalue of $\mathbf{A}$.

For λ to be an eigenvalue of $\mathbf{A}$, it must be a root of the nth order polynomial

$$p_A(\lambda) = \det(\mathbf{A} - \lambda\mathbf{I}) \tag{A.11}$$

where $\mathbf{I}$ is the identity matrix of the same size as $\mathbf{A}$. This is known as the characteristic polynomial of $\mathbf{A}$.

The geometrical interpretation of (A.10) is that the matrix $\mathbf{A}$ is a transformation such that it transforms a vector into another, of different length but the same direction. However, the main use of eigenvalues and eigenvectors is that they can be used to find the spectral representation of $\mathbf{A}$. The theorem below describes this further.

Theorem A.3.2. *Let $\mathbf{A}$ be an $n \times n$ matrix. Then:*

1. *If $\mathbf{A}$ has n linearly independent real or complex eigenvectors, there is a change of basis in $\mathbb{R}^n$ or $\mathbb{C}^n$ so that $\mathbf{A}$ is diagonal relative to the new basis.*
2. *If $\mathbf{T}$ is the matrix whose columns are the eigenvectors of $\mathbf{A}$, then $\mathbf{T}^{-1}\mathbf{A}\mathbf{T} = \Lambda$ is the diagonal matrix of eigenvalues.*

The factorisation $\mathbf{A} = \mathbf{T}\Lambda\mathbf{T}^{-1}$ is called the spectral representation of $\mathbf{A}$.

Theorem A.3.2 requires that $n \times n$ matrix $\mathbf{A}$ has n linearly independent eigenvectors so that it can be diagonalised. The following theorem describes the conditions under which this requirement is met.

Theorem A.3.3. *If* $\mathbf{A}$ *has* n *distinct eigenvalues, then it has* n *linearly independent eigenvectors.*

There is also a class of matrices which can always be diagonalised. These matrices are known as self-adjoint matrices. Firstly however, the matrix adjoint must be defined, and this is done below.

Definition A.3.4. Adjoint

The adjoint or conjugate transpose of any matrix $\mathbf{A}$ is the matrix $\mathbf{A}^H$ such that $\langle \mathbf{Ax}, \mathbf{y} \rangle = \langle \mathbf{x}, \mathbf{A}^H\mathbf{y} \rangle$ for all $\mathbf{x}$, $\mathbf{y}$ in $\mathbb{C}^n$.

Definition A.3.5. Self-Adjoint

A matrix $\mathbf{A}$ is self-adjoint if $\mathbf{A}^H = \mathbf{A}$.

If $\mathbf{A}$ is self-adjoint and complex, then it is a Hermitian matrix whereas if it is self-adjoint and real, it is a symmetric matrix.

The following theorem describes the attractive properties of a self-adjoint matrix.

Theorem A.3.6. *If* $\mathbf{A}$ *is a self-adjoint matrix, then:*

1. $\langle \mathbf{Ax}, \mathbf{x} \rangle$ *is real for all* $\mathbf{x}$
2. *All eigenvalues are real*
3. *Eigenvectors of distinct eigenvalues are orthogonal to each other*
4. *The eigenvectors form an orthonormal basis*
5. $\mathbf{A}$ *can be diagonalised.*

Finally, the properties of the spectral decomposition of a self-adjoint matrix are described by the theorem.

Theorem A.3.7. ***Spectral Decomposition Theorem***

If $\mathbf{A}$ *is an* $n \times n$ *self-adjoint matrix, there is an orthogonal basis* $\{\mathbf{x}_1, \mathbf{x}_2, \ldots, \mathbf{x}_n\}$ *for which*

1. $\mathbf{Ax}_i = \lambda_i \mathbf{x}_i$ *where* λ_i *is real.*

2. $\langle \mathbf{x}_i, \mathbf{x}_j \rangle = \delta_{ij}$ [1] *which implies the mutual orthogonality of vectors* $\mathbf{x}_i$.

3. *The matrix* $\mathbf{Q}$ *which has* $\mathbf{x}_j$ *as its* j^{th} *column vector is unitary. That is,* $\mathbf{Q}^{-1} = \mathbf{Q}^H$.

4. $\mathbf{Q}^* \mathbf{A} \mathbf{Q} = \Lambda$ *where* λ *is a diagonal matrix with real entries* λ_i.

This theorem greatly simplifies the procedure of solving the matrix equation $\mathbf{Ax} = \mathbf{b}$. The commutating diagram in Figure A.2 shows the procedures that can be followed to solve this equation, assuming that $\mathbf{A}$ is self-adjoint. What appears to be the simplest method, is to find $\mathbf{x}$ directly by applying the matrix inversion of $\mathbf{A}$ to $\mathbf{b}$. However, it is not always easy to find the matrix inverse of $\mathbf{A}$. Therefore, it is often simpler to follow the second route shown on the diagram. Due to the properties of the spectral representation of a self-adjoint matrix, the inverses of λ and $\mathbf{Q}$ are easily found. Therefore, by changing the coordinate system of $\mathbf{A}$ relative to the the basis function formed by its eigenvalues, $\mathbf{x}'$ can easily be found. $\mathbf{x}'$ is then transformed back to the original co-ordinate system.

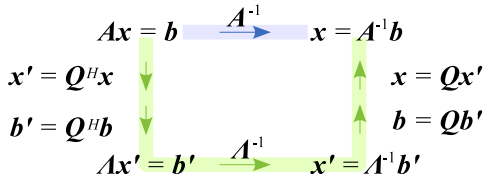

Figure A.2: Commutating diagram for solving a matrix equation where $\mathbf{A}$ is self-adjoint

A.4 Lagrange Multipliers

Lagrange multipliers are a method used to maximise or minimise some function which is subject to a set of constraints. Suppose that there is a scalar-valued function, $f(\mathbf{x})$, for which a maximum or minimum needs to be found. Assume also that the optimisation must be performed subject to some constraint given by $g(\mathbf{x}) = 0$. This is usually expressed as

$$\begin{aligned} &\max_{\mathbf{x}} \text{ or } \min_{\mathbf{x}} f(\mathbf{x}) \\ &\text{subject to } g(\mathbf{x}) = 0. \end{aligned} \tag{A.12}$$

[1] δ_{ij} is the Kronecker delta where $\delta_{ij} = 1$ if $i = j$ and $\delta_{ij} = 0$ if $i \neq j$ [62].

It is necessary that f and g both have continuous first partial derivatives. Also, $\nabla g \neq \mathbf{0}$, where ∇g represents the derivative of g. Then, Lagrange multipliers can be used to find the maximum or minimum [63].

f and g can now be thought of as two surfaces. In order for a maximum or minimum of f to be found on g, it is necessary that the gradient of f must line up with that of g at some point. Mathematically, if the two gradients are parallel or equal to one another, they are a multiple of each other, and therefore, it can be said that

$$\nabla f = \lambda \nabla g \tag{A.13}$$

where λ is known as the Lagrange Multiplier. This equation results in a set of equations

$$\frac{\partial f}{\partial x_k} - \lambda \frac{\partial g}{\partial x_k} = 0 \qquad k = 1, ..., N. \tag{A.14}$$

Thus, there are $N - 1$ equations which can be solved to find the maximum or the minimum.

When $\mathbf{x}$, the variable on which the optimisation is performed, is complex-valued, the Lagrange method can be used, as long as the Lagrange multiplier is real [64]. The complex-valued Lagrangian equation for multiple constraints, based on that in [65], is

$$\frac{\partial}{\partial \mathbf{x}^*} \left(f(\mathbf{x}) \right) + \sum_{k=1}^{K} \frac{\partial}{\partial \mathbf{x}^*} \left(\mathrm{Re}\{\lambda_k^* g_k(\mathbf{x})\} \right) = 0. \tag{A.15}$$

Appendix B

The Covariance Matrix

The covariance or correlation matrix is commonly used in statistical analysis of stochastic processes. The covariance matrix is often defined for a time process, where it is important in the analysis and design of discrete time filters [51]. However, in the realm of phased arrays, which implement spatial filtering, the spatial covariance matrix is of more importance. It is extensively used in the selection of weights for phased array beamforming, MIMO beamforming as well as phased array and MIMO parameter estimation methods.

In this chapter, the covariance matrix is introduced for stochastic discrete time processes, and its properties, and those of its eigenvalues and eigenvectors are presented, based on [51]. The spatial covariance matrix is then introduced. Finally, methods for estimating the spatial covariance matrix are presented.

B.1 The Discrete Time Covariance Matrix

Consider a discrete time stochastic process with N time samples given by

$$\mathbf{u}(n) = [u(n) \quad u(n-1) \quad \dots \quad u(n-N+1)]^T. \tag{B.1}$$

The mean of this process is defined as

$$\mu(n) = \mathrm{E}[\mathbf{u}(n)] \tag{B.2}$$

where $\mathrm{E}[\cdot]$ is the statistical expectation.

The autocorrelation function of the process is defined as

$$r(n, n-k) = \mathrm{E}[\mathbf{u}(n)\mathbf{u}^*(n-k)] \quad k = 0, \pm 1, \pm 2... \tag{B.3}$$

The mean and autocorrelation function are important for the partial characterisation of a discrete time stochastic process. If the process is strictly stationary, then its mean and autocorrelation take on simpler forms. The mean is constant for all values of n, so can be given by

$$\mu(n) = \mu, \quad \forall\ n. \tag{B.4}$$

Also, the autocorrelation function does not depend on the time values, but on the difference between the times, $\Delta_n = n - (n-k) = k$. Therefore

$$r(n, n-k) = r(\Delta_n) = r(k). \tag{B.5}$$

If Equation (B.4) and Equation (B.5) hold, it does not necessarily follow that the observation vector $\mathbf{u}(n)$ is strictly stationary. However, if the conditions hold, and the process is not strictly stationary, then it is said to be wide sense stationary.

For a stationary process, the covariance or correlation matrix $\mathbf{R}$ is defined as the expectation of the outer product of the observation vector $\mathbf{u}(n)$ with itself. Represented as a $N \times N$ matrix, it is

$$\mathbf{R} = \mathrm{E}[\mathbf{u}(n)\mathbf{u}^H(n)].$$

$\mathbf{R}$ has form,

$$\mathbf{R} = \mathrm{E}\begin{bmatrix} u(n)u^*(n) & u(n)u^*(n-1) & \dots & u(n)u^*(n-\bar{N}) \\ u(n-1)u^*(n) & u(n-1)u^*(n-1) & \dots & u(n-1)u^*(n-\bar{N}) \\ \vdots & \vdots & \ddots & \vdots \\ u(n-\bar{N})u^*(n) & u(n-\bar{N})u^*(n-1) & \dots & u(n-\bar{N})u^*(n-\bar{N}) \end{bmatrix} \tag{B.6}$$

where $\bar{N} = N - 1$.

But, it can be noted, by moving the expected value into the matrix, that each element of the covariance matrix has the form of the autocorrelation function of $\mathbf{u}(n)$ for different values of k, as given in Equation (B.3). Assuming that the process is wide sense stationary, the covariance matrix becomes

$$\mathbf{R} = \mathrm{E}\begin{bmatrix} r(0) & r(1) & \dots & r(N-1) \\ r(-1) & r(0) & \dots & r(N-2) \\ \vdots & \vdots & \ddots & \vdots \\ r(-N+1) & r(-N) & \dots & r(0) \end{bmatrix}. \tag{B.7}$$

Then, $r(0)$ on the main diagonal is always real valued, but the other elements can be complex.

B.2 Properties of the Covariance Matrix

The covariance matrix of a discrete time stochastic process has the properties listed below and based on [51]

1. The covariance matrix of a stationary process is Hermitian. Therefore $\mathbf{R} = \mathbf{R}^H$. This also means that $r(-k) = r^*(k)$. If the process is real, then $\mathbf{R}$ is symmetric.

2. The covariance matrix of a stationary process is Toeplitz. This means that the elements on the main diagonal and on every diagonal parallel to the main diagonal are equal. For $\mathbf{R}$ to be Toeplitz, it is also necessary that the process is weakly stationary.

3. The covariance matrix is always non-negative definitive and almost always positive definitive. Also, the correlation matrix is almost always non-singular, and therefore almost always has an inverse.

4. When the elements of the vector $\mathbf{x}$ are arranged backwards, the covariance matrix of the new vectors is the transposition of the covariance matrix of the original vectors. That is, if

$$\mathbf{u}^B(t) = [\ u(t-N+1) \quad \dots \quad u(t-1) \quad u(t)\ ]^T$$

then

$$\mathrm{E}[\mathbf{u}^B(t)\mathbf{u}^{BH}(t)] = \mathbf{R}^T.$$

5. The correlation matrices $\mathbf{R}_L$ and$\mathbf{R}_{N+1}$, relating to N and $N+1$ observations of a process are related by

$$\mathbf{R}_{N+1} = \begin{bmatrix} r(0) & \mathbf{r}^H \\ \mathbf{r} & \mathbf{R}_M \end{bmatrix} \tag{B.8}$$

where $r(0)$ is the autocorrelation with zero lag and $\mathbf{r}^H = [r(1), r(2), \dots, r(N)]$.

B.3 Properties of the Covariance Matrix Eigenvalues and Eigenvectors

The properties of the eigenvalues and eigenvectors of the covariance matrix are used in spectral analysis. Many of these properties are direct results of the Hermitian

property and almost always positive definite property of the covariance matrix. Let $\lambda_1, \lambda_2, \ldots, \lambda_L$ denote the eigenvalues of the correlation matrix $\mathbf{R}$ and $\mathbf{q}_1, \mathbf{q}_2, \ldots, \mathbf{q}_L$ denote the corresponding eigenvectors. The properties of these eigenvalues and eigenvectors are listed below.

1. The eigenvalues of the covariance matrix $\mathbf{R}^k$ are given by $\lambda_1^k, \lambda_2^k, \ldots, \lambda_L^k$. This is since
$$\mathbf{R}^k\mathbf{q} = \lambda^k\mathbf{q}.$$
This also has the result that every eigenvector of $\mathbf{R}$ is also an eigenvector of $\mathbf{R}^k$.
2. The eigenvectors of $\mathbf{R}$ are linearly independent.
3. The eigenvalues of $\mathbf{R}$ are all real and non-negative.
4. The eigenvectors of $\mathbf{R}$ are mutually orthogonal to one another.
5. Define the matrices $\mathbf{Q} = [\mathbf{q}_1\ \mathbf{q}_2\ \ldots\ \mathbf{q}_L]$ and $\Lambda = \text{diag}(\lambda_1, \lambda_2, \ldots, \lambda_L)$. Then $\mathbf{R}$ can be diagonalised as $\mathbf{Q}^H\mathbf{R}\mathbf{Q} = \Lambda$.
6. The sum of the eigenvalues of $\mathbf{R}$ is equal to $\text{tr}(\mathbf{R})$.
7. The largest eigenvalue of $\mathbf{R}$ is bounded by
$$\lambda_{max} \leq \sum_{k=0}^{N-1} r(k).$$
The smallest eigenvalue of $\mathbf{R}$ is bounded by
$$\lambda_{min} \geq r(0) - \sum_{k=1}^{N-1} r(k).$$
8. The covariance matrix $\mathbf{R}$ is ill conditioned if the ratio of the largest eigenvalue to the smallest eigenvalue is large.

Many of these properties are used by the MUSIC and DML phased array algorithms and the AML MIMO algorithm.

B.4 The Spatial Covariance Matrix

In the case of phased array systems, the observation vector $\mathbf{x}(n)$ represents a single time sample of the received signal on all channels in the array. Therefore, the covariance matrix of interest is a spatial covariance matrix [14].

It is still represented by

$$\mathbf{R}_X = \mathrm{E}\left[\mathbf{x}(n)\mathbf{x}^H(n)\right]. \tag{B.9}$$

However, the spatial covariance matrix has the expanded form

$$\mathbf{R}_X = \mathrm{E}\begin{bmatrix} x_1(n)x_1^*(n) & x_1(n)x_2^*(n) & \dots & x_1(n)x_{L-1}^*(n) \\ x_2(n)x_1^*(n) & x_2(n)x_2^*(n) & \dots & x_2(n)x_{L-1}^*(n) \\ \vdots & \vdots & \ddots & \vdots \\ x_{L-1}(n)x_1^*(n) & x_{L-1}(n)x_2^*(n) & \dots & x_{L-1}(n)x_{L-1}^*(n) \end{bmatrix} \tag{B.10}$$

where $x_i(n)$ is the received signal on the ith channel and there are L receiver channels.

The principles discussed above for the temporal covariance matrix also apply to the transmitted signal covariance matrix $\mathbf{R}_S$, the received signal covariance matrix $\mathbf{R}_X$ and all other covariance matrices discussed in the dissertation.

B.5 Methods for Spatial Covariance Matrix Estimation

In practice, the infinite time samples required to generate exact covariance matrices are not available. Only a finite data set of N observations of $\mathbf{s}(t)$ and $\mathbf{x}(t)$ is at hand. Thus, there are methods devised to estimate the transmitted or received data covariance matrix $\mathbf{R}$. A number of these methods are described below. They are based on van Wyk [25]

Sample Averaging

This is an estimate of $\mathbf{R}$ over a finite number of samples and is given by

$$\hat{\mathbf{R}} = \frac{1}{N}\sum_{i=1}^{N}\mathbf{x}(t_i)\mathbf{x}^H(t_i). \tag{B.11}$$

Forward-Backward Averaging

The forward-backward averaging technique of estimating a signal covariance matrix is given by

$$\hat{\mathbf{R}}_{FB} = \frac{1}{2(N-L-1)}\Phi \tag{B.12}$$

where $\Phi = \mathbf{A}^H\mathbf{A}$ for the M array elements and N snapshots and

$$\begin{aligned}\mathbf{A}^H &= [\mathbf{x}_F(t_1), ..., \mathbf{x}_F(t_N), \mathbf{x}^*(t_1), ..., \mathbf{x}^*(t_N)] \\ &= \begin{bmatrix} x_L(t_1) & \cdots & x_L(t_N) & x_1^*(t_1) & \cdots & x_1^*(t_N) \\ x_{L-1}(t_1) & \cdots & x_{L-1}(t_N) & x_2^*(t_1) & \cdots & x_2^*(t_N) \\ \vdots & \ddots & \vdots & \vdots & \ddots & \vdots \\ x_1(t_1) & \cdots & x_1(t_N) & x_L^*(t_1) & \cdots & x_L^*(t_N) \end{bmatrix}\end{aligned} \tag{B.13}$$

This method implements more smoothing than the estimate of the sample averaging technique. This can be illustrated by expressing the forward-backward estimate in terms of the sample averaging estimate

$$\hat{\mathbf{R}}_{FB} = \frac{1}{2}(\hat{\mathbf{R}} + \mathbf{J}\hat{\mathbf{R}}^*\mathbf{J}) \tag{B.14}$$

where $\mathbf{J}$ is a matrix in which all elements are zero except for the anti-diagonal elements (the elements on the diagonal from the top right to bottom left) which are one.

However, the forward-backward estimate does not produce good results if there are more than two coherent signals.

Spatial Smoothing

Spatial smoothing applies when there are more than two coherent signals. The array is split into a number of equal sub-arrays which overlap. The sub-arrays are all assumed to have different phase factors but otherwise identical steering vectors. If there are K sub-arrays, then each sub-array has $L_K = L - K + 1$ array elements. The estimate of the covariance matrix is then given by

$$\hat{\mathbf{R}}_{SS} = \frac{1}{K}\sum_{k=1}^{K}\hat{\mathbf{R}}_k \tag{B.15}$$

where $\mathbf{R}_k$ has the size L_k by L_k and is given by

$$\hat{\mathbf{R}}_k = \begin{bmatrix} R_{k,k} & \cdots & R_{k+L_k,k} \\ \vdots & \ddots & \vdots \\ R_{k,k+L_k} & \cdots & R_{k+L_k,k+L_k} \end{bmatrix} \tag{B.16}$$

where elements $R_{k,k}$... are the elements in $\hat{\mathbf{R}}$. Note that the diagonal elements of matrix $\hat{\mathbf{R}}_k$ are also diagonal elements in $\hat{\mathbf{R}}$.

If the spatial smoothing method is used to obtain an estimate of the covariance matrix, then the effective array has smaller dimensions than the physical array. The more sub-arrays used, the smaller the dimensions of the covariance matrix.

Appendix C

MIMO Communications

The use of multiple transmitter or receiver antennas is not unknown in wireless communication systems. Multiple transmit and receive antennas can be used to provide a diversity gain, and increase the reliability of a link. Alternatively, an array of transmitter antennas can be used to perform beamforming, which gives a power gain in a desired direction. Beamforming can also be performed on the receiver. There is a third benefit that can be obtained from using multiple transmit and receive antennas. This is a degree of freedom gain, which allows spatial multiplexing. The rest of this section describes briefly the channel conditions and MIMO system architectures that best exploit this degree of freedom gain. By highlighting the benefit of a MIMO system to communications, its benefits to radar-type systems can be developed. The development of the MIMO communications model, as well as the system and receiver architectures is based on Tse and Viswanath [37]. Many of the detailed concepts of wireless communications are only summarised, and are not discussed in full.

C.1 A Wireless Communication System compared to Radar

Wireless communication systems share many similarities to radar-type systems. Both usually consist of a transmitter, a channel across which a signal propagates, and a receiver. Therefore, many of the same principles apply to both. However, there are also key differences in the purposes of the two systems. A radar-type system uses signals in the audio or electromagnetic frequencies, and is able to use the signals to obtain information about the environment. This can range from tracking

a moving target, to mapping or imaging a landscape or object. Contrary to this, a wireless communications system attempts to transmit and receive a signal across some channel. Therefore, in a wireless communications system, the signal itself contains information. However, in a radar-type system, the signal is the medium used to determine the characteristics of the channel.

C.2 Degrees of Freedom

In a communications system, the degree of freedom of a received signal space determines the number of parameters which can be extracted from the signal [66]. In a communications system, this will often be equivalent to how many signals the system can reliably received. Consider a complex signal of duration T and with a frequency band $[-W/2, W/2]$ and thus a bandwidth of W. Then, to accurately represent this signal, a sampled signal of dimension $2WT$ given by WT complex samples is required. (This is equivalent to Nyquist's Sample Theorem.) If this signal is sampled, so that it has W samples per second, then the band-limited continuous time signal is able to have W degrees of freedom per second. Consider the transmission of this signal across some channel. Then the received signal also has an approximate bandwidth of W (neglecting Doppler spread). So, in communications systems, the degree of freedom of the channel is defined as the dimension of the received signal space. Together with an analysis of the capacity of the channel, the number of signals that can be received can be determined.

C.3 SIMO System

Consider a Single Input Multiple Output (SIMO) system with a single transmitter and L_r receivers such as shown in Figure C.1. It can be modelled using the same phased array model as that developed in Section 2.2 with only one source. Assume that the transmitter (or source) and the array of receivers are separated by a distance R, and that the transmitted signal is narrowband (see Section 2.1.4). Consider the case that there are no objects between the transmitter and the receiver. Thus, the signal arriving at the receiver follows a line of sight path from the transmitter. Given that the angle of the transmitter from the receiver is θ_r, as defined in Figure C.2, the received signals are given by

$$\mathbf{x}(t) = \mathbf{h}_r(\theta_r)s(t) + \mathbf{z}(t) \tag{C.1}$$

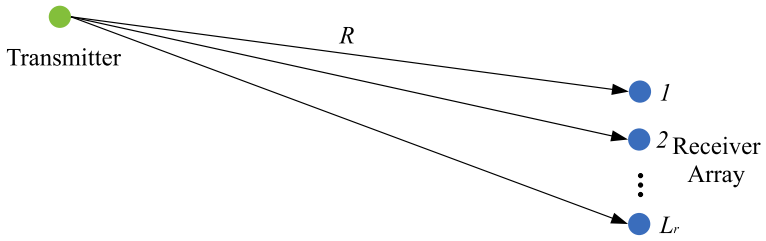

Figure C.1: A SIMO system.

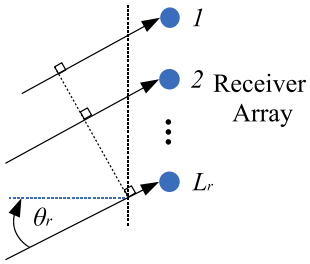

Figure C.2: Definition of the angle of a wave travelling from the transmitter to the array of receivers, assuming that the receivers are in the far field of the transmitter.

Note that slightly different notation has been used for the communications example, to differentiate between it and radar. The received signal steering vector which is known as a channel vector in the communications field has been represented by $\mathbf{h}_r$ instead of $\mathbf{a}_r$.

The dimensions of the SIMO channel vector $\mathbf{h}_r$ are L_r-dimensional vector. Therefore, the rank of the received signal space is one, and the degree of freedom of the channel is also one. The array of receivers therefore adds no additional spatial degree of freedom to the system.

C.4 MISO System

Similarly, consider a line-of-sight Multiple Input Single Output (MISO) system with L_t transmitters and a single receiver such as that shown in Figure C.3. The separation between the first element of the transmitter array and the receiver is R. Each transmitter transmits a narrowband signal and the set of transmitted signals are represented by the column vector of signals $\mathbf{s}(t)$. The angle of the transmitters to the receiver, θ_t is as defined in Figure C.4. The MISO system is reciprocal to the SIMO system, and the received signal (a scalar) will be given by

$$x(t) = \mathbf{h}_t^H(\theta_t)\mathbf{s}(t) + z(t) \tag{C.2}$$

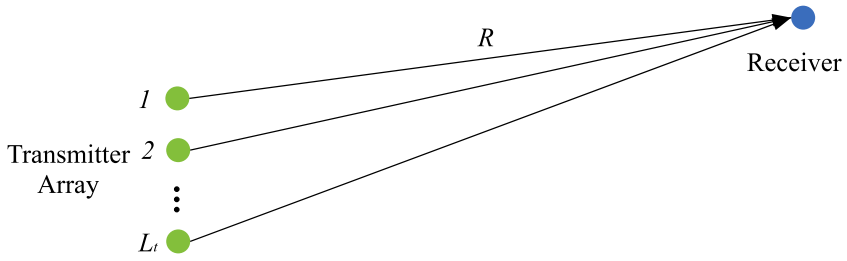

Figure C.3: A MISO system.

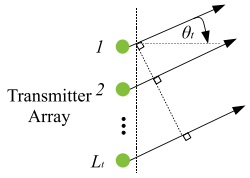

Figure C.4: Definition of the angle of a wave travelling from the transmitter array to the receiver, assuming that the receiver is in the far field of the transmitters.

where $\mathbf{h}_t(\theta_t)$ is the channel vector for the transmitter array.

Again, the channel is represented by a vector $\mathbf{h}_t$, and thus the degree of freedom of the system is one.

C.5 MIMO System

Now, consider combining the above two systems, to create a line of sight MIMO system with L_t transmitter antennas and L_r receiver antennas both arranged as ULAs. This system is shown in Figure C.5. Assume that the attenuation along the line of sight path is identical and unity for all of the antennas, since the separation between the transmitter and receiver arrays R (along the path joining the first transmit antenna and the first receive antenna) is far greater than that between antenna's within an array. The received signal becomes

$$\mathbf{x}(t) = \mathbf{h}_r(\theta_r)\mathbf{h}_t^H(\theta_t)\mathbf{s}(t) + \mathbf{z}(t). \tag{C.3}$$

Let $\mathbf{H} = \mathbf{h}_r(\theta_r)\mathbf{h}_t^H(\theta_t)$. Then, $\mathbf{H}$ is a matrix of dimensions L_t by L_r, but of rank one. This means that the received signal space has dimension one, as each row is a multiple of the row vector $\mathbf{h}_t^H$. Therefore, the channel only has one degree of freedom. The use of a transmitting and receiving array does not increase the number

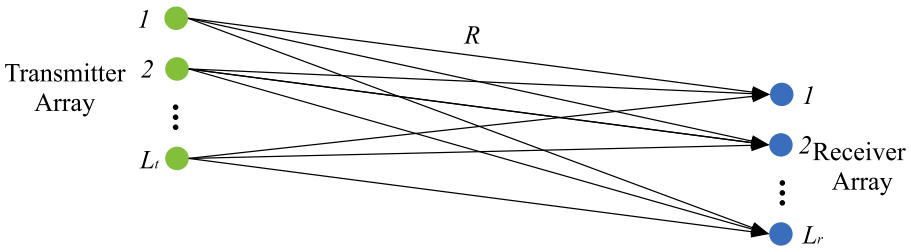

Figure C.5: Line of sight MIMO system.

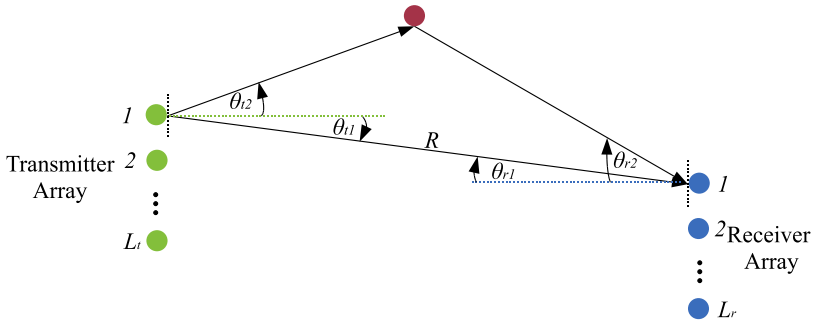

Figure C.6: MIMO system with a reflecting object between the transmitter and the receiver, with multiple signal paths from one transmitter to one receiver shown.

of degrees of freedom of the system, under these conditions, when there is only one available path from the transmitter to the receiver.

However, consider a MIMO system with an obstacle between the transmitter and the receiver as shown in Figure C.6. In this example, the receiver receives the signal that has followed the direct path between the transmitter and receiver arrays, as well as a signal that has been reflected by the object. Applying the principle of superposition, the matrix of steering vectors becomes

$$\mathbf{H} = \mathbf{h}_r(\theta_{r1})\mathbf{h}_t^H(\theta_{t1}) + \mathbf{h}_r(\theta_{r2})\mathbf{h}_t^H(\theta_{t2}). \tag{C.4}$$

Thus, provided that the angle pairs θ_{t1}, θ_{t2} and θ_{r1}, θ_{r2} are sufficiently separated, the channel matrix will now have a rank of two. The condition given in [37] for the angular separation of the pairs of directions to be sufficient, provided that the antennas in the arrays are separated by a distance less than or equal to half a wavelength of the highest frequency component of the signal is

$$\Omega_{r2} \neq \Omega_{r1} \quad \text{and} \quad \Omega_{t2} \neq \Omega_{t1} \tag{C.5}$$

where $\Omega_{ri} = \cos(\theta_{ri})$ and $\Omega_{ti} = \cos(\theta_{ti})$ and $\theta_{ri}, \theta_{ti} \in [0, \pi)$.

So, the received signal space now has two degrees of freedom, and the receiver will be able to distinguish between two signals transmitted by the transmitter array provided that the angular condition is met.

C.6 MIMO System Architectures

Wireless communication channels are usually split into two categories, namely fast fading channels and slow fading channels. A fast fading channel is a channel which varies significantly over the transmission time. In a communications system which usually has continuous transmission, the transmission time refers to the time taken from transmission to reception of a single bit. This is due to the Doppler shift of moving reflecting objects, transmitters or receivers, and thus a single path through the channel experiences different responses over the time of interest. A slow fading channel is one that is approximately constant over the transmission and reception time. For a fast fading channel, the Vertical Bell labs space time architecture, commonly known as the V-BLAST architecture, is optimum. The signal is multiplexed by some arbitrary co-ordinate system and decoded jointly on reception by the V-BLAST architecture.

For a slow fading channel, the V-BLAST architecture is modified to minimise outages across the channel rather than maximise capacity. The modified algorithm is called D-BLAST, where the "D" stands for diagonal. Instead of transmitting one data stream on one transmitter, the data streams are coded across the transmitter channels. On reception, each data stream is decoded sequentially, and cancelled before the following one is decoded.

Under different channel conditions, different MIMO receiver architectures for the decoding of the transmitted data streams provide better performance. A decorrelator bank is optimal under low SNR conditions. A bank of matched filters is optimal under high SNR conditions. A Minimum Mean Square Error (MMSE) receiver bank is able to meet the performance of a decorrelator bank under low SNR conditions and a matched filter bank under high SNR conditions, while exceeding the performance of both at SNRs in between. The use of a Successive Interference Cancellation (SIC) scheme can also improve the receiver's performance.

Each of the receiver architectures mentioned above is explained in more detail in SectionsC.6.1 to C.6.3 that follow.

C.6.1 Decorrelator Bank Architecture

Consider a MIMO system where each transmitter antenna transmits an independent data stream. Let the channel be linear and time invariant. The signal at the receiver is then given by

$$\mathbf{x}[m] = \sum_{i=1}^{L_t} \mathbf{h}_i \mathbf{s}_i[m] + \mathbf{z}[m]. \tag{C.6}$$

The channel matrix $\mathbf{H}$ has columns $\mathbf{h}_i$. All of the channel matrix columns are independent. Also, all of the transmitted data streams $s_i[m]$ are independent.

It is now possible to focus on the kth data stream. The received data then becomes

$$\mathbf{x}[m] = \mathbf{h}_k s_k[m] + \sum_{\substack{i=1 \\ i \neq k}}^{L_t} \mathbf{h}_i \mathbf{s}_i[m] + \mathbf{z}[m]. \tag{C.7}$$

From this equation, it can be seen that the kth data stream experiences interference from all of the other data streams, which needs to be removed to successfully recover the data. Therefore, $\mathbf{x}$ can be projected onto the subspace which is orthogonal to the space spanned by $\mathbf{h}_1, ..., \mathbf{h}_{k-1}, \mathbf{h}_{k+1}, ..., \mathbf{h}_{nt}$. Let this d_k-dimensional space be called V_k. The projection onto this orthogonal space can be represented by a matrix $\mathbf{Q}_k$, whose rows form an orthonormal basis of V_k. Thus, $\mathbf{Q}_k\mathbf{v}$ is the projection of vector $\mathbf{v}$ onto V_k.

The projection of $\mathbf{h}_k$ onto V_k will be non-zero, only if $\mathbf{h}_k$ is not a linear combination of any of the columns $\mathbf{h}_i$ where $i \neq k$. It must be noted that in order for the decorrelation to be successful, the number of transmitted data streams (usually L_t must be less than or equal to the number of receivers L_r).

The projection operation is followed by matched filtering. The combination of projection and matched filtering maximises the SNR of the received signal and is known as decorrelation. It can be represented by a linear filter

$$\mathbf{c}_k^H = (\mathbf{Q}_k \mathbf{h}_k)^H \mathbf{Q}_k. \tag{C.8}$$

This filter is only for the kth data stream. To formulate a filter for all streams, consider that the Moore-Penrose pseudo-inverse of the channel matrix is given by

$$\mathbf{H}^\dagger = (\mathbf{H}^H \mathbf{H})^{-1} \mathbf{H}^H. \tag{C.9}$$

Consider the multiplication of the received data by the pseudo-inverse of the channel matrix $\mathbf{H}^{\dagger}$:

$$\begin{aligned} \mathbf{H}^{\dagger}\mathbf{x}[m] &= \mathbf{H}^{\dagger}\mathbf{H}\mathbf{s}[m] + \mathbf{H}^{\dagger}\mathbf{z}[m] \\ &= (\mathbf{H}^{H}\mathbf{H})^{-1}\mathbf{H}^{H}\mathbf{H}\mathbf{s}[m] + (\mathbf{H}^{H}\mathbf{H})^{-1}\mathbf{H}^{H}\mathbf{z}[m] \\ &= \mathbf{s}[m] + \tilde{\mathbf{z}}[m] \end{aligned} \tag{C.10}$$

where $\tilde{\mathbf{z}}[m] = (\mathbf{H}^{H}\mathbf{H})^{-1}\mathbf{H}^{H}\mathbf{z}[m]$ is coloured Gaussian noise.

Therefore, it can be seen that a bank of decorrelators can be described by the pseudo-inverse of the channel matrix. Each row of the pseudo-inverse channel matrix is equivalent to the kth decorrelator described by Equation (C.8).

The decorrelator bank can achieve close to capacity performance under high SNR conditions. However, under low SNR conditions, the decorrelator cannot achieve capacity. This can be explained by considering that the projection operation used by the decorrelator always has the effect of reducing the norm of the projected vector. Therefore, when the SNR is low, the signals are weak, and the projection further weakens them. This degrades the receiver array's performance. Under low SNR conditions, close to capacity performance can be obtained by only using a bank of matched filters. This operation is effectively the matching of the received signal with each column of the channel matrix $\mathbf{H}$.

C.6.2 Linear MMSE Receiver Architecture

It would be beneficial to have a receiver which can perform close to capacity at both high and low SNR. The Minimum Mean Square Error (MMSE) receiver is able to achieve this. It is derived in the sections following.

Consider a channel over which a single signal is transmitted given by

$$\mathbf{x} = \mathbf{h}s + \mathbf{z} \tag{C.11}$$

where $\mathbf{z}$ is complex circular symmetric coloured noise, which has a covariance matrix $\mathbf{R}_z$ which is invertible. The channel vector $\mathbf{h}$ is deterministic and s is the scalar data symbol that must be determined.

The optimal recovery of s can be obtained by projecting $\mathbf{x}$ along the direction of the channel vector $\mathbf{h}$. However, the noise must firstly be whitened. This is done by performing the transformation $\mathbf{R}_z^{-\frac{1}{2}}$ on $\mathbf{x}$, which produces white noise $\tilde{\mathbf{z}} = \mathbf{R}_z^{-\frac{1}{2}}\mathbf{z}$.

So, the received signal becomes

$$\mathbf{R}_z^{-\frac{1}{2}}\mathbf{x} = \mathbf{R}_z^{-\frac{1}{2}}\mathbf{h}s + \tilde{\mathbf{z}} \tag{C.12}$$

Then, to recover s, the signal with the whitened noise is projected in the direction of $\mathbf{R}_z^{-\frac{1}{2}}\mathbf{h}$. This operation reveals that the output of the MMSE receiver is

$$\begin{aligned}(\mathbf{R}_z^{-\frac{1}{2}}\mathbf{h})^H\mathbf{R}_z^{-\frac{1}{2}}\mathbf{x} &= (\mathbf{R}_z^{-\frac{1}{2}}\mathbf{h})^H\mathbf{R}_z^{-\frac{1}{2}}\mathbf{h}s + (\mathbf{R}_z^{-\frac{1}{2}}\mathbf{h})^H\tilde{\mathbf{z}} \\ \mathbf{h}^H\mathbf{R}_z^{-1}\mathbf{x} &= \mathbf{h}^H\mathbf{R}_z^{-1}\mathbf{h}s + \mathbf{h}^H\mathbf{R}_z^{-1}\mathbf{z}.\end{aligned} \tag{C.13}$$

Therefore, the MMSE linear receiver can be represented by

$$\mathbf{v}_{mmse} = \mathbf{R}_z^{-1}\mathbf{h}. \tag{C.14}$$

It can be shown that this receiver maximises the SNR and minimises the mean square error.

This MMSE receiver structure can now be further analysed. Consider the kth stream of a channel. The received data can be given by

$$\mathbf{x}[m] = \mathbf{h}_k\mathbf{s}_k[m] + \mathbf{z}_k[m] \tag{C.15}$$

where $\mathbf{z}_k[m]$ is the noise plus interference seen at the receivers, due to channel k.

Assume that each channel transmits a signal with power P_i. Then, the covariance matrix of $\mathbf{z}_k$ is given by

$$\mathbf{R}_{z_k} = Z_0\mathbf{I}_{L_r} + \sum_{\substack{i=1 \\ i\neq k}}^{L_t} P_i\mathbf{h}_i\mathbf{h}_i^H \tag{C.16}$$

where Z_0 is the noise power.

So, the kth stage of the MMSE receiver is

$$\mathbf{v}_{mmse_k} = (Z_0\mathbf{I}_{L_r} + \sum_{\substack{i=1 \\ i\neq k}}^{L_t} P_i\mathbf{h}_i\mathbf{h}_i^H)^{-1}\mathbf{h}_k. \tag{C.17}$$

Now, the performance of the MMSE receiver can be analysed at low and high SNR conditions. When the SNR is very low, the signal powers P_i are small in comparison to the noise power Z_0. Therefore, the interference covariance matrix reduces to

$$\mathbf{R}_{z_k} = Z_0\mathbf{I}_{L_r} \tag{C.18}$$

and the MMSE operates as a bank of matched filters.

At high SNR, Z_0 is negligible and $\mathbf{R}_{z_k}$ reduces to the projection of $\mathbf{h}_k$ onto the space which is orthogonal to that spanned by the vectors $\mathbf{h}_1, ..., \mathbf{h}_{k-1}, \mathbf{h}_{k+1}, ..., \mathbf{h}_{L_t}$.

A bank of MMSE filters is found to perform better than a bank of matched filters and a bank of decorrelators, over all SNRs.

C.6.3 Successive Interference Cancellation (SIC) Architecture

All of the mentioned receivers rely on a bank of filters which operate in parallel to cancel out the interference. However, in many cases, the results can be improved by successive processing. Such a process requires that the first data stream is recovered by a technique such as an MMSE filter. It is then subtracted from the received signal $\mathbf{x}$. The second data stream is then recovered from the received signal with the effect of the first data stream removed. The second data stream is then also subtracted from the received signal, so that the third data stream can be recovered without interference from the first or second data streams. This process continues until the final data stream is recovered with no interference from any of the other streams. This process is known as Successive Interference Cancellation (SIC) and is illustrated in Figure C.7.

For the first data stream, SIC offers no performance gain. However, for each successive recovered data stream, the expected SNR increases. A problem with

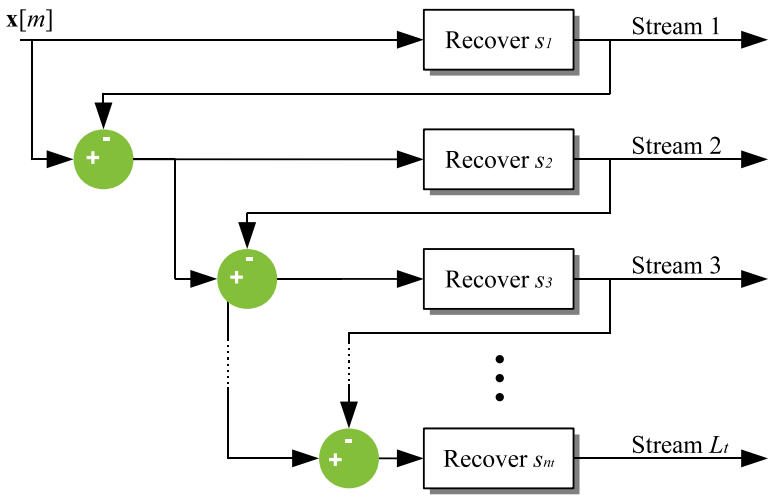

Figure C.7: Successive Interference Cancellation

SIC is error propagation because it relies on each signal being perfectly recovered and subtracted. The error propagation is minimised when the data streams are well coded and sufficiently long. The MMSE SIC is the best performing receiver, and is able to achieve capacity for high and low SNR for an independently and identically distributed (i.i.d.) channel.

Appendix D

Mathematical Derivations

Consider a model with L_t transmitter antennas and L_r receiver antennas. $\mathbf{S}$ is the matrix of the transmitted signals and $\mathbf{X}$ is the matrix of received signals and each have N time samples. Note that it is assumed that the received signal is that for a particular range bin in which one or more targets are known to be located. The signal at the receiver will be given by

$$\mathbf{X} = \mathbf{a}_r^*(\theta)\beta(\theta)\mathbf{a}_t^H(\theta)\mathbf{S} + \mathbf{Z} \tag{D.1}$$

where $\mathbf{Z}$ is a residual term which includes the unmodelled noise, interference and any jamming signals. $\mathbf{a}_t(\theta)$ is the L_t-dimensional steering vector from the transmitter to a target location, and $\mathbf{a}_r(\theta)$ is the L_r-dimensional steering vector from the receiver to the target location. $\beta(\theta)$ is the complex amplitude proportional to the radar cross section of the target.

The covariance matrix of the received data is

$$\hat{\mathbf{R}}_X = \frac{1}{N}\mathbf{X}\mathbf{X}^H. \tag{D.2}$$

The Capon, APES and GLRT techniques were presented in the paper by Xu et al. [32], and the gaps in the derivations have merely been filled in below. The dependency of β, $\mathbf{a}_t$ and $\mathbf{a}_r$ on θ has been omitted in the derivations for notational simplicity.

D.1 Derivation of the Capon Method

The Capon minimisation is

$$\begin{aligned} &\min_{\mathbf{w}} \mathbf{w}^T \hat{\mathbf{R}}_X \mathbf{w}^* \\ &\text{subject to } \mathbf{w}^T \mathbf{a}_r = 1. \end{aligned} \tag{D.3}$$

Let $f = \mathbf{w}^T \hat{\mathbf{R}}_X \mathbf{w}^*$ and $g = \mathbf{w}^T \mathbf{a}_r - 1$. Then, using matrix calculus identities from [67], the expressions become

$$\begin{aligned} \frac{\delta f}{\delta \mathbf{w}^*} &= \frac{\delta}{\delta \mathbf{w}^*} \left(\mathbf{w}^T \hat{\mathbf{R}}_X \mathbf{w}^* \right) \\ &= \frac{\delta}{\delta \gamma} \left(\gamma^H \hat{\mathbf{R}}_X \gamma \right) \text{ where } \gamma = \mathbf{w}^* \\ &= \gamma^H \hat{\mathbf{R}}_X \\ &= \mathbf{w}^T \hat{\mathbf{R}}_X \end{aligned} \tag{D.4}$$

and

$$\begin{aligned} \frac{\delta}{\delta \mathbf{w}^*} \left(\text{Re}\{\lambda^* (\mathbf{w}^T \mathbf{a}_r - 1)\} \right) &= \frac{\delta}{\delta \mathbf{w}^*} \left(\frac{1}{2} \lambda^* \mathbf{w}^T \mathbf{a}_r + \frac{1}{2} \lambda \mathbf{w}^H \mathbf{a}_r^* - \text{Re}\{\lambda^*\} \right) \\ &= \lambda^* \mathbf{a}_r^H. \end{aligned} \tag{D.5}$$

Using the complex case of the method of Lagrange multipliers to optimise gives

$$\begin{aligned} \frac{\delta f}{\delta \mathbf{w}^*} + \frac{\delta}{\delta \mathbf{w}^*} \left(\text{Re}\{\lambda^* g\} \right) &= 0 \\ \mathbf{w}^T \hat{\mathbf{R}}_X + \lambda^* \mathbf{a}_r^H &= 0 \\ \mathbf{w}^T &= -\lambda^* \mathbf{a}_r^H \hat{\mathbf{R}}_X^{-1}. \end{aligned} \tag{D.6}$$

But, applying the constraint

$$\begin{aligned} \mathbf{w}^T \mathbf{a}_r &= 1 \\ -\lambda^* \mathbf{a}_r^H \hat{\mathbf{R}}_X^{-1} \mathbf{a}_r &= 1 \\ \lambda^* &= -\frac{1}{\mathbf{a}_r^H \hat{\mathbf{R}}_X^{-1} \mathbf{a}_r}. \end{aligned} \tag{D.7}$$

Therefore

$$\mathbf{w}^T = \frac{\mathbf{a}_r^H \hat{\mathbf{R}}_X^{-1}}{\mathbf{a}_r^H \hat{\mathbf{R}}_X^{-1} \mathbf{a}_r} \tag{D.8}$$

and the Capon weights are

$$\mathbf{w}_{Capon}(\theta) = \frac{\hat{\mathbf{R}}_X^{-1} \mathbf{a}_r^*(\theta)}{\mathbf{a}_r^T(\theta) \hat{\mathbf{R}}_X^{-1} \mathbf{a}_r^*(\theta)}. \tag{D.9}$$

Then, to find the Capon estimate of β, the least squares difference between the weighted received signal, and the product of the transmitted signal and the complex amplitude at location θ is minimised. Therefore

$$\min_{\beta} \left\| \mathbf{w}^T\mathbf{X} - \beta\mathbf{a}_t^H\mathbf{S} \right\|^2. \tag{D.10}$$

Let $h = \left\| \mathbf{w}^T\mathbf{X} - \beta\mathbf{a}_t^H\mathbf{S} \right\|^2$. Then, by expanding the square

$$\begin{aligned} h &= \left(\mathbf{w}^T\mathbf{X} - \beta\mathbf{a}_t^H\mathbf{S}\right)\left(\mathbf{w}^T\mathbf{X} - \beta\mathbf{a}_t^H\mathbf{S}\right)^H \\ &= \left(\mathbf{w}^T\mathbf{X} - \beta\mathbf{a}_t^H\mathbf{S}\right)\left(\mathbf{X}^T\mathbf{w} - \beta^*\mathbf{S}^H\mathbf{a}_t\right) \\ &= \mathbf{w}^T\mathbf{X}\mathbf{X}^T\mathbf{w} - \beta^*\mathbf{w}^T\mathbf{X}\mathbf{S}^H\mathbf{a}_t - \beta\mathbf{a}_t^H\mathbf{S}\mathbf{X}^T\mathbf{w} + \|\beta\|^2\mathbf{a}_t^H\mathbf{S}\mathbf{S}^H\mathbf{a}_t. \end{aligned} \tag{D.11}$$

Differentiating to solve the minimisation gives

$$\begin{aligned} \frac{\delta h}{\delta \beta} &= 0 \\ -2\mathbf{w}^T\mathbf{X}\mathbf{S}^H\mathbf{a}_t + 2\beta\mathbf{a}_t^H\mathbf{S}\mathbf{S}^H\mathbf{a}_t &= 0 \\ \beta &= \frac{\mathbf{w}^T\mathbf{X}\mathbf{S}^H\mathbf{a}_t}{\mathbf{a}_t^H\mathbf{S}\mathbf{S}^H\mathbf{a}_t}. \end{aligned} \tag{D.12}$$

Finally substituting Equation (D.8) into Equation (D.12) gives

$$\hat{\beta}_{Capon}(\theta) = \frac{\mathbf{a}_r^H(\theta)\hat{\mathbf{R}}_X^{-1}\mathbf{X}\mathbf{S}^H\mathbf{a}_t(\theta)}{N\left[\mathbf{a}_r^T(\theta)\hat{\mathbf{R}}_X^{-1}\mathbf{a}_r^*(\theta)\right]\left[\mathbf{a}_t^H(\theta)\hat{\mathbf{R}}_S\mathbf{a}_t(\theta)\right]} \tag{D.13}$$

where

$$\hat{\mathbf{R}}_S = \frac{1}{N}\mathbf{S}\mathbf{S}^H. \tag{D.14}$$

D.2 Derivation of the APES Method

The optimisation criteria for the APES method is

$$\begin{aligned} &\min_{\mathbf{w},\beta} \left\| \mathbf{w}^T\mathbf{X} - \beta\mathbf{a}_t^H\mathbf{S} \right\|^2 \\ &\text{subject to } \mathbf{w}^T\mathbf{a}_r = 1. \end{aligned} \tag{D.15}$$

Let the minimisation criteria be given by

$$f(\mathbf{w}, \beta) = \left\| \mathbf{w}^T\mathbf{X} - \beta\mathbf{a}_t^H\mathbf{S} \right\|^2$$

and the constraint be given by

$$g(\mathbf{w}) = \mathbf{w}^T\mathbf{a}_r - 1.$$

Firstly, minimise f with respect to β. The minimisation is

$$\min_{\beta} f(\mathbf{w}, \beta) = \min_{\beta} \left\| \mathbf{w}^T \mathbf{X} - \beta \mathbf{a}_t^H \mathbf{S} \right\|^2 . \tag{D.16}$$

The derivative of f with respect to β must therefore equal zero and β can be evaluated to be

$$\begin{aligned}
\frac{\delta f}{\delta \beta} &= 0 \\
\frac{\delta}{\delta \beta} \left\| \mathbf{w}^T \mathbf{X} - \beta \mathbf{a}_t^H \mathbf{S} \right\|^2 &= 0 \\
\frac{\delta}{\delta \beta} (\mathbf{w}^T \mathbf{X} - \beta \mathbf{a}_t^H \mathbf{S})(\mathbf{w}^T \mathbf{X} - \beta \mathbf{a}_t^H \mathbf{S})^H &= 0 \\
\frac{\delta}{\delta \beta} (\mathbf{w}^T \mathbf{X} - \beta \mathbf{a}_t^H \mathbf{S})(\mathbf{X}^T \mathbf{w} - \beta^* \mathbf{S}^H \mathbf{a}_t) &= 0 \\
\frac{\delta}{\delta \beta} (\mathbf{w}^T \mathbf{X}\mathbf{X}^T \mathbf{w} - \beta^* \mathbf{w}^T \mathbf{X}\mathbf{S}^H \mathbf{a}_t - \beta \mathbf{a}_t^H \mathbf{S}\mathbf{X}^T \mathbf{w} + \|\beta\|^2 \mathbf{a}_t^H \mathbf{S}\mathbf{S}^H \mathbf{a}_t) &= 0 \\
-2\mathbf{w}^T \mathbf{X}\mathbf{S}^H \mathbf{a}_t + 2\beta \mathbf{a}^H \mathbf{S}\mathbf{S}^H \mathbf{a}_t &= 0 \\
2\beta \mathbf{a}_t^H \mathbf{X}\mathbf{S}^H \mathbf{a}_t &= 2\mathbf{w}^T \mathbf{X}\mathbf{S}^H \mathbf{a}_t \\
\beta &= \frac{\mathbf{w}^T \mathbf{X}\mathbf{S}^H \mathbf{a}_t}{N \mathbf{a}_t^H \hat{\mathbf{R}}_S \mathbf{a}_t}.
\end{aligned} \tag{D.17}$$

Then, by substituting Equation (D.17) into f, and minimising with respect to $\mathbf{w}$, the optimisation problem becomes

$$\begin{gathered}
\min_{\mathbf{w}} \left\| \mathbf{w}^T \mathbf{X} - \frac{\mathbf{w}^T \mathbf{X}\mathbf{S}^H \mathbf{a}_t \mathbf{a}_t^H \mathbf{S}}{N \mathbf{a}_t^H \hat{\mathbf{R}}_S \mathbf{a}_t} \right\|^2 \\
\text{subject to } \mathbf{w}^T \mathbf{a}_r = 1.
\end{gathered} \tag{D.18}$$

It can be verified that this can be reduced to

$$\begin{gathered}
\min_{\mathbf{w}} \mathbf{w}^T \hat{\mathbf{Q}} \mathbf{w}^* \\
\text{subject to } \mathbf{w}^T \mathbf{a}_r = 1
\end{gathered} \tag{D.19}$$

where

$$\hat{\mathbf{Q}} = \hat{\mathbf{R}}_X - \frac{\mathbf{X}\mathbf{S}^H \mathbf{a}_t \mathbf{a}_t^H \mathbf{S}\mathbf{X}^H}{N^2 \mathbf{a}_t^H \hat{\mathbf{R}}_S \mathbf{a}_t}. \tag{D.20}$$

Then, let the new optimisation criteria be $\tilde{f} = \mathbf{w}^T \hat{\mathbf{Q}} \mathbf{w}^*$ and $\tilde{g} = \mathbf{w}^T \mathbf{a}_r - 1$. The method of Lagrange multipliers can be used to solve this problem. Firstly, the derivatives of the optimisation and constraint criteria are evaluated as

$$\frac{\delta \tilde{f}}{\delta \mathbf{w}*} = \mathbf{w}^T \hat{\mathbf{Q}} \quad \text{and} \quad \frac{\delta}{\delta \mathbf{w}^*} \left(\mathrm{Re}\{\lambda^* \tilde{g}\} \right) = \lambda^* \mathbf{a}_r^H . \tag{D.21}$$

$\hat{\mathbf{Q}}$ is a Hermitian matrix and therefore $\hat{\mathbf{Q}} = \hat{\mathbf{Q}}^H$.

Using the Lagrange method

$$\begin{aligned} \frac{\delta \tilde{f}}{\delta \mathbf{w}} + \frac{\delta}{\delta \mathbf{w}^*} \left(\mathrm{Re}\{\lambda^* \tilde{g}\} \right) &= 0 \\ \mathbf{w}^T \hat{\mathbf{Q}} + \lambda^* \mathbf{a}_r^H &= 0 \\ \mathbf{w}^T &= -\lambda^* \mathbf{a}_r^H \hat{\mathbf{Q}}^{-1}. \end{aligned} \tag{D.22}$$

But, by the constraint

$$\begin{aligned} \mathbf{w}^T \mathbf{a}_r &= 1 \\ -\lambda^* \mathbf{a}_r^H \hat{\mathbf{Q}}^{-1} \mathbf{a}_r &= 1 \\ \lambda &= -\frac{1}{\mathbf{a}_r^H \hat{\mathbf{Q}}^{-1} \mathbf{a}_r} \end{aligned} \tag{D.23}$$

Therefore

$$\mathbf{w}^T = \frac{\mathbf{a}_r^H \hat{\mathbf{Q}}^{-1}}{\mathbf{a}_r^H \hat{\mathbf{Q}}^{-1} \mathbf{a}_r} \tag{D.24}$$

and finally

$$\mathbf{w}_{APES}(\theta) = \frac{\hat{\mathbf{Q}}^{-1} \mathbf{a}_r^*(\theta)}{\mathbf{a}_r^T(\theta) \hat{\mathbf{Q}}^{-1} \mathbf{a}_r^*(\theta)}. \tag{D.25}$$

Therefore, by substituting Equation (D.25) into Equation (D.17), the APES estimate of β is

$$\hat{\beta}_{APES}(\theta) = \frac{\mathbf{a}_r^H(\theta) \hat{\mathbf{Q}}^{-1} \mathbf{X} \mathbf{S}^H \mathbf{a}_t(\theta)}{N \left[\mathbf{a}_r^T(\theta) \hat{\mathbf{Q}}^{-1} \mathbf{a}_r^*(\theta) \right] \left[\mathbf{a}_t^H(\theta) \hat{\mathbf{R}}_S \mathbf{a}_t(\theta) \right]}. \tag{D.26}$$

D.3 Derivation of the GLRT

For the derivation of the GLRT it is assumed that the columns of the residual term $\mathbf{Z}$ in Equation (D.1) are i.i.d. circularly symmetric complex Gaussian random vectors. All columns are assumed to have zero mean and unknown but equal covariance matrices $\mathbf{\Psi}$.

Probability Density Function of X

Before defining the GLRT, the Probability Density Function (PDF) of the residual term $\mathbf{Z}$ is defined. The PDF for $\mathbf{Z}_i$, the complex Gaussian random column with zero mean, is

$$f(\mathbf{Z}_i) = \frac{1}{\pi^{L_r} |\mathbf{\Psi}|} \mathrm{e}^{-\left[\mathbf{Z}_i^H \mathbf{\Psi}^{-1} \mathbf{Z}_i \right]}. \tag{D.27}$$

But then, since $\mathbf{Z}_1, \ldots, \mathbf{Z}_N$ are all independent of each other,

$$\begin{aligned} f(\mathbf{Z}) &= \prod_{i=1}^{N} f(\mathbf{Z}_i) \\ &= \prod_{i=1}^{N} \frac{1}{\pi^{L_r} \left|\boldsymbol{\Psi}\right|} \mathrm{e}^{-\left[\mathbf{Z}_i^H \boldsymbol{\Psi}^{-1} \mathbf{Z}_i\right]} \\ &= (\pi)^{-NL_r} \left|\boldsymbol{\Psi}\right|^{-N} \mathrm{e}^{-\left[\sum_{n=1}^{N} \mathbf{Z}_i^H \boldsymbol{\Psi}^{-1} \mathbf{Z}_i\right]} \\ &= (\pi)^{-NL_r} \left|\boldsymbol{\Psi}\right|^{-N} \mathrm{e}^{-\operatorname{tr}\left[\mathbf{Z}^H \boldsymbol{\Psi}^{-1} \mathbf{Z}\right]} \\ &= (\pi)^{-NL_r} \left|\boldsymbol{\Psi}\right|^{-N} \mathrm{e}^{-\operatorname{tr}\left[\boldsymbol{\Psi}^{-1} \mathbf{Z}\mathbf{Z}^H\right]} \end{aligned} \tag{D.28}$$

The GLR is defined as

$$\rho = 1 - \left[\frac{\max_{\boldsymbol{\Psi}} f(\mathbf{X}|\beta = 0, \boldsymbol{\Psi})}{\max_{\beta, \boldsymbol{\Psi}} f(\mathbf{X}|\beta, \boldsymbol{\Psi})}\right]^{\frac{1}{N}} \tag{D.29}$$

where

$$f(\mathbf{X} \mid \beta, \boldsymbol{\Psi}) = \pi^{-NL_r} \left|\boldsymbol{\Psi}\right|^{-N} \mathrm{e}^{-\operatorname{tr}[\boldsymbol{\Psi}^{-1}(\mathbf{X} - \mathbf{a}_r^* \beta \mathbf{a}_t^H \mathbf{S})(\mathbf{X} - \mathbf{a}_r^* \beta \mathbf{a}_t^H \mathbf{S})^H]} \tag{D.30}$$

is the PDF of the observed data matrix $\mathbf{X}$, given parameters β and $\boldsymbol{\Psi}$, which is equivalent to the PDF of the residual term $\mathbf{Z} = \mathbf{X} - \mathbf{a}_r^* \beta \mathbf{a}_t^H \mathbf{S}$ as derived in Equation (D.27) and Equation (D.28).

Therefore, the GLR measures the difference in the PDF when there is no target and when a target with complex amplitude β is present. When a target is present, the second term will be small, and ρ will be close to one. When there is no target, the second term will be close to one, and ρ will be close to zero.

Consider the maximisation in the numerator of the second term of the GLR. This optimisation is

$$\max_{\boldsymbol{\Psi}} f(\mathbf{X} \mid \beta = 0, \boldsymbol{\Psi}) = \max_{\boldsymbol{\Psi}} \pi^{-NL_r} \left|\boldsymbol{\Psi}\right|^{-N} \mathrm{e}^{-\operatorname{tr}[\boldsymbol{\Psi}^{-1} \mathbf{X}\mathbf{X}^H]}. \tag{D.31}$$

But, noting that $\hat{\mathbf{R}}_X = \frac{1}{N}\mathbf{X}\mathbf{X}^H$, and using the properties of the trace this becomes

$$\begin{aligned} &\max_{\boldsymbol{\Psi}} \pi^{-NL_r} \left|\boldsymbol{\Psi}\right|^{-N} \mathrm{e}^{-\operatorname{tr}[\boldsymbol{\Psi}^{-1} N \hat{\mathbf{R}}_X]} \\ &= \max_{\boldsymbol{\Psi}} \pi^{-NL_r} \left|\boldsymbol{\Psi}\right|^{-N} \mathrm{e}^{-N \operatorname{tr}[\boldsymbol{\Psi}^{-1} \hat{\mathbf{R}}_X]} \\ &= \max_{\boldsymbol{\Psi}} \left(\pi^{L_r} \left|\boldsymbol{\Psi}\right| \mathrm{e}^{\operatorname{tr}[\boldsymbol{\Psi}^{-1} \hat{\mathbf{R}}_X]}\right)^{-N} \\ &= \left(\min_{\boldsymbol{\Psi}} \pi^{L_r} \left|\boldsymbol{\Psi}\right| \mathrm{e}^{\operatorname{tr}[\boldsymbol{\Psi}^{-1} \hat{\mathbf{R}}_X]}\right)^{-N}. \end{aligned} \tag{D.32}$$

Now, replace $\boldsymbol{\Psi}$ with the equivalent expression $\hat{\mathbf{R}}_X\hat{\mathbf{R}}_X^{-1}\boldsymbol{\Psi}$. Then, ignoring the factor π_r^L, the objective of the minimisation in Equation (D.32) is

$$|\boldsymbol{\Psi}|\,\mathrm{e}^{\mathrm{tr}[\boldsymbol{\Psi}^{-1}\hat{\mathbf{R}}_X]} = \left|\hat{\mathbf{R}}_X\right|\left|\hat{\mathbf{R}}_X^{-1}\boldsymbol{\Psi}\right|\mathrm{e}^{\mathrm{tr}[\boldsymbol{\Psi}^{-1}\hat{\mathbf{R}}_X]}\,. \tag{D.33}$$

Then, let $\mathbf{A} = \boldsymbol{\Psi}^{-1}\hat{\mathbf{R}}_X$. Also, diagonalise $\mathbf{A}$ so that $\mathbf{A} = \mathbf{P}\boldsymbol{\Lambda}\mathbf{P}^{-1}$. By the properties of the determinant, it should be noted that $|\mathbf{A}| = |\boldsymbol{\Lambda}|$ and also that $\left|\mathbf{A}^{-1}\right| = \left|\boldsymbol{\Lambda}^{-1}\right|$ where $\boldsymbol{\Lambda} = \mathrm{diag}(\lambda_i)$, $\boldsymbol{\Lambda}^{-1} = \mathrm{diag}(\frac{1}{\lambda_i})$, λ_i are the eigenvalues of $\mathbf{A}$ and $i = 1,\ldots,L_r$. Also $\mathrm{tr}[\mathbf{A}] = \mathrm{tr}[\boldsymbol{\Lambda}]$. Note that since the matrices $\boldsymbol{\Psi}$ and $\hat{\mathbf{R}}_X$ are both covariance matrices and therefore positive semi-definite, so is the matrix $\mathbf{A}$. Therefore the eigenvalues λ_i are all positive.

Now

$$\begin{aligned}
\left|\hat{\mathbf{R}}_X\right|\left|\hat{\mathbf{R}}_X^{-1}\boldsymbol{\Psi}\right|\mathrm{e}^{\mathrm{tr}[\boldsymbol{\Psi}^{-1}\hat{\mathbf{R}}_X]} &= \left|\hat{\mathbf{R}}_X\right|\left|\mathbf{A}^{-1}\right|\mathrm{e}^{\mathrm{tr}[\mathbf{A}]} \\
&= \left|\hat{\mathbf{R}}_X\right|\left|\boldsymbol{\Lambda}^{-1}\right|\mathrm{e}^{\mathrm{tr}[\boldsymbol{\Lambda}]} \\
&= \left|\hat{\mathbf{R}}_X\right|\left(\prod_{i=1}^{L_r}\lambda_i^{-1}\right)\mathrm{e}^{\sum_{i=1}^{L_r}\lambda_i} \\
&= \left|\hat{\mathbf{R}}_X\right|\prod_{i=1}^{L_r}\left(\frac{\mathrm{e}^{\lambda_i}}{\lambda_i}\right).
\end{aligned} \tag{D.34}$$

However, it can be shown that $\frac{\mathrm{e}^x}{x} \geq \mathrm{e}^1$ when x is positive. Therefore, since the eigenvalues λ_i are positive, it follows that

$$\frac{\mathrm{e}^{\lambda_i}}{\lambda_i} \geq \mathrm{e}\,. \tag{D.35}$$

Thus

$$\prod_{i=1}^{L_r}\frac{\mathrm{e}^{\lambda_i}}{\lambda_i} \geq \mathrm{e}^{L_r}\,. \tag{D.36}$$

The lower bound of this inequality will be reached when $\lambda_i = 1$ for $i = 1,\ldots,L_r$. In this case, $\boldsymbol{\Lambda} = \mathbf{I}$ and therefore, $\mathbf{A} = \mathbf{P}\mathbf{P}^{-1} = \mathbf{I}$. For this to be true, it is required that $\boldsymbol{\Psi}^{-1}\hat{\mathbf{R}}_X = \mathbf{I}$ so $\boldsymbol{\Psi} = \hat{\mathbf{R}}_X$. Finally, substituting Equation (D.36) into Equation (D.32) gives

$$\begin{aligned}
\max_{\boldsymbol{\Psi}} f(\mathbf{X}\mid\beta=0,\boldsymbol{\Psi}) &= \left(\min \pi^{L_r}\left|\hat{\mathbf{R}}_X\right|\prod_{i=1}^{L_r}\frac{\mathrm{e}^{\lambda_i}}{\lambda_i}\right)^{-N} \\
&= \left(\pi^{L_r}\left|\hat{\mathbf{R}}_X\right|\mathrm{e}^{L_r}\right)^{-N} \\
&= (\pi\,\mathrm{e})^{-NL_r}\left|\hat{\mathbf{R}}_X\right|^{-N}.
\end{aligned} \tag{D.37}$$

Similarly, the maximum value of the denominator of the second term in the GLR can be found.

$$\max_{\boldsymbol{\Psi},\beta} f(\mathbf{X}\mid\beta,\boldsymbol{\Psi}) = \max_{\boldsymbol{\Psi},\beta}\pi^{-NL_r}\left|\boldsymbol{\Psi}\right|^{-N}\mathrm{e}^{-\mathrm{tr}[\boldsymbol{\Psi}^{-1}(\mathbf{X}-\mathbf{a}_r^*\beta\mathbf{a}_t^H\mathbf{S})(\mathbf{X}-\mathbf{a}_r^*\beta\mathbf{a}_t^H\mathbf{S})^H]}\,. \tag{D.38}$$

Let $\mathbf{B} = \mathbf{X} - \mathbf{a}_r^* \beta \mathbf{a}_t^H \mathbf{S}$. Then, the maximisation becomes

$$\max_{\boldsymbol{\Psi},\beta} f(\mathbf{X} \mid \beta, \boldsymbol{\Psi}) = \max_{\boldsymbol{\Psi},\beta} \pi^{-NL_r} \left|\boldsymbol{\Psi}\right|^{-N} \mathrm{e}^{-\operatorname{tr}[\boldsymbol{\Psi}^{-1}\mathbf{B}\mathbf{B}^H]} \tag{D.39}$$

which is of the same form as Equation (D.31). Thus, the maximum can be shown to be

$$\max_{\boldsymbol{\Psi},\beta} f(\mathbf{X} \mid \beta, \boldsymbol{\Psi}) = (\pi\,\mathrm{e})^{-NL_r} \left(\min_{\beta} \left| \frac{1}{N} (\mathbf{X} - \mathbf{a}_r^* \beta \mathbf{a}_t^H \mathbf{S})(\mathbf{X} - \mathbf{a}_r^* \beta \mathbf{a}_t^H \mathbf{S})^H \right| \right)^{-N}. \tag{D.40}$$

It is now necessary to analyse the minimisation. Let $\hat{\mathbf{Q}}$ be defined as in Equation (D.20). Then, it can be shown that

$$\begin{aligned} &\left| \frac{1}{N} (\mathbf{X} - \mathbf{a}_r^* \beta \mathbf{a}_t^H \mathbf{S})(\mathbf{X} - \mathbf{a}_r^* \beta \mathbf{a}_t^H \mathbf{S})^H \right| \\ &= \left| \hat{\mathbf{Q}} + (\mathbf{a}_t^H \hat{\mathbf{R}}_S \mathbf{a}_t) \left(\beta \mathbf{a}_r^* - \frac{\mathbf{X}\mathbf{S}^H \mathbf{a}_t}{N(\mathbf{a}_t^H \hat{\mathbf{R}}_S \mathbf{a}_t)} \right) \left(\beta \mathbf{a}_r^* - \frac{\mathbf{X}\mathbf{S}^H \mathbf{a}_t}{N(\mathbf{a}_t^H \hat{\mathbf{R}}_S \mathbf{a}_t)} \right)^H \right|. \end{aligned} \tag{D.41}$$

Now, let $\mu = (\mathbf{a}_t^H \hat{\mathbf{R}}_S \mathbf{a}_t)$ and move $\hat{\mathbf{Q}}$ out of the determinant so the equation becomes

$$\left|\hat{\mathbf{Q}}\right| \left| \mathbf{I} + \mu \hat{\mathbf{Q}}^{-1} \left(\beta \mathbf{a}_r^* - \frac{\mathbf{X}\mathbf{S}^H \mathbf{a}_t}{N\mu} \right) \left(\beta \mathbf{a}_r^* - \frac{\mathbf{X}\mathbf{S}^H \mathbf{a}_t}{N\mu} \right)^H \right|. \tag{D.42}$$

Consider the property on matrix determinants given by

$$|\mathbf{I} + \mathbf{A}\mathbf{B}| = |\mathbf{I} + \mathbf{B}\mathbf{A}|. \tag{D.43}$$

Note that this property allows the dimensions of the matrix whose determinant is being evaluated to change.

Therefore, letting $\mathbf{C} = \beta \mathbf{a}_r^* - \frac{\mathbf{X}\mathbf{S}^H \mathbf{a}_t}{N\mu}$, Equation (D.42) can be written as

$$\left|\hat{\mathbf{Q}}\right| \left| \mathbf{I} + \mu \hat{\mathbf{Q}}^{-1} \mathbf{C}\mathbf{C}^H \right| = \left|\hat{\mathbf{Q}}\right| \left[1 + \mu \mathbf{C}^H \hat{\mathbf{Q}}^{-1} \mathbf{C} \right]. \tag{D.44}$$

Therefore, the matrix argument of the second determinant has been transformed to a scalar.

Consider the inequality on Equation (D.44) (with $\mathbf{C}$ resubstituted) given by

$$\begin{aligned} &\left|\hat{\mathbf{Q}}\right| \left[1 + \mu \left(\beta \mathbf{a}_r^* - \frac{\mathbf{X}\mathbf{S}^H \mathbf{a}_t}{N\mu} \right)^H \hat{\mathbf{Q}}^{-1} \left(\beta \mathbf{a}_r^* - \frac{\mathbf{X}\mathbf{S}^H \mathbf{a}_t}{N\mu} \right) \right] \\ &\geq \left|\hat{\mathbf{Q}}\right| \left[1 + \frac{\mathbf{a}_t^H \mathbf{S}\mathbf{X}^H}{N^2 \mu} \hat{\mathbf{Q}}^{-1} \left(\mathbf{I} - \frac{\mathbf{a}_r^* \mathbf{a}_r^T \hat{\mathbf{Q}}^{-1}}{\mathbf{a}_r^T \hat{\mathbf{Q}}^{-1} \mathbf{a}_r^*} \right) \mathbf{X}\mathbf{S}^H \mathbf{a}_t \right] \end{aligned} \tag{D.45}$$

To prove the inequality holds, expand the Left Hand Side (LHS) to give

$$\begin{aligned} \left|\hat{\mathbf{Q}}\right| [1+ \quad & \mu \left|\beta\right|^2 \mathbf{a}_r^T \hat{\mathbf{Q}}^{-1} \mathbf{a}_r^* - \frac{1}{N} \beta^* \mathbf{a}_r^T \hat{\mathbf{Q}}^{-1} \mathbf{X}\mathbf{S}^H \mathbf{a}_t \\ & - \frac{\mu}{N\mu^*} \beta \mathbf{a}_t^H \mathbf{S}\mathbf{X}^H \hat{\mathbf{Q}}^{-1} \mathbf{a}_r^* + \frac{\mu}{N^2 \left\|\mu\right\|^2} \mathbf{a}_t^H \mathbf{S}\mathbf{X}^H \hat{\mathbf{Q}}^{-1} \mathbf{X}\mathbf{S}^H \mathbf{a}_t \Big]. \end{aligned} \tag{D.46}$$

Define the scalars

$$\sigma = \mathbf{a}_r^T \hat{\mathbf{Q}}^{-1} \mathbf{a}_r^*$$
$$\eta = \mathbf{a}_r^T \hat{\mathbf{Q}}^{-1} \mathbf{X} \mathbf{S}^H \mathbf{a}_t.$$

Also note that μ and σ are real and positive because $\hat{\mathbf{R}}_S$ and $\hat{\mathbf{Q}}$ are Hermitian positive semi-definite. Therefore the LHS becomes

$$\left|\hat{\mathbf{Q}}\right| \left[1 + \frac{\mathbf{a}_t^H \mathbf{S} \mathbf{X}^H \hat{\mathbf{Q}}^{-1} \mathbf{X} \mathbf{S}^H \mathbf{a}_t}{N^2 \mu} + \mu\sigma \left|\beta\right|^2 - \frac{\beta^* \eta}{N} - \frac{\beta \eta^*}{N}\right]. \tag{D.47}$$

Analysing the Right Hand Side (RHS) of the equation and using the same scalars gives

$$\begin{aligned} &\left|\hat{\mathbf{Q}}\right| \left[1 + \frac{\mathbf{a}_t^H \mathbf{S} \mathbf{X}^H \hat{\mathbf{Q}}^{-1} \mathbf{X} \mathbf{S}^H \mathbf{a}_t}{N^2 \mu} - \frac{(\mathbf{a}_t^H \mathbf{S} \mathbf{X}^H \hat{\mathbf{Q}}^{-1} \mathbf{a}_r^*)(\mathbf{a}_r^T \hat{\mathbf{Q}}^{-1} \mathbf{X} \mathbf{S}^H \mathbf{a}_t)}{N^2 \mu \mathbf{a}_r^T \hat{\mathbf{Q}}^{-1} \mathbf{a}_r^*}\right] \\ &= \left|\hat{\mathbf{Q}}\right| \left[1 + \frac{\mathbf{a}_t^H \mathbf{S} \mathbf{X}^H \hat{\mathbf{Q}}^{-1} \mathbf{X} \mathbf{S}^H \mathbf{a}_t}{N^2 \mu} - \frac{\left|\eta^2\right|}{N^2 \mu \sigma}\right]. \end{aligned} \tag{D.48}$$

Comparing Equations (D.47) and (D.48) the following must be true for the inequality in Equation (D.45) to hold:

$$\mu\sigma \left|\beta\right|^2 - \frac{\beta^* \eta}{N} - \frac{\beta \eta^*}{N} \geq \frac{\left|\eta^2\right|}{N^2 \mu \sigma}. \tag{D.49}$$

This reduces to

$$\frac{1}{N^2 \mu \sigma} \left|\eta - N \mu \sigma \beta\right|^2 \geq 0. \tag{D.50}$$

This inequality will always hold provided μ and σ are positive, which is true. For equality, $\beta = \frac{\eta}{N\mu\sigma}$, which gives the same estimation for β as the APES algorithm.

So it has been proved that the inequality Equation (D.45) can achieve equality. Now using the identity given in Equation (D.43) to rewrite the RHS of the inequality in Equation (D.45) gives

$$\begin{aligned} &\left|\hat{\mathbf{Q}} + \hat{\mathbf{Q}} \hat{\mathbf{Q}}^{-1} \left(\mathbf{I} - \frac{\mathbf{a}_r^* \mathbf{a}_r^T \hat{\mathbf{Q}}^{-1}}{\mathbf{a}_r^T \hat{\mathbf{Q}}^{-1} \mathbf{a}_r^*}\right) \mathbf{X} \mathbf{S}^H \mathbf{a}_t \left(\frac{\mathbf{a}_t^H \mathbf{S} \mathbf{X}^H}{N^2 \mu}\right)\right| \\ &= \left|\hat{\mathbf{Q}} + \frac{1}{N^2 \mu} \mathbf{X} \mathbf{S}^H \mathbf{a}_t \mathbf{a}_t^H \mathbf{S} \mathbf{X}^H - \frac{\mathbf{a}_r^* \mathbf{a}_r^T \hat{\mathbf{Q}}^{-1} \mathbf{X} \mathbf{S}^H \mathbf{a}_t \mathbf{a}_t^H \mathbf{S} \mathbf{X}^H}{N^2 \mu \left(\mathbf{a}_r^T \hat{\mathbf{Q}}^{-1} \mathbf{a}_r^*\right)}\right|. \end{aligned} \tag{D.51}$$

Replacing μ and $\hat{\mathbf{Q}}$ with their expressions in the equation gives

$$\left|\hat{\mathbf{R}}_X - \frac{\mathbf{a}_r^* \mathbf{a}_r^T \hat{\mathbf{Q}}^{-1} \mathbf{X} \mathbf{S}^H \mathbf{a}_t \mathbf{a}_t^H \mathbf{S} \mathbf{X}^H}{N^2 \left(\mathbf{a}_t^H \hat{\mathbf{R}}_S \mathbf{a}_t\right) \left(\mathbf{a}_r^T \hat{\mathbf{Q}}^{-1} \mathbf{a}_r^*\right)}\right|. \tag{D.52}$$

$\hat{\mathbf{R}}_X$ is then moved out of the equation giving

$$\left|\hat{\mathbf{R}}_X\right| \left|\mathbf{I} - \frac{\hat{\mathbf{R}}_X^{-1} \mathbf{a}_r^* \mathbf{a}_r^T \hat{\mathbf{Q}}^{-1} \mathbf{X} \mathbf{S}^H \mathbf{a}_t \mathbf{a}_t^H \mathbf{S} \mathbf{X}^H}{N^2 \left(\mathbf{a}_t^H \hat{\mathbf{R}}_S \mathbf{a}_t\right) \left(\mathbf{a}_r^T \hat{\mathbf{Q}}^{-1} \mathbf{a}_r^*\right)}\right|. \tag{D.53}$$

Once again, the matrix whose determinant is being calculated is reshaped by the identity Equation (D.43), by moving the matrix $\hat{\mathbf{R}}_X^{-1}\mathbf{a}_r^*$ to the back, to give

$$\left|\hat{\mathbf{R}}_X\right| \left[1 - \frac{\mathbf{a}_r^T\hat{\mathbf{Q}}^{-1}\mathbf{X}\mathbf{S}^H\mathbf{a}_t\mathbf{a}_t^H\mathbf{S}\mathbf{X}^H\hat{\mathbf{R}}_X^{-1}\mathbf{a}_r^*}{N^2\left(\mathbf{a}_t^H\hat{\mathbf{R}}_S\mathbf{a}_t\right)\left(\mathbf{a}_r^T\hat{\mathbf{Q}}^{-1}\mathbf{a}_r^*\right)}\right]. \tag{D.54}$$

It is noted that

$$\frac{\mathbf{X}\mathbf{S}^H\mathbf{a}_t\mathbf{a}_t^H\mathbf{S}\mathbf{X}^H}{N^2\mathbf{a}_t^H\hat{\mathbf{R}}_S\mathbf{a}_t} = \hat{\mathbf{R}}_X - \hat{\mathbf{Q}}$$

and therefore Equation (D.54) becomes

$$\begin{aligned}&\left|\hat{\mathbf{R}}_X\right| \left[1 - \frac{\mathbf{a}_r^T\hat{\mathbf{Q}}^{-1}(\hat{\mathbf{R}}_X - \hat{\mathbf{Q}})\hat{\mathbf{R}}_X^{-1}\mathbf{a}_r^*}{\mathbf{a}_r^T\hat{\mathbf{Q}}^{-1}\mathbf{a}_r^*}\right] \\ &= \left|\hat{\mathbf{R}}_X\right| \frac{\mathbf{a}_r^T\hat{\mathbf{R}}_X^{-1}\mathbf{a}_r^*}{\mathbf{a}_r^T\hat{\mathbf{Q}}^{-1}\mathbf{a}_r^*}.\end{aligned} \tag{D.55}$$

So, the maximisation in Equation (D.40) evaluates to

$$\max_{\boldsymbol{\Psi},\beta} f(\mathbf{X} \mid \beta, \boldsymbol{\Psi}) = (\pi\,\mathrm{e})^{-NL_r}\left|\hat{\mathbf{R}}_X\right|^{-N}\left(\frac{\mathbf{a}_r^T\hat{\mathbf{R}}_X^{-1}\mathbf{a}_r^*}{\mathbf{a}_r^T\hat{\mathbf{Q}}^{-1}\mathbf{a}_r^*}\right)^{-N}. \tag{D.56}$$

Thus, substituting into Equation (D.29)

$$\rho = 1 - \left[\frac{(\pi\,\mathrm{e})^{-NL_r}\left|\hat{\mathbf{R}}_X\right|^{-N}}{(\pi\,\mathrm{e})^{-NL_r}\left|\hat{\mathbf{R}}_X\right|^{-N}\left(\frac{\mathbf{a}_r^T\hat{\mathbf{R}_X}^{-1}\mathbf{a}_r^*}{\mathbf{a}_r^T\hat{\mathbf{Q}}^{-1}\mathbf{a}_r^*}\right)^{-N}}\right]^{-N} \tag{D.57}$$

and the GLR is

$$\rho(\theta) = 1 - \frac{\mathbf{a}_r^T(\theta)\hat{\mathbf{R}}_X^{-1}\mathbf{a}_r^*(\theta)}{\mathbf{a}_r^T(\theta)\hat{\mathbf{Q}}^{-1}\mathbf{a}_r^*(\theta)} \tag{D.58}$$

Appendix E

Implementation of the Beampattern Matching Design

The beampattern matching design, a form of beampattern synthesis for MIMO radar, was discussed in Sections 2.9.3. Below the method followed to perform this optimisation using MATLAB and the third party toolbox, Self-Dual-Minimisation (SeDuMi) is described.

Firstly recall the beampattern matching optimisation criterion in SQP form as given in (2.140) is

$$\begin{aligned} &\min_{\delta,\rho} \delta \\ &\text{subject to } \left\| \mathbf{\Gamma}^{\frac{1}{2}} \rho \right\| \leq \delta \\ R_{S,ll} &= \frac{c}{L_t} \quad l = 1, \ldots, L_t \\ &\mathbf{R}_S \geq 0. \end{aligned} \tag{E.1}$$

In this equation, $\mathbf{\Gamma}$ is a known constant for a given problem (see (2.139)). The second optimisation variable is

$$\rho = \begin{bmatrix} \alpha \\ \mathbf{r} \end{bmatrix}. \tag{E.2}$$

$\mathbf{R}_S$ and $\mathbf{r}$ are related by

$$\text{vec}\left[\mathbf{R}_S\right] = \mathbf{J}\mathbf{r}. \tag{E.3}$$

To begin the implementation of this problem in MATLAB, a vector of the locations covering the area of interest, $\{\mu_q\}_{q=1}^{Q}$, is generated. Estimates of the target locations $\{\hat{\theta}_k\}_{k=1}^{\tilde{K}}$ are obtained to generate the desired beampattern. For the purposes of this work, the desired beampattern is set equal to one at all $\hat{\theta}_k \pm \Delta/2$, where Δ is the beam width of the pattern and zero elsewhere. Also the weights w_q at all of the

locations of interest, and the weight for the cross-correlation pattern w_c are assigned values. The matrix $\mathbf{\Gamma}$, defined in (2.139), can then be evaluated.

Next, a general expression for the constant matrix $\mathbf{J}$ is required. Consider a MIMO system with $L_t = 3$ transmitting antennas. Then, for the 3×3 matrix $\mathbf{R}_S$, the vectors

$$\text{vec}\left[\mathbf{R}_S\right] = \begin{bmatrix} r_{11} & r_{21} & r_{31} & r_{12} & r_{22} & r_{32} & r_{13} & r_{23} & r_{33} \end{bmatrix}^T$$

and

$$\mathbf{r} = \begin{bmatrix} r_{11} & r_{22} & r_{33} & \Re(r_{12}) & \Re(r_{23}) & \Re(r_{13}) & \Im(r_{12}) & \Im(r_{23}) & \Im(r_{13}) \end{bmatrix}^T$$

are defined. Due to the Hermitian symmetry of $\mathbf{R}_S$, it can then be shown that the matrix $\mathbf{J}$ required to transform $\mathbf{r}$ to $\text{vec}\left[\mathbf{R}_S\right]$ is

	1	*2*	*3*	*4*	*5*	*6*	*7*	*8*	*9*
1	1	0	0	0	0	0	0	0	0
2	0	0	0	1	0	0	-j	0	0
3	0	0	0	0	0	1	0	0	-j
4	0	0	0	1	0	0	j	0	0
5	0	1	0	0	0	0	0	0	0
6	0	0	0	0	1	0	0	-j	0
7	0	0	0	0	0	1	0	0	j
8	0	0	0	0	1	0	0	j	0
9	0	0	1	0	0	0	0	0	0

Using the above, an algorithm to generate the matrix $\mathbf{J}$ for a MIMO system with L_t transmitter elements can be derived. It requires a matrix of $L_t^2 \times L_t^2$ to be initialised to contain only zeros. Then, the following elements are set

$$\begin{aligned} J_{(i-1)L_t+i,i} &= 1 \\ J_{p,q} &= 1 \\ J_{p+(L_t-1)k,q} &= 1 \\ J_{p,q+\frac{1}{2}(L_t^2-L_t)} &= -j \\ J_{p+(L_t-1)k,q+\frac{1}{2}(L_t^2-L_t)} &= j \end{aligned} \tag{E.4}$$

where

$$\begin{aligned} p &= k + m(1 + L_t) - L_t \\ q &= m + \sum_{l=1}^{k} (L_t - l + 1) \\ i &= 1, \ldots, L_t \\ k &= 1, \ldots, L_t - 1 \\ m &= 1, \ldots, L_t - k. \end{aligned}$$

The optimisation problem can now be solved using the SeDuMi toolbox. This is a toolbox for MATLAB which solves optimisation problems with linear, quadratic and semi-definiteness constraints with real or complex data and variables [42].

SeDuMi solves optimisation problems in either primal standard form,

$$\begin{aligned} &\min_{\mathbf{x}} \mathbf{c}^T \mathbf{x} \\ &\text{subject to } \mathbf{A}\mathbf{x} = \mathbf{b} \\ &x_i \geq 0 \text{ for } i = 1, 2, \ldots, n, \end{aligned} \tag{E.5}$$

or dual standard form

$$\begin{aligned} &\max_{\mathbf{y}} \mathbf{b}^T \mathbf{y} \\ &\text{subject to } c_i - \mathbf{a}_i^T \mathbf{y} \geq 0 \text{ for } i = 1, 2, \ldots, n. \end{aligned} \tag{E.6}$$

The optimisation problem in (E.1) has equality constraints ($\mathbf{R}_{S,ll} = \frac{c}{L_t}$), implied linear constraints ($\delta, \alpha \geq 0$), quadratic constraints $\left(\left\| \mathbf{\Gamma}^{\frac{1}{2}} \rho \right\| \leq \delta \right)$ and positive semi-definite constraints ($\mathbf{R}_S \geq 0$). Given these constraints, the dual standard form is chosen to solve the problem. Then define the ith constraint as

$$z_i = c_i - \mathbf{a}_i^T \mathbf{y} \tag{E.7}$$

where $\mathbf{a}_i$ is the ith column of $\mathbf{A}$.

The optimisation problem is now put into a form to be solved by SeDuMi. Firstly, the optimisation variable is defined as

$$\mathbf{y} = \begin{bmatrix} \delta \\ \alpha \\ \mathbf{r} \end{bmatrix}. \tag{E.8}$$

It is noted that $\mathbf{y}$ has dimension $L_t^2 + 2$.

Next, the vector $\mathbf{b}$ can be found. Since the dual standard form requires maximisation, the problem of minimisation is reformatted to be the maximisation of $-\delta$ with the addition of the constraint $\delta \geq 0$. Therefore,

$$\mathbf{b} = \begin{bmatrix} -1 \\ \mathbf{0}_{[L_t^2+1\times 1]} \end{bmatrix} \tag{E.9}$$

where the notation $\mathbf{X}_{[Y\times Z]}$ specifies matrix $\mathbf{X}$ to be Y-by$Z$ dimensional.

The vector $\mathbf{c}$ and matrix $\mathbf{A}$ are found by reformulation of the constraints such that they can be interpreted by SeDuMi. A structure K, which represents a cone is used to define the constraints. SeDuMi expects the constraints to be given in the order free variable constraints ($K.f$), linear constraints ($K.l$), quadratic constraints ($K.q$) and finally semi-definite constraints ($K.s$) [43]. Each field of K holds the number of constraints of that type which SeDuMi should expect. Each set of constraints will be described below. The vector $\mathbf{c}$ and matrix $\mathbf{A}$ are constructed below separately for each set of constraints and concatenated at the end.

Free Variable Constraints

In the primal standard form, free variables can be used to introduce inequality constraints. This is possible because the inequality $f_i(x) \leq 0$ only holds if there is a variable $s_i \geq 0$, called the free or slack variable, that satisfies $f_i(x) + s_i = 0$. In the dual form, free variables allow equality constraints. Therefore, the elemental power constraint is defined using free variables. The constraint is

$$\mathbf{R}_{S,ll} = \frac{c}{L_t}. \tag{E.10}$$

Therefore, in the form of SeDuMi, it is required that $y_3, \ldots, y_{L+2} = r_{11}, \ldots r_{L_tL_t} = \frac{c}{L_t}$. Thus, since the ith free variable constraint has the form

$$z_{fi} = 0, \tag{E.11}$$

it can be seen that $\mathbf{c}$ and $\mathbf{A}$ must be

$$c_{f1}, \ldots, c_{fL_t} = \frac{c}{L_t} \tag{E.12}$$

and

$$\mathbf{A}_f^T = \begin{bmatrix} \mathbf{0}_{[L_t\times 2]} & \mathbf{I}_{[L_t\times L_t]} & \mathbf{0}_{[L_t\times(L_t^2-L_t)]} \end{bmatrix}. \tag{E.13}$$

Then, SeDuMi is informed that the first L_t constraints are free variable constraints by setting $K.f = L_t$.

Linear Constraints

Due to the fact that δ is greater than or equal to a norm, δ has to be positive.

Therefore, the linear constraint $\delta \geq 0$ is included. Also, since α is a weighting it must also be restricted to be positive and the second linear constraint is $\alpha \geq 0$. Therefore,

$$c_l = \mathbf{0}_{[2\times 1]} \tag{E.14}$$

and

$$\mathbf{A}_l^T = \begin{bmatrix} -1 & 0 & \mathbf{0}_{[1\times L_t^2]} \\ 0 & -1 & \mathbf{0}_{[1\times L_t^2]} \end{bmatrix}. \tag{E.15}$$

$K.l$ is set equal to two to specify the two constraints following the free variable constraints are linear constraints.

Quadratic Constraints

The Euclidean norm of a vector is denoted by $\|\mathbf{x}\|$ and is given by $(\mathbf{x}^H\mathbf{x})^{\frac{1}{2}}$ which is a quadratic function (see Equation (A.1) in Appendix A). Therefore, the constraint $\left\|\mathbf{\Gamma}^{\frac{1}{2}}\rho\right\| \leq \delta$ is quadratic. $K.q$ is assigned the value of L_t^2+2. This informs the SeDuMi algorithm that the $L_t^2 + 2$ quadratic constraints have the form $z_{q1} \geq \left\|z_{q(2:L_t^2+2)}\right\|$. The first constraint specifies that δ is the variable which the norm must be less than. The following constraints give the argument of the norm. Thus, the matrix $\mathbf{A}$ and vector $\mathbf{c}$ can be formulated as

$$\mathbf{c}_q = \mathbf{0}_{[L_t^2+2\times 1]} \tag{E.16}$$

and

$$\mathbf{A}_q^T = \begin{bmatrix} -1 & \mathbf{0}_{[1\times L_t^2+1]} \\ \mathbf{0}_{[L_t^2+1\times 1]}, & \mathbf{\Gamma}^{\frac{1}{2}} \end{bmatrix}. \tag{E.17}$$

Semi-definite Constraints

Finally, it is required that the matrix $\mathbf{R}_S$ is positive semi-definite. Define the operation mat[$\cdot$] as the reciprocal operation of vec[$\cdot$], which only holds when the original matrix was square. Therefore, mat[$\cdot$] takes a column vector and turns it into a square matrix. By setting $K.s$ equal to L_t, the SeDuMi algorithm is informed that the $L_t \times L_t$ matrix mat[$\mathbf{z}_s$] is positive semi-definite. Using the relationship between $\mathbf{R}_S$ and $\mathbf{r}$ stated in (E.3), $\mathbf{c}$ and $\mathbf{A}$ are defined to be

$$\mathbf{c}_s = \mathbf{0}_{[L_t^2\times 1]} \tag{E.18}$$

and

$$\mathbf{A}_s^T = \begin{bmatrix} \mathbf{0}_{[L_t^2\times 2]} & -\mathbf{J} \end{bmatrix}. \tag{E.19}$$

Also, $K.scomplex$ is set equal to one to indicate that the positive semi-definite matrix contains complex elements, and thus must be a Hermitian matrix.

Performing the Optimisation

The vector $\mathbf{c}$ and matrix $\mathbf{A}$ are now constructed by concatenation giving

$$\mathbf{c} = \begin{bmatrix} \mathbf{c}_f \\ \mathbf{c}_l \\ \mathbf{c}_q \\ \mathbf{c}_s \end{bmatrix} \tag{E.20}$$

which is $(2L_t^2 + L_t + 4)$-by-1 dimensional and

$$\mathbf{A} = \begin{bmatrix} \mathbf{A}_f & \mathbf{A}_l & \mathbf{A}_q & \mathbf{A}_s \end{bmatrix} \tag{E.21}$$

which is $(L_t^2 + 2)$-by-$(2L_t^2 + L_t + 4)$ dimensional.

The problem is then solved in MATLAB with the following code

```
[x,y,info] = sedumi(A,b,c,K);
z = c - A.'*y;
R = mat(z(Lt^2 + Lt + 5:length(z)));
```

The matrix $\mathbf{R}_S$ is given by the last L_t^2 constraints.

Appendix F

Transmitter Design

Three transmitter amplifier prototypes that were built and tested are presented in this appendix. The test results of the three prototypes, which validate the choice of the Class AB amplifier described in the main section of this dissertation, are presented. In addition, more detailed results obtained with a prototype of the chosen model are given.

F.1 Amplifier Prototypes

Due to the crossover distortion seen on the transmitter amplifier presented in Section 6.3.3, two other transmitter amplifier configurations were investigated. The circuit shown in Figure 6.13, will be referred to as Prototype 1.

Prototype 2 is a class AB amplifier and is shown in Figure F.1. It includes a diode to bias the base-emitter voltages of the transistors, and thereby minimise the correction required by the operational amplifier. In addition, a resistor is connected across the base-collector of the PNP transistor to bias the transistors. This resistor sets the current that flows into the base of each of the transistors, and can limit the current output of the circuit. This amplifier should result in a reduced total harmonic distortion, due to reduced crossover distortion, and thus should provide better results than the implemented amplifier.

The third transmitter amplifier that was tested, Prototype 3, was a TDA2822 audio amplifier chip. This option could potentially improve the system performance, as the amplifier chip is custom built for audio applications. In addition, it would help to decrease the component count. The circuit is shown in Figure F.2.

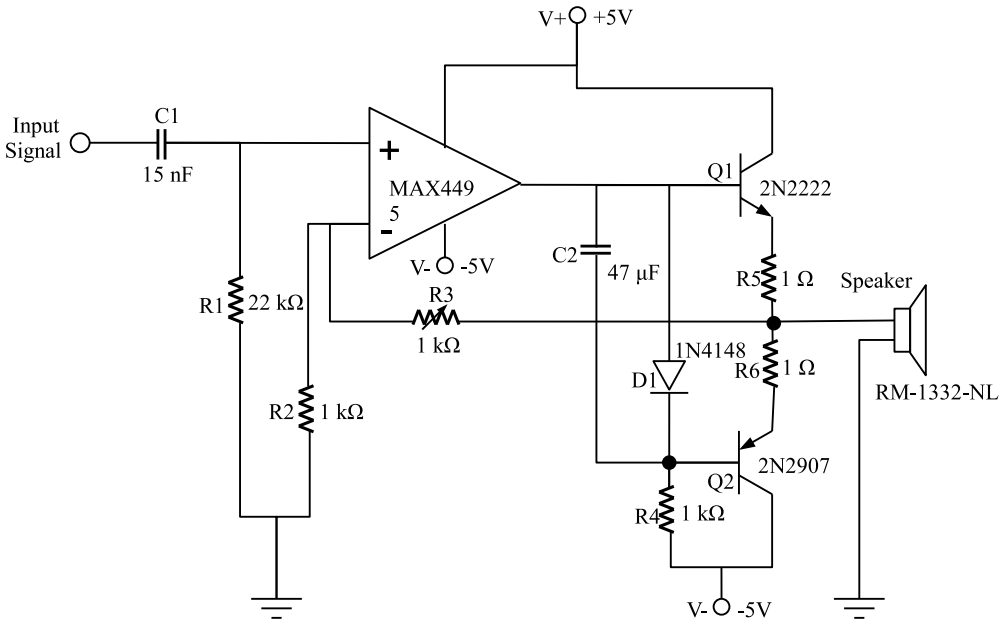

Figure F.1: Prototype 2: Class AB amplifier with a diode for crossover distortion correction.

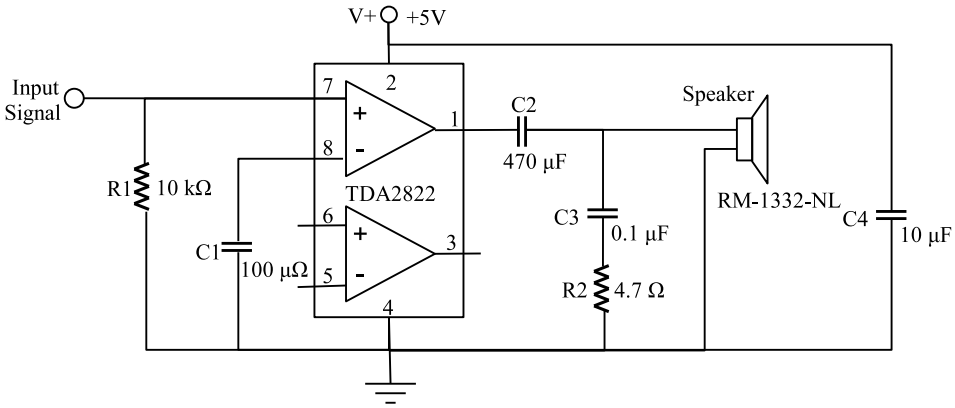

Figure F.2: Prototype 3: Audio amplifier chip circuit.

Measurements were taken on the three prototypes to compare their performance. Note that Prototypes 2 and 3 were built on breadboard, whereas Prototype 1 was built on a custom designed prototype PCB which included the reconstruction filter, the output of which is the input to the amplifier. For all of the measurements, the input signal was a 10 kHz sine wave, of the maximum possible voltage which does not result in clipping on the output.

Firstly, the Total Harmonic Distortion (THD) of the amplifier outputs was measured. An 8 Ω load was connected to each of the outputs to model the speaker. The output of the amplifiers was connected to a 10 Hz to 500 MHz spectrum analyser. The

Prototype	*1*	*2*	*3*
THD (%)	0.011	0.004	0.013
Maximum Power (mW)	723	508	170

Table F.1: Performance measures of the three prototypes

THD, up to the nth harmonic, as calculated as

$$THD = \frac{P_2 + P_3 + P_n}{P_1} \tag{F.1}$$

where P_i is the power of the ith harmonic. The THDs of the three prototypes, up to the 10th harmonic are shown in Table F.1.

Secondly, the maximum power that each prototype could supply to an 8 Ω load was measured. The maximum peak to peak output voltage was determined by adjusting the amplitude of the input voltage and the gain of the amplifiers. The maximum power was then calculated as

$$P_{max} = \frac{V^2_{(p-p)max}}{2\sqrt{2}R} \tag{F.2}$$

where R is the load resistance. The maximum power results are also shown in Table F.1.

Prototype 2, which included compensation for crossover distortion had the lowest THD, as was expected. However, all of the prototypes display THDs of below 0.1% at their maximum power. Therefore, by analysis of the THD alone, any of the prototypes would be suitable for implementation in the system.

It is also important that the speakers are driven close to their maximum power, so that the transmitted signal has the greatest amplitude possible, and the system SNR is increased. The speakers which will be connected to the transmitter have a maximum power rating of 0.8 W and a typical power of 0.5 W. Prototype 2, which has the lowest THD, cannot output sufficient power, since the resistor inserted across the base-collector junction of the PNP transistor limits the current which flows into the transistors, and therefore also limits the output current. Prototype 3 has the highest THD and the lowest output power and is therefore the least suitable amplifier. However, Prototype 1, the class AB amplifier, has acceptable THD and can supply the maximum power. Therefore, it is the selected amplifier.

F.2 Transmitter Prototype Measurements

An initial prototype of the transmitter was built using through-hole components and a poured copper PCB. A photograph of the transmitter prototype board is shown in Figure F.3. Measurements were taken on the board to investigate its performance. These results are presented below.

A function generator was connected to the input of the filter. The signal chosen for testing was a sine wave, with a peak to peak amplitude of approximately 3.8 V and a DC offset of 2.3 V so that the minimum signal value is greater than the 400 mV required to prevent clipping. Figure F.4(a) shows the input signal and the output signal at 8 kHz (the signal was AC coupled so the offset is not displayed. No distortion is visible on the output signal.

Figure F.4(b) is the FFT of the input and output signals of the transmitter board. The resolution of the FFT is extremely course, due to the short duration of the measured signals. However, it still illustrates that the input and output FFTs are almost identical, indicating that the filter and amplifier cause little distortion. The peak power at 8 kHz is over 40 dB above the first harmonic at 16 kHz.

The frequency of the clock applied to the filter is 1.515 MHz, and therefore, since the clock to corner frequency ratio is 100:1, the filter is expected to have a cutoff frequency of approximately 15 kHz. Figure F.5 shows the frequency response of the circuit. Figure F.5(a) is the amplitude response which was calculated by measuring

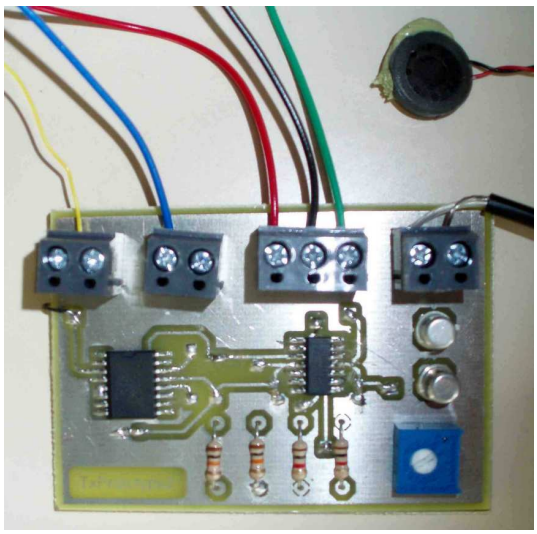

Figure F.3: The transmitter prototype board.

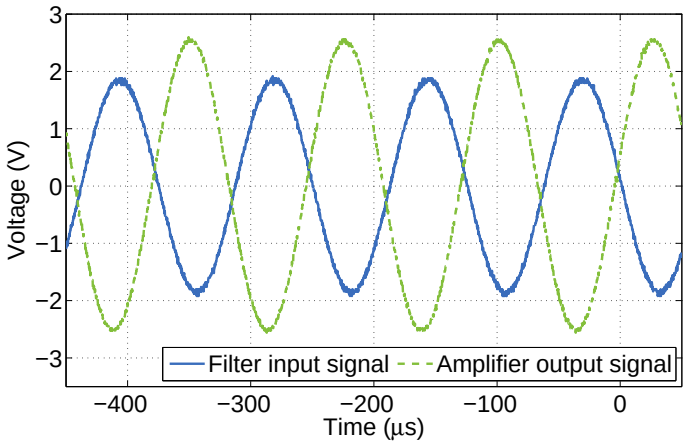

(a) Time varying input and output signals.

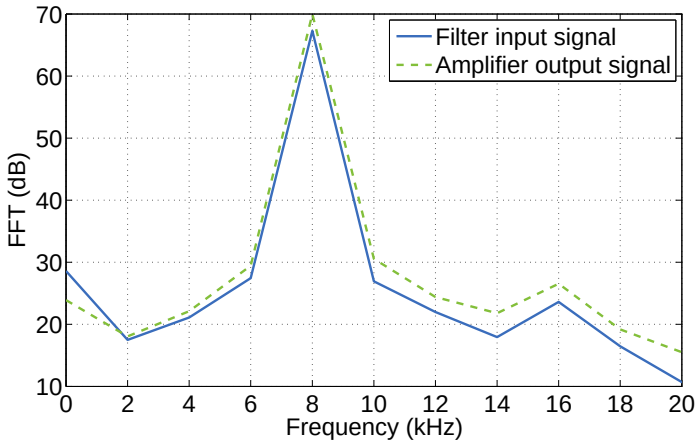

(b) FFT of input and output signals.

Figure F.4: Example transmitter prototype input and output signals and their frequency responses at 8 kHz.

the output signal at frequencies from 6 kHz to 20 kHz in 500 Hz intervals and then calculating the RMS voltage at each point. It can be seen that the corner frequency is slightly above 15 kHz. The attenuation of the signal is lower than expected. It is only approximately 30 dB, whereas an attenuation of 50 dB was expected. It is however possible that the 30 dB power is the noise floor of the oscilloscope and the filters attenuation at 20 kHz could therefore be lower than illustrated.

The phase response of the circuit was analysed by measuring the phase shift in degrees between the input signal and the output signal, at different frequencies between 6 kHz and 12.5 kHz. It is shown in Figure F.5(b), and it can be seen that the phase response is approximately linear, as expected from the data sheet of the MAX293 filter.

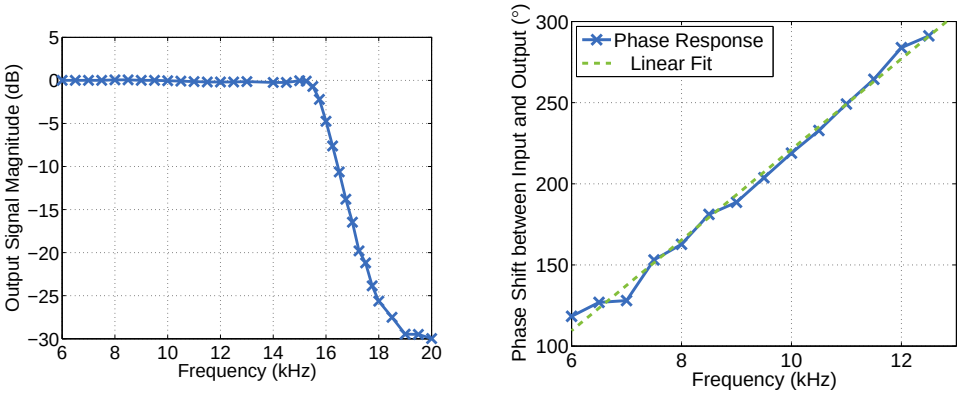

(a) Amplitude response.

(b) Phase response.

Figure F.5: Frequency response of the transmitter prototype.

Apart from the lower than expected attenuation at the Nyquist frequency, the measurements show that the transmitter prototype operates as desired, and will be suitable for use in the acoustic phased array transmitter system.

Appendix G

Photographs of the Hardware System

Photographs of the components making up the hardware system are included in this appendix.

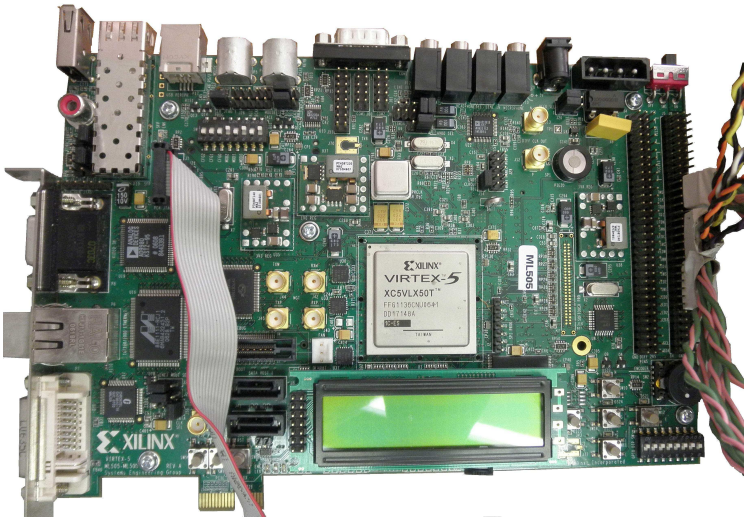

Figure G.1: The Virtex 5 FPGA on an ML505 development board.

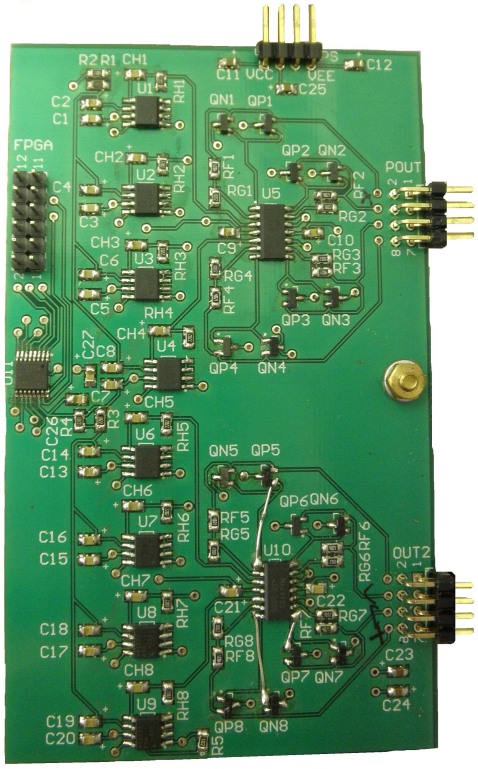

(a) The transmitter analogue electronics.

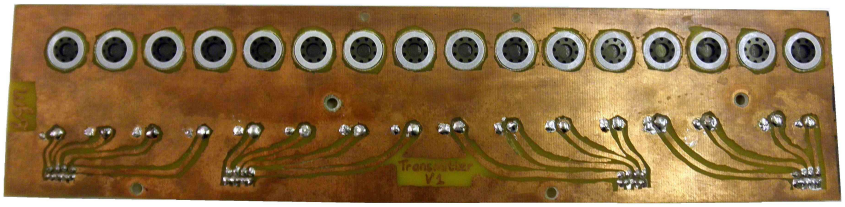

(b) Front of the speaker board.

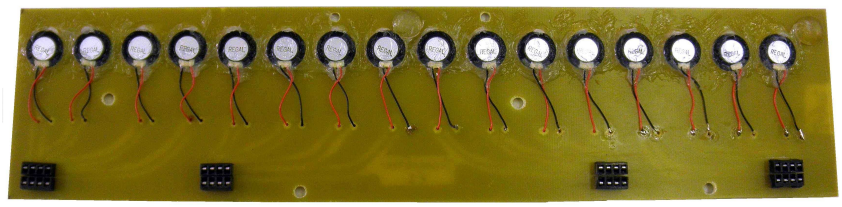

(c) Back of the speaker board.

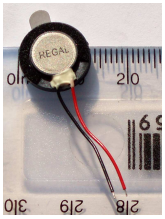

(d) The speaker.

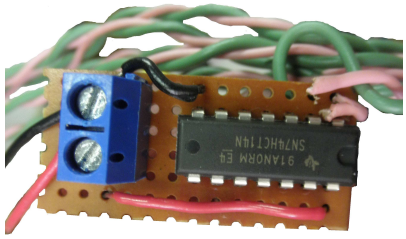

(e) The Schmitt trigger to convert the FPGA clock from TTL to CMOS.

Figure G.2: The transmitter components.

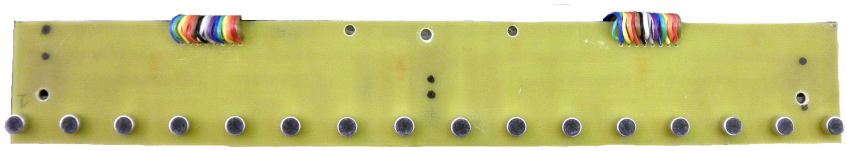

(a) The microphone board.

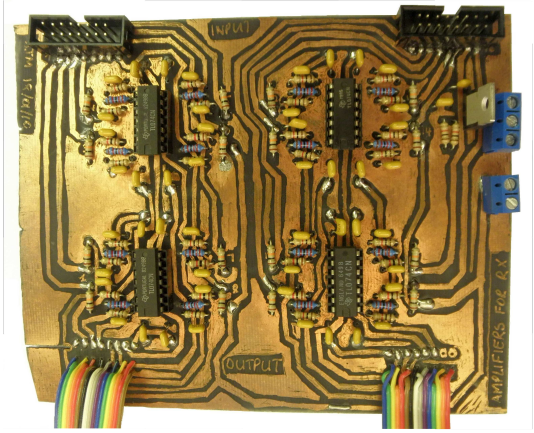

(b) The additional amplifier board, with a 2.5 V voltage regulator.

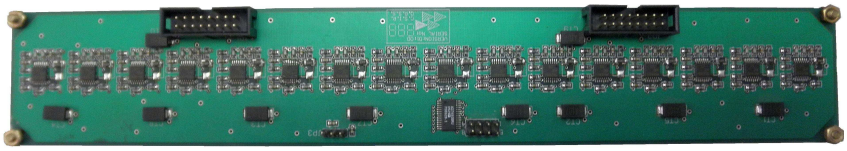

(c) The receiver analogue electronics board.

Figure G.3: The receiver components



(a) The transmitter and receiver arrays mounted on the front of the box.

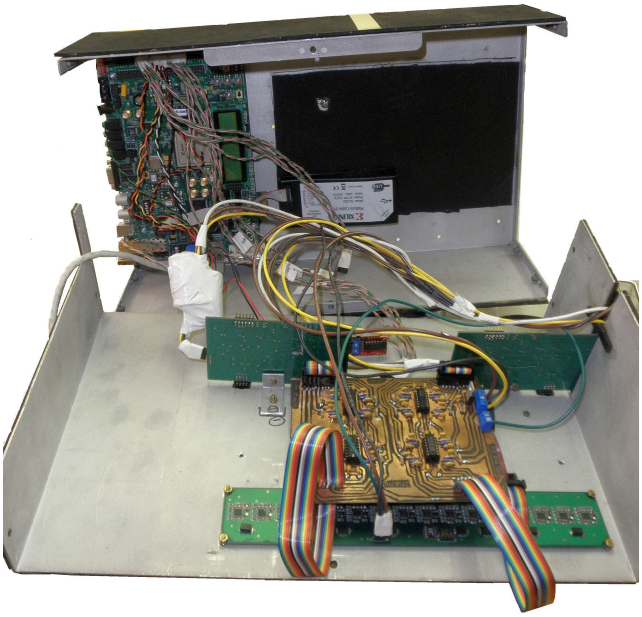

(b) The FPGA and electronics contained inside the box.

Figure G.4: The integrated hardware system.

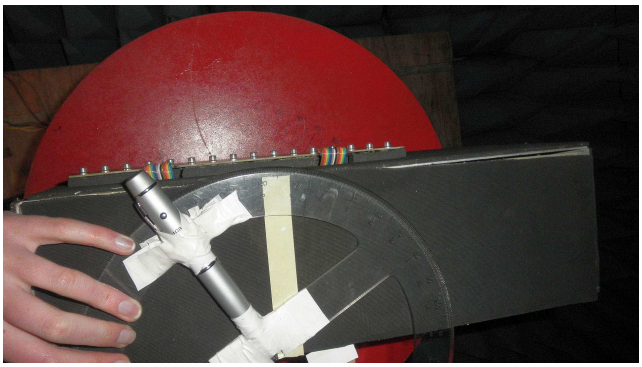

Figure G.5: Angle measurement system: a protractor and laser pointer used to measure the angle of the array relative to the target(s) or receiver.



(a) A target detection experiment in the anechoic chamber with three targets.



(b) A corner reflector target.

Figure G.6: Target detection.

Appendix H

PCB Designs

A number of PCBs were designed to allow easy interfacing between all of the hardware modules. The receiver analogue circuit was implemented on a PCB which was designed by Stanton and documented in [8]. A microphone board and add-on amplifier board were built to interface to Stanton's board. For the transmitter array, a speaker board was designed and built. Also, a PCB for the analogue transmitter electronics was designed and a PCB company was sourced to manufactured it. The MCU board was the FPGA ML505 development board, and this was not customised in any way. The methods used to design and manufacture each of these boards are described below.

H.1 Microphone Board

The microphone board was designed so that the microphones were accurately soldered into place at intervals of 17 mm. Tracks then connected the microphones to a connector. Two cables were used to connect the microphone board to Stanton's analogue receiver board (and later, the add-on amplifier board). The receiver board is shown in Figure H.1, and a photograph of the populated board is shown in Figure G.3(a).

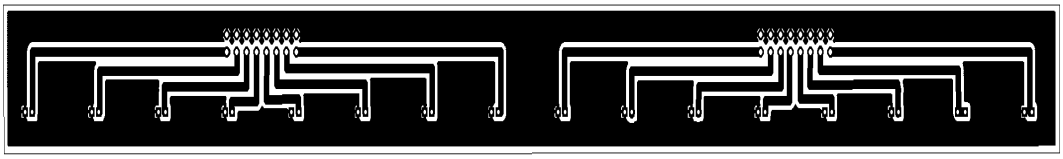

Figure H.1: The microphone PCB.

The microphone board was the first board to be undertaken and therefore, the general PCB design rule of avoiding right angles had not yet been encountered, and was not implemented. The frequency of the signals received by the microphones is however low, so this should not be a problem.

H.2 Add-on Receiver Amplifier Board

The add-on receiver amplifier board was built to fit in between the microphone board and the receiver analogue board. In addition to including the amplifiers required to increase the receiver gain, an LM317 regulator to supply a 2.5 V supply for the ADC reference voltage and microphone biasing was included on the board.

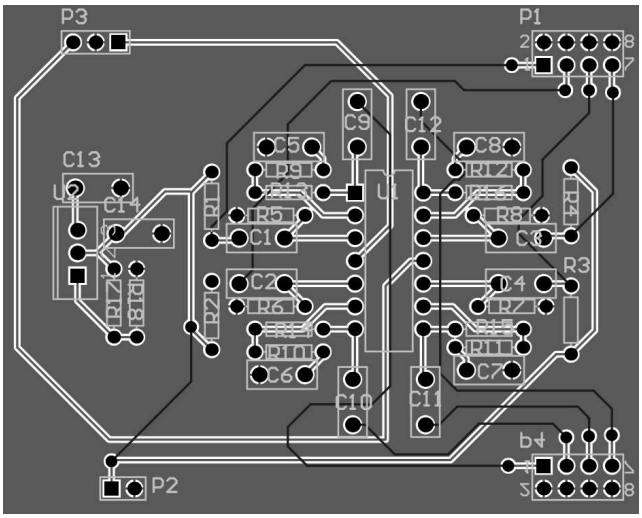

Figure H.2: Add-on Receiver amplifier board.

Figure H.2 shows the board which was designed in Altium Winter Version 2009, and Figure G.3(b) is a photograph of the populated receiver amplifier board. The amplifier circuit, described in Section 6.2.7 was implemented on a four channel TL074N operational amplifier chip, and four of the chips were used to amplify all 16 signals. The board diagram in Figure H.2 only shows one of the amplifiers, and the same circuit needs to be replicated four times.

Using the image in Figure H.2 as a guide, the chemical etching process described in Section H.5 was used to manufacture the PCB. The amplifier section of the figure was duplicated four times for the 16 channels.

Table H.1: Bill of materials for the receiver add-on amplifier board.

Component	Value	Quantity	Names
TL074N Amplifier	-	4	U1
LM317 Regulator	-	1	U2
Resistor	10 kΩ	16	R1, R2, R3, R4
	1 kΩ	34	R5, R6, R7, R8, R9, R10, R11, R12, R17, R18
	22 kΩ	16	R13, R14, R15, R16
Capacitor	1 μF	49	C1, C2, C3, C4, C5, C6, C7, C8, C9, C10, C11, C12, C14
	0.1 μF	1	C13
2 Pin Terminal Block	-	1	P2
3 Pin Terminal Block	-	1	P3
8 Pin Dual Row Connector	-	2	P4

Table H.1 shows the bill of materials for the amplifier board. Under the column, "Quantity" the total number of components required is listed. Under "Names", only the elements shown in Figure H.2 are listed. Also, connectors P1 and P4 are shown to be 4 pin dual row connectors. In the implementation of the board, to cater for the 16 channels, P4 was replaced with 8 pin dual row connectors which served two amplifier chips. An additional 8 pin dual row connectors was used for the output of the other two amplifier chips. A cable which could be connected to the microphone board was soldered directly into the holes for the connector marked P1, and for the other three amplifier chips.

H.3 Transmitter Analogue Board

After verifying the performance of the transmitter analogue electronics in a prototype, a PCB was designed to integrate the DAC, reconstruction filter, high pass filter and amplifier. Because each DAC has 8 channels, the board was designed to include a single DAC and therefore 8 transmitter channels. Therefore, for the 16 element transmitter, two identical boards could be used.

The PCB design was performed in Altium Winter Version 2009. Some simple PCB design rules were followed. First of all, right angles were avoided in all tracks and 45° angles were used. From the filter and beyond, all of the signals are low frequency signals in the audible acoustic range. Therefore, the effects of EMC were disregarded in the design of the board from the filters onward. However, the SPI signals operate at a frequency of 15 MHz, and the filter clock is 1.5 MHz and therefore, these signals can be badly affected by poor EMC design. Therefore, the SPI tracks were kept as short as possible. The filter clock has to supply all eight filters, and therefore it is difficult to minimise its length.

The top and bottom side of the final implementation of the board are shown in Figures H.3(a) and H.3(b). Except for the connectors, all components used on the board were surface mount components. The bill of materials for the board is given in Table H.2.

The PCB was manufactured by Bosco Printed Circuits (Pty) Ltd. The board has the following characteristics:

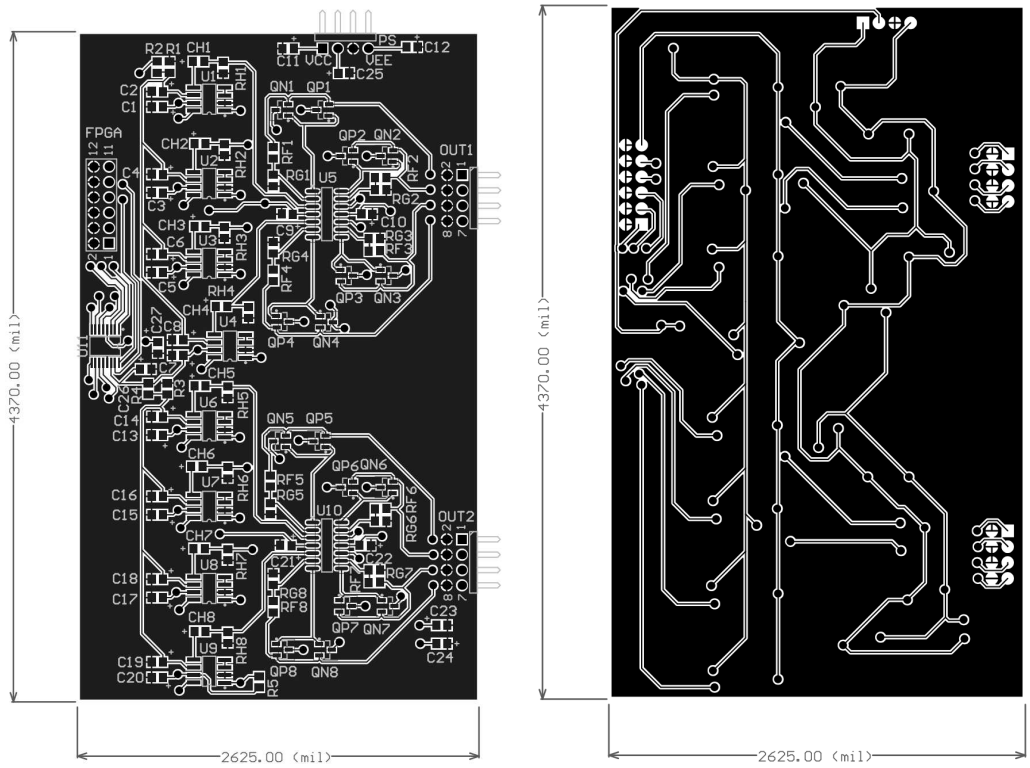

(a) Top side.

(b) Bottom side.

Figure H.3: The transmitter PCB layout with component names and placing.

Table H.2: Bill of materials for the transmitter analogue board.

Component	**Footprint**	**Value**	**Quantity**	**Names**
Capacitor	0805	0.1 μF	22	C1, C2, C3, C4, C5, C6, C7, C8, C9, C10, C13, C14, C15, C16, C17, C18, C19, C20, C21, C22, C26, C27
		4.7 μF	5	C11, C12, C22, C23, C24
		21 nF	8	CH1, CH2, CH3, CH4, CH5, CH6, CH7, CH8
Resistor	0805	2.2 kHz	4	R1, R2, R3, R4
		22 kΩ	8	RH1, RH2, RH3, RH4, RH5, RH6, RH7, RH8
		1 kΩ	8	RG1, RG2, RG3, RG4, RG5, RG6, RG7, RG8
		401 Ω	8	RF1, RF2, RF3, RF4, RF5, RF6, RF7, RF8
		10 kΩ	1	R5
2N2222 Transistor	SOT23	NPN	8	QN1, QN2, QN3, QN4, QN5, QN6, QN7, QN8
2N2907 Transistor	SOT23	PNP	8	QP1, QP2, QP3, QP4, QP5, QP6, QP7, QP8
MAX293 Filter	SO8	-	8	U1, U2, U3, U4, U6, U7, U8, U9
MAX4495 Amplifier	SOIC14	-	8	U5, U10
MAX5306 DAC	TSSOP16	-	1	U11
4 Pin R/A Header	2.54 mm	-	1	PS
4 Pin Dual Row R/A Header	2.54 mm	-	2	OUT1, OUT2
6 Pin Dual Row Header	2.54 mm	-	2	FPGA

- The board is double sided and has through hole plating.
- The board dimensions are 112 mm by 67 mm (4405 mil by 2625 mil).
- The base material is FR4.
- The minimum conductor width and minimum spacing between conductors is 0.2 mm.
- The board includes solder resist and silk screening.

A photograph of the manufactured and populated board is shown in Figure G.2(a).

H.4 Speaker Board

A single speaker board was required. Therefore, due to the high setup costs, and relatively large physical size, a board was not professionally manufactured. Instead the board was made using chemical etching.

The main requirement of the board was to accurately fix the separation between the speakers to 17 mm as described in Section 6.3.4. The variation between channels must be as small as possible to limit inaccuracies in the operation of the phased array transmitter.

Also, the speakers need to be rigidly fixed, so that they cannot easily move, and so that they all point in the same direction. This will help to eliminate the necessity of software calibration. The speakers used were circular with two wires extending from the back as shown in Figure G.2(d). Therefore, the approach chosen, was to drill holes in a copper clad board, into which the speakers could be pressed. Tracks to which the speaker wires could be soldered were etched onto the board. The tracks were terminated in connectors to interface the speakers with the transmitter board. The board was designed such that the right angle pins of the transmitter analogue board plugged into connectors appropriately placed on the speaker board. Thus no wires are necessary between the two boards.

A single sided copper-clad board was used to create the speaker board. The manufacture of the board is described below:

1. The circuit board was designed in PCB designing software (Altium) and is shown in Figure H.4.

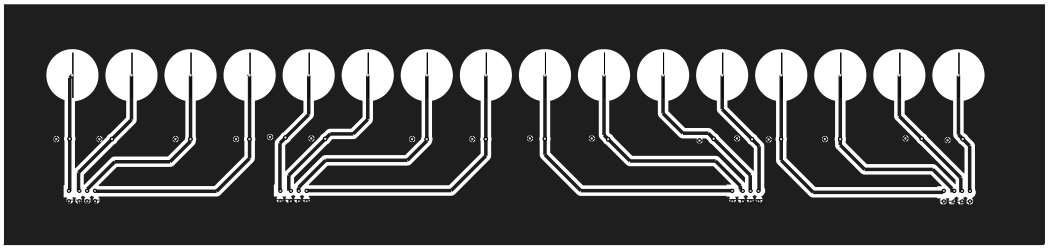

Figure H.4: Speaker board PCB design.

2. The hole positions of the speakers were carefully measured using a vernier and marked.
3. The centre of each hole was marked with a centre punch.
4. A hole of smaller diameter (about 6 mm) was drilled at the centre of each hole.
5. A 12.5 mm drill bit was used to increase the size of the holes.
6. A file was used to increase the diameter of the holes to 13 mm so that the speakers could be pushed into the holes, and remain clamped in position by the PCB.
7. Using the copper clad board with speaker holes, the process of chemical etching described in Section H.5 was applied to etch the tracks to which the speaker wires were soldered.

The accuracy attained in the gaps between speakers is given in Table H.3. The gaps were measured using a vernier twice, and the average of the two measurements is presented here. The standard deviation between the two measurements was 0.14 mm. The gaps between speakers vary with a standard deviation of 0.29 mm. Therefore, it would have been better to have the holes cut with a laser cutter which can achieve an accuracy of 10 μm and a repeatability of 5 μm. Photographs of the board are shown in Figures G.2(b) and G.2(c).

H.5 Chemical Etching Process

The process of chemical etching which was used for the add-on receiver amplifier board and the speaker board is detailed below.

1. The image of the desired board is printed, to scale.

Table H.3: Measurement of the spacing between speaker pairs from left to right on the speaker board.

Gap Number	*Spacing (mm)*
1	17.0
2	17.4
3	16.8
4	17.2
5	16.8
6	17.1
7	17.2
8	17.0
9	16.8
10	16.9
11	16.6
12	16.9
13	16.1
14	16.8
15	16.9
Mean	16.9
Standard Deviation	0.29
Minimum	16.1
Maximum	17.4

2. The printed image is placed on the copper clad board, and fixed in position with masking tape. The holes for the connectors and any through-hole components are marked and drilled using the printed image as a guide for position. The printed image is then removed from the board.

3. The board is scrubbed with benzene to remove any greasy markings that resist the application of the photo-resist agent.

4. The PCB design is copied from the printed design onto the board using permanent markers or nail polish. For the amplifier and speaker boards, the tracks were created in permanent marker, and the ground plane was filled in with nail polish. The photo-resist qualities of the permanent marker pen and

nail polish were tested on a small piece of copper clad board before being used.

5. The board is immersed in ferric chloride. To hasten the process, the basin containing the board and acid can be agitated. The board is only removed when all of the copper in the areas unprotected by photo-resist has been etched away.

6. The board is rinsed in water to remove the ferric chloride.

7. The photo-resist (marker and nail polish) is removed by cleaning the board with benzene.

Appendix I

MCU Architecture and Operation

The master control unit (MCU), which is implemented on a FPGA, consists of a MicroBlaze processor, with peripherals which perform specialised functions. The architecture of the control unit, and the functioning of the modules that it controls are described here.

I.1 MCU Architecture

The architecture of the MCU is specified in Figure I.1, which is the block diagram of the FPGA system (based on that generated by XPS). Each of the modules which appears in the block diagram is described in more detail in Table I.1. Also the inputs and outputs are listed and described in Table I.2. These low level modules, inputs and outputs all combine to perform the display and communication functions of the high level modules of the MCU.

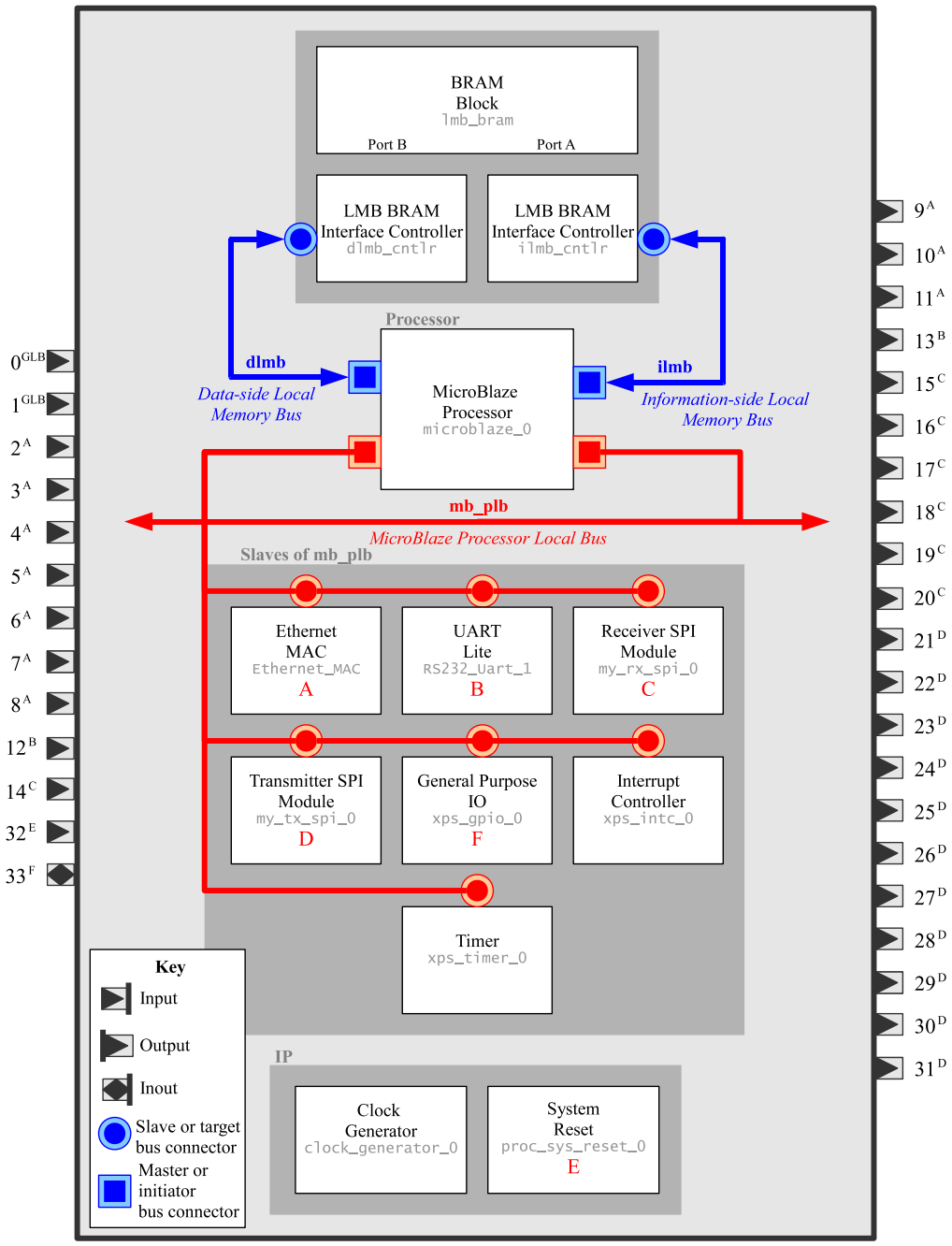

Figure I.1: MCU system block diagram.

Table I.1: FPGA IP modules.

Module	**Description**
MicroBlaze Processor	MicroBlaze is a soft processor core which is provided by Xilinx for use on their FPGAs. It is a processor which is implemented in the general purpose memory of the FPGA, and which can be programmed in C. The Base System Builder in XPS was used to instantiate a MicroBlaze processor which was included to allow programming of all of the modules.
Ethernet MAC	The Ethernet Media Access Controller (MAC) supports the IEEE Std. 802.3 Media Independent Interface (MII) to the Physical Layer (PHY) devices on the evaluation platform. It allows the implementation of 10 or 100 Mbps Ethernet connections. C drivers for the MicroBlaze processor are provided by XPS. The Ethernet MAC was used for the FPGA to PC connection.
UART Lite	The UART Lite module and its drivers allow serial communications between the FPGA and PC. It was included for easy debugging while Ethernet was being configured, but was not used in the implementation of the radar system.
Receiver SPI Module	The receiver SPI module is a custom designed peripheral. It was implemented in VHDL and added as an IP. The module is described in detail in Sections 6.4.2 and I.3.
Transmitter SPI Module	The transmitter SPI module is also a custom designed peripheral. It was also implemented in VHDL and added as an IP. It is described in detail in Sections 6.4.2 and I.4.
General Purpose IO	The GPIO module is for configuration of the LCD screen. Together with its drivers, it allows easy configuration and use of the input and output ports.
Interrupt Controller	The interrupt controller transforms multiple interrupts from all peripheral devices into a single interrupt. It was required by the Ethernet MAC module and was included for this reason.
Timer	The timer peripheral was included for configuration of the LCD. It was also used to implement time delays in between MCU operations.
Clock Generator	The clock generator provides the system clocks. It was included by default.
System Reset	The system reset module allows configuration of parameters to enable and disable features. It was included by default.

Table I.2: FPGA inputs and outputs.

No.	Name	Dir	L:M	Description
0^{GLB}	my_rx_spi_0_t_ul_clk_pin	I	1	Clock for receiver SPI module.
1^{GLB}	sys_clk_pin	I	1	System clock of 100 MHz.
2^{A}	fpga_0_Ethernet_MAC_PHY_col_pin	I	1	Ethernet collision detection (for half duplex).
3^{A}	fpga_0_Ethernet_MAC_PHY_crs_pin	I	1	Ethernet carrier sense (for half duplex).
4^{A}	fpga_0_Ethernet_MAC_PHY_dv_pin	I	1	Indicates if data received by Ethernet is valid.
5^{A}	fpga_0_Ethernet_MAC_PHY_rx_clk_pin	I	1	Ethernet receiver clock.
6^{A}	fpga_0_Ethernet_MAC_PHY_rx_data_pin	I	3:0	Data received by Ethernet.
7^{A}	fpga_0_Ethernet_MAC_PHY_rx_er_pin	I	1	Indicates if errors are present in Ethernet received data.
8^{A}	fpga_0_Ethernet_MAC_PHY_tx_clk_pin	I	1	Ethernet transmitter clock.
9^{A}	fpga_0_Ethernet_MAC_PHY_rst_n_pin	O	1	Ethernet reset.
10^{A}	fpga_0_Ethernet_MAC_PHY_tx_data_pin	O	3:0	Data to be transmitted by Ethernet.
11^{A}	fpga_0_Ethernet_MAC_PHY_tx_en_pin	O	1	Enables Ethernet transmission.
12^{B}	fpga_0_RS232_Uart_1_RX_pin	I	1	Enables serial reception.
13^{B}	fpga_0_RS232_Uart_1_TX_pin	O	1	Enables serial transmission.

Continued on next page...

No.	Name	Dir	L:M	Description
14[C]	my_spi_din_pin	I	1	DIN for receiver SPI.
15[C]	my_led2_pin	O	1	Diagnostic LED.
16[C]	my_led_pin	O	1	Diagnostic LED.
17[C]	my_mock_din_pin	O	1	Diagnostic output.
18[C]	my_spi_clk_pin	O	1	SCLK for receiver SPI.
19[C]	my_spi_cs_pin	O	1	CS for receiver SPI.
20[C]	my_spi_dout_pin	O	1	DOUT for receiver SPI.
21[D]	my_filter_clk_1_pin	O	1	Filter clock for first transmitter SPI.
22[D]	my_filter_clk_pin	O	1	Filter clock for second transmitter SPI.
23[D]	my_ldac_0_pin	O	1	DAC update for first transmitter SPI.
24[D]	my_ldac_1_pin	O	1	DAC update for second transmitter SPI.
25[D]	my_tx_cs_0_pin	O	1	CS for first transmitter SPI.
26[D]	my_tx_cs_1_pin	O	1	CS for second transmitter SPI.
27[D]	my_tx_dout_0_pin	O	1	DOUT for first transmitter SPI.
28[D]	my_tx_dout_1_pin	O	1	DOUT for second transmitter SPI.
29[D]	my_tx_led_0_pin	O	1	Diagnostic LED.
30[D]	my_tx_spi_clk_0_pin	O	1	SCLK for first transmitter SPI.
31[D]	my_tx_spi_clk_1_pin	O	1	SCLK for second transmitter SPI.
32[E]	sys_rst_pin	I	1	System reset.
33[F]	LCD_IO_pin	IO	0:6	Data to be displayed on the LCD.

I.2 Ethernet

Ethernet capabilities were incorporated into the FPGA with the inclusion of the Ethernet MAC module described in Table I.1. The driver specified in the file `xemaxlite.h` and supplied by Xilinx was used to implement Ethernet transmission and reception.

A brief description of the steps taken to implement Ethernet reception in the MicroBlaze software, using the `xemaxlite.h` driver is given below:

1. The following static variables were defined:
   `u8 LocalAddress[]` is the MAC address to be assigned,
   `XemacLite EmacLiteInstance` is the active EMAC instance,
   `u8 txFrame[]` stores the data to be transmitted.

2. The following variables were defined:
   `XemacLite *EmacLiteInstPtr` points to the active EMAC,
   `XemacLite_CONFIG *EmacLiteConfigPtr` stores configuration data,
   `u32 EffectiveAddr` points to the EMAC base address,
   `unsigned ByteCount` holds the length of the frame,
   `u8 *FramePtr` points to the frames to be transmitted.

3. Finally, the following functions were called for configuration and transmission:
   `XemacLite_LookupConfig()` fills the configuration variable,
   `XemacLite_CfgInitialize()` initialises the EMAC,
   `XemacLite_SetMacAddress()` sets the MAC address,
   `myStatus = XemacLite_Send()` sends the specified packet.

The implementation of this can be seen in the software repository on the project DVD together with the driver documentation which describes the above variables and functions in more detail.

The Ethernet packet format is specified in the datasheet for the Ethernet MAC module [68]. It is illustrated in Figure I.2.

The preamble and Start of Frame Delimiter (SFD) are added automatically by the Ethernet MAC. The destination address is the MAC address of the computer which the Ethernet cable is connected to. The source address is the address of the FPGA which is assigned in the MicroBlaze application by the call to the function

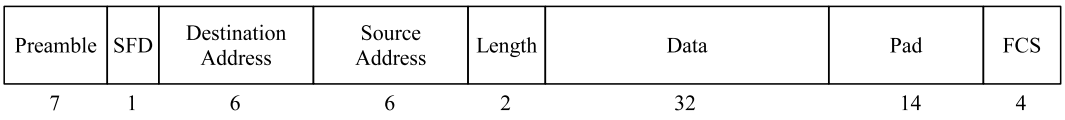

Figure I.2: The Ethernet packet with the number of bytes of each component.

`XemacLite_SetMacAddress()`. The length field indicates the length of the data to be transmitted. For the radar application, this is 32 bits, and therefore the value of the field is 0x0020. In the MicroBlaze application, the destination address, source address and length field, none of which changed, were stored in the static variable `static u8 header[14]`.

The data field can be of length 0 to 1500 bytes. For the radar system, the data field contained the 2 byte numbers from a single conversion cycle for all 16 channels. Therefore, the data field contained 32 bytes. Overhead time was required to transmit the Ethernet packet after each conversion cycle. The data field is large enough so that 46 conversions could be performed before transmitting a packet, and this would allow a higher sample rate. However, after sampling for the 46th time, the packet would have to be sent, which would require more time, and result in a delay before the 47th conversion could be performed. Thus, although the sample rate would be higher, a steady rate could not be maintained. This could be corrected by storing the data while the receiver is sampling the microphone signal, and only transmitting the signal by Ethernet after sampling is finished. However, this was not implemented.

The minimum frame length (destination address, source address, length, data and pad field) is 64 bytes. Therefore, the pad field is used only if the data field is shorter than 46 bytes, to ensure that the minimum length criteria is met. Because the data field for this application was only 32 bytes, the pad field contained 14 bytes which were all assigned values of 0. The Frame Check Sequence (FCS) was calculated over the packet fields from the destination address to the pad using a 32-bit Cyclic Redundancy Check (CRC). It is inserted automatically by the Ethernet MAC.

In the MicroBlaze application, the Ethernet packet for transmission must be an array of unsigned 8 bit integers. A union, which allows a single memory location to be shared by different data types, was used to simplify the construction of the packet. A structure `s_packet` which held the Ethernet header (an array of 14 bytes), and the data (an array of 16 two byte words) was generated. This structure was a member of the union `u_packet`. The other member of the union was the 64 byte Ethernet packet. Therefore, as a 16 bit word was received from the ADC by the receiver SPI

interface, it was written directly into an element of the data array of the structure `s_packet`. This was repeated for all 16 ADC conversions. After all of the conversions had been completed the second member of the union, the Ethernet packet, could be accessed and directly transmitted over Ethernet, without any modifications of the format.

I.3 Receiver SPI

Firstly, the operation of the SPI which controls the ADC is described. The VHDL module written to perform the required functions is then documented.

I.3.1 SPI Interface

$\overline{\text{CS}}$ is the Chip Select input to the ADC. It is an active low logic input. When $\overline{\text{CS}}$ is driven low, conversion on the ADC is initiated. Also, it must be held low for the serial transmission of data.

SCLK is the serial clock which is provided to the ADC by the FPGA. It is the clock used for the process of transferring data on DIN and DOUT. Also, it is the clock source for the ADC's conversion process. The maximum frequency for SCLK, with a 5 V supply voltage is 20 MHz.

DIN is the serial logic data input to the ADC. Data is sent serially and is clocked into the register on the falling edge of SCLK, when $\overline{\text{CS}}$ is low. Data from the FPGA was transmitted on DIN to be written to the control register of the ADC.

DOUT is the serial logic output from the ADC. The bits are clocked on the falling edge of SCLK when $\overline{\text{CS}}$ is low. The data stream from each ADC channel consists of 16 bits. The first four bits are address bits which indicate which channel the conversion corresponds to. The following 12 bits are the conversion data, with the MSB provided first. The conversions of the ADC were transmitted on this pin as a serial data stream, and received by the FPGA.

The operation of SPI on the receiver is summarised in Figure I.3, which is based on the timing diagram in the ADC datasheet [69]. When $\overline{\text{CS}}$ is driven low, data is clocked into the control register on the falling edge of SCLK.

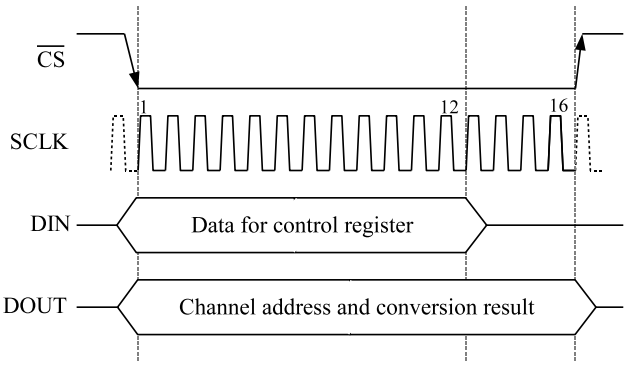

Figure I.3: Timing diagram for the receiver SPI.

MSB											LSB
WRITE	SEQ	ADD3	ADD2	ADD1	ADD0	PM1	PM0	SHADOW	WEAK/TRI	RANGE	CODING
11	10	9	8	7	6	5	4	3	2	1	0

Figure I.4: The receiver ADC SPI control register.

Initially, after applying power to the ADC, three dummy conversions are required to put the ADC into a known state. The first two dummy conversions are performed with the DIN line tied HIGH, and in the third conversion, DIN should be used to send values to the control register to configure the ADC for the first conversion.

The control register is shown in Figure I.4 (based on that in [69]) and a description of each of the bits and how they were set for the purposes of this project is given in Table I.3. The bits SHADOW and SEQ are used to put the ADC into a mode where it samples a consecutive sequence of channels. Since all 16 channels are used, the ADC is configured to sample from Channel 1 to Channel 16. Therefore, on the first cycle, the code 111111111001 (xFF9) is sent on DIN to the control register. This sets up consecutive sampling. The data on DOUT should be ignored during the first cycle. $\overline{\text{CS}}$ is then driven high at the end of the first cycle, and low to start the second cycle. For each of the following 16 cycles, the data on DOUT will correspond to the result of the conversion on each of the channels from 1 to 16. On the cycles 2 to 16, the WRITE bit is set to 0, so the remainder of the bits are not shifted into the control register. On the 17th cycle, when the data corresponding to the last conversion is read out, the code given in Table I.3 should be retransmitted on DIN to set up the second 16 channel conversion cycle. This process continues for as long as samples are required.

Table I.3: Receiver ADC control register bit settings.

Bit	Register	Description	Value
11	WRITE	Specifies if the 11 following bits are to be loaded into the control register. 1 specifies that they must be written and 0 specifies that they must not be written	1
10	SEQ	Used with SHADOW to program a continuous conversions on a consecutive sequence of channels.	1
9 - 6	ADD	The address of the next channel to be converted. This address is also the address which is output on DOUT as the first 4 bits.	1111
5 - 4	PM	Power management options. Normal operation is used.	11
3	SHADOW	Used with SEQ to program continuous conversions on a consecutive sequence of channels.	1
2	WEAK/TRI	Used to set DOUT to three-state at the end of the conversion.	0
1	RANGE	Sets the analogue range from 0 V to $2\,\mathrm{REF_{IN}}$ since the reference voltage is 2.5 V but the signal varies from 0 V to 5 V.	0
0	CODING	Sets the coding of the signal output on DOUT to straight binary	1

I.3.2 VHDL Module for SPI

The SPI interface between the FPGA and the receiver analogue board was implemented with a VHDL module which was added as a peripheral to the MicroBlaze processor, and controlled by drivers from the processor. The receiver SPI module in the file `my_receiver_top.vhd` contains three VHDL components. The first is `led_counter.vhd`, which divides the system clock to output a low frequency clock which controls the flashing of a diagnostic LED to indicate that the receiver module has been instantiated and is running. The second module is `spi_counter.vhd` which generates the 20 MHz SPI clock. The final module is `update_clock.vhd` which drives a clock to ensure that sampling of the receiver is performed at a frequency of 40 kHz.

Figure I.5 illustrates the timing of the receiver SPI process. The SPI process is clocked by the signal `spi_clk`, which also drives the SCLK input on the ADC. The figure illustrates that firstly, a decision is made to enable or disable SPI communications by setting `spi_enable` high or low. If `channel_count`, which keeps count of how many channels have been sampled, is equal to zero, then SPI is only enabled if `master_enable` and `tx_start` are both high. `master_enable` is a 40 kHz clock. Before it was included, it was found that the sample frequency on the receiver varied between about 40 and 42 kHz. This is due to slight variations in the length of time taken by the MicroBlaze processor to transmit the set of received signals by Ethernet in between each ADC conversion cycle. By only enabling SPI when `master_clock` is high, the sample rate was limited to 40 kHz and kept constant. `tx_start` is a 32 bit register which was used for communications between the MicroBlaze application and the receiver SPI VHDL peripheral. The processor sets all bits high to indicate a request to start SPI communications. The bits are set low again once the processor is notified that SPI transmission is finished. If `channel_count` is greater than 0, the SPI peripheral is in the middle of a 16 channel conversion cycle and SPI is enabled regardless of the value of `master_enable` if `tx_start` is high.

When SPI is enabled, `spi_cs` which drives $\overline{\text{CS}}$ on the ADC is immediately driven low. `spi_bit_count` keeps track of the number of SPI clock cycles. On each falling clock edge, `spi_din`, which drives DIN on the ADC, is updated. The value for `spi_din`, which configures the ADC, is obtained from a register which has a value assigned to it in the MicroBlaze application. Also on each falling clock edge, the value from `spi_dout` which is driven by DOUT on the ADC is read into a register which can be accessed by the MicroBlaze application. When `spi_bit_count` reaches 16, the conversion for one channel is complete. `spi_cs` and `tx_fin(0)` are driven high and `channel_count` is incremented. `tx_fin` is a register which is polled by the MicroBlaze application once SPI communications have been initiated. As soon as the MicroBlaze application polls a high on `tx_fin`, `tx_start` is driven low again. The falling clock edge after `tx_start` goes low, `spi_enable` is driven low and `spi_bit_count` is reset to 0.

The VHDL peripheral then awaits the moment that `tx_start` is driven high and the second channels conversion is received. This process is repeated until the conversion cycle for all 16 channels has been completed, when `channel_count` is reset to zero, and the VHDL peripheral waits for `master_enable` and `tx_start` to be high for the next conversion cycle.

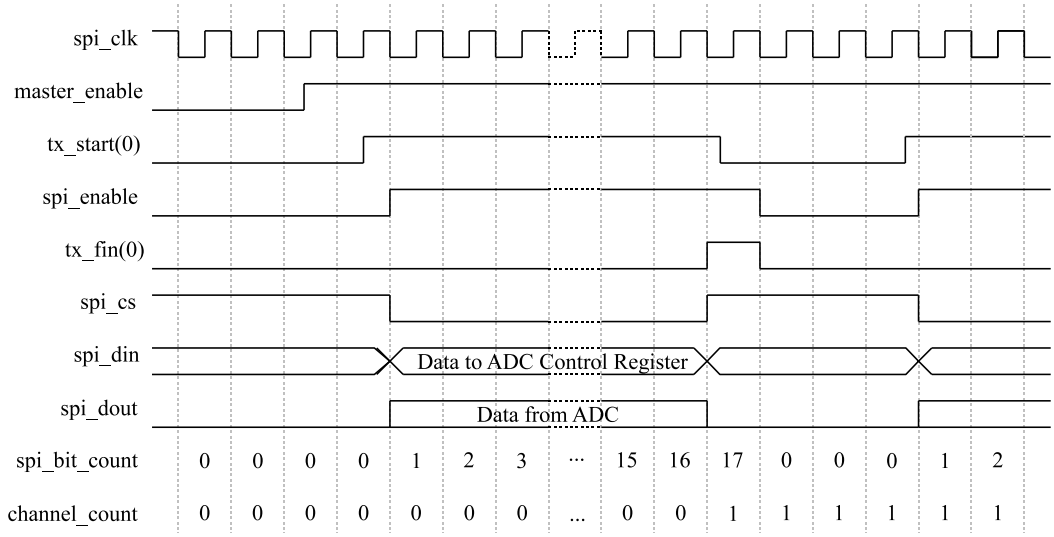

Figure I.5: Timing diagram for the receiver SPI VHDL peripheral.

I.4 Transmitter SPI

The SPI communication protocol used by the DACs on the transmitter boards is documented here. The VHDL module which was implemented to provide the SPI link between the FPGA and DAC is then described.

I.4.1 SPI Interface

The SPI interface timing diagram is shown in Figure I.6 (based on that from [70]. Each serial word consists of 16 bits. The first four bits are control bits which control which register the data should be loaded into for a conversion or configure the power settings. The following 12 bits are data bits which are loaded into the specified register for conversion to analogue. Initially, all DAC channels must be powered up by sending a signal 0xFFFF. Data is clocked on the falling edge of SCLK. As shown in Figure I.6, CS, which is active high, is driven high for 16 clock cycles and data for conversion is sent. CS is then driven low for a minimum of 20 ns, before data for the following channel is sent. Once all 16 words have been transmitted and loaded into their relevant registers, $\overline{\text{LDAC}}$ is driven low, and all 16 output pins are simultaneously updated with the output of the most recent DAC conversion. Subsequent conversion continue in the same manner.

$\overline{\text{LDAC}}$ is the clock which updates the DAC outputs and has a frequency of 40 kHz. The analogue conversions are updated on the falling edge of the clock.

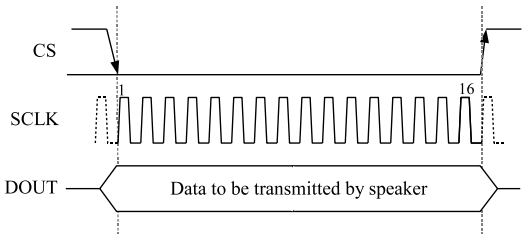

Figure I.6: Timing diagram for the transmitter SPI interface

I.4.2 VHDL Module for SPI

The above signals were implemented with a VHDL module which was added as a peripheral to the MicroBlaze processor. The structure of the module is very similar to that of the receiver SPI module. The functions of the module are defined in the file `tx_spi.vhd`. The included components are `counter1.vhd` which generates a low frequency clock for a diagnostic LED, `counter2.vhd` which generates the 1.5 MHz clock for the reconstruction filters, `counter3.vhd` which generates an 80 kHz clock from which $\overline{\text{LDAC}}$ is derived and `counter4.vhd` which generates the 15 MHz SPI clock.

The important signals of the transmitter VHDL module are illustrated in Figure I.7. On every rising edge of the SPI clock `spi_clk`, the value of bit zero in register `tx_enable` is checked. If it is high, SPI transmission is enabled. If the number of bits counted by `cs_count` is less than 16, then `cs_int` is driven low, and `dout1` and `dout2` are loaded with the current bit value for the ith and $(i+8)^{\text{th}}$ channels. When `cs_count` reaches 16, then `cs_int` goes high and `tx_fin(0)` and `spi_fin` go high. `tx_fin(0)` is a bit in a register which is polled by the MicroBlaze application to determine when a single SPI cycle is complete. Once it goes high, `tx_enable(0)` is driven high. `spi_fin` is used internally. It is checked on every rising edge of `spi_clk`, and when it is high, the data for the following two channels is loaded from the appropriate registers written by the MicroBlaze application into the signals `dtx_current1` and `dtx_current2`. The registers are 32-bits wide, so the data for two channels is stored in a single register, with the first channel's data stored in bits 0 to 15, and the second channel's data in bits 16 to 31. After the new data has been loaded, `spi_clk` is driven low again. The signals are then unchanged until the next SPI cycle is enabled.

A separate process determines when the channels must be updated. $\overline{\text{LDAC}}$ is toggled so that it has a frequency of 40 kHz only if the MicroBlaze application has enabled it. It is enabled by the setting of bit one of the register `tx_enable`. After data

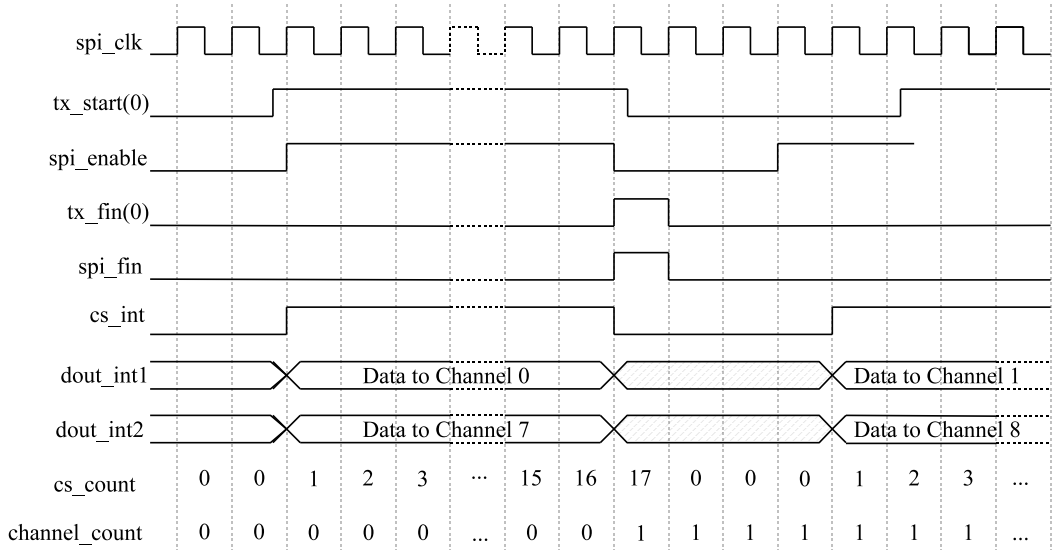

Figure I.7: Timing diagram for the signals in the transmitter SPI VHDL peripheral module. (Excludes the process that drives $\overline{\text{LDAC}}$)

has been loaded into all 16 channels by the process described above, taking 8 SPI transmission cycles, the MicroBlaze application polls bit one of `tx_fin`. As soon as $\overline{\text{LDAC}}$ is driven low and the outputs of the DACs are updated `tx_fin(1)` is driven high, and the MicroBlaze application continues with the next conversion sequence.

In the VHDL module, some of the processes drive internal signals which are denoted with the inclusion of the name `_int`. The internal signal is then used to update the external signal, at the system clock rate, which is 100 MHz. For example, the signal `cs_int` is described above and illustrated in Figure I.7. It then drives `cs1` and `cs2` for the two DACs. Not all of these signals have been documented here.

Appendix J

Speaker and Array Characterisation

The beampatterns measured transmitted by the speaker array approximately matched the theoretical patterns, but the side lobe levels were significantly higher than dictated by the theory. To better understand these array patterns, the beampatterns of the individual speakers were investigated. The findings were surprising, and led to an extensive study of speakers which is described in this appendix.

In all of the simulations, the transmitter elements were assumed to be omnidirectional. However, the speakers are not expected to have an omnidirectional pattern in reality. The pattern is expected have nulls at -90° and 90°, and the width of the pattern is expected to get narrower, as the frequency increases. Therefore, at the lower frequencies (the lowest investigated was 6 kHz), the speaker will be closer to omnidirectional than at higher frequencies [71]. However, due to the small physical size of the speakers, even at the maximum frequency of interest of 12 kHz, the pattern is not expected to be very directional.

The beampatterns of 5 speakers randomly distributed across the array were measured and are shown in Figure J.1. Four patterns were measured for each of the speakers, when sine waves of 10 ms duration and 6 kHz, 8 kHz, 10 kHz and 12 kHz were transmitted. For these measurements, the array was fixed on the hardware box as illustrated in Figure G.4(a). The patterns are incredibly erratic, with "ripple" of over 20 dB in some cases. This caused great alarm, and many experiments were undertaken to determine the cause of these patterns.

Firstly however, a number of potential causes for these varying patterns were hypothesised. These were:

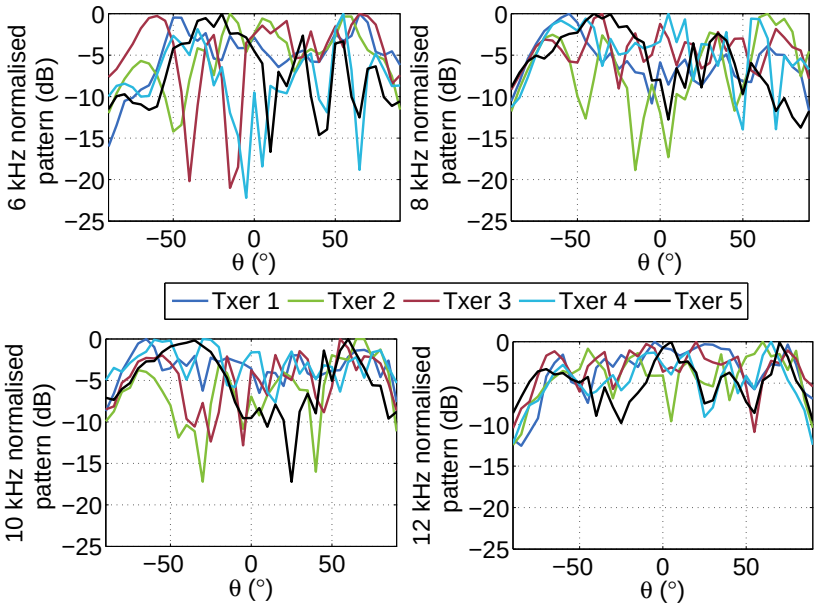

Figure J.1: Beampatterns of 5 speaker elements randomly distributed across the array at four different frequencies.

- **Coupling:** The construction of the speaker array board was questioned on discovering the speaker patterns. The board on which the speakers are mounted is a single-sided copper-clad board. Holes of diameter slightly larger than the speakers were drilled with spacing of 17 mm and the 16 speakers were pressed into the holes. The speakers were fixed into position with silicon sealant. The erratic patterns raised suspicions that the speakers might be coupling to the board, and that the whole board might be transmitting. A solution to this would be to stiffen the speaker array.

- **Anechoic Chamber:** The anechoic chamber in which the measurements were taken is an RF anechoic chamber which differs from an acoustic anechoic chamber, although the wavelengths are of similar order (a 10 kHz acoustic signal has approximately the same wavelength as an 8.7 GHz RF signal). The properties of acoustic absorbing material and RF absorbing materials differ, and therefore, while an RF anechoic chamber does have some sound absorbing properties, it is not ideal. In particular, the anechoic chamber at the University of the Witwatersrand in which the array and speaker pattern measurements were taken has wooden walkways, which can be seen in the photo in Figure G.6(a). Therefore, it is possible that the noisy patterns are due to echoes off the walkways, or even the cones in the anechoic chamber.

- **Reverberation:** The speaker array was mounted on a box, as shown in

Figure G.4(a). It is possible that the transmitted signal excites the box, or reverberates off the inside walls of the box. If this is true, it could be corrected by filling the box with an acoustic absorbing material to minimise the reflections. Also, when mounted on the box, the microphone array overhangs the speaker array by about 8 mm, and therefore there could also be reflections off the edge of the microphone array.

The first step that was taken, to further evaluate the cause of the erratic speaker patterns was to remove the array from the box, and remeasure the pattern of an individual element. In addition, the pattern of a loose speaker was measured to determine the effect of the copper-clad mounting board. These speaker patterns are shown in Figure J.2. The pattern of a single speaker in the array, when the array is not attached to the box is improved, with a slightly more dome-like shape than the original measurement of the speaker pattern when the array is attached to the box. The individual speaker pattern is the closest to the expected pattern. However, the pattern is still jagged, contrary to expectations. Therefore, further investigations were performed in an attempt to explain the fluctuations.

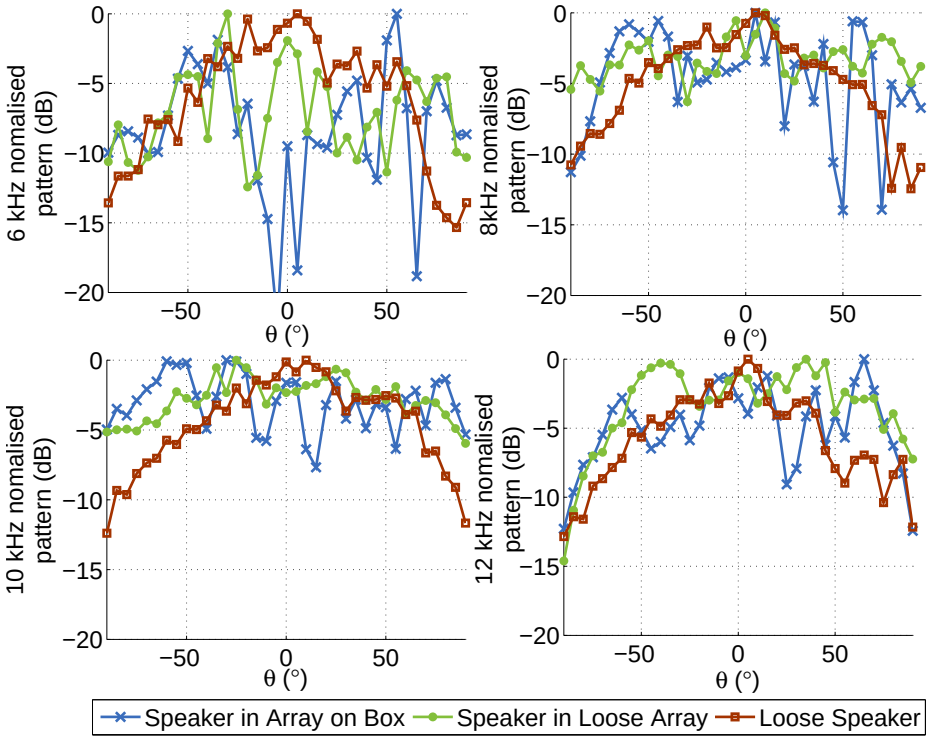

Figure J.2: Speaker patterns for a speaker in the array attached to the box, a speaker in the loose array, and a loose speaker.

Figure J.3 is a summary of the investigations into the speaker beampatterns. These pattern measurements were taken in an RF anechoic chamber at the CSIR. This chamber does not have the reflective wooden walkways present in the chamber at the University of the Witwatersrand, which could be causing reflections which appear as ripple on the patterns. The speaker patterns were measured when a function generator was used to drive a single, loose speaker, and the effect of any of the transmitter electronics is therefore moved. In addition, the patterns are measured with a high quality omnidirectional microphone, which has a passband ripple below 2 dB between 15 Hz and 20 kHz. The patterns are measured at 6 kHz and 8 kHz.

An electronically controlled turntable was used to rotate the speaker at a constant speed from -90° to 90°. During this rotation, a million data samples at a sample frequency of 40 kHz were recorded by the microphone. The spectrogram of the received data was determined, giving the variation of the signal frequency response with time. The angular response of the speaker was obtained by extracting the amplitude of the spectrogram at the frequency of transmission.

The conditions under which Figure J.3(a) was measured are comparable to those under which the loose speaker patterns in Figure J.2 were measured. The 6 kHz pattern has a similar dome shape, although the difference between maximum and minimum values is reduced. The 8 kHz pattern however has deteriorated in comparison to that in Figure J.2.

The paper tab on the speakers as shown in Figure J.4(a), was removed to eliminate its effect in altering the beampatterns and the pattern of the speaker was measured. The patterns obtained with this modification are shown in Figure J.3(b). The 8 kHz pattern is similar to that in Figure J.3(a), but the 6 kHz pattern deteriorates.

The gauze covering the speakers was then removed (see Figure J.4(b)), and the patterns of the speakers obtained are shown in Figure J.3(c). The 6 kHz and 8 kHz patterns both assume a more dome-like shape, as was originally expected on measuring the speaker patterns. Therefore, it is suspected that the gauze and the double-sided tape which attached it to the speakers had an effect on the patterns.

Finally, in an attempt to find the cause of the ripples in the patterns, a cone was fixed around the microphone as shown in Figure J.4(c) to minimise the reception of any reflections from the anechoic chamber. The patterns in Figure J.3(d) do not have reduced amplitude ripple. The increase in the pattern amplitude is most likely due to the position of the microphone being changed to take this measurement.

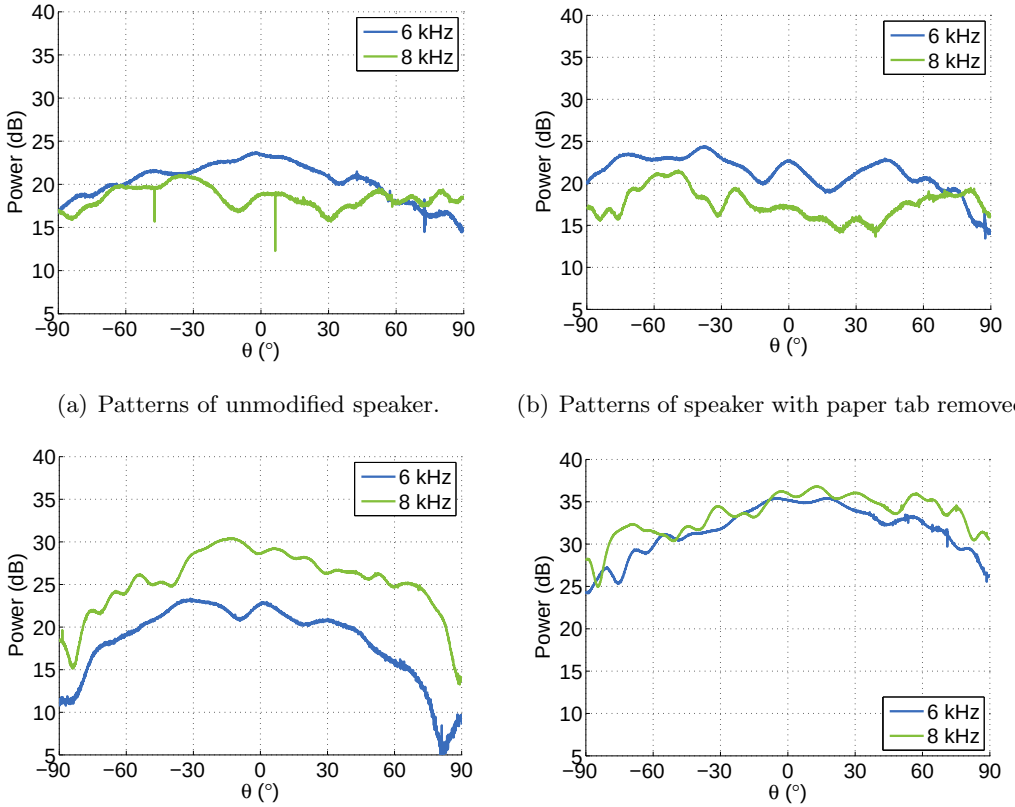

(a) Patterns of unmodified speaker.

(b) Patterns of speaker with paper tab removed.

(c) Patterns of speaker with gauze removed.

(d) Patterns of speaker with gauze removed and a cone around the receiver.

Figure J.3: Patterns of a loose RM-1332 speaker under different conditions when a 6 kHz and an 8 kHz sine wave is transmitted.

These results indicate that reflections from the anechoic chamber were not the cause of the ripple.

In an attempt to stiffen the speaker array to reduce the suspected coupling effects experienced, a second array prototype was constructed. A four element array was built by gluing speakers to a piece of chip board. The wooden array is shown in Figure J.6. Also, noting the apparent improvements to the speaker beampatterns with the removal of the gauze covering the speaker aperture, the gauze was removed from all of the speakers.

The 8 kHz and 10 kHz patterns of the elements in the wooden array and the original array were then measured, in the anechoic chamber at the CSIR and are shown in Figure J.5. The gauze was removed from all of the speakers to take these measurements. For both of the arrays, the power of the 10 kHz patterns is on average 5 dB below that of the 8 kHz patterns. The difference between the patterns on all speakers at any point is below 5 dB for all speakers in the wooden array, whereas it

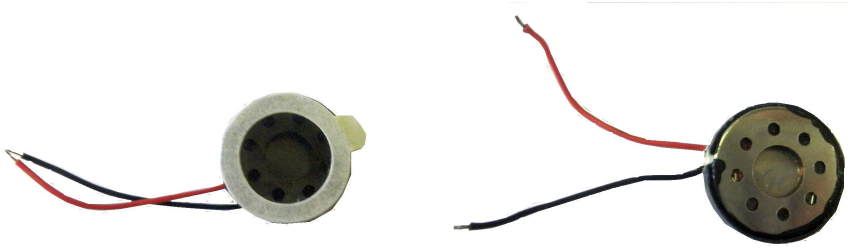

(a) Unmodified speaker.

(b) Speaker with gauze removed.

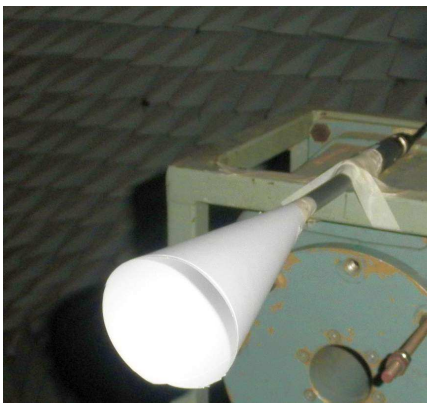

(c) Microphone with cone.

Figure J.4: Hardware modifications made to investigate the speaker patterns.

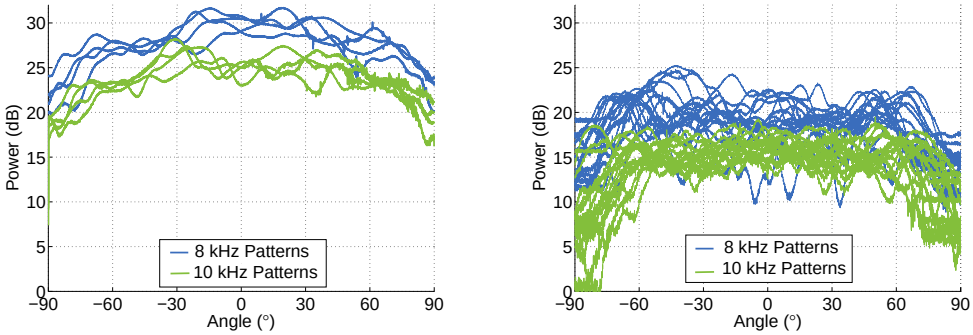

(a) Speaker elements in the wooden array.

(b) Speaker elements in the original array.

Figure J.5: 8 kHz and 10 kHz beampatterns of individual speakers.

is up to almost 15 dB on the original array. All of the patterns have nulls at $-90°$ and $90°$ as expected. However, the patterns for the speakers on the original array are approximately flat apart for the high amplitude ripple between $-50°$ and $50°$. However, the patterns of the array elements are improved in comparison to those measured initially, by the removal of the gauze, and removal of the array from the box.

Figure J.7, shows the array pattern of the wooden array in comparison to four

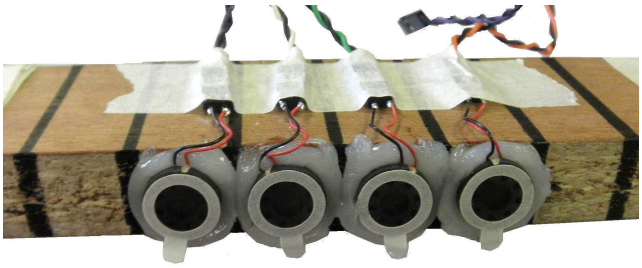

Figure J.6: The wooden array prototype.

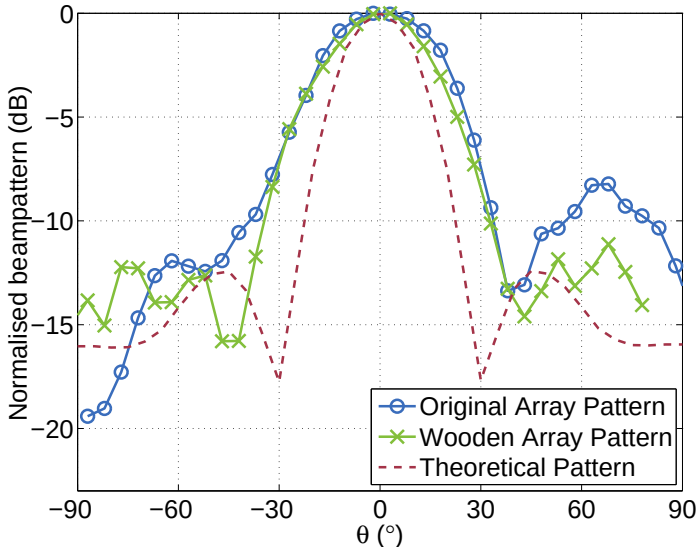

Figure J.7: asdfas

elements of the original array, and the theoretical four element pattern, when a chirp signal of bandwidth 4 kHz was transmitted, and no beamforming was performed. If the speakers in the transmitter array are numbered from one to sixteen from left to right, then elements five to eight were used to generate the pattern in Figure J.7. The array patterns are surprisingly similar to the theoretical patterns and free of ripple, given the erratic speaker patterns. The wooden array has lower side lobe levels (except between $-90°$ and $-70°$). However, this final result indicates that despite the difficult-to-characterise patterns of the speaker elements, relatively accurate array patterns can still be generated.

Appendix K

Tables of Results

The abbreviation used in the tables, which are not defined elsewhere are:

PA1	Phased array pattern with one main lobe.
OMNI	Omnidirectional pattern.
MIMOPD1	MIMO pattern designed by Pascale's design with one main lobe.
MIMOBM1	MIMO pattern designed by the beampattern matching design with one main lobe.
PABM3	Phased array pattern designed by beampattern matching with three main lobes.
PALCMV	Phased array pattern designed by the LCMV with three main lobes.
MIMOPD3	MIMO pattern designed by Pascale's design with three main lobes.
MIMOBM3	MIMO pattern designed by the beampattern matching design with three main lobes.
Param Est	Parameter Estimation.
WB	Wideband.
NB	Narrowband.
Uncal Tx	Uncalibrated transmitter pattern.
Cal Tx	Calibrated transmitter pattern.
Tx-On-Rx	Transmitter beamforming on reception (TBR).

Table K.1 gives an estimate of the average SNRs of the received signals, before any processing, and after the signal has been band-pass filtered, demodulated and low-pass filtered. The SNR was estimated by comparing the power in the frequency band occupied by the signal, to the power outside this band. This estimate gives the upper most limit of the SNR, as the ideal condition of a noise free signal frequency band is assumed.

Table K.1: Received signal SNRs when target detection was performed. BB stands for baseband and PB stands for passband.

No. Targets	*Pattern*	*Without Calibration*		*With Calibration*	
		PB SNR	BB SNR	PB SNR	BB SNR
1	PA1	-0.2	27.1	0.2	25.8
	OMNI1	2.3	28.1	-1.0	27.8
	MIMOPD1	-4.7	27.9	-4.6	22.7
	MIMOBM1	-3.9	27.8	-3.0	25.4
3	PABM3	3.4	27.6	6.5	29.8
	PALCMV3	-5.0	26.7	-3.5	27.5
	OMNI	3.2	27.5	3.7	29.4
	MIMOPD3	0.1	26.5	-3.6	28.5
	MIMOBM3	0.2	26.9	-0.3	27.9
2	PA1	1.9	28.4	3.8	29.0
	OMNI1	0.7	29.0	1.3	29.8
	MIMOPD1	-1.4	31.6	0.2	25.4
	MIMOBM1	-0.9	30.7	-1.6	31.2

Table K.2: Single target location estimates when PA1 was transmitted.

Pattern	*Processing*	*Range* (m)	*Angle* (°)				
			Conventional	*Capon*	*MUSIC*	*DML*	*Range-Angle*
Uncal Tx	Param Est	3.01	19	20	19	14.26	-
	WB Param Est	3.01	19	23	19	21.98	
	NB Range-Angle	3.00	-	-	-	-	20
	TDWB Range-Angle	2.99	-	-	-	-	20
Cal Tx	Param Est	3.01	19	19	19	25.45	
	WB Param Est	3.01	20	24	20	21.96	
	NB Range-Angle	3.00	-	-	-	-	19
	TDWB Range-Angle	2.99	-	-	-	-	20

Table K.3: Single target location estimates when OMNI was transmitted.

Pattern	*Processing*	*Range* (m)	*Angle* (°)			
			Capon	*APES*	*GLRT*	*Tx-On-Rx*
Uncal Tx	Param Est	2.60	14	13	12	-
	WB Param Est	-	57	57	30	-
	Param Est *	2.97	20	20	21	-
	Param Est WB *	-	20	20	71	-
	NB Tx-on-Rx	3.51	-	-	-	18
	TDWB Tx-on-Rx	2.98	-	-	-	20
	FWWB Tx-on-Rx	-	-	-	-	57
Cal Tx	Param Est	2.71	19	-34	29	-
	Param Est WB	-	36	-50	0	-
	Param Est *	2.91	19	15	21	-
	Param Est WB *	-	20	20	20	-
	NB Tx-on-Rx	1.90	-	-	-	84
	TDWB Tx-on-Rx	2.98	-	-	-	20
	FWWB Tx-on-Rx	-	-	-	-	20

∗ Range was fixed

Table K.4: Single target location estimates when MIMOPD1 was transmitted.

Pattern	*Processing*	*Range* (m)	*Angle* (°)			
			Capon	*APES*	*GLRT*	*Tx-On-Rx*
Uncal Tx	Param Est	2.95	24	46	22	-
	Param Est Wb	-	24	-2	-2	-
	Tx-On-Rx NB	2.95	-	-	-	20
	Tx-On-Rx TDWB	2.99	-	-	-	20
	Tx-On-Rx FWWB	-	-	-	-	20
Cal Tx	Param Est	2.94	23	-24	21	-
	Param Est WB	-	21	-24	21	-
	Tx-On-Rx NB	2.94	-	-	-	20
	Tx-On-Rx TDWB	2.98	-	-	-	21
	Tx-On-Rx FWWB	-	-	-	-	20

Table K.5: Single target location estimates when MIMOBM1 was transmitted.

Pattern	*Processing*	*Range* (m)	*Angle* (°)			
			Capon	*APES*	*GLRT*	*Tx-On-Rx*
Uncal Tx	Param Est	2.95	21	36	21	-
	Param Est WB	-	21	78	21	
	Tx-On-Rx NB	2.94	-	-	-	20
	Tx-On-Rx TDWB	2.99	-	-	-	20
	Tx-On-Rx FWWB	-	-	-	-	20
Cal Tx	Param Est	2.98	23	24	23	-
	Param Est WB	-	21	45	22	
	Tx-On-Rx NB	2.93	-	-	-	16
	Tx-On-Rx TDWB	3.00	-	-	-	21
	Tx-On-Rx FWWB	-	-	-	-	19

Table K.6: Three target location estimates when PABM3 was transmitted.

Pattern	*Processing*	*Range* (m)	*Angle* (°)														
			Conventional			*Capon*			*MUSIC*			*DML*			*Range-Angle*		
Uncal Tx	Param Est	3.01	-18	1	22	-18	1	22	-17	-17	22	-21.20	-0.96	17.96	-		
	Param Est WB	-	-19	1	22	-21	0	28	-17	2	22	-22.01	-0.16	29.99	-		
	Range-Angle NB	3.01		-			-			-			-		-20	23	23
	Range-Angle TDWB	2.99		-			-			-			-		10	19	22
Cal Tx	Param Est	3.00	-18	20	22	-18	0	22	-18	22	22	-21.50	-1.14	17.80	-		
	ParamEstWB	-	-18	2	22	-18	0	27	-18	2	22	-16.78	-0.17	29.98			
	Range-Angle NB	3.01		-			-			-			-		-19	0	23
	Range-Angle TDWB	2.99		-			-			-			-		-20	19	22

Table K.7: Three target location estimates when PALCMV3 was transmitted.

Pattern	*Processing*	*Range* (m)	*Angle* (°)														
			Conventional			*Capon*			*MUSIC*			*DML*			*Range-Angle*		
Uncal Tx	Param Est	3.03	-18	1	22	-18	0	24	-18	0	23	-22.11	-0.55	17.94	-		
	Param Est WB	-	-18	0	23	-16	0	27	-18	0	23	-14.68	-0.12	43.25	-		
	Range-Angle NB	3.11	-			-			-			-			-19	-19	25
	Range-Angle TDWB	2.98	-			-			-			-			-22	2	21
Cal Tx	Param Est	3.03	-19	0	22	-19	0	24	-18	-18	22	-21.45	-0.25	18.43	-		
	Param Est WB	-	-19	0	22	-18	0	60	-18	0	22	-18.32	0.10	60.90	-		
	Range-Angle NB	3.10	-			-			-			-			- 19	-19	25
	Range-Angle TDWB	2.98	-			-			-			-			-21	20	22

Table K.8: Three target location estimates when OMNI was transmitted.

Pattern	*Processing*	*Range* (m)	*Angle* (°)											
			Capon			*APES*			*GLRT*			*Tx-On-Rx*		
Uncal Tx	Param Est	2.45	-18	21	35	-56	-18	21	-56	-18	21		-	
	Param Est WB	-	-44	21	56	-58	21	72	-86	-86	-13		-	
	Param Est*	2.91	0	23	61	-24	0	23	-25	0	24		-	
	Param Est WB*	-	-20	-1	22	-58	-20	22	-86	-86	38		-	
	Tx-On-Rx NB	3.47		-			-			-		-18	19	23
	Tx-On-Rx TDWB	2.98		-			-			-		0	20	21
	Tx-On-Rx FWWB	-		-			-			-		-54	24	54
Cal Tx	Param Est	2.45	-22	17	52	-37	-20	53	-37	-20	11		-	
	Param Est WB	-	1	19	35	-18	-3	72	-86	-86	8		-	
	Param Est*	2.91	-22	1	22	-20	1	22	-73	1	22		-	
	Param Est WB*	-	1	1	22	-21	0	20	-56	1	41		-	
	Tx-On-Rx NB	2.74		-			-			-		-17	1	20
	Tx-On-Rx TDWB	3.00		-			-			-		-1	20	21
	Tx-On-Rx FWWB	-		-			-			-		-18	-1	67

∗ Range was fixed

Table K.9: Three target location estimates when MIMOPD3 was transmitted.

Pattern	*Processing*	*Range* (m)	*Angle* (°)											
			Capon			*APES*			*GLRT*			*Tx-On-Rx*		
Uncal Tx	Param Est	2.95	28	36	46	-58	28	66	-21	1	23		-	
	Param Est WB	-	-71	-45	45	-70	36	45	1	10	22		-	
	Tx-On-Rx NB	2.91		-			-			-		-20	0	21
	Tx-On-Rx TDWB	2.98		-			-			-		-21	0	21
	Tx-On-Rx FWWB	-		-			-			-		0	0	21
Cal Tx	Param Est	2.92	-22	0	23	1	24	43	-21	1	23		-	
	Param Est WB	3.05	-26	0	22	-14	1	22	1	1	22		-	
	Tx-On-Rx NB	2.92		-			-			-		-18	1	19
	Tx-On-Rx TDWB	2.97		-			-			-		-23	0	21
	Tx-On-Rx FWWB	-		-			-			-		0	0	21

Table K.10: Three target location estimates when MIMOBM3 was transmitted.

Pattern	*Processing*	*Range* (m)	*Angle* (°)											
			Capon			*APES*			*GLRT*			*Tx-On-Rx*		
Uncal Tx	Param Est	2.93	0	28	48	-29	24	81	-44	0	23		-	
	Param Est WB	-	-51	0	22	-50	-9	0	-31	0	22		-	
	Tx-On-Rx NB	2.93		-			-			-		-20	0	21
	Tx-On-Rx TDWB	2.98		-			-			-		-21	0	21
	Tx-On-Rx FWWB	-		-			-			-		0	0	21
Cal Tx	Param Est	2.92	-19	0	12	-12	0	25	-19	0	23		-	
	Param Est WB	-	-26	0	22	-12	0	22	0	0	22		-	
	Tx-On-Rx NB	2.91		-			-			-		-19	0	24
	Tx-On-Rx TDWB	3.00		-			-			-		0	20	20
	Tx-On-Rx FWWB	-		-			-			-		-20	0	0

Table K.11: Small separation location estimates when PA was transmitted.

Pattern	*Processing*	*Range* (m)	*Angle* (°)									
			Conventional		*Capon*		*MUSIC*		*DML*		*Range-Angle*	
Uncal Tx	Param Est	3.0	14	21	18	20	16	21	22.95	22.95	-	
	Range-Angle NB	2.98	-		-		-		-		18	20
	Range-Angle TDWB	3.01	-		-		-		-		15	26
Cal Tx	Param Est	3.01	15	19	18	20	17	18	22.59	22.60	-	
	Range-Angle NB	2.98	-		-		-		-		17	19
	Range-Angle TDWB	3.0	-		-		-		-		13	17

Table K.12: Small separation location estimates when OMNI was transmitted.

Pattern	*Processing*	*Range* (m)	*Angle* (°)							
			Capon		*Apes*		*GLRT*		*Range-Angle*	
Uncal Tx	Param Est	2.82	-3	14	-3	26	-3	63	-	
	Param Est WB	-	19	26	19	27	-79	27	-	
	Range-Angle NB	3.14	-		-		-		15	16
	Range-Angle TDWB	3.00	-		-		-		12	16
	Range-Angle FWWB	-	-		-		-		15	27
Cal Tx	Param Est	2.89	14	18	14	24	-27	24	-	
	Param Est WB	-	16	50	26	50	26	50	-	
	Range-Angle NB	2.83	-		-		-		15	16
	Range-Angle TDWB	2.98	-		-		-		14	17
	Range-Angle FWWB	-	-		-		-		18	25

Table K.13: Small separation location estimates when MIMOPD was transmitted.

Pattern	*Processing*	*Range* (m)	*Angle* (°)							
			Capon		*Apes*		*GLRT*		*Range-Angle*	
Uncal Tx	Param Est	2.95	17	24	-65	-25	-26	18	-	
	Param Est WB	-	17	24	58	58	58	58	-	
	Range-Angle NB	2.85	-		-		-		19	20
	Range-Angle TDWB	3.01	-		-		-		17	24
	Range-Angle FWWB	-	-		-		-		17	18
Cal Tx	Param Est	2.94	19	23	-23	54	13	17	-	
	Param Est WB	-	18	19	-24	54	-23	39	-	
	Range-Angle NB	2.94	-		-		-		15	17
	Range-Angle TDWB	2.98	-		-		-		15	19
	Range-Angle FWWB	-	-		-		-		16	17

Table K.14: Small separation location estimates when MIMOBM was transmitted.

Pattern	*Processing*	*Range* (m)	*Angle* (°)							
			Capon		*Apes*		*GLRT*		*Range-Angle*	
Uncal Tx	Param Est	2.95	-28	18	28	36	8	18	-	
	Param Est WB	-	-28	17	28	77	-24	16	-	
	Range-Angle NB	2.98	-		-		-		19	20
	Range-Angle TDWB	3.01	-		-		-		17	24
	Range-Angle FWWB	-	-		-		-		17	18
Cal Tx	Param Est	2.95	17	20	20	23	23	24	-	
	Param Est WB	-	23	25	-8	26	-8	26	-	
	Range-Angle NB	2.91	-		-		-		18	24
	Range-Angle TDWB	3.00	-		-		-		26	44
	Range-Angle FWWB	-	-		-		-		23	26

Bibliography

[1] T. Jeffrey. *Phased-Array Radar Design: Application of Radar Fundamentals.* ScitTech Publishing, 2009.

[2] A.R. Thompson, J. M. Moran, and Jr G. W. Swenson. *Interferometery and Synthesis in Radio Astronomy.* John Wiley and Sons Inc., 2001.

[3] M Halliwell and P.N.T Wells, editors. *Acoustical Imaging.* Springer US, 2001.

[4] F.E. Whiteway. The Use of Arrays for Earthquake Seismology. *Proceedings of the Royal Society of London. Series A, Mathematial and Physical Sciences*, 290:328–342, 1966.

[5] M. Kopf K. Jaksch, F. Giese. Seismic Preditions While Drilling (SPWD): Seismic exploration ahead of the drill bit using phased array sources. *Geophysical Research Abstracts*, 12, 2010.

[6] S. Andersson, B. Calrqvist, B. Hagerman, and R. Lagerholm. Enhancing Cellular Network Capacity with Adaptive Antennas. *Ericsson Review*, 3:138 – 141, 1999.

[7] J.J. de Witt. Design of an acoustic simulator of a phased array radar. Master's thesis, Department of Electrical, Electronic and Computer Engineering, University of Pretoria, 2004.

[8] D.C. Stanton. Design of an Acoustic Two-Dimensional Phased Array Radar Simulator System. Master's thesis, Department of Electrical, Electronic and Computer Engineering, University of Pretoria, 2005.

[9] T. Haynes. A Primer on Digital Beamforming. *Spectrum Signal Processing*, March 1998.

[10] F. Daum and J. Huang. MIMO Radar: Snake Oil or Good Idea? *IEEE Aerospace and Electronic Systems Magazine*, pages 8–12, May 2009.

[11] J. Li and Petre Stoica. MIMO Radar with Colocated Antennas: Review of Some Recent Work. *IEEE Signal Processing Magazine*, 24(5):106–114, September 2007.

[12] D.W Bliss and K.W. Forsythe. Multiple-input multiple-output (MIMO) Radar and Imaging: Degrees of Freedom and Resolution. In *Conference Record of the Thirty-Seventh Asilomar Conference on Signals, Systems and Computers, 2003.*, volume 1, pages 54–59, November 2003.

[13] D.E. Dudgeon and R.M. Mersereau. *Multidimensional Digital Signal Processing.* Prentice-Hall, 1984.

[14] H. Krim and M. Viberg. Two Decades of Array Signal Processing Research. *IEEE Signal Processing Magazine*, 13(4):67–94, July 1996.

[15] J.E. Hudson. *Adaptive Array Principles.* The Institution of Electrical Engineers, 1981.

[16] F. G. Stremler. *Introduction to Communication Systems.* Addison-Wesley Publishing Company, second edition, 1982.

[17] C.A. Balanis. *Antenna Theory Analysis and Design.* John Wiley and Sons Inc., 1997.

[18] B. R. Mahafza. *Radar System Design and Analysis using MATLAB.* Chapman and Hall, 2000.

[19] H. Urkowitz. *Signal Theory and Random Processes.* Artech House, 1983.

[20] J.G. Proakis and D.G. Manolakis. *Digital Signal Processing.* Prentice Hall International Editions, third edition, 1996.

[21] Federal Communications Commision Document FCC 02-48, 2002.

[22] J.D. Taylor, editor. *Introduction to Ultra-Wideband Radar Systems.* CRC Press, 1995.

[23] H. Urkowitz, C. A. Hauer, and J. F. Koval. Generalized Resolution in Radar Systems. *Proceedings of the IRE*, 50(10):2093–2105, October 1962.

[24] B.D. Van Veen and K.M. Buckley. Beamforming: A Versatile Approach to Spatial Filtering. *IEEE ASSP Magazine*, 5(2):4–24, April 1988.

[25] A. van Wyk. Super-Resolution Techniques.

[26] J. Capon. High-Resolution Frequency-Wavenumber Spectrum Analysis. *Proceedings of the IEEE ASSP Magazine*, 57(8):1408–1418, August 1969.

[27] O.L. Frost. An Algorithm for Linearly Constrained Adaptive Array Processing. *IEEE Proc.*, 60:926–935, 1972.

[28] F.C. Robey, S. Coutts, D. Weikle, J.C. McHarg, and K. Cuomo. MIMO Radar Theory and Experimental Results. In *Conference Record of the Thirty-Eighth Asilomar Conference on Signals, Systems and Computers*, volume 1, pages 300–304, 2004.

[29] E. Fishler, A. Haimovich, R.S. Blum, Jr L.J. Cimini, D. Dhizhik, and R.A. Valenzuela. Spatial Diversity in Radars - Models and Detection Performance. *IEEE Transactions on Signal Processing*, 54:823–838, 2006.

[30] D.R. Fuhrmann and G.S. Antonio. Transmit Beamforming for MIMO Radar Systems Using Partial Signal Correlation. In *Proceedings of the 38th Asilomar Conference on Signals, Systems and Computers*, volume 1, pages 295–299, November 2004.

[31] G.J. Frazer, Y.I. Abramovich, B.A. Johnson, and F.C. Robey. Recent Results in MIMO Over-the-Horizon Radar. In *IEEE Radar Conference Proceedings*, 2008.

[32] L. Xu, J. Li, and P. Stoica. Radar Imaging via Adaptive MIMO Techniques. In *Proceedings of 14th European Signal Processing Conference (EUSIPCO '06)*, September 2006.

[33] E. Fishler, A. Haimovich, R. Blum, L. Cimini, D. Chizhik, and R. Valenzuela. MIMO Radar: An Idea whose Time has Come. In *Proceedings of IEEE Radar Conference*, pages 71–78, April 2004.

[34] N.H. Lehmann, E. Fishler, A.M. Haimovich, R.S. Blum, D Chizhik, Jr L.J. Dimini, and Valenzuela R.A. Evaluation of Transmit Diversity in MIMO-radar Direction Finding. *IEEE Transactions on Signal Processing*, 55(5):2215–2225, May 2007.

[35] N.H. Lehmann, A.M. Haimovich, R.S. Blum, and L. Cimini. High Resolution Capabilities of MIMO Radar. In *Fortieth Asilomar Conference on Signals, Systems and Computers (ACSSC)*, pages 25–30, October 2006.

[36] P. Stoica, J. Li, and Y. Xie. On Probing Signal Design for MIMO Radar. *IEEE Transactions on Signal Processing*, 55(8):4151–4161, August 2007.

[37] D. Tse and P. Viswanath. *Fundamentals of Wireless Communication*. Cambridge University Press, draft edition, September 2004.

[38] K.W. Forsythe, D. W. Bliss, and G.S. Fawcett. Multiple-input Multiple-Output (MIMO) Radar: Performance Issues. In *Asilomar Conference on Signals, Systems and Computers*, volume 1, pages 310–315, November 2004.

[39] P.P. Vaidyanathan, Pal. P., and C. Chen. MIMO Radar with Broadband waveforms: Smearing Filter Banks and 2D Virtual Arrays. In *42nd Asimolar Conference on Signals, Systems and Computers*, pages 188–192, 2008.

[40] J. Li and P. Stoica, editors. *"MIMO Radar Signal Processing"*. Wiley, first edition, 2009.

[41] L. Xu, P. Stoica, and J. Li. A Diagonal Growth Curve Model and Some Signal-Processing Applications. *IEEE Transactions on Signal Processing*, 54(9):3363–3371, September 2006.

[42] J. F. Sturm. Using SeDuMi 1.02, A MATLAB Toolbox for Optimization over Symmetric Cones. 2001.

[43] I. Polik. Addendum to the SeDuMi User Guide Version 1.1. 2005.

[44] L. Vandenberghe and S. Boyd. Semidefinite Programming. *Society for Industrial and Applied Mathematics Review*, 38:49–95, 1996.

[45] A. Hassanien and S.A. Vorobyov. Phased-MIMO Radar: A Tradeoff Between Phased-Array and MIMO Radars. *IEEE Transactions on Signal Processing*, 58 (6):3137–3151, June 2010.

[46] Y. Qu, G. S. Liao, S. Q. Zhu, X. Y. Liu, and H. Jiang. Performance Analysis of Beamforming for MIMO Radar. *Progress in Electromagnetics Research*, 84: 123–134, 2008.

[47] Y.I. Abramovich and G.J. Frazer. Bounds on the Volume and Height Distributions for the MIMO Radar Ambiguity Function. *IEEE Signal Processing Letters*, 15:505–508, 2008.

[48] J.C. Smit, J.E. Cilliers, C.J. Baker, and Hanekom J. J. X-Band High Range Resolution Radar Measurements of Sea Surface Forward Scatter at Low Grazing Angles. In *2008 IEEE Radar Conference*, pages 2031–2034, May 2008.

[49] D. W. Bliss, K.W. Forsythe, Davis S. K., G. S. Fawcett, Rabideau D.J., L.L. Horowitz, and Kraut S. GMTI MIMO Radar. In *2009 International Waveform Diversity and Design Conference*, pages 118 – 122, February 2009.

[50] G.W. Stimson. *Introduction to Airborne Radar*. Scitech Publishing, Inc, second edition, 1998.

[51] J.H. Justice, N.L. Owsley, J.L. Yen, and A.C. Kak. *Array Signal Processing*. Prentice-Hall, 1985.

[52] T.I. Laakso, V. Valimaki, M Karjalainen, and U.K. Laine. Splitting the Unit Delay: Tools for fractional filter design. *IEEE Signal Processing Magazine*, 13 (1):30–60, January 1996.

[53] J. Tang, C. Sun, Y. Yang, and J. Zhuo. Optimum Design on Time Domain Wideband Beamformer with Constant Beamwidth for Sonar Systems. In *IEEE Techno-Ocean '04*, volume 2, pages 625–630, November 2004.

[54] D.K Barton. *Modern Radar System Analysis*. Artech House, 1988.

[55] *Omnidirectional Back Electret Condenser Microphone Cartridge - F6035AP*. JLI Electronics Inc.

[56] B. Baker. What does the ADC SNR mean. *EDN Magazine*, page 24, May 2004.

[57] *ML505/ML506/ML507 Evaluation Platform User Guide*. Xilinx, ug347 v3.0.1 edition, July 2008.

[58] J Johnson. Microblaze 16x2 LCD Driver, . URL `http://www.fpgadeveloper.com/2008/10/microblaze-16x2-lcd-driver.html`.

[59] WinPcap: The Windows Packet Capture Library. URL `http://www.winpcap.org/`.

[60] S. Leach. Singular Value Decomposition - A Primer. *Department of Computer Science, Brown University*, Draft Version.

[61] J.P. Keener. *Principles of Applied Mathematics: Transformations and Approximation*. Westview Press, 1999.

[62] L.E. Franks. *Signal Theory*. Prentice Hall, September 1969.

[63] S. Haykin. *Adaptive Filter Theory*. Prentice Hall.

[64] D. Johnson. Constrained optimization, . URL `http://cnx.org/content/m11223/latest/`.

[65] T. K. Moon and W. C. Stirling. *Mathematical Methods and Algorithms for Signal Processing*. Prentice Hall, Upper Saddle River, NJ, 2000.

[66] M. Godavarti and A.O. Hero. Diversity and Degrees of Freedom In Wireless Communication. *Proceedings of the IEEE International Conference on Acoustic Speech and Signal Processing*, May 2001.

[67] M. Brookes. The Matrix Reference Manual, [online]. URL `http://www.ee.ic.ac.uk/hp/staff/dmb/matrix/intro.html`.

[68] *XPS Ethernet Lite Media Access Controller (v2.00a).* Xilinx, ds580 edition, December 2007.

[69] *AD7490 16-Channel, 1 MSPS, 12-Bit ADC with Sequencer in 28-Lead TSSOP.* Analog Devices, 2002.

[70] *MAX5306/MAX5307 Low Power, Low-Glitch, Octal 12-Bit Voltage-Output DACs with Serial Interface.* Maxim, 19-2132 edition, 2001.

[71] H. F. Olson. *Elements of Acoustical Engineering.* D. Van Nostrand Company Inc., second edition, 1948.